INFORMATION TO USERS

This manuscript has been reproduced from the microfilm master. UMI films the text directly from the original or copy submitted. Thus, some thesis and dissertation copies are in typewriter face, while others may be from any type of computer printer.

The quality of this reproduction is dependent upon the quality of the copy submitted. Broken or indistinct print, colored or poor quality illustrations and photographs, print bleedthrough, substandard margins, and improper alignment can adversely affect reproduction.

In the unlikely event that the author did not send UMI a complete manuscript and there are missing pages, these will be noted. Also, if unauthorized copyright material had to be removed, a note will indicate the deletion.

Oversize materials (e.g., maps, drawings, charts) are reproduced by sectioning the original, beginning at the upper left-hand corner and continuing from left to right in equal sections with small overlaps.

Photographs included in the original manuscript have been reproduced xerographically in this copy. Higher quality 6" x 9" black and white photographic prints are available for any photographs or illustrations appearing in this copy for an additional charge. Contact UMI directly to order.

Bell & Howell Information and Learning
300 North Zeeb Road, Ann Arbor, MI 48106-1346 USA

UMI®
800-521-0600

TECHNETIUM(VII) AND RHENIUM(VII) OXOFLUORIDES AND THE ROLE OF NOBLE-GAS FLUORIDES IN THEIR SYNTHESES

By

NICOLAS LEBLOND

A Thesis

Submitted to the School of Graduate Studies

in Partial Fulfilment of the Requirements

for the Degree

Doctor of Philosophy

McMaster University

TECHNETIUM(VII) AND RHENIUM(VII) OXOFLUORIDES AND THE ROLE OF NOBLE-GAS FLUORIDES IN THEIR SYNTHESES

DOCTOR OF PHILOSOPHY (1998)
(Chemistry)

McMaster University
Hamilton, Ontario

TITLE: Technetium(VII) and Rhenium(VII) Oxofluorides and the Role of Noble-Gas Fluorides in Their Syntheses.

AUTHOR: Nicolas LeBlond, B.Sc. (Université Laval)

SUPERVISOR: Professor G.J. Schrobilgen

NUMBER OF PAGES: xxiv, 336

ABSTRACT

Technetium, a β-particle emitter with a half-life of 2.12×10^5 years, represents 6% of the fission products in commercial nuclear reactors. Although ^{99}Tc is not released during normal operation of nuclear power reactors, technetium may be introduced into the environment at other stages of the nuclear fuel cycle and is particularly prevalent as a contaminant near uranium enrichment facilities using recycled UF_6.

Until recently, the only known fluorine derivatives of Tc were the two binary fluorides, TcF_5 and TcF_6, two oxofluorides, $TcOF_4$ and TcO_3F and the four anions TcF_6^{2-}, TcF_6^-, TcF_7^- and TcF_8^{2-}. The fluorine chemistry of technetium was recently extended with the preparation of the fluorine-bridged infinite-chain polymer TcO_2F_3 by fluorination of TcO_3F by XeF_6 in anhydrous HF. The purpose of this work was to study the fluoride-ion donor and acceptor properties of TcO_2F_3 and its rhenium analog, ReO_2F_3, as well as the synthesis and characterization of $TcOF_5$ and possibly TcF_7.

The significant Lewis acidity of TcO_2F_3 toward the fluoride ion and CH_3CN led to the preparation of the $TcO_2F_4^-$ anion as its Li^+, Cs^+ and $N(CH_3)_4^+$ salts, and the $TcO_2F_3(CH_3CN)$ adduct. Characterization by ^{17}O, ^{19}F, ^{99}Tc NMR and Raman spectroscopy established that the $TcO_2F_4^-$ anion has a *cis*-dioxo geometry, which was confirmed by a single-crystal X-ray structure determination of $Li^+TcO_2F_4^-$.

By analogy, ReO_2F_3 is also a Lewis acid forming $M^+ReO_2F_4^-$ [M = Li, Na, K, Cs, $N(CH_3)_4$] and $ReO_2F_3(CH_3CN)$. In addition, the oligomeric anions $Re_2O_4F_7^-$ and $Re_3O_6F_{10}^-$ were isolated and their structures were determined by X-ray diffraction. These anions

consist of two and three fluorine-bridged ReO_2F_4-units in which the oxygen atoms are *cis* to each other and *trans* to the bridging fluorines. The X-ray structure of ReO_2F_3 was also determined for the first time and is similar to that of TcO_2F_3.

Both TcO_2F_3 and ReO_2F_3 behave as fluoride-ion donors, dissolving readily in hydrogen fluoride solutions acidified with the strong Lewis acids AsF_5 and SbF_5, and forming $MO_2F_3 \cdot PnF_5$ adducts (M = Tc, Re; Pn = As, Sb). The structures of $TcO_2F_3 \cdot SbF_5$ and $ReO_2F_3 \cdot SbF_5$ consist of infinite chains of alternating fluorine-bridged MO_2F_4- and SbF_6-units with the oxygen atoms *cis* to each other and *trans* to the bridging fluorines. The crystal structure of $TcO_2F_3 \cdot XeO_2F_2$, a byproduct of the synthesis of TcO_2F_3, was also determined by X-ray crystallography and consists of TcO_2F_3 infinite chains linked together by a layer of XeO_2F_2 through xenon-fluorine long contacts.

The structures of TcO_2F_3 and ReO_2F_3 in SO_2ClF solution were elucidated by ^{19}F NMR spectroscopy and consist of cyclic fluorine-bridged species, $(MO_2F_3)_n$, where n = 3 for M = Tc and n = 3, 4 and 5 for M = Re.

A new technetium(VII) oxofluoride, $TcOF_5$, was prepared from the reaction of TcO_2F_3 with an excess of KrF_2 in anhydrous HF. This volatile orange solid was characterized by NMR and Raman spectroscopy which confirmed its pseudooctahedral geometry. The fluoride-ion donor behaviour of $TcOF_5$ was investigated resulting in the preparation of the dinuclear cation $Tc_2O_2F_9^+$ as its $Sb_2F_{11}^-$ and AsF_6^- salts, and the structure of $Tc_2O_2F_9^+Sb_2F_{11}^-$ was determined by X-ray crystallography. Attempts to prepare the heptacoordinated species $TcOF_6^-$ and TcF_7 were unsuccessful.

ACKNOWLEDGMENTS

I wish to thank Prof. Gary Schrobilgen for his guidance, enthusiasm and for sharing some of his vast experience with me. These were appreciated in all aspects of this challenging and exciting project.

I would like to acknowledge the other members of my supervisor committee, Dr. Raman Chirakal for his help and Dr. Ronald Gillespie for accepting to fill in after the passing of Dr. Lock.

Je voudrais remercier mes parents et mes frères pour leur support et encouragements tout au long de ce projet.

I am grateful to the many people who have offered their friendship and support during my stay at McMaster, especially Drs. Hélène Mercier, Ayaaz Pirani, Janette Campbell, Marc Whalen, Bill Casteel, Jr. and Jeremy Sanders. I also enjoyed the company of Barbara Fir, Bernard Pointner, and particularly Michael Gerken, with whom I had many fascinating discussions on chemistry, movies, art and the meaning of life. How can I forget Dave Green, my always punctual work-out partner!

I would like to thank Dr. Jim Britten, Brian Sayer, Dr. Don Hughes, George Timmins, Michael Palme, Mike Mallot and Karen Neumann for there valuable assistance over the years.

Finally, I gratefully acknowledge the Natural Sciences and Engineering Research Council of Canada, le Fonds pour la Formation de Chercheurs et l'Aide à la Recherche and the Department of Chemistry of McMaster University for their financial support.

To the dull mind all nature is leaden. To the illumined mind the whole world burns and sparkles with light.

Ralph Waldo Emerson

LIST OF ABBREVIATIONS AND SYMBOLS

General

bpy	2,2'-bipyridine
DMF	dimethylformamide
FEP	perfluoroethylene/perfluoropropylene copolymer
i.d.	inner diameter
IR	infrared spectroscopy
Kel-F	chlorotrifluoroethylene polymer
MS	mass spectrometry
MW	microwave spectroscopy
o.d.	outer diameter
PTFE	tetrafluoroethylene polymer
SAE	Society of Automotive Engineers
THF	tetrahydrofuran
UV	ultraviolet-visible spectroscopy

Nuclear Magnetic Resonance Spectroscopy

FID	free-induction decay
I	nuclear spin quantum number
J	scalar coupling constant in hertz
ppm	parts per million
TMS	tetramethylsilane

TABLE OF CONTENTS

LIST OF TABLES

LIST OF FIGURES

CHAPTER 1

INTRODUCTION

Discovery, Production and Applications of Technetium

Technetium is a member of Group 7 along with manganese, rhenium and bohrium and is the lightest element (Z = 43) in the periodic table that does not have a stable isotope. Technetium was first detected in 1937 by C. Perrier and E. Segré in a sample of molybdenum that had been bombarded with deuterons.[1] It was later detected in the spectra of numerous MS-, S- and N-type stars.[2] Today, technetium is produced in kilogram amounts in commercial nuclear reactors where it represents about 6% of the fission products.[3] After removal of the plutonium and uranium for recycling, technetium is recovered from the other waste products by solvent extraction or ion-exchange techniques. Technetium produced by this method consists exclusively of the ^{99}Tc isotope which undergoes β^- decay (293 keV) with a half-life of 2.12×10^5 years.

The long radioactive half-life and emission of low-energy β^- radiation of Tc allow it to be used with a minimum of controls in some specific applications.[4] Technetium has been shown to be a superconductor, having the second highest critical temperature of any element (T_c = 7.75 K). Higher critical temperatures were observed in alloy phases with V, Zr, Nb and Mo, reaching a maximum of 15.8 K for Tc_3Mo.[5] The TcO_4^- anion exhibits impressive properties as a corrosion inhibitor in steel. As little as 50 ppm of Tc is needed

to reduce the corrosion rate of carbon steel by four orders of magnitude.[6] Alumina-supported technetium catalysts were shown to have good resistance against poisoning by organic sulfur compounds. Their use has been proposed in the refining of hydrocarbon fuels in which they could partly substitute for the more expensive platinum-based catalysts.[4]

Technetium in the Nuclear Fuel Cycle

The fluorine chemistry of technetium is particularly relevant to the nuclear fuel cycle since ^{99}Tc makes up an important fraction of the uranium fission products in nuclear reactors. In the United States, the partially depleted uranium is recovered and reenriched in ^{235}U by gaseous diffusion of UF_6, which contains trace amounts of volatile TcO_3F, TcF_6 and other uncharacterized technetium oxofluorides.[3] In the last 40 years of operation, large quantities of these technetium compounds have accumulated within the diffusion cascades of the reenrichment plants. Accidental releases of technetium into the environment are frequent, both at the plant site and where the nuclear fuel is refabricated.[3] Consequently, an understanding of the fluoride and oxofluoride chemistry of high-valent technetium is of fundamental importance to the reprocessing of nuclear fuels, particularly in terms of its environmental impact.

Technetium in Nuclear Medicine

Another isotope of technetium, ^{99m}Tc, is already used extensively in nuclear medicine as an imaging agent for organs, bones and other tissues.[7] This metastable isotope

is produced from the β^- decay of ^{99}Mo with a 87.2% probability. Technetium-99*m* then almost quantitatively converts to the ground state ^{99}Tc by isomeric transition with a half-life of 6.01 h and emission of photons of 140.5 keV (89%) (Scheme I). The ^{99m}Tc, which

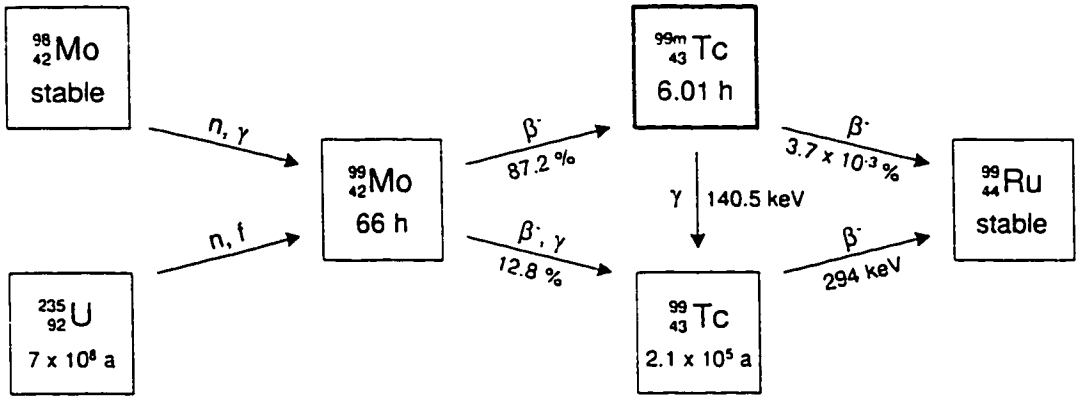

Scheme I

is injected into the body as TcO_4^- or in the form of a low-valent organometallic complex, concentrates in the organ to be investigated and emits a 140.5 keV photon which is detected by planar scintigraphy or emission tomography to produce an image of the organ. Over 80% of the radiopharmaceuticals currently used are labelled with ^{99m}Tc, whose nuclear properties are almost optimal with regard to low radiation exposure of the patient and effective detection of the emitted γ photon. For imaging and functional testing of organs in human bodies, about 0.5-30 mCi (18.5-1110 MBq) ^{99m}Tc are needed, which corresponds to a maximum of 6 ng.[7]

Previously Known Technetium and Rhenium Fluorides and Oxofluorides

The radioactivity of technetium has been a limiting factor in the development of its chemistry, particularly in the case of the fluorides and oxofluorides. A significant

amount of the synthetic work related to technetium fluorides and oxofluorides was published in the early 1960's when macroscopic amounts of the element first became available. In contrast, the chemistry of rhenium and its compounds is better documented. Tables 1.1 lists the known rhenium fluorides and oxofluorides along with their syntheses, physical properties and some of the methods used for their characterization. Important similarities are expected between the chemistries of technetium and rhenium as is observed for other pairs of row 5 and 6 transition elements. For example, when Tc or Re metal is combusted in an oxygen atmosphere, each attains its highest oxidation state (+7) producing volatile dimetal heptoxides according to equation (1.1).[30] This relative ease in

$$2\ M + {}^{7}/_{2}\ O_2 \xrightarrow{400\ ^\circ C} M_2O_7 \qquad (M = Tc \text{ or } Re) \tag{1.1}$$

going from oxidation state 0 to +7 results from the high oxophilicity of transition metals, particularly in groups 6 to 8. The stabilization of the highest oxidation states of these elements results from extensive pπ-dπ bonding between filled p orbitals of the oxygen ligands and the metal atom.

The binary fluorides of technetium, TcF_5 and TcF_6, can be prepared by direct fluorination of the metal at 350-400 °C, either in a closed nickel can, which promotes higher yields of TcF_6,[31] or in a flow system, which produces a mixture of fluorides as shown in equation (1.2).[32] There is no evidence for the formation of TcF_7 under these conditions.

$$Tc \xrightarrow[350\ ^\circ C]{F_2/N_2\ flow} TcF_5 + TcF_6 \tag{1.2}$$

Table 1.1 Rhenium Fluorides and Oxofluorides

Compound	Oxidation	Colour	m.p.(°C)	b.p.(°C)	Methods of Preparation	Characterization	Ref.
ReO_3F	VII	yellow	147	164	ReO_3Cl + HF $KReO_4$ in IF_5 Re_2O_7 + ReF_7	MW, IR, Raman, UV, MS	8,9,10,11,12,13
ReO_2F_3	VII	white	115		ReO_2 or $KReO_4$ or Re_2O_7 + F_2	IR, Raman, UV, MS	10,12,13,14
$ReOF_5$	VII	cream	34.5	55	ReO_2 or $ReOF_4$ + F_2	IR, Raman, NMR, ED, UV, MS	10,13,15,16,17
ReF_7	VII	yellow	48.3	73.72	Re + F_2	IR, Raman, NMR, powder X-ray	15,18,19,20,21
ReO_2F_2	VI	reported but not isolated					22
$ReOF_4$	VI	blue	108	171	ReF_6 + $M(CO)_x$ hydrolysis of ReF_6 Re + O_2/F_2	IR, Raman, X-ray, UV, MS	10,13,23,24,25,26
ReF_6	VI	yellow	18.5	33.68	Re + F_2	IR, Raman, powder X-ray	19,27
ReO_2F	V	-	-	-	hydrolysis of ReF_5	IR	28
$ReOF_3$	V	black	-	-	$ReOF_4$ + Pyrex glass	powder X-ray	23
ReF_5	V	green	48	d 140	ReF_6 + $W(CO)_6$ in WF_6		23
$ReOF_2$	IV	-	-	-	hydrolysis of ReF_4	IR	28
ReF_4	IV	blue	subl. 300		thermal decomp. of ReF_5 ReF_5 + Re	powder X-ray	23,29

Both the pentafluoride and the hexafluoride of technetium are volatile yellow solids with melting points of 50 °C and 37.4 °C, respectively. The X-ray powder diffraction shows that TcF_5 is isostructural with CrF_5 and VF_5, in which the MF_6-units are linked in endless chains through *cis*-fluorine bridges.[32] Technetium hexafluoride was characterized by vibrational spectroscopy and X-ray powder diffraction and is isomorphous with other transition metal hexafluorides (Mo, Ru, Rh, W, Re, Os, Ir and Pt) with an orthorhombic to body-centred cubic transition temperature of -5.3 °C.[33]

Reduction of TcF_6 to TcF_6^- is achieved by reaction with chlorides[32,34] or nitric oxide according to equations (1.3) and (1.4).[34-36] Technetium hexafluoride also behaves as a fluoride-ion acceptor in the presence of nitryl fluoride and nitrosyl fluoride to form TcF_7^- and TcF_8^{2-}, respectively [eq. (1.5) and (1.6)].[35] The principal methods of

$$TcF_6 + MCl \xrightarrow{IF_5} M^+TcF_6^- \ (M = Na, K, Rb, Cs) \qquad (1.3)$$

$$TcF_6 + NO \longrightarrow NO^+TcF_6^- \qquad (1.4)$$

$$TcF_6 + NO_2F \longrightarrow NO_2^+TcF_7^- \qquad (1.5)$$

$$TcF_6 + 2\ NOF \longrightarrow (NO^+)_2TcF_8^{2-} \qquad (1.6)$$

characterization used for these compounds were infrared spectroscopy and X-ray powder diffraction. The fluoride-ion affinity of TcF_6 is exploited in its separation from recycled UF_6 before reenrichment in diffusion plants. For this purpose, MgF_2 pellets are used as the fluoride-ion source.[3]

The fluorination of technetium by the flow method [eq. (1.2)] yields small amounts of $TcOF_4$.[32,37] This compound crystallizes in two distinct phases which have been characterized by single-crystal X-ray diffraction.[37] The structure of the more volatile green form of $TcOF_4$ consists of discrete trimeric units, with the Tc atoms forming a triangle linked asymmetrically by *cis*-bridging fluorine atoms (Figure 1.1a). The blue modification of $TcOF_4$ has a melting point of 134 °C and has a polymeric, fluorine-bridged structure (VF_5-type structure). Two analogous crystallographic modifications have also been characterized for $ReOF_4$, where the polymeric modification is dark blue (Figure 1.1b) and the trimeric modification is light blue.[24,25]

One important difference between the chemistries of Re(VII) and Tc(VII) fluorides and oxofluorides is the fact that, unlike TcF_7, ReF_7 can be prepared relatively easily by direct fluorination of Re metal with 3 atm of fluorine gas, according to equation (1.7).[18,19]

$$Re \xrightarrow{F_2} ReF_6 + ReF_7 \qquad (1.7)$$

Lower temperatures and pressures favour higher yields of the hexafluoride, although ReF_7 is always present in the product mixture. Once ReF_7 is prepared, all the possible oxofluorides of Re(VII) can, in principle, be synthesized either by controlled hydrolysis of ReF_7 or by reaction of stoichiometric amounts of ReF_7 and Re_2O_7, as seen in equation (1.8). The significant oxophilicity of rhenium(VII) rapidly drives these reactions to completion.

$$x\ ReF_7 + 3\ Re_2O_7 \longrightarrow \underset{(x = 1)}{ReO_3F} \text{ or } \underset{(x = 4.5)}{ReO_2F_3} \text{ or } \underset{(x = 15)}{ReOF_5} \qquad (1.8)$$

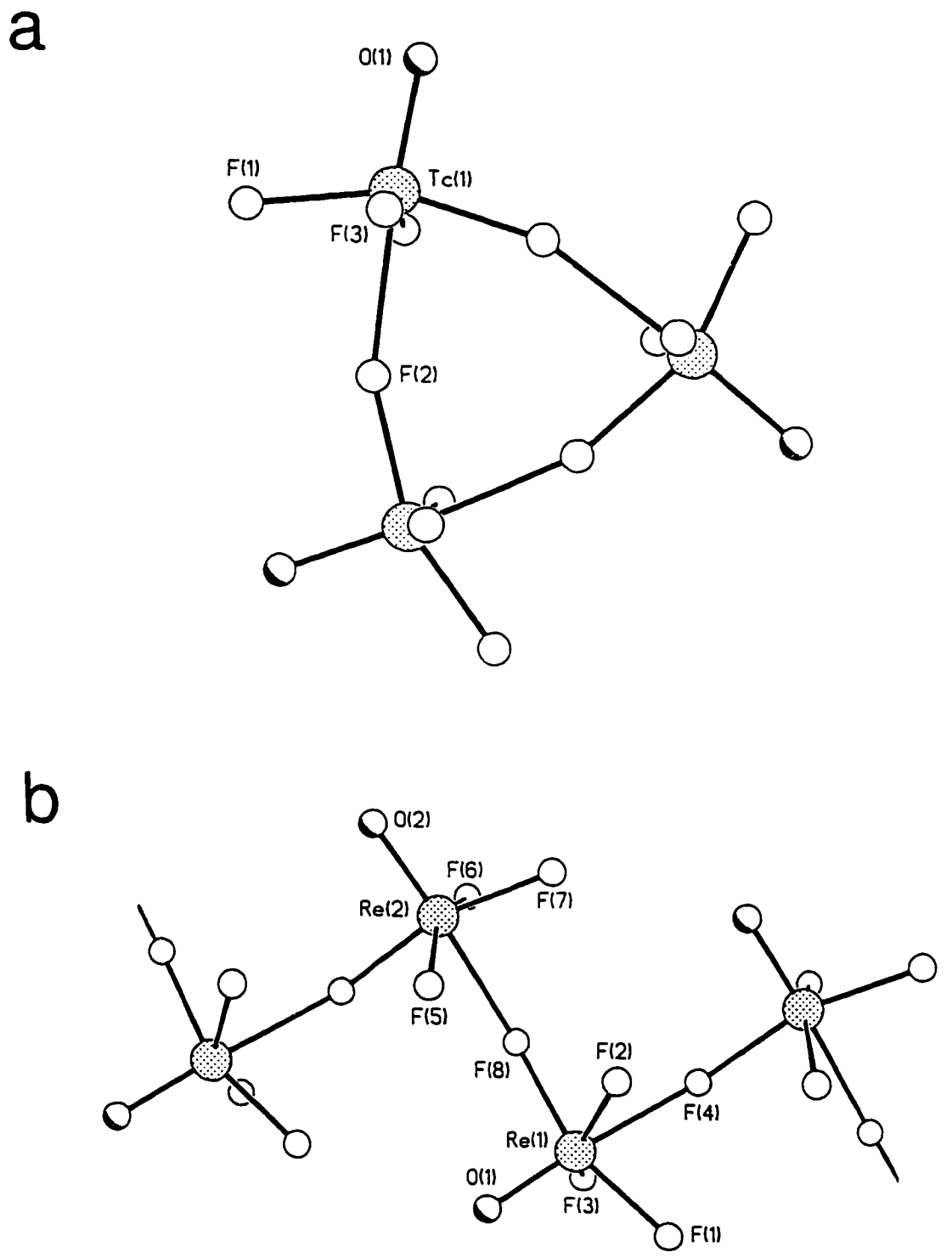

Figure 1.1. Structures of (a) trimeric (green) $TcOF_4$ [37] and (b) polymeric $ReOF_4$.[25]

Because TcF_7 is not yet known, the oxofluorides of Tc(VII) have to be synthesized by fluorination of the oxide. In this case, the high oxophilicity of Tc(VII) makes the replacement of each oxygen ligand with fluorine increasingly more difficult. Pertechnyl fluoride, TcO_3F, was the first oxofluoride of technetium(VII) to be reported.[38] The yellow liquid (m.p. 18.3 °C) was prepared by passing fluorine gas at 250 torr pressure over TcO_2 in a nickel tube at 150 °C, according to equation (1.9). This contrasts with what is observed when ReO_2 is submitted to the same experimental procedure, where the major products are ReO_2F_3 and $ReOF_5$, as seen in equation (1.10).[14] Pertechnyl fluoride, TcO_3F, was characterized by infrared,[39] Raman,[39] ^{19}F, ^{17}O and ^{99}Tc NMR spectroscopy.[40]

$$TcO_2 \xrightarrow[150\ °C]{F_2\ flow} TcO_3F \qquad (1.9)$$

$$ReO_2 \xrightarrow[150\ °C]{F_2\ flow} ReO_2F_3 + ReOF_5 \qquad (1.10)$$

Selig and co-workers showed that TcO_3F can also be produced by solvolysis of TcO_4^- in anhydrous HF, according to equation (1.11).[39]

$$TcO_4^- + 3\ HF \xrightarrow{HF} TcO_3F + H_3O^+_{(solv)} + 2\ F^-_{(solv)} \qquad (1.11)$$

The second oxofluoride of technetium(VII), TcO_2F_3, was synthesized by first dissolving Tc_2O_7 in anhydrous HF and then using XeF_6 as a fluorinating agent and dehydrating agent according to equations (1.12)-(1.14).[41]

$$Tc_2O_7 + 4\ HF \longrightarrow 2\ TcO_3F + H_3O^+ + HF_2^- \qquad (1.12)$$

$$TcO_3F + XeF_6 \longrightarrow TcO_2F_3 + XeOF_4 \quad (1.13)$$

$$XeF_6 + H_3O^+ + HF_2^- \longrightarrow XeOF_4 + 4\ HF \quad (1.14)$$

The bright yellow solid (m.p. 200 °C) was characterized by Raman spectroscopy and by single-crystal X-ray diffraction. The structure of TcO_2F_3 consists of infinite chains of fluorine-bridged TcO_2F_4-units in which the oxygen atoms are *cis* to each other and *trans* to the bridging fluorine atoms (Figure 1.2).

Known Oxofluorocations and Oxofluoroanions of Tc(VII) and Re(VII)

The fluoride-ion donor abilities of TcO_3F were investigated by Schrobilgen et al.[42] who found that reaction with AsF_5 in HF yields the TcO_3^+ cation, according to equation (1.15). The pale yellow salt was characterized by ^{99}Tc NMR[40] and Raman[42] spectroscopy which showed that the cation possesses D_{3h} symmetry.

$$TcO_3F + AsF_5 \xrightarrow{HF} TcO_3^+AsF_6^- \quad (1.15)$$

The ReO_3^+ moiety is well known and was characterized in a number of organometallic complexes such as $(\eta^5\text{-}C_5Me_5)ReO_3$,[43] $[(C_6H_{15}N_3)ReO_3]^+$ [44] and $[(C_6H_{12}S_3)ReO_3]^+$.[45] In these complexes, the cyclic ligands are strongly bonded to ReO_3^+, which adopts a pyramidal geometry with O-Re-O angles of 102.7(4) and 107.4(7)° for the triazo- and trithio-complexes, respectively (Figure 1.3a). The reaction of ReO_3F with strong Lewis acids such as AsF_5 or SbF_5 has not been reported.

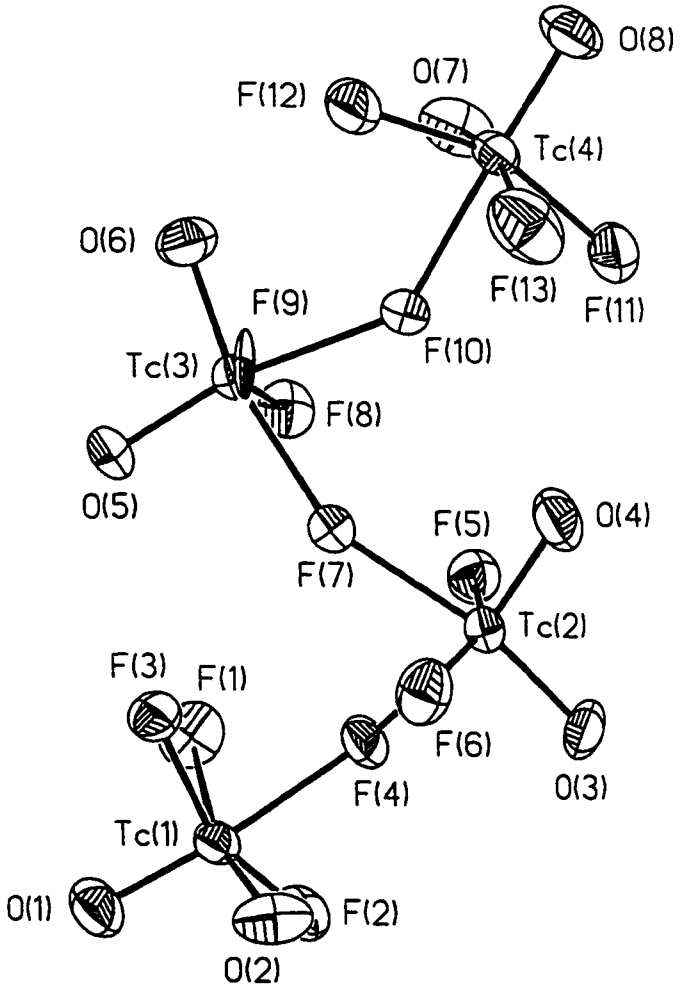

Figure 1.2. Structure of polymeric TcO_2F_3 (thermal ellispoids are at the 50% probability level).[41]

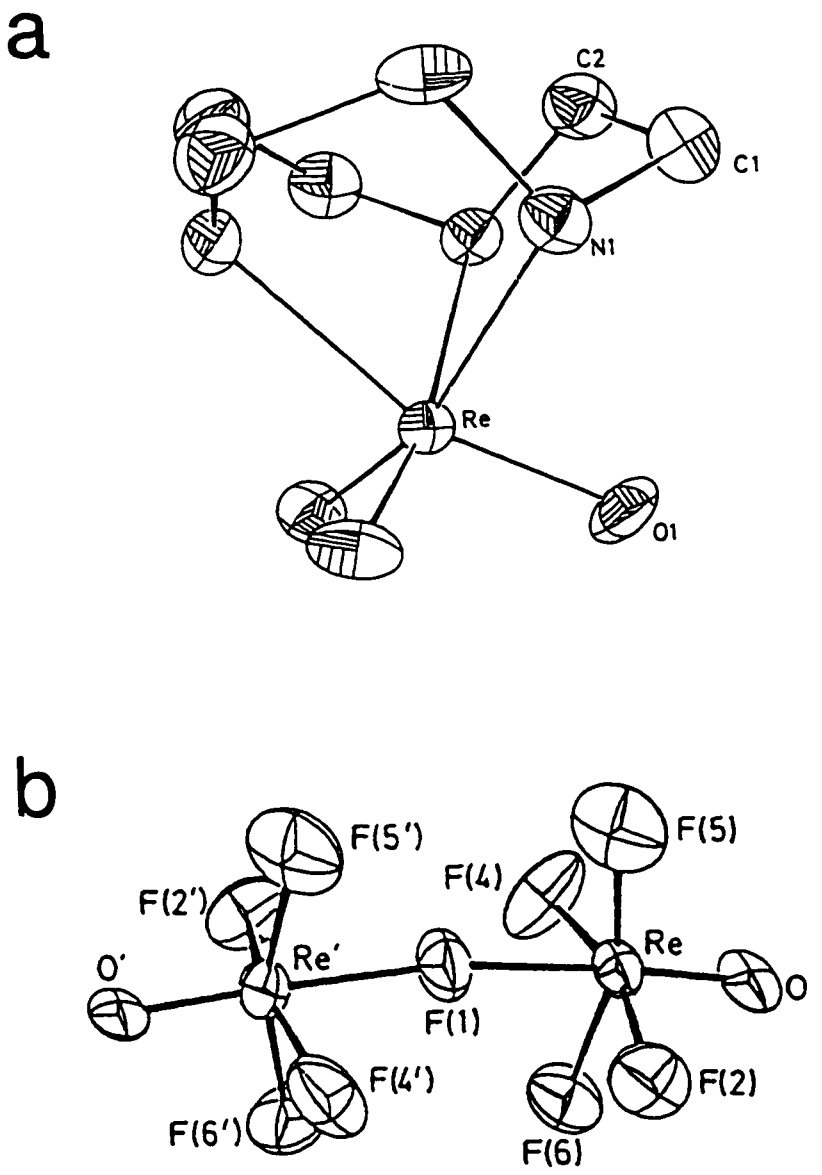

Figure 1.3. Structures of (a) the $(C_6H_{14}N_3)ReO_3^+$ cation[44] and (b) the $Re_2O_2F_9^+$ cation[46] (thermal ellipsoids are at the 50% probability level).

The fluoride-ion donor properties of ReF_7 and $ReOF_5$ where also investigated and the cations ReF_6^+, $ReOF_4^+$ and $Re_2O_2F_9^+$ were synthesized and characterized by vibrational spectroscopy and mass spectrometry.[46] A crystal structure of the $Re_2O_2F_9^+Sb_2F_{11}^-$ salt was reported in which the cation consists of two $ReOF_5$ octahedra bridged by the fluorine *trans* to the oxo ligand (Figure 1.3b). The $ReOF_4^+$ cation was argued to possess a square pyramidal geometry based on the similarities between its vibrational spectrum and those of monomeric $MoOF_4$, WOF_4 and $ReOF_4$.[46]

The fluoride-ion affinity of the Re(VII) oxofluorides was studied using a number of different approaches. Dimethylformamide (DMF) was found to solubilize ReO_3F by forming the adduct $ReO_3F(DMF)_2$, which was then allowed to react with two equivalents of $N(CH_3)_4^+F^-$ to form $ReO_3F_3^{2-}$.[47] The geometry of the anion, based on the number of Re-O stretching bands observed in the infrared spectrum, was proposed to be meridional.[47,48] This contrasts with the facial arrangement observed for $ReO_3Cl_3^{2-}$ [49] (Figure 1.4a) and expected based on Re-O pπ-dπ orbital interaction considerations (see Chapter 3). The $ReO_3F_3^{2-}$ anion was also prepared by fluorination of $KReO_4$ with IF_5 according to equation (1.16).[50]

$$KReO_4 + KF + IF_5 \xrightarrow{IF_5} K_2ReO_3F_3 + IOF_3 \qquad (1.16)$$

The $ReO_2F_4^-$ anion was obtained by Peacock from the reaction of perrhenate with BrF_3 according to equation (1.17).[51] Characterization of the salt by vibrational spectroscopy indicated a *cis* arrangement of the oxo ligands.[48] An alternative preparation involves the fluorination of perrhenate in a solution of 60% HF in ethanol.[52] Even though

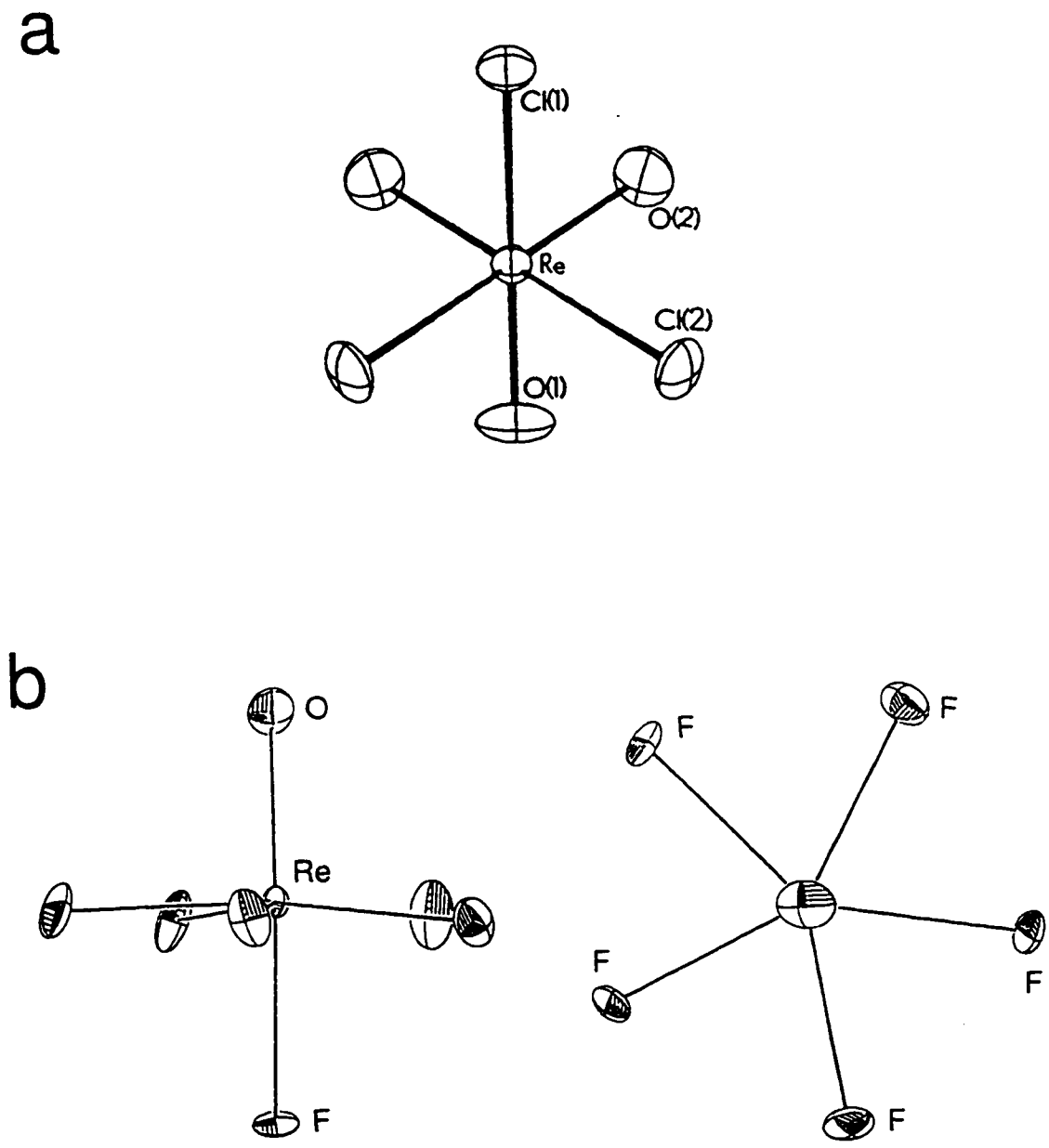

Figure 1.4. Structures of (a) the $ReO_3Cl_3^{2-}$ anion viewed along the idealized three-fold axis[49] and (b) the $ReOF_6^-$ anion viewed along the equatorial plane and down the five-fold axis[54] (thermal ellipsoid are at the 50% probablity level).

$$3\ KReO_4 + 4\ BrF_3 \xrightarrow{BrF_3} 3\ KReO_2F_4 + 2\ Br_2 + 3\ O_2 \qquad (1.17)$$

the ^{19}F NMR spectrum of this solution revealed a mixture of products, it confirmed the *cis*-dioxo arrangement of $ReO_2F_4^-$ based on the observation of two coupled fluorine environments.

Finally, $ReOF_5$ was also found to have an affinity for the fluoride-ion, forming the heptacoordinated $ReOF_6^-$ anion upon reaction with NOF, NO_2F and CsF.[53,54] The anion was characterized by vibrational and ^{19}F NMR spectroscopy as well as X-ray crystallography, which confirmed its pseudopentagonal bipyramidal geometry (Figure 1.4b).[54]

An alternative route for the preparation of the $ReO_3F_3^{2-}$, $ReO_2F_4^-$ and $ReOF_6^-$ anions consists of the direct reaction between the rhenium(VII) oxofluorides and alkali metal at temperatures of 100-200 °C.[55]

NMR Spectroscopy of ^{99}Tc and Other Quadrupolar Nuclei

Nuclei with a magnetic spin quantum number (I) greater than $^1/_2$ have a nonspherical charge distribution and therefore possess an electric quadrupole moment. In a molecule, the interaction of this quadrupole moment with an electric field gradient (EFG) provides a very efficient process for nuclear relaxation *via* molecular rotation. In fact, this mechanism usually dominates the relaxation of such nuclei.[56]

Under the conditions of extreme narrowing, the relaxation of a quadrupolar nucleus is described by equation (1.18):

$$\Delta\nu_{1/2} = \frac{1}{\pi T_2} = \frac{1}{\pi T_1} = \frac{3\pi}{10}\left(\frac{2I+3}{I^2(2I-1)}\right)\left(1+\frac{\eta^2}{3}\right)\left(\frac{e^2qQ}{h}\right)^2\tau_c \qquad (1.18)$$

where $\Delta\nu_{1/2}$ is the line width at half-height, T_2 the spin-spin relaxation time, T_1 the spin-lattice relaxation time, I the nuclear spin quantum number, Q the nuclear quadrupole moment, eq the electric field gradient at the nucleus, η the asymmetry parameter for eq and τ_c the isotropic tumbling correlation time. The factors influencing the quadrupolar relaxation rate can be divided in three distinct components: nuclear properties, molecular geometry and experimental parameters.[57]

Nuclear Properties

A nuclear width factor (WF) can be extracted from equation (1.18) and used to compare the line broadening from quadrupolar relaxation for different quadrupolar nuclei in the same or very similar electronic environments.

$$WF = \left(\frac{2I+3}{I^2(2I-1)}\right)Q^2 \qquad (1.19)$$

It can been seen from equation (1.19) that the effect of I is substantial. All other factors being equal, a nucleus with $I = {}^9/_2$ will have a relaxation rate approximately ${}^1/_{67}$ that of a nucleus with $I = 1$. The relaxation rate is particularly sensitive to the quadrupole moment of the nucleus since it is squared in equation (1.19). Although the values for Q

are not often known accurately, they vary over a large range (e.g., 6.9×10^{-32} m^2 for ^6Li to 4.55×10^{-28} m^2 for ^{235}U). The relative importance of I and Q can be seen clearly for the nuclei that are relevant to this work (Table 1.2). Nuclei with very low quadrupole moments such as ^{17}O have very low width factors whereas nuclei with large values of Q such as ^{185}Re produce very broad, almost unobservable NMR signals, even under ideal conditions (*vide infra*). The effect of I on the width factor becomes obvious when ^{14}N (I = 1) and ^{99}Tc ($I = {}^9/_2$) are compared. Even though the quadrupole moment of ^{99}Tc is almost an order of magnitude larger than that of ^{14}N, ^{99}Tc has a lower width factor than ^{14}N.

Molecular Geometry

The electric field gradient at a nucleus is the result of the electronic symmetry around that nucleus, which depends on the arrangement and nature of the ligands bonded to its atom. For the relaxation rate to be slow, the EFG at the quadrupolar nucleus must be low. A near-zero EFG is observed for atoms surrounded by ligands arranged in a cubic symmetry such as tetrahedral or octahedral (e.g., TcO_4^- and SbF_6^-). However, there are a number of molecules that give narrow lines whose symmetry is not apparently cubic or even regular, which emphasizes the fact that it is not the *molecular symmetry*, but rather the *electronic symmetry* around the quadrupolar nucleus that determines the magnitude of the EFG. Akitt et al.[59] demonstrated how noncubic arrangements of ligands can give rise to zero EFG situations and that the tetrahedron and octahedron are only special cases of an infinite set of possibilities. The pseudooctahedral *fac*-MX_3Y_3 arrangement is one such case in which a zero EFG is predicted to occur at the central atom.

Table 1.2 Properties of Quadrupolar Nuclei Relevant to this Study[58]

Nucleus	I [a]	N.A.(%) [b]	R_c [c]	$Q(10^{-28}\ m^2)$ [d]	Ξ(MHz) [e]	Reference Standard	WF [f]
^{14}N	1	99.63	5.70	0.0167	7.226455	$MeNO_2$	1.4
^{17}O	$^5/_2$	0.037	0.0611	-0.026	13.562	H_2O	0.22
^{75}As	$^3/_2$	100	144	0.29	17.180	AsF_6^- (MeCN)	112
^{99}Tc	$^9/_2$	(100)	2134	-0.13	22.508311	TcO_4^- (aq)	1.25
^{121}Sb	$^5/_2$	57.25	530	-0.33	24.088	$SbCl_6^-$ (MeCN)	35
^{123}Sb	$^7/_2$	42.75	113	-0.68	13.047	$SbCl_6^-$ (MeCN)	63
^{185}Re	$^5/_2$	37.07	292	2.4	22.823	$(PPh_4)(ReO_4)$	1550

[a] Nuclear spin quantum number.

[b] Natural abundance.

[c] Receptivity relative to that of ^{13}C.

[d] Nuclear electric quadrupole moment.

[e] Resonance frequency of the standard substance in a magnetic field in which $Si(CH_3)_4$ proton resonate at precisely 100 MHz.

[f] Width factor derived from equation (1.18).

Experimental Parameters

The only term of equation (1.18) over which some experimental control may be exercised is the rotational correlation time, τ_c, which is given by equation (1.20).

$$\tau_c = \frac{V\eta f}{kT} \qquad (1.20)$$

where V is the volume of the solute molecule, η is the solvent viscosity, f is the microviscosity coefficient, k is the Boltzmann constant and T is the absolute temperature. It can be seen from equation (1.18) that the quadrupolar relaxation rate is proportional to τ_c and that the slowest relaxation rate is obtained when τ_c is small. Therefore the ideal experimental conditions which minimize τ_c are (a) to have a small solute molecule, (b) to use a low viscosity solvent, (c) to use dilute solutions which keep η low and minimize ion-pairing effects and (d) to obtain the spectrum at elevated temperature.

In the present work, ^{99}Tc NMR was used as a characterization method for all technetium compounds that were prepared. The high receptivity of ^{99}Tc, 0.275 relative to ^{1}H and 2.134×10^3 relative to ^{13}C, makes it an easy nucleus to observe.[60] Although ^{99}Tc possesses a significant quadrupolar moment, it has a large nuclear spin ($I = {}^9/_2$) which results in a relatively small line width factor (Table 1.2) and it is reasonable to expect that coupling to other nuclei should be observed for molecular geometries which give rise to low EFG's at the ^{99}Tc nucleus.

Table 1.3 lists a selected number of ^{99}Tc NMR chemical shifts and coupling constants. It is worth noting that these chemical shifts range from -3672 to 806 ppm for

Table 1.3 ^{99}Tc NMR Chemical Shifts and Coupling Constants for Selected Technetium Species

Species	$\delta(^{99}Tc)$	$\Delta\nu_{1/2}$ (Hz)	^1J (Hz)			Ref.
			^{99}Tc-^{17}O	^{99}Tc-^{19}F	^{99}Tc-^{1}H	
TcH_9^{2-}	-3672	22			24	40
TcO_4^-	0.0	2.7	131.4			40
TcO_3F	43.7	23	139.8			40
TcO_3^+	160.7	670				40
$TcO_2F_4^-$	245.9	135	87(±5)	259		40
$TcOF_5$	396.3	375				40
$TcOCl_4^-$	5501	20000				61
$[TcO_2(CN)_4]^{3-}$	806.0	642				40
$Tc(CN)_7^{4-}$	-1329	5000				40

Tc(VII) species and is an indication of the high sensitivity of the ^{99}Tc nucleus to its chemical environment.

Because ^{99}Tc is quadrupolar, the fast relaxation of the nucleus in high EFG situations often yield broad resonances in which coupling information to other nuclei cannot be resolved, either in the ^{99}Tc spectrum or in the spectrum of the nucleus coupled to ^{99}Tc. This situation usually occurs when the quadrupolar relaxation rate is much larger than the coupling constant between the nuclei, i.e., $T_1^{-1} >> 2\pi J(A\text{-}X)$. In some cases, the EFG is sufficiently small at the ^{99}Tc nucleus that coupling can be partially resolved as for TcH_9^{2-}.[40] The ^{99}Tc and ^{1}H NMR spectra of TcH_9^{2-} (D_{3h} point symmetry) are shown in Figure 1.5. The ^{99}Tc resonance is found at -3672 ppm and exhibits a partially resolved binomial decet fine structure with a $^1J(^{99}Tc\text{-}^1H)$ = 24 Hz. This coupling is consistent with the ^{1}H spectrum, a partially quadrupole-collapsed decet having a width at half-height of 224 Hz. The "flat-top" shape of the ^{1}H resonance is commonly observed in the spectra of spin-$^1/_2$ nuclei coupled to quadrupolar nuclei when the quadrupolar relaxation rate $T_1^{-1} \approx 2\pi J(A\text{-}X)$.[40]

Figures 1.6 and 1.7 show a rare example of well resolved coupling between two quadrupolar nuclei. The ^{17}O NMR spectrum of ^{17}O (21.9%) and ^{18}O (42.7%) enriched $KTcO_4$ in H_2O (Figure 1.4) shows an equi-intense decet arising from spin-spin coupling of ^{17}O to ^{99}Tc. This "ideal" situation occurs only for highly symmetric molecules and when the electric field gradient is zero or near zero. This in turn slows down quadrupolar relaxation and results in sharper lines (in this case $\Delta\nu_{1/2}$ = 23 Hz), so that the quadrupolar relaxation rate is small with respect to the coupling constant between the nuclei, i.e.,

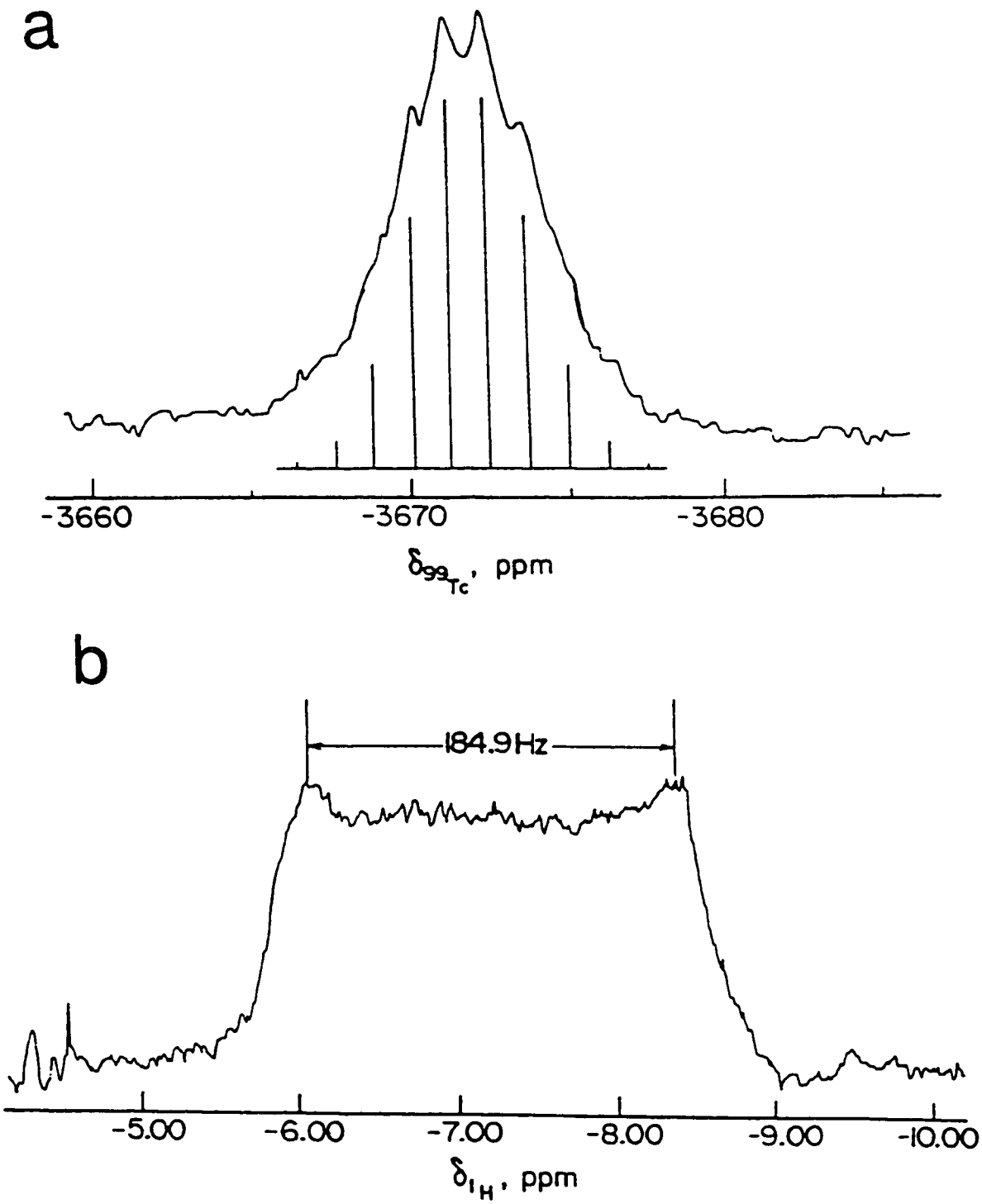

Figure 1.5. The ^{99}Tc (a) and ^{1}H (b) NMR spectra of TcH_9^{2-} (K_2TcH_9 dissolved in 40% KOH) recorded at -12 °C.[40]

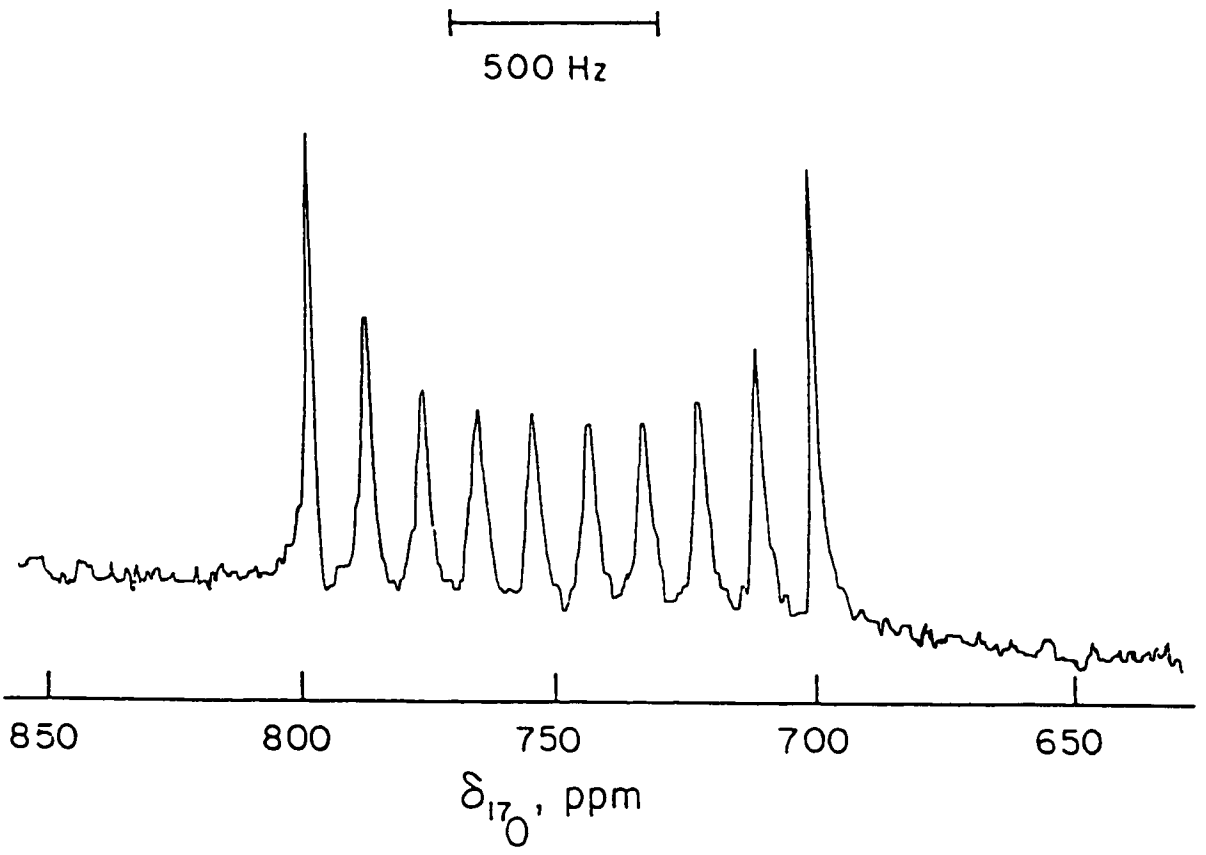

Figure 1.6. The ^{17}O NMR spectrum of ^{17}O-enriched $KTcO_4$ in H_2O at 25 °C.[40]

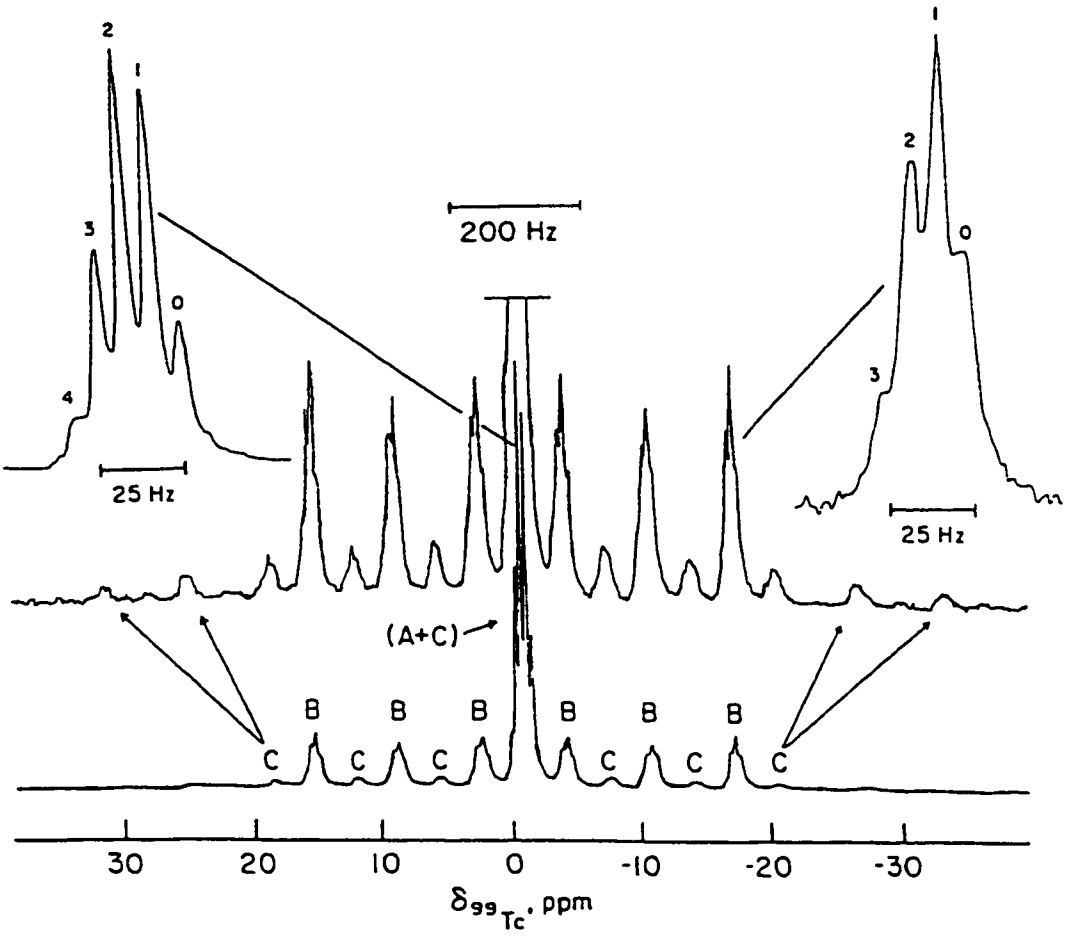

Figure 1.7. The ^{99}Tc NMR spectrum of ^{17}O (21.9) and ^{18}O (2.7%) enriched $KTcO_4$ in H_2O at 25 °C. Isotopic isomers are denoted by (A) TcO_4^-, (B) $Tc^{17}OO_3^-$ and (C) $Tc^{17}O_2O_2^-$, where a non-superscripted O represents ^{16}O and/or ^{18}O. Assignments for the insets corresponding to A and B are $Tc^{16}O_x{}^{18}O_{4-x}^-$ (A) and $Tc^{17}O^{16}O_x{}^{18}O_{3-x}^-$ (B), where x, the number of ^{16}O atoms is indicated.[40]

$T_1^{-1} << 2\pi J(A\text{-}X)$. The ^{99}Tc NMR spectrum of this compound (Figure 1.7) consists of a strong central line and coupling caused by $Tc^{17}OO_3^-$ and $Tc^{17}O_2O_2^-$ (lines caused by $Tc^{17}O_3O^-$ and $Tc^{17}O_4^-$ are too weak to be observed in this case). In addition, a set of smaller splittings (8.8 Hz at 2.114 T) can be observed on each of the main lines. These splittings are attributed to secondary isotopic effects arising from a statistical distribution of $^{16}O/^{17}O/^{18}O$ isotopic isomers.[40]

Purpose and Scope of the Present Study

The purpose of this study is to extend our knowledge of the chemistry of technetium(VII) and rhenium(VII) oxofluorides. In contrast to their rhenium analogues, the syntheses of the last Tc(VII) fluoride and oxofluoride species, $TcOF_5$ and TcF_7, cannot be achieved by high-temperature fluorination of Tc metal or TcO_2 with elemental fluorine. Recently, noble-gas fluorides have been shown to be convenient synthetic reagents for the preparation of high oxidation state compounds such as $CrOF_4$,[62] OsO_2F_4[63] and TcO_2F_3.[41] The first major goal of this work was to use the powerful fluorinating agents KrF_2 and KrF^+ in an attempt to prepare $TcOF_5$, and TcF_7 as its cationic precursor TcF_6^+.

Another goal of this work is to study of the chemical behaviour of TcO_2F_3, ReO_2F_3 and $TcOF_5$. This entails studies of the fluoride-ion affinity of the neutral oxofluorides using alkali metal fluorides and $N(CH_3)_4F$ as the fluoride sources, as well as their Lewis acidity toward CH_3CN. The fluoride-ion donor properties of the Tc(VII) and Re(VII) oxofluorides were determined by their reactions with the strong Lewis acids AsF_5 and SbF_5.

Structural characterization of the compounds synthesized in this study were achieved by using a combination of ^{1}H, ^{13}C, ^{17}O, ^{19}F and ^{99}Tc NMR spectroscopy, Raman and infrared spectroscopy as well as single-crystal X-ray diffraction.

CHAPTER 2

EXPERIMENTAL SECTION

Monitoring of Radioactive Contamination

All operations were conducted in laboratories that were monitored routinely by the McMaster University Health Physics Group for radioactive contamination. A Dosimeter Model 3100 survey meter equipped with a pancake probe was used to routinely monitor contamination. The maximum radioactivity level allowed on working surfaces was 5 Bq/cm^2 averaged over 100 cm^2, and 10% of that value everywhere else. All work involving ^{99}Tc was licenced and performed according to the regulations and recommendations of the Canadian Atomic Energy Control Board.[64]

Vacuum Techniques

The compounds used in the course of this work were all moisture-sensitive. For that reason, all manipulations were carried out under rigorously anhydrous conditions in glass or metal vacuum lines or in the oxygen- and moisture-free (<0.1 ppm) nitrogen atmosphere of a Vacuum Atmospheres Model DLX drybox. Volatile reagents and solvents were manipulated by vacuum transfer using two vacuum lines. Volatile materials which were noncorrosive toward glass in the absence of water such as organic solvents (e.g., CH_3CN and CH_2Cl_2) and SO_2ClF were manipulated using a vacuum line constructed of

Pyrex with grease-free 6-mm J. Young glass valves with PTFE barrels (Figure 2.1). Pressures within the manifold of the glass vacuum line were monitored with a mercury manometer. Volatile materials that attack glass, such as HF solvent, were manipulated by vacuum transfer on a vacuum line constructed from nickel and 316 stainless steel valves and fittings (Autoclave Engineers, Inc.), PTFE, FEP and Kel-F (Figure 2.2). Pressures were measured at ambient temperature with an MKS Model PDR-5B power supply and digital readout in conjunction with pressure transducers having inert wetted surfaces made of Inconel. Two transducers of different dynamic pressure ranges were used, 0 to 1100 torr and 0 to 100 torr. The pressures were accurate to ±0.5% of scale.

Vacuum on the glass line and metal line was attained with Edwards two-stage E2M8 direct-drive high-vacuum pumps. Two vacuum pumps were used on the metal line; one, a roughing pump, was used for the removal and disposal of volatile reactive fluorinated compounds by pumping through an entrapment on a bed of soda lime, which consisted of a copper tube (ca. 60-cm length, 15-cm diameter) packed with soda lime absorbent (Fisher Scientific, 4-8 mesh). The second vacuum pump provided the high-vacuum source for the manifold (ca. 10^{-4} torr). In the construction of the glass and metal vacuum lines, traps cooled to -196 °C were attached immediately before the vacuum pumps to prevent passage of condensible volatile materials into the pumps.

Preparative Apparatus and Sample Vessels for Raman and NMR Spectroscopy

All synthetic procedures were performed in apparatus built from 304 and 316 stainless steel, glass, Kel-F and FEP. Sample preparations involving materials which

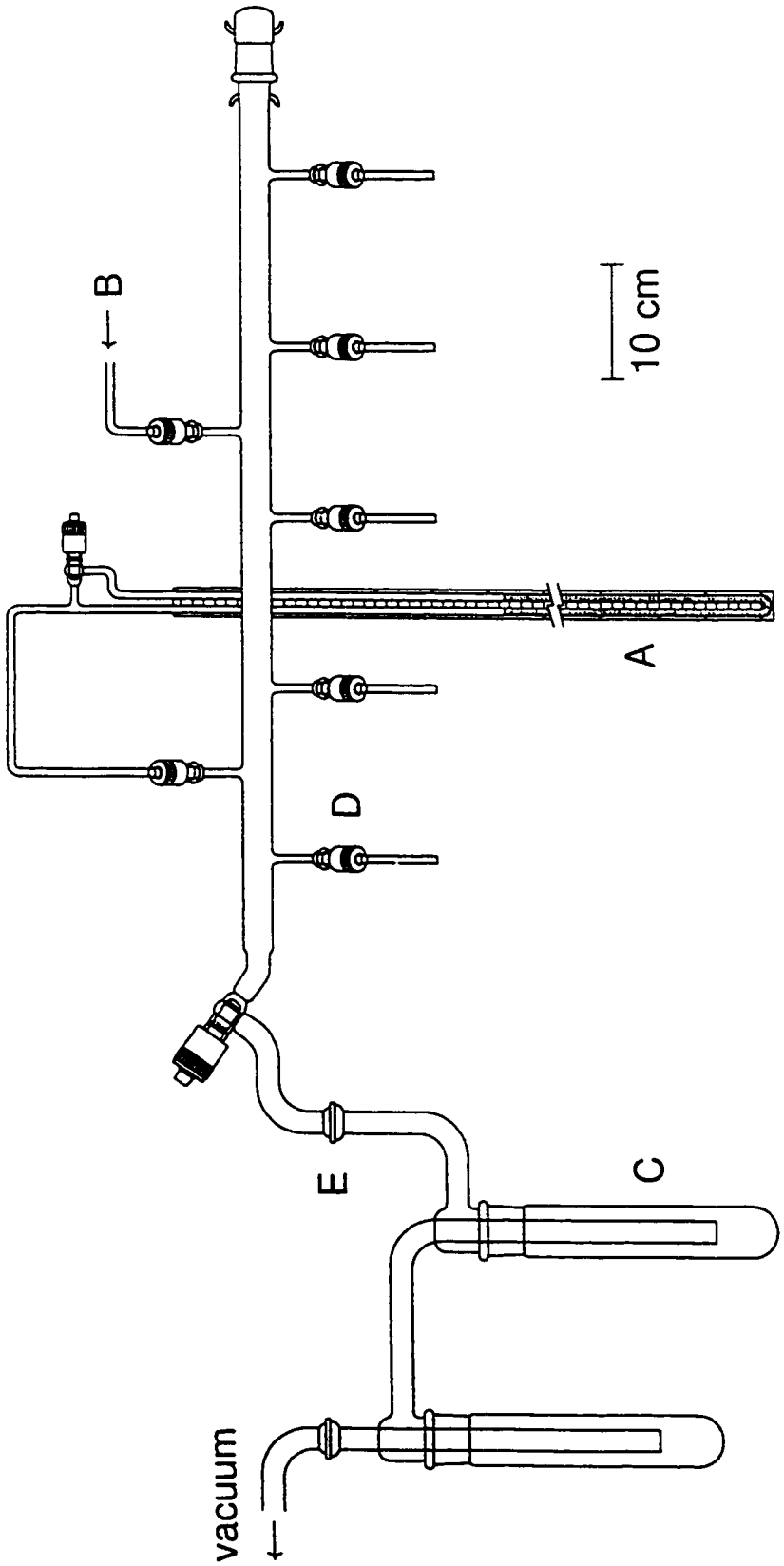

Figure 2.1. Glass vacuum line system; (A) mercury manometer, (B) dry N_2 inlet, (C) liquid nitrogen trap, (D) 6-mm J. Young PTFE/glass valve, (E) ball and socket joint.

Figure 2.2. Metal vacuum line; (A) outlet to liquid nitrogen and charcoal traps followed by a two-stage direct-drive rotary vacuum pump - hard vacuum, (B) outlet to soda lime and liquid nitrogen traps followed by a two-stage direct-drive rotary vacuum pump - rough vacuum, (C) dry N_2 inlet, (D) F_2 inlet, (E) MKS pressure transducers (0-1000 torr), (F) MKS pressure transducer (0-1 torr), (G) pressure gauge (0-1500 torr), (H) $^3/_8$-in stainless steel high pressure valve, (I) 316 stainless steel cross, (J) 316 stainless steel T-piece, (K) 316 stainless steel L-piece, (L) $^3/_8$-in o.d., $^1/_8$-in i.d. nickel connectors, (M) $^1/_4$-in o.d., $^1/_8$-in i.d. nickel tube.

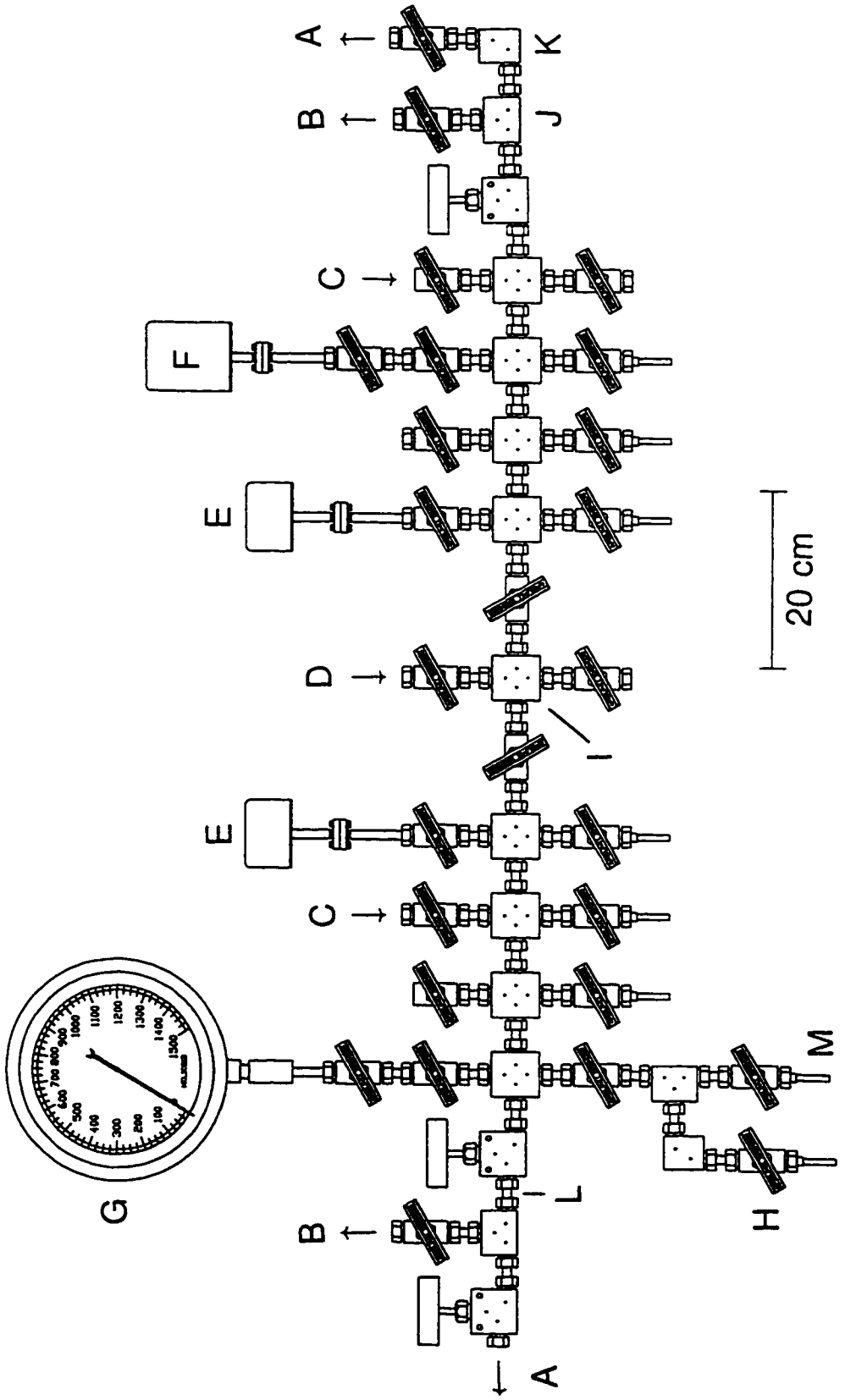
A
B
C
D
E
F
G
H
I
J
K
L
M
20 cm

attack glass were carried out in reactors constructed from lengths of $^{1}/_{4}$-in (7-mm) and $^{3}/_{8}$-in (9.5-mm) o.d. FEP tubing which were heat-sealed at one end and heat-flared (45° SAE) at the other. The tubes were then attached to Kel-F valves encased in aluminum housings by flare fittings. All vessels built in this way were dried by first pumping on a glass vacuum line for at least 5 h followed by passivation on a metal vacuum line with ca. 1000 torr of fluorine overnight. All volatiles were then removed under vacuum and the vessel pressurized with 900 torr of dry nitrogen gas.

Nuclear magnetic resonance (NMR) spectra were recorded on samples prepared in FEP tubes (9-mm and 4-mm o.d.). The 9-mm o.d. FEP NMR tubes were built from lengths of $^{3}/_{8}$-in. (9.5-mm) o.d. FEP tubing by reducing their diameter to 9 mm o.d. in a heated brass cylindrical form with mechanical pressure. One end of the tube was heat-sealed by pushing it into the end of a thin-walled 10-mm o.d. glass NMR tube previously heated in a Bunsen flame. The other end was heat-flared (45° SAE) for direct attachment to a Kel-F valve. The 4-mm o.d. FEP tubing had one end sealed by pushing the tube into the end of a thin-walled 5-mm o.d. NMR tube and the other end was heat-flared (45° SAE) for direct attachment to a Kel-F valve. The sample tubes used for recording the NMR spectra were heat-sealed with a small diameter nichrome wire resistance furnace.

Room temperature Raman spectra of solids were recorded on samples in Pyrex melting point capillaries. Before use, the melting point capillaries were heated under dynamic vacuum for 24 h at 200 °C and then stored in a dry nitrogen-filled drybox where they were loaded with the appropriate materials. The ends of the loaded melting point capillaries were filled with Kel-F grease before removal from the drybox. The capillaries

were then immediately sealed with a miniature oxygen-natural gas torch. Raman spectra at low temperatures or of liquids were recorded on samples in FEP or glass tubes. Glass tubes for low temperature Raman spectroscopy were constructed from 3-mm o.d. glass tubes that were heat-sealed at one end and glassblown onto ca. 5-cm lengths of $^1/_4$-in o.d. glass tubing onto the other end. The $^1/_4$-in o.d. end of each glass tube was attached to a 4-mm J. Young glass valve with a PTFE barrel and dried overnight under dynamic vacuum. The appropriate materials were loaded into each tube in a drybox, followed by heat-sealing below the valve with an oxygen-natural gas torch.

Vessel were attached to vacuum lines through thick-walled FEP tubing and $^1/_4$-in PTFE Swagelok connectors with PTFE compression fittings or $^1/_4$-in stainless steel Cajon Ultra-Torr connectors with Viton rubber O-rings. The fluoroplastic valves and connectors have been described in greater detail elsewhere.[65]

PREPARATION AND PURIFICATION OF STARTING MATERIALS

Purification of HF and SO_2ClF Solvents

Anhydrous hydrogen fluoride (Harshaw Chemical Co.) was purified by treatment with 5 atm of F_2 gas in a nickel can for a period of several months, converting residual water to HF and O_2 gas. The anhydrous HF was then vacuum distilled into a dry Kel-F storage vessel equipped with a Kel-F valve and stored at room temperature until used. Hydrogen fluoride was transferred into reaction vessels by vacuum distillation on a metal vacuum line through connections constructed from PTFE, Kel-F and FEP as shown in Figure 2.3.

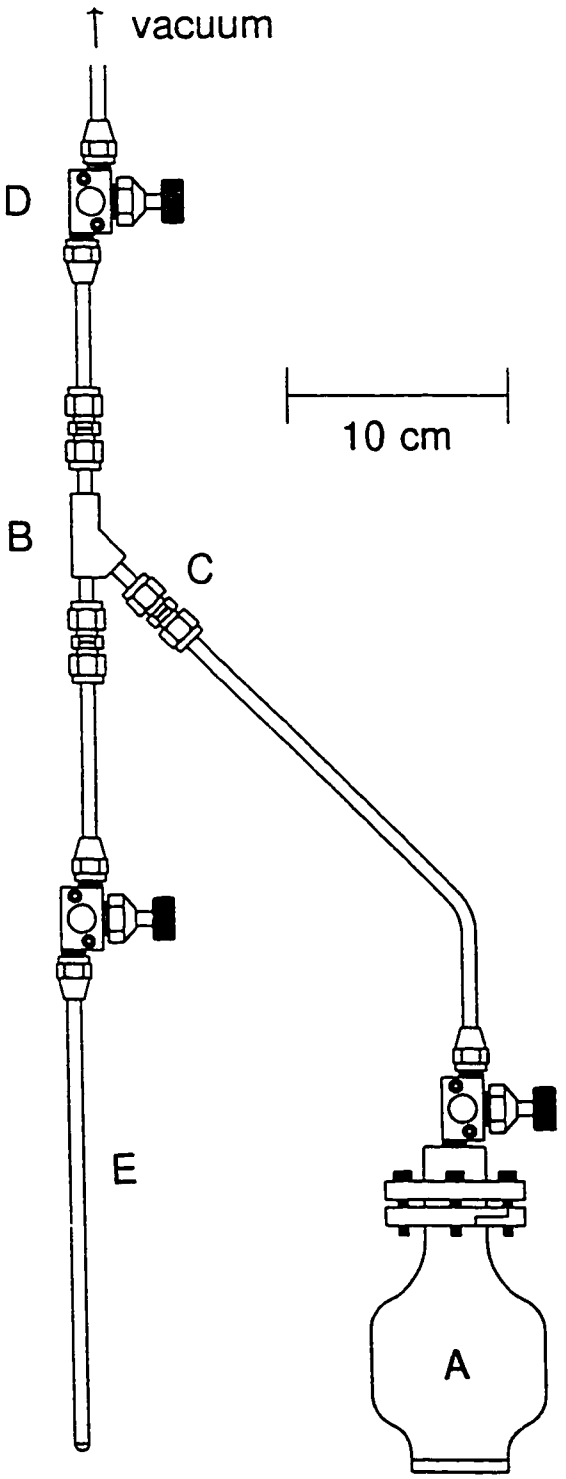

Figure 2.3. Hydrogen fluoride distillation apparatus; (A) Kel-F HF storage vessel, (B) Kel-F Y-piece, (C) $^1/_4$-in PTFE Swagelok connector, (D) Kel-F valve, (E) FEP reaction vessel.

Sulfuryl chloride fluoride, SO_2ClF (Aldrich) was purified according to the literature method[66] and stored over KF in a glass vessel equipped with a 6-mm glass J. Young glass valve with a glass barrel. Transfers of SO_2ClF were performed under vacuum using a vacuum line and tubing constructed of glass similar to that shown in Figure 2.4. Fluorine-19 NMR indicated the presence of a trace of SO_2F_2 impurity [$\delta(^{19}F)$ = 32.4 ppm] in the solvent.

Purification of CH_2Cl_2 and CH_3CN Solvents

Dichloromethane, CH_2Cl_2 (Caledon Reagent Grade) was dried by combining the solvent with Davison Type 3A molecular sieves (Fisher Scientific) for 3 days followed by vacuum distillation into a dry glass bulb equipped with a 4-mm glass J. Young glass valve with a PTFE barrel. The molecular sieves were dried under dynamic vacuum for 24 h at 120 °C prior to use as a drying agent.

Acetonitrile, CH_3CN (Caledon HPLC Grade) was purified according to the literature procedure[67] and was transferred into reaction vessels by vacuum distillation on a glass vacuum line as shown in Figure 2.4.

Purification of SbF_3, SbF_5 and Preparation of AsF_5

Antimony trifluoride, SbF_3 (Aldrich) was sublimed under vacuum and transferred into a drybox prior to use.

Antimony pentafluoride, SbF_5 (Ozark-Mahoning Co.) was purified by the literature method[68] and stored in a glass vessel. Subsequent transfers of SbF_5 were performed with

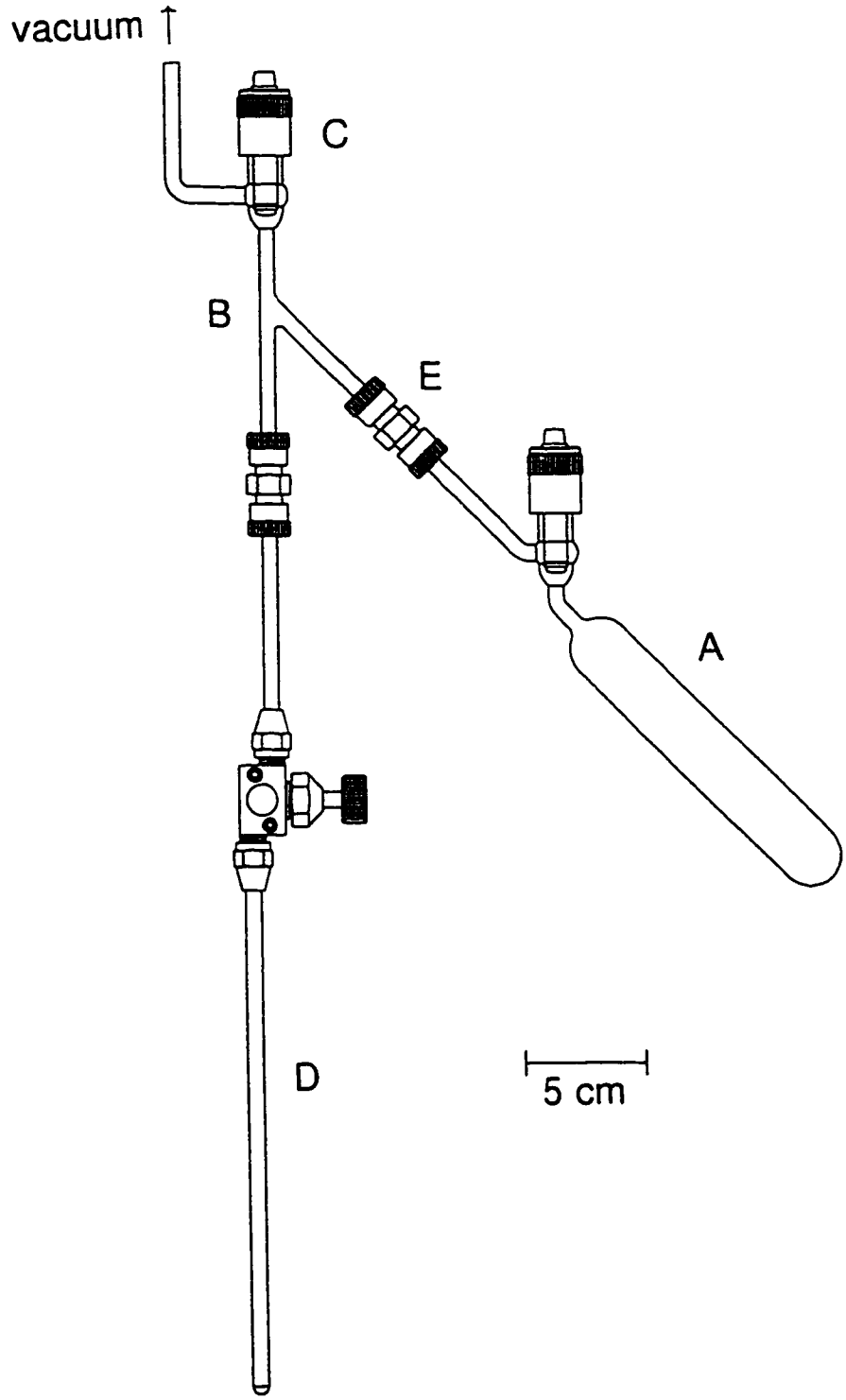

Figure 2.4. Acetonitrile distillation apparatus; (A) Pyrex CH_3CN storage vessel, (B) glass Y-piece, (C) 6-mm J. Young PTFE/glass valve, (D) FEP reaction vessel fitted with a Kel-F valve, (D) stainless steel Cajon connector.

an all-glass syringe in the inert atmosphere of a glove bag which had been previously purged with dry nitrogen for 12 h.

Arsenic pentafluoride was prepared according to the literature method[69] by the fluorination of AsF_3 in a nickel can. The AsF_5 was distilled into a nickel storage cylinder from which it was used without further purification.

Preparation of XeF_6 and KrF_2

Xenon hexafluoride was prepared by a method similar to that outlined by Chernik and Malm[70] and was ascertained to contain only small amounts of XeF_4 contaminant by Raman spectroscopy by comparing the sharp, intense XeF_4 bands (503, 543 cm^{-1}) to the broad XeF_6 bands (582, 636, 655 cm^{-1}). Xenon (Air Products, 99.995%) and fluorine gas (Air Products) were transferred into a nickel can with a xenon-to-fluorine ratio of 1:22 and a total autogenous pressure of 56 atm at room temperature. The mixture was heated to 250 °C for 24 h and slowly cooled to 47 °C over a period of 16 h before turning off the furnace and allowing the mixture to cool to room temperature. The product was vacuum distilled into a $^1/_2$-in FEP storage vessel equipped with a Whitey ORM2 stainless steel valve.

Krypton difluoride was prepared by a method similar to that originally described by Bezmel'nitsyn et al.[71] and subsequently modified by Kinkead et al.[72] The stainless steel hot-wire reactor used in the present work is a modification of the design reported by Kinkead et al.[72] (Figure 2.5) The hot-wire reactor was immersed into a 20-L dewar filled with liquid nitrogen and the DC power source (Miller, Thunderbolt AC/DC arc welder)

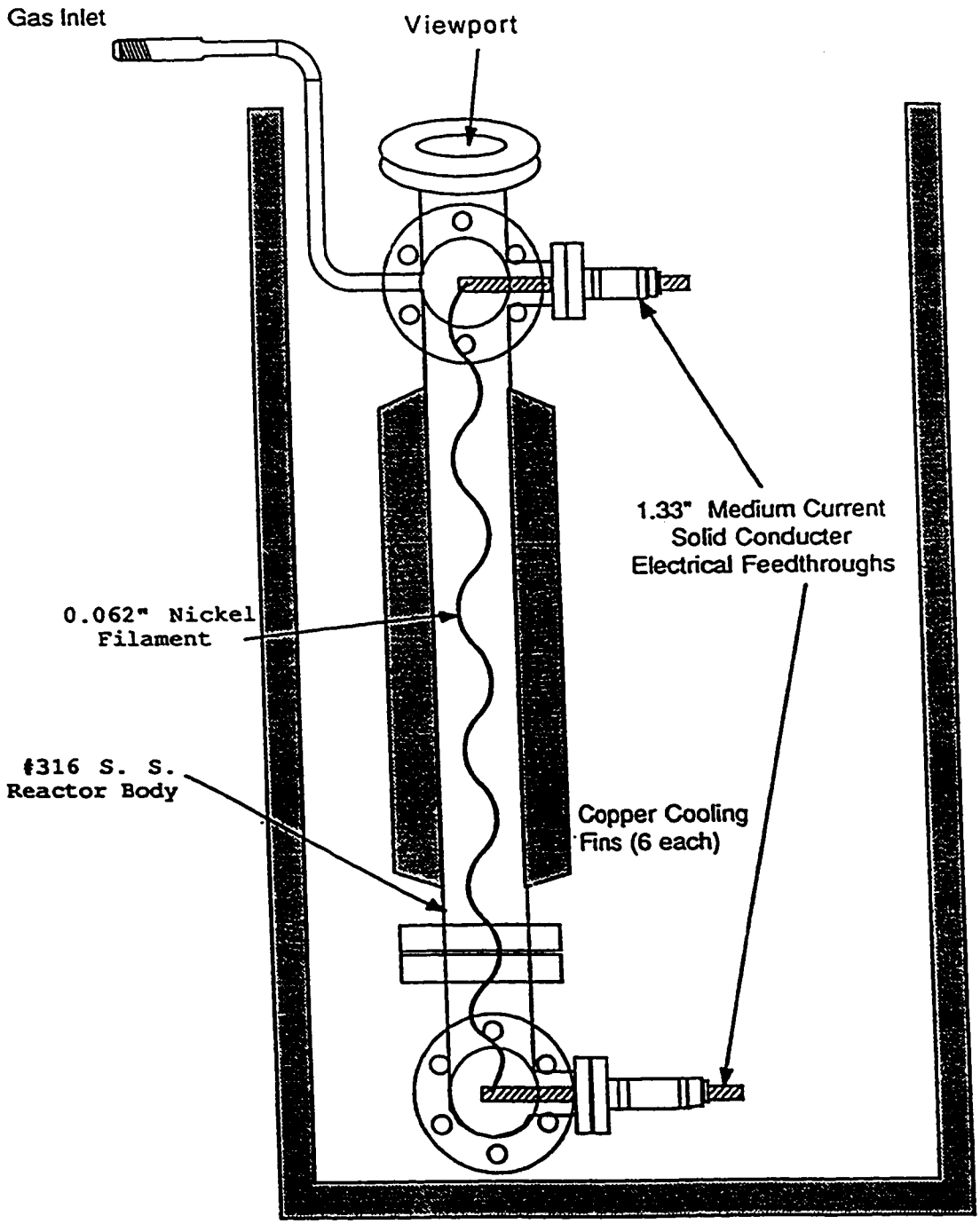

Figure 2.5. Hot-wire reactor used for the preparation of KrF_2.

was adjusted to 6 V and 30 A. Approximately 700 torr (0.35 mol) of krypton (Air Products, 99.995%) was condensed into the reactor which was then filled with a 1:1 mixture of Kr and F_2 to ca. 45 torr and the pressure inside the hot-wire reactor was kept between 35 and 40 torr for each 8 h run. Excess fluorine was then removed at -196°C before allowing the reactor to warm to room temperature. The pink, crude KrF_2 contaminated with CrO_2F_2 and $CrOF_4$ was distilled into a $^1/_2$-in FEP U-trap at -78 °C followed by flash distillation of some of the crude KrF_2 with the more volatile chromium oxofluorides from the U-trap into a 9-mm FEP tube equipped with a Kel-F valve. The remaining white KrF_2 was finally distilled into a 9-mm FEP tube equipped with a Kel-F valve for storage at -78 °C.

Drying of LiF, NaF, KF and CsF, and Preparation of $N(CH_3)_4F$

Lithium fluoride (Research Inorganic Chemicals) and NaF (Matheson) were dried under vacuum at 125 °C prior to their use. Potassium fluoride (Allied) and CsF (Merck) were dried by fusion in a platinum crucible, followed by transfer of the hot clinker to a drybox port where its was immediately evacuated. Upon transferring to the dry nitrogen atmosphere of a drybox, the samples were ground to a fine powder. Tetramethylammonium fluoride, $N(CH_3)_4F$, was prepared as described in the literature.[73]

Preparation of Tc_2O_7, Re_2O_7 and $^{17,18}O$-Enriched Tc_2O_7

Ditechnetium(VII) heptoxide, Tc_2O_7, was prepared by combustion of the metal powder as a modification of the method described by Selig and Fried.[74] The metal was

prepared by reduction of crude $NH_4^+TcO_4^-$ (Oak Ridge National Laboratories) with hydrogen (Canadian Liquid Air, 99.99%). In a typical experiment, crude $NH_4^+TcO_4^-$ (0.6500 g) was added to the bottom of a 9-mm o.d. quartz reaction tube through a 6-mm o.d. side tube joined at 90° near the bottom of the reaction tube (Figure 2.6) and heat-sealed under vacuum. The opposite end of the reaction vessel was equipped with a 4-mm J. Young glass valve with a PTFE barrel. Reduction was achieved by initially heating $NH_4^+TcO_4^-$ with a natural gas-oxygen torch in the presence of successive aliquots of H_2 (ca. 850 torr) followed by removal of H_2O and NH_3 under vacuum. In the latter stages of reduction, the residue was heated to redness in the presence of each H_2 aliquot and repeated until water evolution ceased. The dry metal was then quantitatively converted to Tc_2O_7 by admitting aliquots of oxygen gas (Canadian Liquid Air, 99.99%), dried by passing through a copper coil immersed in a dry-ice/acetone bath, to the reaction vessel and heating the metal to red heat with a natural gas-oxygen torch until combustion ceased. The Tc_2O_7 that formed condensed as a pale yellow solid in the cooler regions of the reactor. The reactor was allowed to cool to room temperature before a second aliquot of dry oxygen gas was admitted. The procedure was repeated until no technetium metal remained. After combustion was complete, the vessel was evacuated and Tc_2O_7 was melted and poured under static vacuum into the 6-mm o.d. side arm by gently heating the reactor with a heat-gun. The side tube was then sealed off from the main reactor and transferred into a drybox.

Dirhenium heptoxide, Re_2O_7, was prepared in a manner similar to Tc_2O_7 except that rhenium powder (Cleveland Refractory Metals, 325 mesh) was used without prior

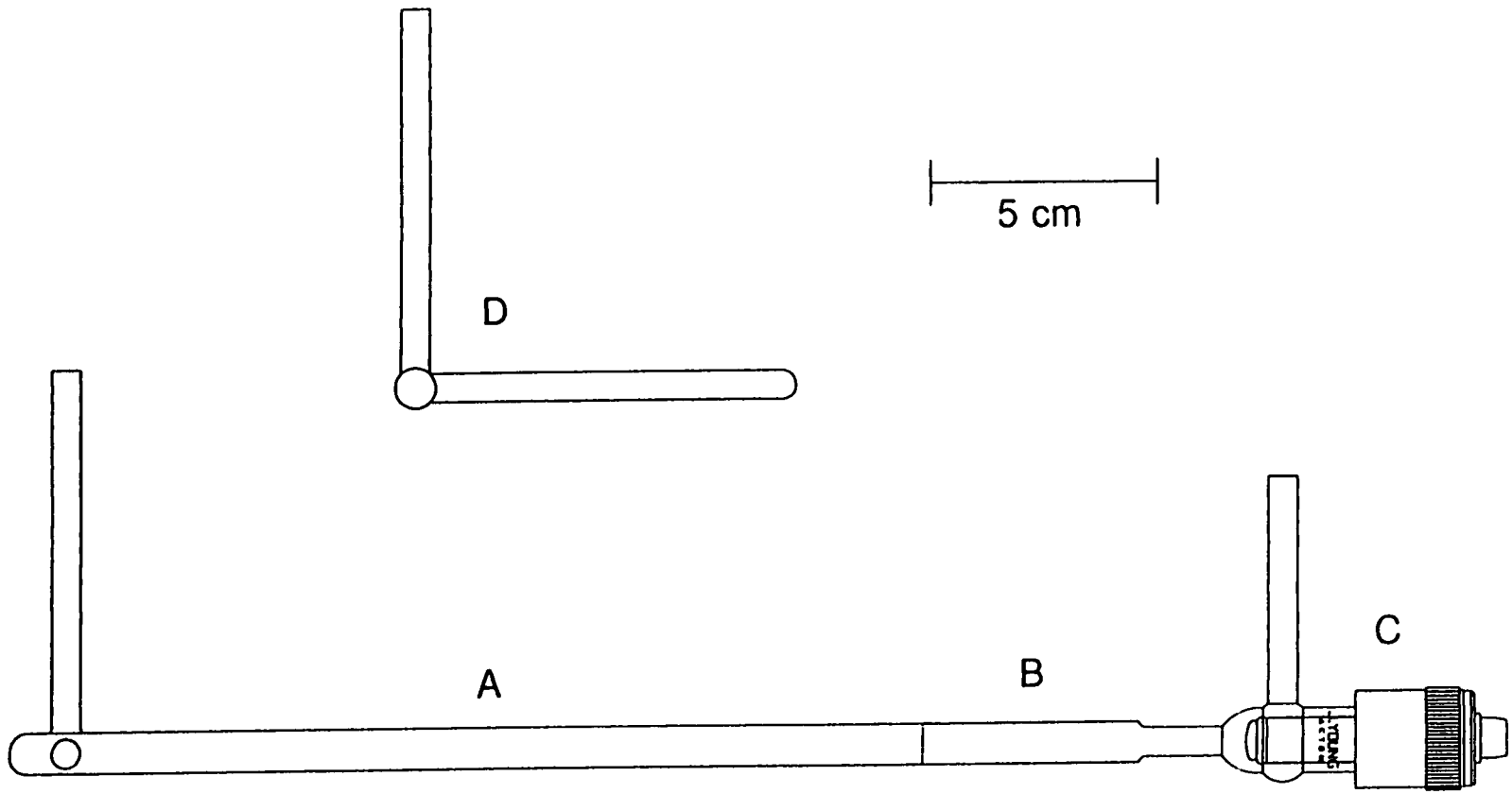

Figure 2.6. Reactor used for the preparation of Tc_2O_7 and Re_2O_7; (A) 9-mm o.d. quartz tube, (B) graded joint, (C) 6-mm J. Young PTFE/glass valve, (D) front-end view showing vertical loading tube and horizontal recovery tube.

reduction with hydrogen. The oxidation of Re (4.94455 g, 2.65541 mmol) was carried out in a slightly larger reaction vessel (15-mm o.d. with 6-mm o.d. side-arms). The yield was 5.89953 g, 1.21788 mmol (92%). The product was a yellow to yellow-green crystalline material.

Gaseous oxygen enriched in ^{17}O (21.87%) and ^{18}O(43.12%) was used for the preparation of an enriched sample of Tc_2O_7 from 0.8354 g of $NH_4^+TcO_4^-$. A separate manifold was built from $^1/_4$-in o.d. copper tubing (Figure 2.7) and connected to the vacuum line. This allowed the recovery and storage of the unused portion of enriched oxygen over a bed of cold 4 Å molecular sieves. These sieves had been previously heated overnight at 250 °C under dynamic vacuum and transferred into a 500-mL flask fitted with a 4-mm J. Young valve with a PTFE barrel. This cryotrap (filled about $^2/_3$ full with molecular sieves) could fully condense at least 300 mL of N_2 or O_2 having a pressure of 1 atm at room temperature when cooled to -196 °C.

DISPOSAL OF HF, KrF_2 AND Xe(VI) COMPOUNDS

Extreme caution is required in the disposal of KrF_2 and Xe(VI) compounds in order to avoid violent detonations. Routine disposal of HF, KrF_2, XeF_6 and $XeOF_4$ was carried out by dynamic pumping through a stainless steel column packed with soda lime. Disposal of samples containing KrF_2 and Xe(VI) compounds in HF was carried out by freezing the sample in liquid nitrogen, cutting one end of the tube before inverting it into a cold aqueous base solution. This procedure should be performed behind a protective

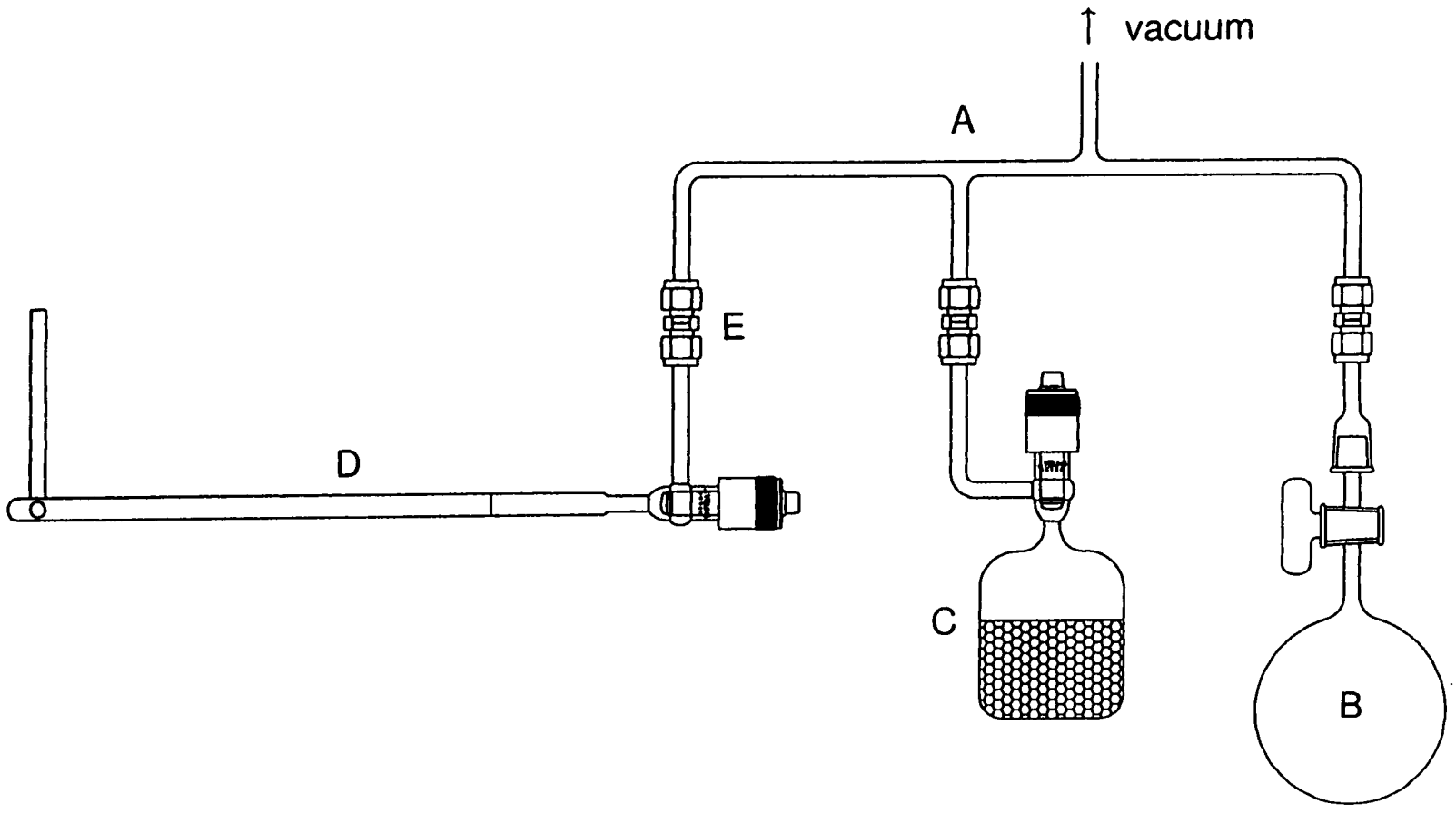

Figure 2.7. Secondary manifold used for the preparation of $^{17,18}O$-enriched Tc_2O_7; (A) $^1/_4$-in copper tubing; (B) original glass vessel with enriched oxygen gas, (C) 500-mL Pyrex glass flask with J. Young PTFE/glass valve filled $^2/_3$ with 4 Å dry molecular sieved - cryopump, (D) quartz reactor from Figure 2.6, (E) $^1/_4$-in PTFE Swagelok connector.

shield. Radioactive samples containing KrF_2 and Xe(VI) compounds in HF were disposed of in a similar manner but inside a stainless steel pipe with screwable lid.

PREPARATION OF TECHNETIUM AND RHENIUM OXOFLUORIDES AND THEIR DERIVATIVES

Preparation of TcO_2F_3

Technetium(VII) dioxotrifluoride was prepared by a method similar to that outlined by Mercier and Schrobilgen.[41] Anhydrous HF (ca. 1 mL) was condensed onto Tc_2O_7 (0.5065 g, 1.635 mmol) in a $^1/_4$-in o.d. FEP T-shape reactor fitted with a Kel-F valve similar to that shown in Figure 2.8. Two liquid phases formed upon warming to room temperature and vigorous agitation. The mixture was allowed to stand at room temperature for 1 h prior to condensing a first aliquot of XeF_6 (0.3198 g, 1.304 mmol) into the sample tube at -196 °C from an FEP weighing vessel (Figure 2.9). When the mixture was warmed to room temperature, a bright yellow precipitate formed at the interface of the two liquid phases as the XeF_6 reacted. Subsequent aliquots of XeF_6 were added until the supernatant over the TcO_2F_3 remained slightly yellow as a consequence of the formation of $XeF_5^+TcO_2F_4^-$ (total amount of XeF_6 added: 0.6939 g, 2.829 mmol). The supernatant was decanted into the side-arm of the reactor and the HF back-distilled onto the solid by slowly cooling the vertical tube at -196 °C. The mixture was then agitated and the supernatant decanted again into the side-arm. This procedure was repeated five times in order to wash the TcO_2F_3 free of $XeOF_4$ and XeO_2F_2. After the side-arm was heat-sealed and disposed of, the yellow solid was dried under dynamic

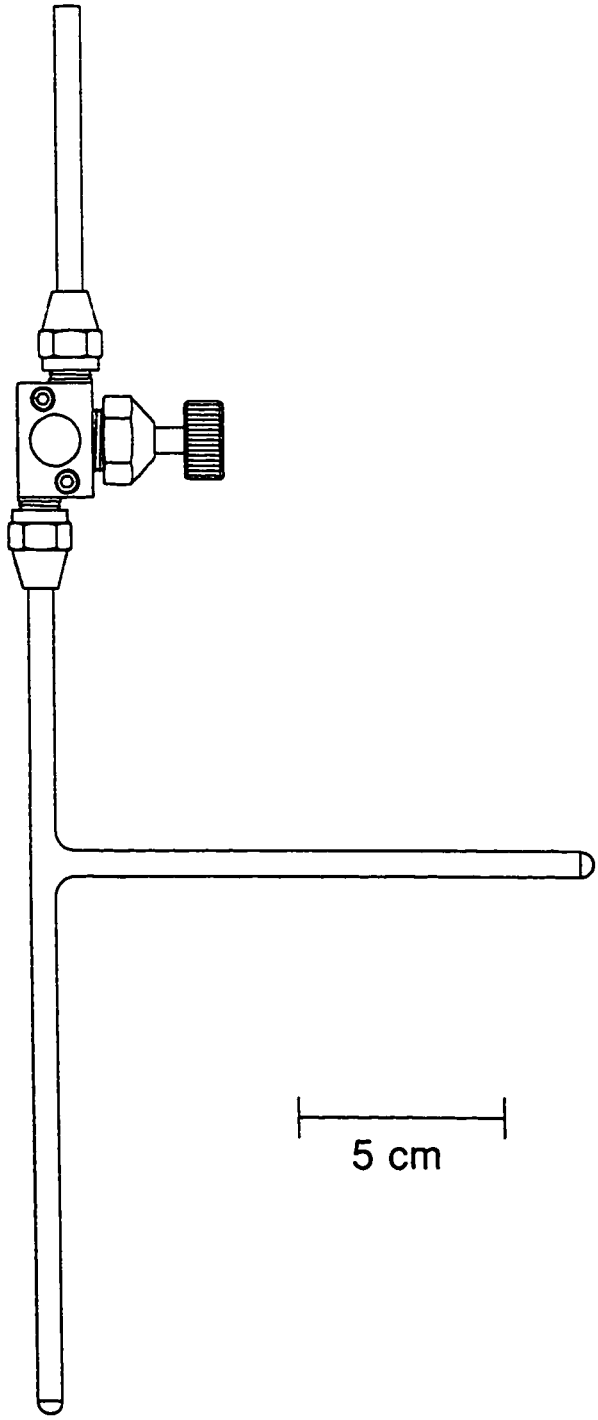

Figure 2.8. T-shaped FEP reaction vessel fitted with a Kel-F valve.

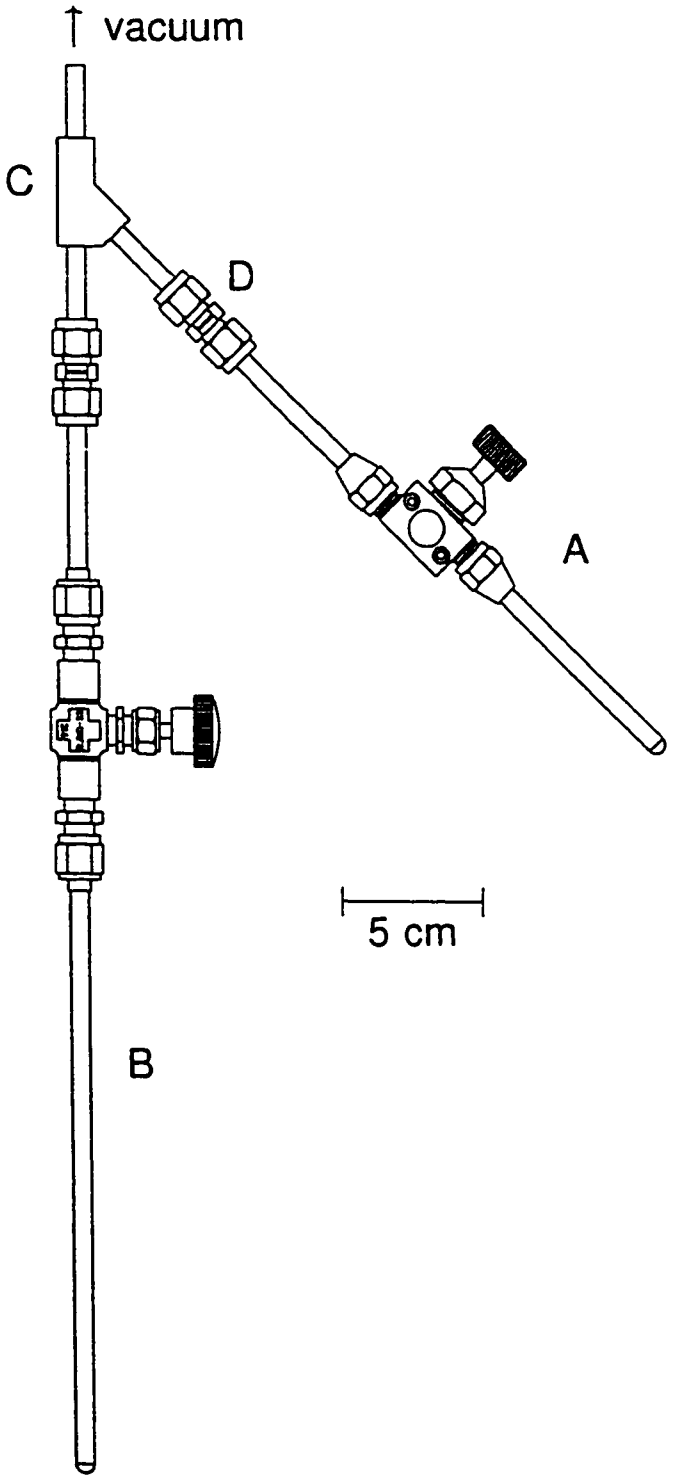

Figure 2.9. Krypton difluoride and XeF_6 distillation apparatus; (A) FEP weighing tube fitted with a Kel-F valve, (B) FEP reactor vessel fitted with a 316 stainless steel valve, (C) Kel-F Y-piece, (D) $^1/_4$-in Swagelok PTFE connector.

vacuum at room temperature through an FEP U-trap at -196 °C for 8 h and stored in a drybox. The purity of the product was verified by Raman spectroscopy. The yields of TcO_2F_3 obtained by this method are essentially quantitative.

Preparation of ReO_2F_3

In a drybox, 1.0293 g (2.1248 mmol) of Re_2O_7 was weighed into a T-reactor built from lengths of $^3/_8$-in o.d. FEP tubing and a Swagelok PTFE T-connector. Anhydrous HF (ca. 4 mL) was condensed onto the solid. A known amount of XeF_6 (0.81494 g, 3.3225 mmol) was then condensed into the reactor from an FEP weighing vessel (Figure 2.9). Upon warming the reactor and its contents, a white precipitate of ReO_2F_3 started to form at 0 °C. The insoluble product was separated from the xenon oxofluoride byproducts by decanting the supernatant into the side-arm of the reactor. The solvent was removed and the ReO_2F_3 was dried under dynamic vacuum at room temperature for 12 h, yielding a friable white solid which was immediately transferred to a drybox (1.11062 g, 4.03567 mmol, 95.0% yield), melting point 113-116 °C. The purity of the sample was verified by Raman spectroscopy.

Preparation and Decomposition of $TcO_2F_3(CH_3CN)$

In a drybox, 0.0202 g (0.108 mmol) of TcO_2F_3 was loaded into a 4-mm o.d. FEP tube fitted with a Kel-F valve. Dry CH_3CN (ca. 0.3 mL) was condensed onto the TcO_2F_3 which completely dissolved to give a clear yellow solution. The reactor was then heat-sealed and stored in liquid nitrogen until the NMR experiment was performed. Another

sample was prepared by dissolving 0.0316 g (0.168 mmol) of TcO_2F_3 in 0.0439 g (1.069 mmol) of dry CH_3CN in a 4-mm o.d. FEP tube followed by addition of ca. 0.3 mL of SO_2ClF.

In a drybox, 0.0423 g (0.225 mmol) of TcO_2F_3 was loaded into a $^1/_4$-in o.d. FEP tube fitted with a Kel-F valve. Dry CH_3CN (ca. 2 mL) was condensed onto the solid which dissolved to form a yellow solution. The solvent was then removed at -40 °C over a period of 3 h to yield a light orange solid. The reactor was back-filled with dry nitrogen and warmed to room temperature. Over the next 3 h, the solid turned yellow again and was shown to be TcO_2F_3 by Raman spectroscopy.

Preparation of $ReO_2F_3(CH_3CN)$

In a drybox, ReO_2F_3 (0.2114 g, 0.7682 mmol) was weighed into a $^1/_4$-in FEP reaction vessel fitted with a Kel-F valve. Dry CH_3CN (ca. 1 mL) was condensed onto the solid which dissolved completely at room temperature to yield a pale yellow solution. The excess CH_3CN was removed at 0 °C for 12 h and a white powder was isolated which was stable at room temperature. A sample for NMR spectroscopy was prepared by dissolving 0.0402 g (0.146 mmol) of ReO_2F_3 in 0.0100 g (0.244 mmol) of dry CH_3CN in a 4-mm o.d. FEP tube followed by addition of ca. 0.3 mL of SO_2ClF.

Preparation of $N(CH_3)_4^+TcO_2F_4^-$

In a typical preparation, 0.0652 g (0.347 mmol) of TcO_2F_3 and 0.0328 g (0.352 mmol) of $N(CH_3)_4F$ were loaded inside a drybox into a $^1/_4$-in o.d. FEP tube fitted

with a Kel-F valve. Anhydrous HF (ca. 2 mL) was condensed onto the solids which did not dissolve entirely upon warming the orange solution to room temperature, even after 30 min of vigorous agitation. The solvent was then removed at room temperature and the microcrystalline orange solid was dried under dynamic vacuum for 6 h and transferred into a drybox.

A sample for ^{19}F and ^{99}Tc NMR spectroscopy was prepared by weighing 0.0320 g (0.170 mmol) of TcO_2F_3 and 0.0162 g (0.174 mmol) of $N(CH_3)_4F$ into a 4-mm o.d. FEP NMR tube inside a drybox and condensing anhydrous HF (ca. 0.3 mL) onto the solids. After 30 min of vigorous agitation at room temperature, the solvent was removed and the light orange solid was dried under dynamic vacuum overnight. Dry CH_3CN (ca. 0.3 mL) was then condensed into the NMR tube which was then heat-sealed. Before running the NMR spectrum, the undissolved pale orange solid was centrifuged to the top of the FEP sample tube.

Preparation of $M^+TcO_2F_4^-$ (M = Li, Cs) and Crystal Growth of $Li^+TcO_2F_4^-$

In a typical preparation, 0.0591 g (0.315 mmol) of TcO_2F_3 and 0.00990 g (0.382 mmol) of finely powdered LiF were loaded inside a drybox into a $^1/_4$-in o.d. FEP tube fitted with a Kel-F valve. Anhydrous HF (ca. 1 mL) was condensed onto the solids, which did not dissolve entirely upon warming the solution to room temperature. The orange solution was agitated vigorously for 30 min before removing the solvent at room temperature. The microcrystalline orange $Li^+TcO_2F_4^-$ was then dried under vacuum for 6 h

and stored in a drybox. The cesium salt of $TcO_2F_4^-$ was similarly prepared by allowing 0.0618 g (0.329 mmol) of TcO_2F_3 to react with 0.0512 g (0.337 mmol) of CsF.

Single crystals of $Li^+TcO_2F_4^-$ suitable for X-ray structure determination were prepared by the following method: lithium fluoride (0.0062 g, 0.24 mmol) and TcO_2F_3 (0.0304 g, 0.162 mmol) were weighed inside a drybox into one arm of a $^1/_4$-in T-shaped FEP reactor fitted with a Kel-F valve (Figure 2.10) and anhydrous HF (ca. 1 mL) was condensed onto the solids. Excess LiF was necessary to completely solubilize the TcO_2F_3. The reactor was then pressurized to 900 torr with dry nitrogen and clamped in a horizontal position with the empty side-arm immersed in an ice/water bath. The HF slowly condensed into the cooler part of the reactor over a period of three days, concentrating the solution until deep-orange plates formed. The solution was then decanted off the crystals and the residual HF was removed under dynamic vacuum for 12 h. The reactor was then transferred into a drybox where single crystals were selected under a microscope and individually sealed inside Lindemann or quartz capillaries (0.3- and 0.5-mm i.d., respectively). The crystal used for the data acquisition had the dimensions 0.58 × 0.56 × 0.15 mm^3.

Preparation and Crystal Growth of $Li^+ReO_2F_4^-$

In a drybox, ReO_2F_3, 0.3868 g (1.406 mmol) and LiF, 0.0369 g (1.42 mmol), were loaded into one arm of a $^1/_4$-in o.d. FEP T-reactor (Figure 2.10). Anhydrous HF (ca. 1 mL) was condensed onto the solids, yielding a yellow solution at room temperature. Enough HF was then removed to precipitate ca. 50 mg of solid $Li^+ReO_2F_4^-$ at 20 °C. Both

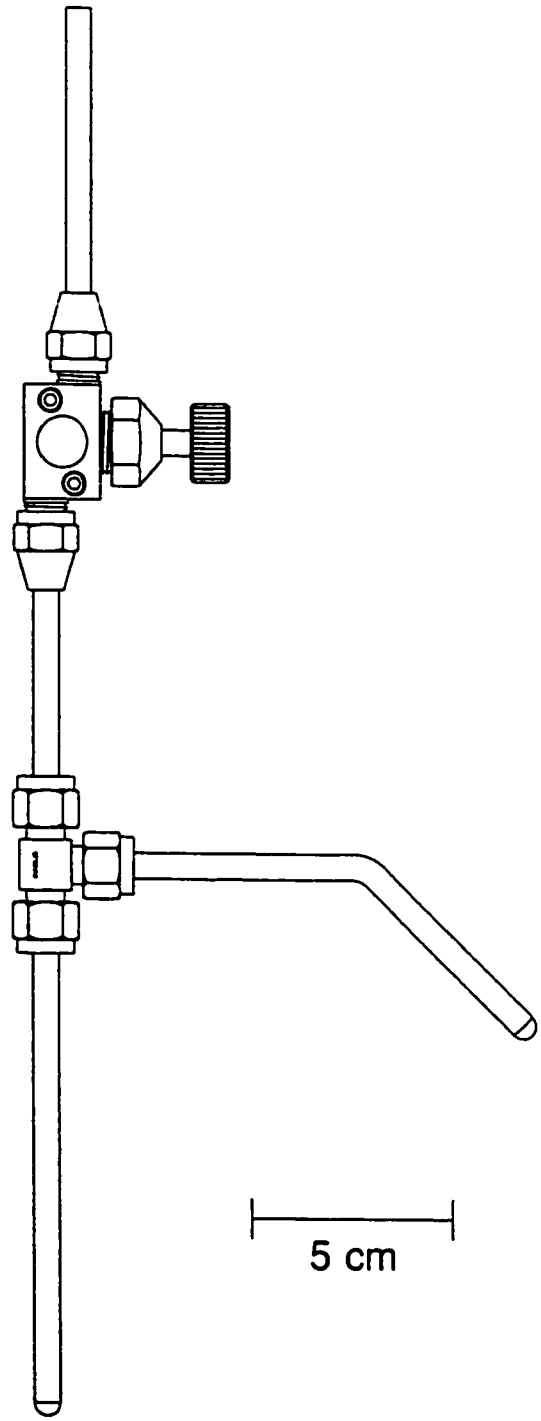

Figure 2.10. T-shaped FEP reaction vessel constructed from $^{1}/_{4}$-in lengths of FEP tubing, a PTFE Swagelok T-connector and a Kel-F valve.

arms of the T-reactor were heated in warm water baths to 40 °C and the yellow solution was decanted off the remaining solid into the free arm of the reactor. Both arms of the reactor were allowed to cool to 20 °C over an 8 h period, at the end of which yellow plate-like crystals were obtained in the yellow solution. The supernatant was then decanted back into the original reaction arm, and the solvent was removed under dynamic vacuum at 20 °C. The crystals showed no signs of decomposition under vacuum, nor did the yellow microcrystalline $Li^+ReO_2F_4^-$ isolated in the other arm. The entire reactor was transferred into a drybox, where single crystals were selected under a microscope and individually sealed inside 0.2-mm i.d. Lindemann capillaries. The crystals were stored at room temperature since they were observed to undergo a phase transition below 0 °C.

Preparation of $Na^+ReO_2F_4^-$ and $Cs^+ReO_2F_4^-$

In a drybox, ReO_2F_3, 0.1597 g (0.5803 mmol) and NaF, 0.0291 g (0.693 mmol), were loaded into a $^1/_4$-in o.d. FEP tube fitted with a Kel-F valve. Anhydrous HF (ca. 1 mL) anhydrous HF was condensed onto the solids, yielding a yellow solution at room temperature. Removal of the solvent under dynamic vacuum at room temperature left yellow, microcrystalline $Na^+ReO_2F_4^-$ in quantitative yield.

An analogous procedure was used to prepare $Cs^+ReO_2F_4^-$ [ReO_2F_3, 0.1422 g (0.5167 mmol) and CsF, 0.0813 g (0.538 mmol)]. The yellow, microcrystalline $Cs^+ReO_2F_4^-$ was obtained in quantitative yield.

Preparation of $N(CH_3)_4^+ReO_2F_4^-$

In a drybox, ReO_2F_3 (0.4053 g, 1.473 mmol) and $N(CH_3)_4F$ (0.1356 g, 1.456 mmol) were loaded into a $^1/_4$-in o.d. FEP reactor fitted with a Kel-F valve. Anhydrous HF (ca. 3 mL) was condensed onto the solids which dissolved to give a pale yellow solution at room temperature. Removal of the solvent under dynamic vacuum at room temperature yielded 0.5236 g (1.421 mmol, 98% yield) of pale yellow microcrystalline $N(CH_3)_4^+ReO_2F_4^-$, which was recovered and transferred into a drybox.

In an attempt to prepare $N(CH_3)_4^+ReO_2F_4^-$ in CH_3CN solvent, $N(CH_3)_4F$ (0.17393 g, 1.8673 mmol) and ReO_2F_3 (0.50717 g, 1.8428 mmol) were weighed into a 4-mm o.d. FEP reaction vessel fitted with a Kel-F valve. Dry CH_3CN (ca. 2 mL) was distilled onto the solids at -196 °C. It was observed, however, that the ReO_2F_3 was a sufficiently powerful oxidizer to char the $N(CH_3)_4F$ at -40 °C, and produce a black carbonaceous mass.

Preparation of $N(CH_3)_4^+Re_2O_4F_7^-$

In a drybox, $N(CH_3)_4^+ReO_2F_4^-$ (0.0457 g, 0.124 mmol) and ReO_2F_3 (0.0347 g, 0.126 mmol) were loaded into a 4-mm o.d. FEP tube fitted with a Kel-F valve. Dry CH_3CN (ca. 0.5 mL) was condensed onto the solids, which dissolved completely at room temperature to yield a pale yellow solution. The reactor was then heat-sealed and stored at -196 °C until the NMR experiment was performed.

Preparation and Crystal Growth of $K^+Re_2O_4F_7^-$

In a drybox, ReO_2F_3 (0.1514 g, 0.5502 mmol) and KF (0.0160 g, 0.2767 mmol) were loaded into a $^1/_4$-in o.d. FEP T-reactor fitted with a Kel-F valve (Figure 2.10). Anhydrous HF (ca. 0.5 mL) was condensed onto the solids, which partially dissolved at room temperature forming a pale yellow solution and a white residue. The reactor was pressurized to 2 atm with nitrogen and both arms of the reactor were warmed to 40 °C and agitated before decanting the supernatant into the empty arm of the reactor. Colourless plates grew over a 24 h period as the solution was allowed to cool to room temperature. The solution was decanted off the crystals and the solvent was removed under dynamic vacuum for 24 h before transferring the reactor into a drybox. Single crystals were selected under a microscope and individually sealed inside Lindemann capillaries (0.1- to 0.5-mm i.d.).

Preparation and Crystal Growth of $K^+Re_2O_4F_7^-\cdot 2ReO_2F_3$

In a drybox, ReO_2F_3 (0.1573 g, 0.5716 mmol) and KF (0.0173 g, 0.298 mmol) were loaded into a bent $^1/_4$-in o.d. FEP reactor fitted with a Kel-F valve. Anhydrous HF (ca. 0.5 mL) was distilled onto the solids, which partially dissolved at room temperature, forming a pale yellow solution and a white residue. The reactor was pressurized with dry nitrogen (1100 torr), warmed to 40 °C and sonicated for 5 min. The solution was then carefully decanted to the bent portion of the reactor which was submerged into a water bath at 45 °C. Large plates and small needles formed after 48 h, at which point the solution was decanted to the bottom of the reactor. The solvent was removed and the

crystals were dried under dynamic vacuum for 24 h before transferring the reactor into a drybox. Single crystals were selected under a microscope and individually sealed inside Lindemann capillaries (0.1- to 0.5-mm i.d.). The crystal used for data acquisition had the dimensions 0.36 × 0.10 × 0.08 mm^3.

Preparation and Crystal Growth of $Cs^+Re_3O_6F_{10}^-$

In a drybox, ReO_2F_3 (0.2039 g, 0.7409 mmol) and CsF (0.0439 g, 0.289 mmol) were weighed into one arm of $^3/_8$-in. o.d. FEP T-reactor fitted with a Kel-F valve. Anhydrous HF (ca. 4 mL) was condensed on to the solids and the reactor was pressurized to 2 atm with dry N_2. The tube containing anhydrous HF was heated to 40 °C and agitated. Over one half (by volume) of the solid observed at room temperature dissolved at this point. The colourless supernatant solution was decanted into the free arm of the reactor, which had also been heated to 40 °C using a Dewar flask filled with water, and allowed to cool slowly to room temperature. Colourless needles and plates grew over a period of 8 h. The supernatant was decanted off the crystals and the solvent was removed under dynamic vacuum at room temperature for 12 h. The crystalline material was transferred into a drybox where single crystals were selected under a microscope and individually sealed inside Lindemann capillaries (0.2-mm i.d.) and stored at -10 °C prior to mounting on the diffractometer. The crystals used in this study had the following dimensions: 0.2 × 0.2 × 0.03 mm^3.

Crystal Growth of $ReO_3F(CH_3CN)_2 \cdot CH_3CN$

Crystals of $ReO_3F(CH_3CN)_2 \cdot CH_3CN$ were grown from an NMR sample of ReO_2F_3 in CH_3CN. The clear pale yellow solution was heated to 40 °C in a water bath and allowed to cool down to room temperature over two days, yielding large cubic crystals. The FEP tube was transferred to a glove bag filled with dry nitrogen and cut open. The supernatant was removed using a disposable pipette and the tube containing the crystals was inserted into a $^1/_4$-in o.d. FEP tube which was fitted with a Kel-F valve. The remaining solvent was then removed from the crystals under dynamic vacuum for 10 s, before transferring the vessel into a drybox, where single crystals were selected under a microscope and individually sealed inside Lindemann capillaries (0.3- to 0.5-mm i.d). Only one crystal was suitable for X-ray structure determination and had dimensions $0.50 \times 0.35 \times 0.30$ mm^3.

Preparation and Crystal Growth of $TcO_2F_3 \cdot SbF_5$

In a drybox, 0.0737 g (0.392 mmol) of TcO_2F_3 and 0.0783 g (0.438 mmol) of SbF_3 were loaded into the vertical and horizontal arms, respectively, of a $^1/_4$-in o.d. FEP T-reactor fitted with a Kel-F valve (Figure 2.10). Anhydrous HF (ca. 0.3 mL) was condensed onto the SbF_3. The reactor was then pressurized with 1000 torr of fluorine gas and the horizontal arm was sonicated at room temperature for 1 h until a clear, colourless solution was obtained. The SbF_5/HF solution was then decanted onto the TcO_2F_3, which dissolved upon agitation. The reactor was evacuated and the HF and excess SbF_5 were removed at room temperature through an FEP U-trap cooled to -196 °C yielding a pale

yellow solid which was dried overnight under dynamic vacuum; yield, 0.1616 g (0.399 mmol). Single crystals were grown by dissolving 0.1100 g of $TcO_2F_3 \cdot SbF_5$ in 0.3 mL of HF inside a $^1/_4$-in o.d. FEP reaction tube pressurized with ca. 1000 torr of nitrogen and allowing the HF to slowly diffuse through the walls of the tube for five days. The solution was decanted off the pale yellow plates and the remaining HF was removed under vacuum before transferring the reactor into a drybox. Single crystals were selected under a microscope and individually sealed inside Lindemann capillaries (0.2- to 0.5-mm i.d.). The crystal used for data acquisition had the dimensions 0.35 × 0.25 × 0.10 mm^3.

Preparation and Crystal Growth of $ReO_2F_3 \cdot SbF_5$

In a drybox, 0.1305 g (0.474 mmol) of ReO_2F_3 and 0.0884 g (0.495 mmol) of SbF_3 were loaded into the vertical and horizontal arms, respectively, of a $^1/_4$-in o.d. T-shaped FEP reactor (Figure 2.10). Anhydrous HF (ca. 0.3 mL) was condensed onto the SbF_3. The reactor was then pressurized with 1000 torr of fluorine gas and the horizontal arm was sonicated at room temperature for 1 h until a clear, colourless solution was obtained. The SbF_5/HF solution was then decanted onto the ReO_2F_3, which dissolved upon agitation. The reactor was evacuated and the HF and excess of SbF_5 were removed at room temperature yielding a white solid which was dried overnight under dynamic vacuum; yield, 0.1842 g (0.374 mmol). Single crystals were grown by dissolving 0.2483 g of $ReO_2F_3 \cdot SbF_5$ in approximately 0.5 mL of SO_2ClF in a bent $^1/_4$-in o.d. FEP reaction tube fitted with a Kel-F valve. The solution was sonicated at 40 °C and the supernatant was

decanted into the bent portion of the reaction tube which was then immersed into a Dewar filled with water at 40 °C and left to cool overnight. Colourless blocks formed above the solution and the SO_2ClF was removed under vacuum before transferring the reactor to a drybox. Single crystals were selected under a microscope and individually sealed inside Lindemann capillaries (0.2- to 0.5-mm i.d.). The crystal used for the data acquisition had the dimensions 0.31 × 0.25 × 0.20 mm^3.

Preparation of $TcO_2F_3 \cdot AsF_5$ and $ReO_2F_3 \cdot AsF_5$

The preparation procedure for $ReO_2F_3 \cdot AsF_5$ was similar to that of the Tc analog except where indicated in brackets. In a drybox, 0.0500 g (0.266 mmol) of TcO_2F_3 [0.1298 g (0.4715 mmol) of ReO_2F_3] was loaded into a 4-mm o.d. FEP reactor fitted with a Kel-F valve. Anhydrous HF (ca. 0.3 mL) was distilled into the reactor followed by ca. 1000 torr of AsF_5 (1.20 mmol) which was condensed into the solution at -196 °C. The yellow [colourless] solid dissolved completely upon warming to room temperature and agitation. Hydrogen fluoride and excess AsF_5 were then removed at -45 °C through an FEP U-trap at -196 °C, yielding a pale yellow [colourless] solid which was then dried under dynamic vacuum at -45 °C for 8 h [16 h].

Preparation of $[ReO_2F_2(CH_3CN)_2]^+SbF_6^-$

In a drybox, 0.0744 g (0.151 mmol) of $ReO_2F_3 \cdot SbF_5$ was loaded into a 4-mm o.d. FEP tube fitted with a Kel-F valve. Dry CH_3CN (ca. 0.4 mL) was condensed into the reactor at -196 °C, which was then warmed to room temperature and sonicated for 1 min

until the solid dissolved. The solvent was then removed at -40 °C to yield a white solid. An NMR sample was prepared by condensing 0.4 mL of CH_3CN onto 0.0251 g (0.0510 mmol) of $ReO_2F_3 \cdot SbF_5$ at -196 °C. The sample was only warmed to 0 °C immediately before acquisition of the NMR spectrum.

Preparation and Crystal Growth of $TcO_2F_3 \cdot XeO_2F_2$

Anhydrous HF (ca. 1 mL) was condensed onto Tc_2O_7 (0.4280 g, 1.1.382 mmol) in a $^1/_4$-in FEP T-shaped reactor fitted with a Kel-F valve (Figure 2.8). Two liquid phases formed upon warming at room temperature and vigorous agitation. The mixture was allowed to stand at room temperature for 1 h prior to condensing XeF_6 (0.4234 g, 1.726 mmol) into the reaction tube from an FEP weighing vessel (Figure 2.9). A bright yellow precipitate formed upon warming to room temperature and the supernatant over the TcO_2F_3 remained slightly yellow as a consequence of the formation of $XeF_5^+TcO_2F_4^-$. The supernatant was then decanted into the side-arm of the reactor and the solvent back-distilled onto the solid by slowly cooling the vertical tube at -196 °C. The mixture was then agitated and the supernatant decanted again into the side-arm. This procedure was repeated five times in an attempt to wash the TcO_2F_3 free of $XeOF_4$ and XeO_2F_2. The side-arm was then heat-sealed and disposed of and the residual HF was removed from the yellow solid. The lower portion of the reactor was warmed to 45 °C under dynamic vacuum until yellow crystals sublimed which were identified as $TcO_2F_3 \cdot XeO_2F_2$ by Raman spectroscopy. The reactor was transferred into a drybox where single crystals were selected under a microscope and individually sealed inside Lindemann capillaries (0.1-

to 0.3-mm i.d.). The crystal used for the data acquisition had the dimensions 0.25 × 0.15 × 0.05 mm^3.

Preparation of $TcOF_5$

In a typical experiment, 0.0658 g (0.350 mmol) of TcO_2F_3 was loaded into a $^1/_4$-in o.d. FEP reactor fitted with a stainless steel ORF-2 valve. Anhdrous HF (ca. 0.5 mL) was condensed onto the solid. Krypton difluoride (0.33615 g; 2.760 mmol) was sublimed from an FEP weighing vessel (Figure 2.9) into the reactor in three aliquots. The reaction mixture was warmed to room temperature between each addition and periodically sonicated until gas evolution stopped. The incondensible gases were then removed at -196 °C and additional KrF_2 was condensed into the reactor until the insoluble TcO_2F_3 completely reacted to form an deep-orange solution of $TcOF_5$ in HF. The solvent was then removed at -78 °C to yield a volatile orange solid that could be sublimed under static vacuum at room temperature.

Preparation and Crystal Growth of $Tc_2O_2F_9^+Sb_2F_{11}^-$

In a drybox, 0.1040 g (0.582 mmol) of SbF_3 was loaded into a $^1/_4$-in o.d. FEP reactor fitted with a Kel-F valve. Anhydrous HF (ca. 0.5 mL) was condensed onto the solid and the reactor was pressurized with 1100 torr of fluorine. The solution was sonicated for 90 min until complete reaction of the SbF_3. An HF solution of $TcOF_5$ (0.133 mmol) was then distilled into the SbF_5/HF reactor at -196 °C through an FEP Y-piece. A bright yellow solid was formed under a pale yellow solution upon warming to

room temperature. The solvent and excess SbF_5 were then removed under dynamic vacuum at room temperature through an FEP U-trap at -196 °C, yielding a bright yellow free flowing powder after 24 h. Single crystals were grown by dissolving 0.0101 g of $Tc_2O_2F_9^+Sb_2F_{11}^-$ in ca. 0.3 mL of anhydrous HF at room temperature in the vertical arm of a $^1/_4$-in o.d. FEP T-reactor pressurized with 1000 torr of dry nitrogen. The saturated supernatant was decanted into the horizontal arm of the reactor and the vertical portion was immersed into an ice/water bath. Deep orange rod-shaped crystals formed after three days and the remaining solution was carefully decanted from the crystals before removing the solvent under dynamic vacuum at room temperature through an FEP U-trap at -196 °C for 24 h. The reactor was then transferred into a drybox where single crystals were selected under a microscope and individually sealed inside Lindemann capillaries (0.1- to 0.5-mm i.d.). The crystal used for the data acquisition had the dimensions 0.22 × 0.20 × 0.07 mm^3.

Attempted Preparation of $TcF_6^+AsF_6^-$ and Preparation of $TcOF_5 \cdot AsF_5$

An HF solution of $TcOF_5$ (0.187 mmol) was prepared in a $^1/_4$-in o.d. FEP reactor fitted with a stainless steel ORF-2 valve. Krypton difluoride (0.2310 g; 1.904 mmol) was condensed into the reactor from an FEP weighing vessel (Figure 2.9) followed by 0.934 mmol of AsF_5. The reaction mixture was warmed to room temperature for a few seconds to achieve complete dissolution of the solids. The solution was then kept at 0 °C where gas evolution was occurring at a reasonable rate. After 30 min, no obvious change was noted in the colour of the solution. The incondensible gases were removed at -196 °C

and upon warming to 0 °C a yellow solid precipitated from the solution. The reaction was allowed to proceed for another 2 h until gas evolution subsided at which point a large amount of yellow solid was present under a pale yellow solution. The solvent and excess AsF_5 were then removed at -78 °C under dynamic vacuum through an FEP U-trap at -196 °C for 18 h, yielding a free flowing yellow powder which was identified as $Tc_2O_2F_9^+AsF_6^-$ by Raman spectroscopy.

X-RAY CRYSTALLOGRAPHY

Collection and Reduction of X-ray Data

The parameters used for the collection of diffraction data are summarized in Table 2.1. The diffraction data for $Li^+TcO_2F_4^-$, $Li^+ReO_2F_4^-$, $K^+Re_2O_4F_7^-$, $Cs^+Re_3O_6F_{10}^-$, $TcO_2F_3{\cdot}SbF_5$, $ReO_2F_3{\cdot}SbF_5$ and $TcO_2F_3{\cdot}XeO_2F_2$ were collected on a Syntex $P2_1$ diffractometer with graphite-monochromatized Ag-K_α radiation (λ = 0.56086 Å). Integrated diffraction intensities were collected using a θ-2θ scan method with scan rates varying from 1.5 to 14.65°/min in 2θ so that the weaker reflections were examined more slowly to minimize counting errors. During data collection, the intensities of three standard reflections were monitored every 97 reflections to check for crystal decomposition and alignment. The data were corrected for Lorentz and polarization effects and absorption.

The data sets of $K^+Re_2O_4F_7^-{\cdot}2ReO_2F_3$, $ReO_3F(CH_3CN)_2{\cdot}CH_3CN$ and $Tc_2O_2F_9^+Sb_2F_{11}^-$ were collected with the program SMART[75] on a P4 Siemens diffractometer equipped with a Siemens SMART 1K CCD area detector and a rotating anode with graphite-

Table 2.1. Summary of X-Ray Data Collection Parameters

	$Li^+TcO_2F_4^-$	$Li^+ReO_2F_4^-$	$K^+Re_2O_4F_7^-$	$K^+Re_2O_4F_7^-\cdot 2ReO_2F_3$	$Cs^+Re_3O_6F_{10}^-$
diffractometer	Syntex $P2_1$	Syntex $P2_1$	Syntex $P2_1$	Siemens P4 with CCD	Syntex $P2_1$
scan type	θ - 2θ	θ - 2θ	θ - 2θ	see text	θ - 2θ
λ (Å)	0.56086	0.56086	0.56086	0.71073	0.56086
T (°C)	22	24	24	-60	-118
abs. corrections	psi scan	DIFABS[15]	DIFABS[15]	SADABS[14]	DIFABS[15]
h	$-7 \rightarrow 8$	$0 \rightarrow 9$	$0 \rightarrow 6$	$-36 \rightarrow 36$	$0 \rightarrow 12$
k	$0 \rightarrow 8$	$-9 \rightarrow 0$	$-6 \rightarrow 6$	$-7 \rightarrow 7$	$-17 \rightarrow 17$
l	$0 \rightarrow 15$	$-16 \rightarrow 16$	$-18 \rightarrow 17$	$-3 \rightarrow 7$	$-18 \rightarrow 18$
0 (deg)	$5.01 \rightarrow 30.05$	$1.5 \rightarrow 30$	$2.19 \rightarrow 20.04$	$1.51 \rightarrow 28.34$	$1.5 \rightarrow 27.5$
no. measured refl.	973	2994	1671	4192	6700
no. indep. refl.	523	665	801	1719	6095
no. obs. refl. ($I > 2\sigma(I)$)	474	644	631	1690	4857

Table 2.1. continued

	$ReO_3F(CH_3CN)_2$	$TcO_2F_3 \cdot SbF_5$	$ReO_2F_3 \cdot SbF_5$	$TcO_2F_3 \cdot XeO_2F_2$	$Tc_2O_2F_9^+Sb_2F_{11}^-$
diffractometer	Siemens P4 with CCD	Syntex $P2_1$	Syntex $P2_1$	Syntex $P2_1$	Siemens P4 with CCD
scan type	see text	θ - 2θ	θ - 2θ	θ - 2θ	see text
λ (Å)	0.71073	0.56086	0.56086	0.56086	0.71073
T (°C)	-63	24	-50	-100	-90
abs. corrections	SADABS[14]	psi scan	psi scan	psi scan	SADABS[14]
h	-11 → 11	-1 → 11	-1 → 9	-1 → 10	-8 → 8
k	-15 → 15	-15 → 15	-1 → 17	-7 → 22	-23 → 9
l	-11 → 10	-14 → 14	-22 → 22	-7 → 7	-15 → 15
θ (deg)	1.63 → 26.38	2.67 → 25.09	2.07 → 30.09	2.26 → 22.51	2.59 → 27.56
no. measured refl.	8649	3568	5350	609	7810
no. indep. refl.	1194	2442	4042	538	1718
no. obs. refl. ($I > 2\sigma(I)$)	1188	1686	3323	475	1249

monochromated Mo-K_α radiation (λ = 0.71073 Å). The diffraction data collection consisted of a full ψ rotation at χ = 0° using (1200 + 50) 0.3° frames, followed by a series of short (100 frames) ω scans at various χ and ψ settings to fill the gaps. The detector was located at 3.991 cm from the crystal and the complete data set was acquired at a 2θ setting of 330°. The data was reduced with the program SAINT[75] which applied Lorentz and polarization corrections to the three-dimensionally integrated diffraction spots. The program SADABS[76] was used for the scaling of the diffraction data and the application of an empirical absorption correction based on redundant reflections.

Solution and Refinement of the Structures

The final refinement results for each compound are listed in the crystal data and refinement result Tables, which can be found in subsequent Chapters.

General Procedure. The XPREP[78,79] program was used to confirm the unit cells and the crystal lattices. Patterson methods were used to solve the structures in the appropriate space groups which generally located the positions of the heavy atoms. Full-matrix least-square refinements of the positions and isotropic thermal parameters of the assigned atoms and successive difference Fourier syntheses revealed the positions of the remaining atoms. The final structure solutions involved the refinement of anisotropic thermal parameters (except for Li in $Li^+ReO_2F_4^-$) and the setting of the weight factor to the recommended values.

Specific Procedure for $ReO_3F(CH_3CN)_2 \cdot CH_3CN$. No reasonable solution could be obtained for $ReO_3F(CH_3CN)_2 \cdot CH_3CN$ in any of the proposed tetragonal space groups. The structure was first solved successfully in the triclinic space group $P\bar{1}$ and in the monoclinic space group $P2_1/m$. It was then realized that the crystal was in fact orthorhombic and twinned as a result of similar *a*- and *c*-axes. The twinning was modeled and a solution was obtained in the orthorhombic space group *Pnma* using a Patterson function which located the positions of the rhenium atom. Successive difference Fourier syntheses revealed the light atoms. The hydrogen atoms were refined using a riding model. Attempts to model the disordered solvent molecules in the unit cell remained unsuccessful. The final refinement was obtained by introducing anisotropic parameters for all the atoms, an extinction parameter and the recommended weight factor.

Calculations for the structures of $Li^+ReO_2F_4^-$ and $Cs^+Re_3O_6F_{10}^-$ were performed on a 486 personal computer using the SHELXTL PLUS[78] determination package for structure solution and refinement as well as structure determination molecular graphics. Calculations for all the other structures were performed on a Silicon Graphics Model 4600PC workstation with the SHELXL[79] package for structure determination, refinement and molecular graphics.

NUCLEAR MAGNETIC RESONANCE SPECTROSCOPY

Nuclear magnetic resonance spectra were recorded unlocked (field drift < 0.1 Hz h^{-1}) on a Bruker AC-300 (7.0463 T) and a AM-500 (11.7440 T) spectrometer equipped with Aspect 3000 computers. Typical acquisition parameters are given in Table

2.2. For low temperature work, the NMR probe was cooled using a nitrogen flow and variable temperature controller (BV-T 2000). Bruker 5-mm $^{1}H/^{13}C/^{19}F/^{31}P$ QNP and 10-mm broad band probes were used on the AC-300. The AM-500 spectrometer was equipped with a 5-mm combination $^{1}H/^{19}F$ probe and a 10-mm broad-band VSP probe (tunable over the range 23-202 MHz). The ^{1}H, ^{13}C, ^{17}O, ^{19}F and ^{99}Tc NMR spectra were referenced at room temperature to external samples of neat TMS, H_2O, $CFCl_3$, and an aqueous $NH_4^+TcO_4^-$ solution, respectively. The chemical shift convention used is that a positive (negative) sign indicates a chemical shift to high (low) frequency of the reference compound.

T_1 Measurements

Measurement of the spin-lattice relaxation times, T_1, were performed on a Bruker AC-300 spectrometer using a standard inversion-recovery experiment (pulse sequence: π-τ-$^{\pi}/_{2}$-acquisition). Accumulations of 100 scans were done for each NMR spectrum, respectively, which were acquired in 16K memories and spectral widths of 50 kHz. The FIDs were processed with line broadening factors of 20 Hz. Fifteen τ values were used including τ_{∞} = 1 s and 100 μs. The T_1 values were obtained by iterative exponential fitting of the intensity values vs. τ using standard Bruker software.

Spectral Simulations

The spectral simulations of $(ReO_2F_3)_3$ and $(TcO_2F_3)_3$ were carried out using an updated version of the program NUMARIT[80] called XSIM[81] on a Silicon Graphics INDY

Table 2.2. Typical Acquisition Parameters for ^{1}H, ^{13}C, ^{17}O, ^{19}F and ^{99}Tc NMR Spectroscopy

Bruker AC-300

Parameter	^{1}H	^{13}C	^{19}F	^{99}Tc
SF (MHz)	300.000	75.467	282.409	67.555
SI	16K	16K	16K-32K	16K-32K
SW (kHz)	5-10	20-25	10-50	50-100
Hz/data point	0.61-1.22	2.44-3.05	1.22-3.05	3.05-6.10
PW (μs)	2.00	2.00	6.00	9.00
NS	200-1000	10000-15000	1000-10000	1000-5000

Bruker AM-500

Parameter	^{17}O	^{19}F	^{99}Tc
SF (MHz)	67.801	470.599	112.542
SI	16K	16K	16K
SW (Hz)	50	12-25	25-50
Hz/data point	6.10	1.45-3.05	3.05-6.10
PW (μs)	6.40	1.00	14.0
NS	1000-12000	2000-4000	1000-2000

R5000 workstation. Coupling constants were introduced and perturbed one a time until visual agreement between the simulated and the experimental spectra was obtained. Iterative fitting by least-square refinement was not possible because of the very large number (>500 000) of calculated transitions. The estimated error for each coupling constant derived from the simulations is ± 1 Hz. The spectral simulation of $(ReO_2F_3)_4$ was carried out in a similar manner using the PERCH software package[82] on a Pentium 200 computer.

RAMAN SPECTROSCOPY

Instrumentation

Raman spectra were recorded on a Jobin-Yvon Mole S-3000 triple spectrograph system equipped with a 0.32-m prefilter, adjustable 25-mm entrance slit, and a 1.00-m monochromator. Holographic gratings were used for the prefilter (600 grooves mm^{-1}, blazed at 500 nm) and monochromator (1800 grooves mm^{-1}, blazed at 550 nm) stages. The 514.5-nm line of an Ar^+ ion laser (Spectra-Physics Model Stabilite 2016) and the 647.1-nm line of a Kr^+ ion laser (Lexel Model 3500) were used for excitation of the samples. The spectra of room-temperature-stable microcrystalline samples were recorded in Pyrex melting point capillaries using an Olympus metallurgical microscope (model BHSM-L-2) to focus the excitation laser to a 1-μm spot on the samples. The Raman spectra of thermally unstable samples and HF solutions were recorded in FEP at -150 °C and 22 °C, respectively, in the macrochamber of the instrument. Low temperatures were achieved by flowing dry nitrogen gas, chilled by passing through a 50-L tank of liquid

nitrogen, along the outside of the sample tube, which was mounted vertically in an open-ended unsilvered glass Dewar jacket (Figure 2.11). The temperature near the sample was measured with a copper-constantan thermocouple (error ±0.8 °C). The spectra were recorded by signal averaging using a Spectraview-2D CCD detector equipped with a 25-mm chip (1152 × 298 pixels). The laser power measured at the samples was 100-500 mW. Slit settings correspond to a resolution of 0.5-1 cm^{-1}. A total of 10 reads having 10-90 s integration times were summed for each of the Raman spectra. Depolarization measurements were obtained in the macrochamber of the instrument with method VII described by Claassen, Selig and Shamir.[83]

Raman spectra obtained in FEP sample tubes contained lines resulting from the FEP sample tube. The frequencies and relative intensities of the Raman lines at -154 °C are: 203 (2), 278 (6), 294 (45), 309 (9), 381 (36), 387 (26), 579 (13), 598 (3), 734 (100), 752 (9), 1217 (12), 1310 (16) and 1385 (33) cm^{-1}. The prominence of these lines in the Raman spectra depended on the scattering efficiency of the sample and where the laser beam was focused. In the present work, lines arising from FEP have been subtracted out of the spectra reported in the Tables but not in the Figures.

The Raman spectrometer was calibrated with the 1018.3 cm^{-1} line of neat indene in a sealed glass melting point capillary or $^1/_4$-in glass tube at ambient temperature.

Normal Coordinate Analyses

The force constants for $TcOF_5$, $ReOF_5$ and $OsOF_5$ were determined from a general valence force field (GVFF) with the program SVIB.[84] All calculations were carried out

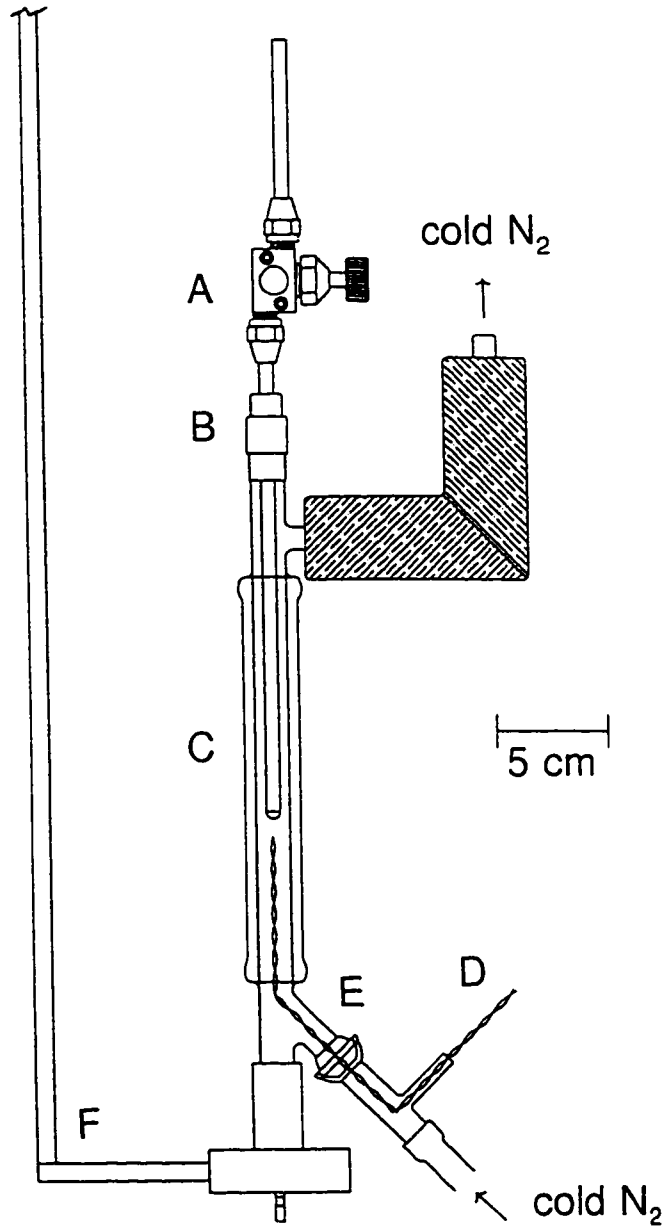

Figure 2.11. Apparatus used to attain low temperatures in the macrochamber of the Raman spectrometer; (A) FEP sample vessel fitted with a Kel-F valve, (B) rubber septum, (C) unsilvered glass Dewar, (D) copper-constantan thermocouple, (E) glass ball and socket joint, (F) steel mount for alignment of the sample in the laser beam.

on a Silicon Graphics 4600PC workstation. The stretching and bending force constants were introduced and perturbed until the best fit between the observed and calculated frequencies was obtained, then the interaction force constants were added one at a time to improve the fit. A final simultaneous refinement of all the force constants was then performed.

THEORETICAL CALCULATIONS

Theoretical calculations were performed by Dr. David A. Dixon of the William R. Wiley Environmental Molecular Science Laboratory, Pacific Northwest Laboratory, 906 Batelle Blvd., P.O. Box 999, KI-83 Richland, Washington 99352.

All calculations were done with the density functional theory program DGauss[35] on SGI computers. The basis set for the oxygen and fluorine atoms[36] is of the form (621/41/1) (DZVP) with a (7/3/3) fitting set. For Tc, the basis set has the form (633321/5321/531) with a fitting basis set of the form (10/5/5). For hydrogen, the basis set has the form (4/1) and a fitting basis set of the form (4). This basis set is denoted DZVP. Additional calculations were done with a slightly larger basis set of the form (7111/411/1) for oxygen and fluorine, with a (7/3/3) fitting basis set, and for technetium a (6333111/531111/5311/1) basis set was used with a fitting basis set of the form (11/6/5) (TZ94P).[37] This basis set is denoted TZVP. The calculations were done at the local level with the potential fit of Vosko, Wilk, and Nusair[38] and at the nonlocal (gradient-corrected) level with the nonlocal exchange potential of Becke[39] combined with the nonlocal

correlation function of Perdew.[90] The geometries were optimized by using analytic gradient methods, and second derivatives were also calculated analytically.[91]

CHAPTER 3

LEWIS ACID PROPERTIES OF TcO_2F_3*

Introduction

Fluorine bridging in the solid state structure of TcO_2F_3 indicates that the TcO_2F_3 monomer should behave as a Lewis acid and possess a significant fluoride-ion affinity. In fact, it was shown by multi-NMR spectroscopy that excess XeF_6 reacts with Tc_2O_7 in HF (molar ratio of XeF_6:Tc_2O_7 = 5:1) to form stable solutions of $XeF_5^+TcO_2F_4^-$.[41]

Transition metal complexes of the type $MO_2F_4^{x-}$ (M = V, Nb, Cr, Mo, W, Re and Os) where the metal is in the d^0 electronic configuration have been prepared. An interesting structural aspect of these compounds is that they all adopt a *cis*-dioxo arrangement, as was determined by vibrational spectroscopy. The valence isoelectronic $VO_2F_4^{3-}$,[101] $MoO_2F_4^{2-}$, $WO_2F_4^{2-}$ [95] and $ReO_2F_4^-$ anions have been structurally characterized by single-crystal X-ray diffraction and OsO_2F_4[93] by electron diffraction in the gas phase, which confirmed the *cis*-dioxo geometries of these compounds.

In this Chapter, the Lewis acid properties of TcO_2F_3 toward the fluoride ion and CH_3CN were investigated in detail, resulting in the full structural characterization of the $TcO_2F_4^-$ anion and the $TcO_2F_3(CH_3CN)$ adduct.

---

* Reprinted in part with permission from *Inorg. Chem.* **1996**, *35*, 929-942. © 1996 American Chemical Society.

Results and Discussion

Syntheses of $TcO_2F_4^-$ Salts and $TcO_2F_3(CH_3CN)$

Technetium dioxotrifluoride, TcO_2F_3, is essentially insoluble in anhydrous HF at room temperature, but readily reacts with HF solutions of LiF, CsF and $N(CH_3)_4F$ in 1:1 molar ratios to form orange, room temperature stable $M^+TcO_2F_4^-$ salts. The solubilities of the Cs^+ and $N(CH_3)_4^+$ salts in anhydrous HF are low when a large excess of solvent is present but increase significantly when the proportion of salt is high. This can be attributed to the comparable Lewis acidities of TcO_2F_3 and HF which compete for the strong Lewis bases CsF and $N(CH_3)_4F$, forming $Cs^+HF_2^-$ and $N(CH_3)_4^+HF_2^-$ salts. Because LiF is a weaker Lewis base, $Li^+TcO_2F_4^-$ is moderately soluble, making it a suitable candidate for single crystal growth.

The Lewis acid properties of TcO_2F_3 are also observed when it is dissolved in CH_3CN and account for the high solubility of the polymeric solid in that solvent (eq. (3.1)). When the solvent was removed at -40 °C, a pale orange adduct, $TcO_2F_3(CH_3CN)$,

$$TcO_2F_3 + CH_3CN \xrightarrow{CH_3CN} TcO_2F_3(CH_3CN) \qquad (3.1)$$

remained, which slowly decomposed at room temperature under nitrogen to the starting materials, as determined by Raman spectroscopy.

Characterization of $TcO_2F_4^-$ by ^{19}F, ^{99}Tc and ^{17}O NMR Spectroscopy

The ^{19}F NMR spectrum of $N(CH_3)_4^+TcO_2F_4^-$ dissolved in CH_3CN at 30 °C consists of a well-resolved 1:2:1 triplet at -14.1 ppm ($\Delta\nu_{1/2}$ = 50 Hz) and a broad saddle-shaped

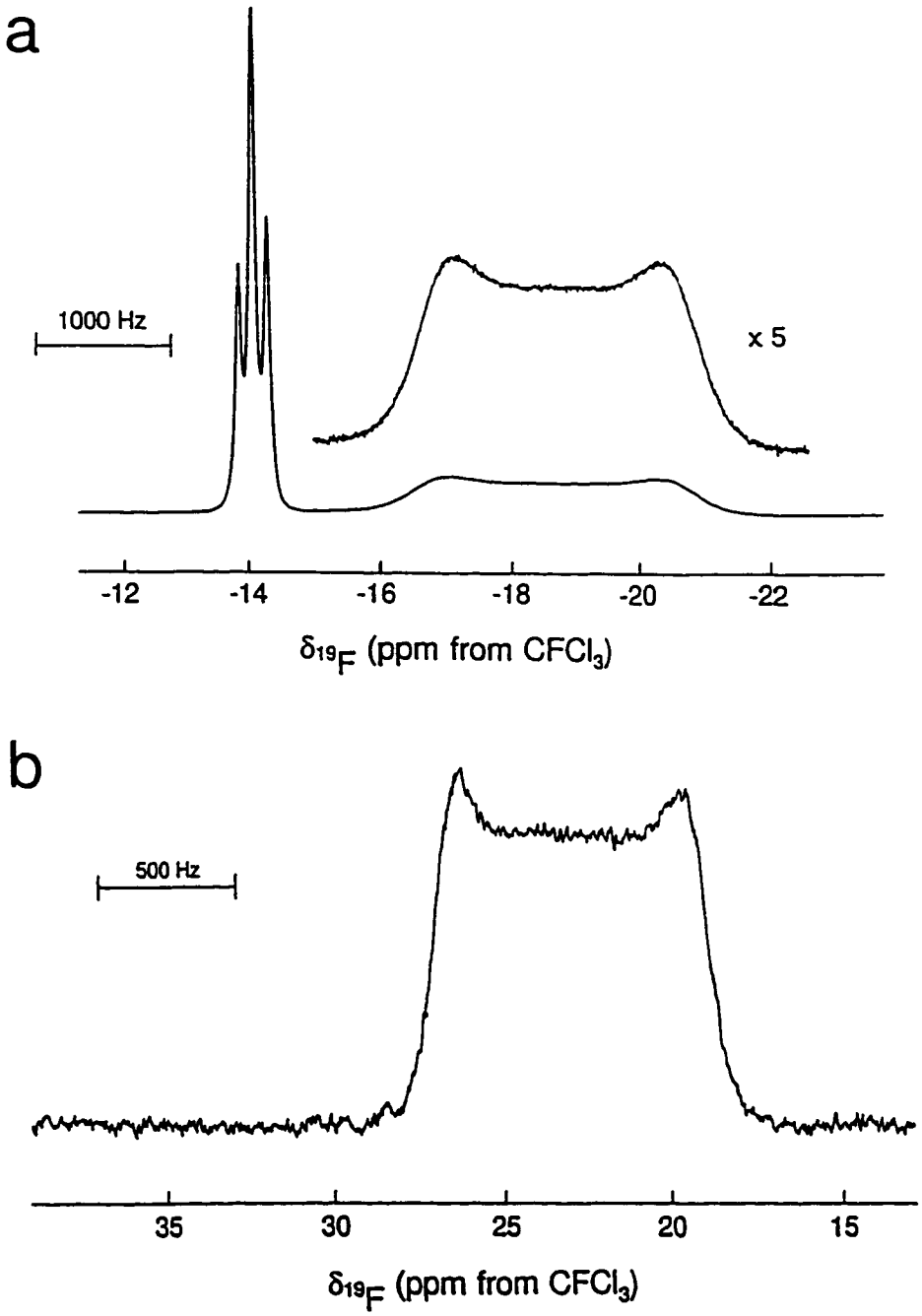

Figure 3.1. NMR spectra of $TcO_2F_4^-$: (a) ^{19}F (470.600 MHz), $N(CH_3)_4^+$ salt in CH_3CN solvent recorded at 30 °C and (b) ^{19}F (470.600 MHz), Cs^+ salt in HF solvent recorded at 30 °C.

feature at -18.7 ppm ($\Delta\nu_{1/2}$ = 1550 Hz), the two components having equal integrated intensities (Figure 3.1a). The observation of two fluorine environments establishes the *cis* geometry adopted by the oxygen ligands in $TcO_2F_4^-$ (Structure I). The saddle-shaped

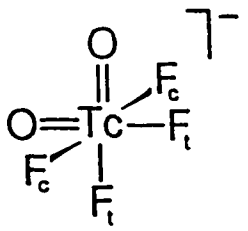

Structure I

feature results from spin-coupling of the fluorine environment to the ^{99}Tc nucleus, yielding a partly quadrupole-collapsed equi-intense decet of 1:2:1 triplets. The triplet in the ^{19}F NMR spectrum arises from the two-bond coupling $^2J(^{19}F_c\text{-}^{19}F_t)$ = 105 Hz (the subscripts denote fluorines *trans* (t) to and *cis* (c) to the oxygen ligands, respectively). Interestingly, the scalar coupling to ^{99}Tc for this resonance is completely quadrupole-collapsed. The assignments of the two signals were based on the relative magnitudes of their one-bond couplings with ^{99}Tc. The Tc-F_t bonds are weaker and longer (see **X-ray Crystal Structure of $Li^+TcO_2F_4^-$**) owing to the *trans* influence of the strongly π-bonded oxygen ligands to the metal $d_{t_{2g}}$ orbitals, so that $^1J(^{99}Tc\text{-}^{19}F_t)$ is expected to be less than $^1J(^{99}Tc\text{-}^{19}F_c)$. The triplet at -14.1 ppm shows only slight line broadening arising from scalar coupling to ^{99}Tc whereas the broad saddle-shaped feature at -18.7 ppm clearly indicates scalar coupling to ^{99}Tc, leading to the assignment of the former resonance to F_t and the latter to F_c. These assignments are supported by a previous ^{19}F NMR study of $WO_2F_4^{2-}$ for which $^1J(^{183}W\text{-}^{19}F_c)$ = 118.0 Hz is significantly larger than

$^1J(^{183}W\text{-}^{19}F_t)$ = 50.0 Hz.[96] The assignment of the two fluorine signals in $WO_2F_4^{2-}$ was confirmed by a variable temperature ^{19}F NMR experiment in which selective broadening of the more weakly bonded F_t resonance arising from fluoride ion/solvent exchange was observed at elevated temperature. A similar experiment was performed with $TcO_2F_4^-$ in HF solvent and confirmed the ^{19}F assignments. The ^{19}F NMR spectrum of $Cs^+TcO_2F_4^-$ at 28 °C consists of only the *cis*-fluorine resonance at 23.0 ppm which showed partly collapsed scalar coupling to the ^{99}Tc nucleus (Figure 3.1b). No resonance corresponding to the *trans*-fluorine environment was observed, even when the spectrum was recorded at -80 °C, indicating rapid exchange of the more labile *trans*-fluorine with the solvent. Increasing the basicity of the solvent by addition of 30% and five-fold molar excesses of CsF did not slow the exchange sufficiently at -80 °C to observe the *trans*-fluorine resonance. The *trans*-fluorine triplet of $ReO_2F_4^-$ was observed for a $CsF:ReO_2F_3$ molar ratio of 5:1 at -80 °C (see Chapter 4) and is consistent with the anticipated stronger Lewis acidity of ReO_2F_3 compared to that of TcO_2F_3.

The ^{19}F NMR spectrum of $N(CH_3)_4^+TcO_2F_4^-$ in CH_3CN appears to be the only example, other than $TcO_2F_3(CH_3CN)$ (*vide infra*), in which a spin-$^1/_2$ nucleus in two different chemical environments directly coupled to the same quadrupolar nucleus exhibits a large difference in their degree of quadrupolar collapse. This difference arises from the relationship between the spin-lattice relaxation rate of the quadrupolar nucleus (T_1^{-1}) and the $^1J(^{99}Tc\text{-}^{19}F)$ coupling constant. For the *trans*-fluorine resonance, the coupling constant is small relative to the relaxation rate of ^{99}Tc, i.e., $2\pi^1J(^{19}F_t\text{-}^{99}Tc) \ll T_1^{-1}$, leading to the observation of essentially complete quadrupole collapse of the scalar coupling. On the

other hand, the larger scalar coupling between the ^{99}Tc nucleus and $^{19}F_c$ leads to a resonance that is only partly quadrupole collapsed, i.e., $2\pi{}^1J(^{19}F_c\text{-}^{99}Tc) \approx T_1^{-1}$. The spin-lattice relaxation time, determined from an inversion-recovery experiment, for ^{99}Tc in $N(CH_3)_4^+TcO_2F_4^-$ is 1.03 ms at 30 °C. This confirmed the assignments in the ^{19}F NMR spectrum since, according to the previous inequalities, a $^1J(^{99}Tc\text{-}^{19}F)$ significantly larger than $(2\pi \cdot 1.03\ ms)^{-1}$ = 155 Hz, as for $^1J(^{99}Tc\text{-}^{19}F_c)$ = 235 Hz (CH_3CN) and 260 Hz (HF) (*vide infra*), would result in a significantly quadrupole broadened fluorine resonance while a $^1J(^{99}Tc\text{-}^{19}F)$ smaller than 155 Hz would show a significantly smaller increase in the line width of the fluorine resonance.

The ^{99}Tc NMR spectrum of $N(CH_3)_4^+TcO_2F_4^-$ dissolved in CH_3CN at 45 °C (Figure 3.2a) displays a broadened 1:2:1 triplet at 343.2 ppm having a coupling constant of 235 Hz (measured after Gaussian multiplication of the free induction decay, otherwise unresolved) arising from $^1J(^{99}Tc\text{-}^{19}F_c)$ and, as in the ^{19}F spectrum, the $^1J(^{99}Tc\text{-}^{19}F_t)$ coupling was not resolved.[103] The ^{99}Tc NMR spectrum of $Cs^+TcO_2F_4^-$ in HF at 30 °C consists of a well-resolved triplet at 247.4 ppm, with a coupling constant of 260 Hz. These results agree well with recently reported[41] values for $XeF_5^+TcO_2F_4^-$ in HF [$\delta(^{99}Tc)$ = 240.0 ppm; $^1J(^{99}Tc\text{-}^{19}F_c)$ = 259 Hz] and it is now clear that in an earlier multi-NMR study,[40] a triplet resulting from the reaction of $K^+TcO_4^-$ with excess XeF_6 or KrF_2 in HF at $\delta(^{99}Tc)$ = 245.9 ppm [$^1J(^{99}Tc\text{-}^{19}F_c)$ = 259 Hz] and tentatively assigned to $Tc_2O_5F_4$, in fact, arose from the $TcO_2F_4^-$ anion.

The ^{17}O NMR spectra of $N(CH_3)_4^+TcO_2F_4^-$ dissolved in CH_3CN at 30 and 63 °C display a single resonance which consists of a partly quadrupole-collapsed multiplet

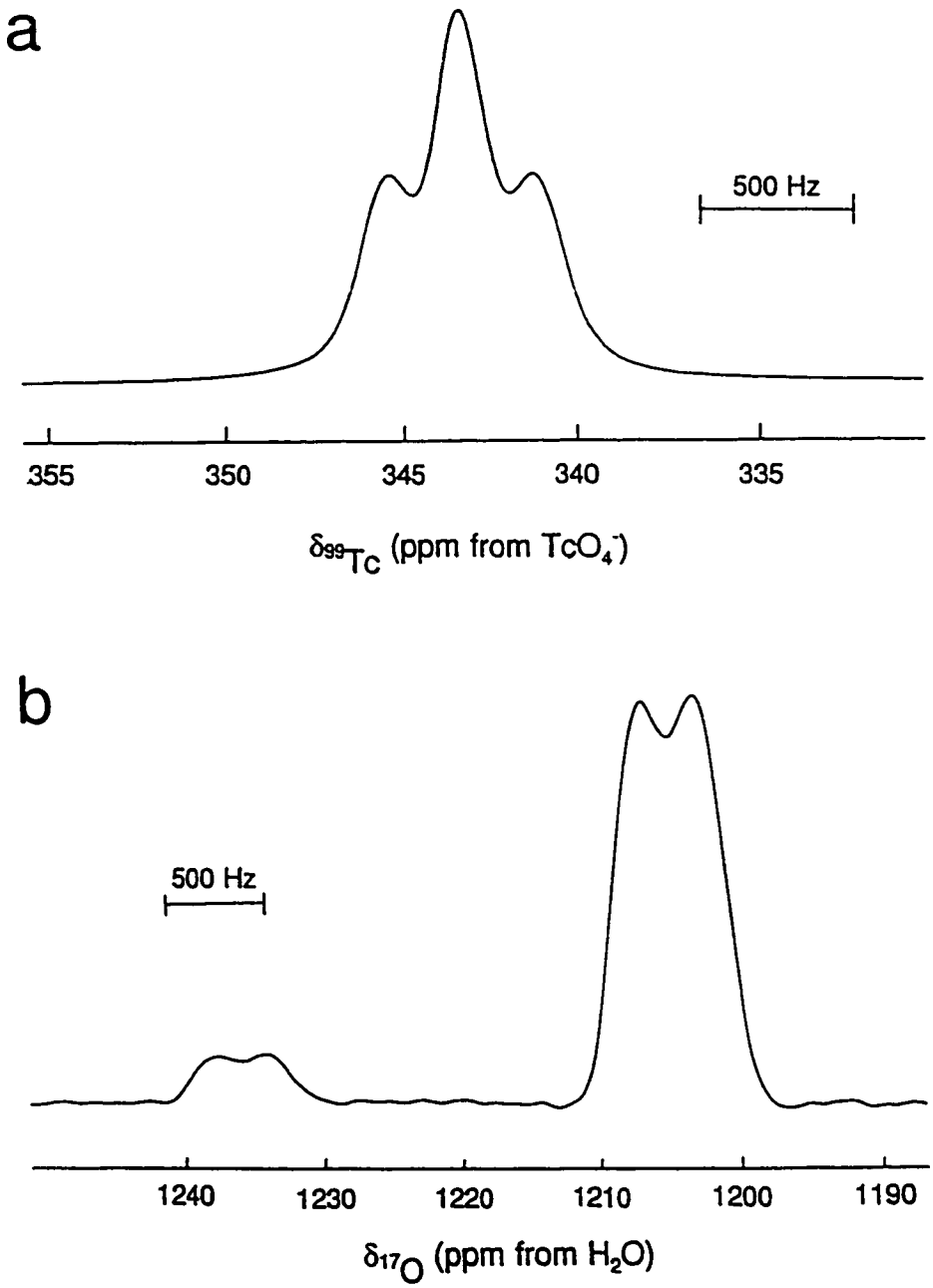

Figure 3.2. NMR spectra of $N(CH_3)_4^+TcO_2F_4^-$: (a) ^{99}Tc (112.570 MHz) in CH_3CN recorded at 45 °C and (b) ^{17}O (67.801 MHz) in CH_3CN recorded at 63 °C (21.87% ^{17}O).

arising from scalar coupling to ^{99}Tc at 1204 ppm ($\Delta\nu_{1/2}$ = 570 Hz at 30 °C, 600 Hz at 63 °C) (Figure 3.2b).[104] The two-bond coupling between ^{17}O and either ^{19}F environment could not be resolved.

Characterization of $TcO_2F_3(CH_3CN)$ by ^{19}F, ^{99}Tc and ^{17}O NMR Spectroscopy

The high solubility of TcO_2F_3 in CH_3CN down to the melting point of the solvent (-45.7 °C) is attributed to complex formation. The ^{19}F NMR spectra of TcO_2F_3 in CH_3CN recorded at -40, 30 and 51 °C display two fluorine resonances (Figure 3.3). The spectrum at -40 °C shows a binomial triplet at 29.8 ppm ($\Delta\nu_{1/2}$ = 29 Hz) and a broad resonance at 23.9 ppm ($\Delta\nu_{1/2}$ = 460 Hz) having relative integrated intensities of 1.0:2.0. Although it was not possible to determine the relative positions of the oxygen atoms from this spectrum, a *cis*-dioxo arrangement (Structure II) is assumed based on the experimental structures of $TcO_2F_4^-$, TcO_2F_3[41] and all other d^0 transition metal dioxofluorides as well as

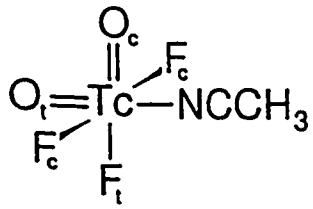

Structure II

the energy-minimized structures determined by local density functional theory (LDFT) (see **Computational Results**). Furthermore, the CH_3CN coordinates *trans* to the oxygen atom in its complexes with WOF_4,[105] $MoOF_4$[106] and VOF_4^-,[107] rendering all fluorine atoms equivalent in their ^{19}F NMR spectra. Consequently, the triplet of the $TcO_2F_3(CH_3CN)$ adduct is reasonably assigned to the fluorine atom *trans* to an oxygen ligand with a two-

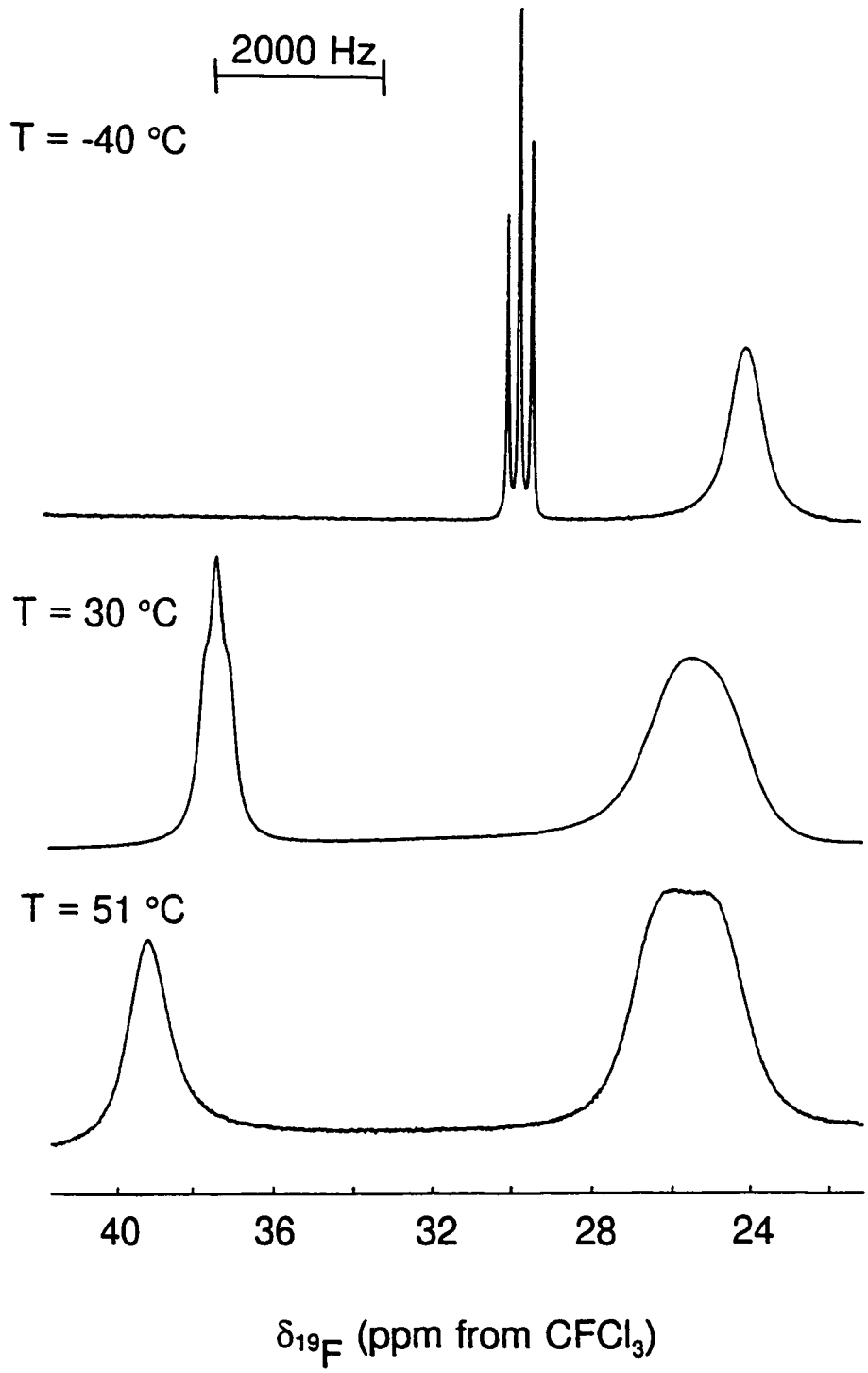

Figure 3.3. Variable temperature ^{19}F NMR spectra (470.600 MHz) of TcO_2F_3 (0.36 M) dissolved in CH_3CN.

bond spin-spin coupling to the *cis*-fluorine atoms, $^2J(^{19}F_c\text{-}^{19}F_t)$ = 147 Hz. This fluorine environment is only very weakly coupled to the ^{99}Tc nucleus owing to the *trans* influence of the oxygen ligands, as noted for $TcO_2F_4^-$. The signal assigned to the *cis*-fluorine atoms occurs at 23.9 ppm and is broadened by partly quadrupole-collapsed spin coupling to ^{99}Tc, and is analogous to what was observed for the $TcO_2F_4^-$ anion. The relative order of the chemical shifts for the two fluorine environments is opposite to that observed for $ReO_2F_3(CH_3CN)$ (triplet, -24.5 ppm and doublet, -31.3 ppm, see Chapter 4). At higher temperatures, the *trans*-fluorine resonance of $TcO_2F_3(CH_3CN)$ is shifted to higher frequency (37.3 ppm at 30 °C; 39.2 ppm at 51 °C) relative to that of the *cis*-fluorine resonance (25.3 ppm at 30 °C; 25.8 ppm at 51 °C). The larger deshielding of the *trans*-fluorine resonance could result from an exchange process between the CH_3CN ligand and the solvent by means of a trigonal bipyramidal TcO_2F_3 intermediate (Scheme I). Under

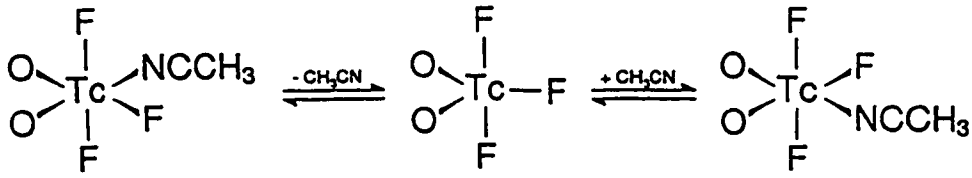

Scheme I

these conditions, intramolecular exchange of the two fluorine environments would be restricted because of the large energy barrier associated with having the oxo ligands of the TcO_2F_3 intermediate in axial positions (see **Computational Results**). The increased linewidths of the *cis*- and *trans*-fluorine resonances with increasing temperature result from decreases in the relaxation rate of ^{99}Tc as the molecular correlation time decreases

at higher temperature. At -40 °C, $^{1}J(^{19}F_{t}\text{-}^{99}Tc)$ spin-coupling is not observed because of the fast relaxation rate of the ^{99}Tc nucleus relative to the $^{1}J(^{19}F_{t}\text{-}^{99}Tc)$ coupling constant, i.e., $1/T_{1}(^{99}Tc) >> 2\pi^{1}J(^{99}Tc\text{-}^{19}F_{t})$.[57] At 30 and 51 °C, the rate of quadrupole relaxation is slower and results in significant broadening of the triplet. A similar effect is observed for the *cis*-fluorine resonance which is a broad singlet at -40 °C that evolves into a "flat-topped" unresolved multiplet (an unresolved doublet of equi-intensity decets) at 51 °C.

Ligand exchange between TcO_2F_3 and CH_3CN solvent was investigated by variable temperature ^{1}H, ^{13}C and ^{19}F NMR spectroscopy for a 1:6 molar mixture of TcO_2F_3 and CH_3CN in SO_2ClF. The ^{19}F NMR spectrum recorded at -75 °C (Figure 3.4) shows a sharp triplet at 32.2 ppm and a broad doublet at 25.9 ppm with a coupling constant $^{2}J(^{19}F_{c}\text{-}^{19}F_{t})$ = 148 Hz. In the ^{1}H NMR spectrum, the resonance attributed to complexed CH_3CN (2.16 ppm) was observed as a shoulder on the free CH_3CN resonance (1.79 ppm). Exchange with free CH_3CN occurs at higher temperatures, leading to the collapse of the ^{1}H resonances of complexed and free CH_3CN at -20 °C and slow decomposition of the sample above 0 °C. Complexation shifts in the ^{13}C NMR spectrum at -75 °C could not be resolved from the free CH_3CN resonances at 1.1 and 117.8 ppm because of line broadening arising from residual spin-spin coupling to the ^{99}Tc nucleus. Furthermore, the CH_3CN complexation shifts are expected to be smaller for the $TcO_2F_3(CH_3CN)$ adduct than for the $ReO_2F_3(CH_3CN)$ adduct because ReO_2F_3 is a stronger Lewis acid than TcO_2F_3 (complexation shifts observed for $ReO_2F_3(CH_3CN)$: ^{1}H, 0.46 ppm; ^{13}CN, 1.54 ppm and $^{13}CH_3$, 1.08 ppm; see Chapter 4).

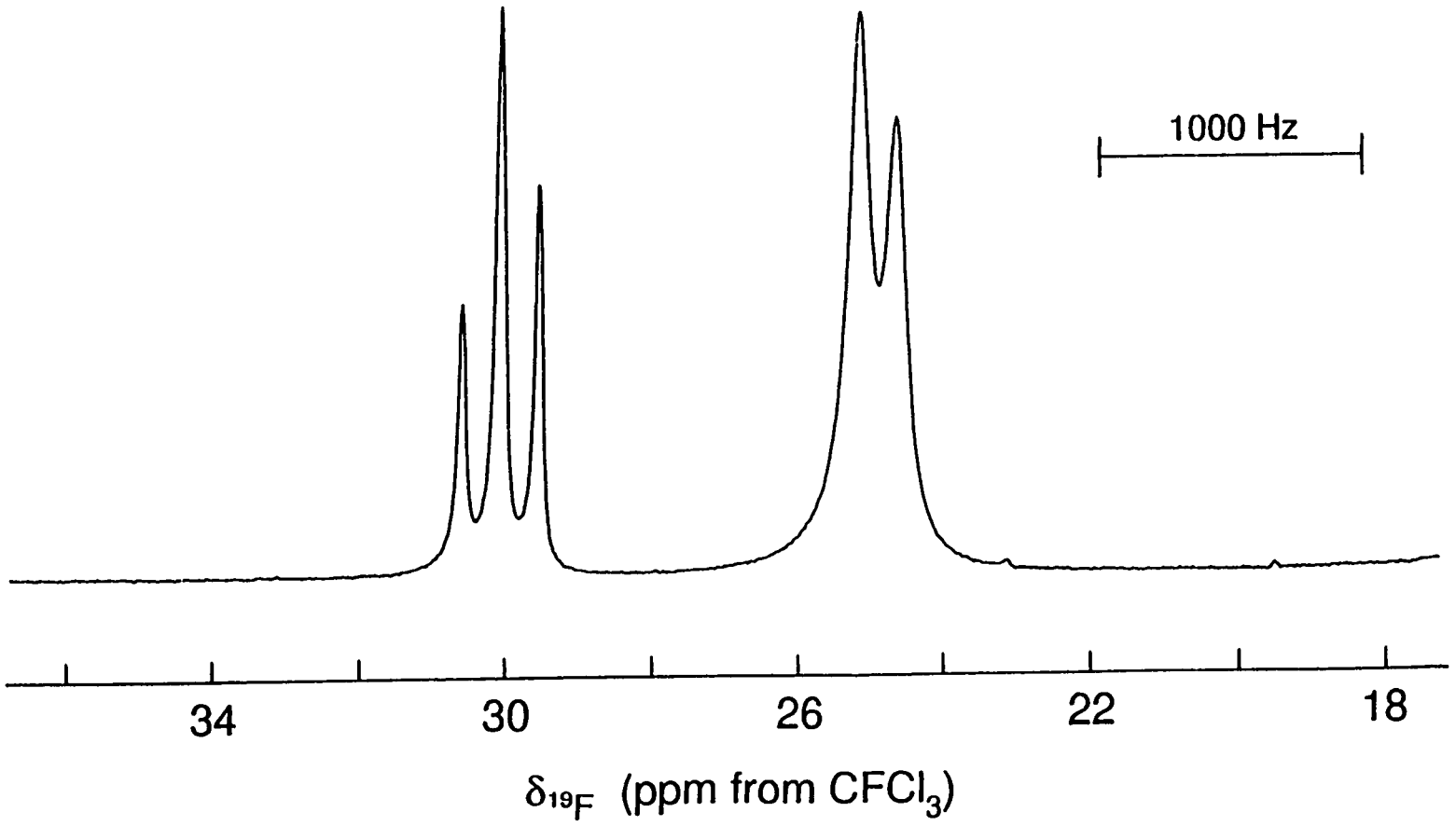

Figure 3.4. ^{19}F NMR spectrum (282.409 MHz) of TcO_2F_3 and CH_3CN (1 : 6 molar ratio) dissolved in SO_2ClF solvent recorded at -78 °C.

The ^{99}Tc NMR resonances of TcO_2F_3 recorded in CH_3CN at -41 and 30 °C are broad (265.3 ppm, $\Delta\nu_{1/2}$ = 4200 Hz at -41 °C; 267.4 ppm, $\Delta\nu_{1/2}$ = 1650 Hz at 30 °C), precluding observation of either $^1J(^{99}Tc\text{-}^{19}F_t)$ or $^1J(^{99}Tc\text{-}^{19}F_c)$ and indicate that the electric field gradient at the technetium nucleus in $TcO_2F_3(CH_3CN)$ is significantly greater than in $TcO_2F_4^-$. This faster quadrupolar relaxation in $TcO_2F_3(CH_3CN)$ was confirmed by an inversion-recovery experiment that yielded a ^{99}Tc relaxation time of 0.258 ms, which is approximately four times faster than in $TcO_2F_4^-$.

The ^{17}O NMR spectra of TcO_2F_3 in CH_3CN recorded at -41 and 30 °C consist of a broad singlet (1205 ppm, $\Delta\nu_{1/2}$ = 264 Hz at -41 °C; 1203 ppm, $\Delta\nu_{1/2}$ = 266 Hz at 30 °C) which is significantly narrower than that of $TcO_2F_4^-$ because of the faster relaxation rate of the ^{99}Tc nucleus in the less symmetric ^{99}Tc environment of $TcO_2F_3(CH_3CN)$. Although theory predicts that the adduct has a *cis*-dioxo arrangement resulting in two ^{17}O environments (O *trans* to F and O *trans* to CH_3CN), only one resonance was detected in the ^{17}O NMR spectra. The observation of a single resonance is consistent with ligand exchange behavior observed in the ^{1}H NMR spectrum. Moreover, the nearly identical ^{17}O chemical shifts in $TcO_2F_4^-$ and in $TcO_2F_3(CH_3CN)$ further support the assumption that the oxygen ligands retain their *cis* arrangement in the adduct.

X-ray Crystal Structure of $Li^+TcO_2F_4^-$

Details of the data collection parameters and other crystallographic information are given in Table 3.1. The final atomic coordinates and the equivalent thermal parameters

Table 3.1. Summary of Crystal Data and Refinement Results for $Li^{+}TcO_2F_4^{-}$

formula	F_4LiO_2Tc
space group	$P\bar{4}2_1m$ (113)
a (Å)	4.706(1)
c (Å)	8.797(2)
V (Å^3)	194.8(1)
molecules/unit cell	2
molecular wt (g mol^{-1})	212.94
calcd density (g cm^{-3})	3.63
T (°C)	22
colour	orange
μ (mm^{-1})	3.689
wavelength (Å)	0.56086
final agreement factors	R^a = 0.0339
	$R_w{}^b$ = 0.0320

[a] $R = \Sigma||F_o|-|F_c||/\Sigma|F_o|$

[b] $R_w = [\Sigma[w(|F_o|-|F_c|)^2]/\Sigma w(|F_o|)^2]^{1/2}$

are summarized in Table 3.2. Important bond lengths, angles, and significant long contacts are listed in Table 3.3.

The structure of the $TcO_2F_4^-$ anion consists of a technetium atom bonded to two oxygen atoms that are *cis* to each other and *trans* to two fluorine atoms (F_t), and two fluorine atoms that are *cis* to oxygen and *trans* to each other (F_c) (Figure 3.5a). The distorted octahedral arrangement of the anion is closely related to the TcO_2F_4-units in polymeric TcO_2F_3 in which the *cis*-oxygen atoms are *trans* to the fluorine bridges. The anion has long contacts with five neighbouring cations through both the *cis*- and the *trans*-fluorine atoms (Figure 3.5b). The extended structure of the salt (Figure 3.6) consists of an infinite layer of cations sandwiched between two infinite layers of anions with the oxygen atoms forming the exterior faces of the anion layers. The structure of $TcO_2F_4^-$ is very similar to that of valence isoelectronic $ReO_2F_4^-$ (see Chapter 4), $WO_2F_4^{2-}$ [95] and $VO_2F_4^{3-}$ [101] which also adopt the *cis*-dioxo geometry and similar extended structures.

The Tc-O distance (1.660(4) Å) is characteristic of a Tc-O double bond. It is slightly longer than the Tc-O bond length found in TcO_2F_3 (1.646(9) Å),[41] slightly shorter than the Tc-O bond lengths found in Tc_2O_7 (1.672(8) Å, terminal),[108] $N(CH_3)_4^+TcO_4^-$ (1.676(8) Å),[109] and similar to that observed in the trimer $(TcOF_4)_3$ (1.66(3) Å)[37] where technetium is in its +6 oxidation state. The Tc-F_c bond length (1.876(3) Å) is longer than the terminal Tc-F bond distances in $(TcOF_4)_3$ (1.81(3) Å) and in TcO_2F_3 (1.834(7) Å), while the Tc-F_t bond (1.986(3) Å) is much longer and can only be compared to the Tc-F bridging bonds in TcO_2F_3 (average, 2.080(5) Å), which are also *trans* to oxygen atoms. These variations in the Tc-F and Tc-O bond lengths in $TcO_2F_4^-$ relative to the model

Table 3.2. Final Atomic Coordinates (× 10^4) and Equivalent Isotropic Displacement Coefficients ($Å^2$ × 10^3) in $Li^+TcO_2F_4^-$

	x	*y*	*z*	U_{eq} [a]
Tc(1)	0	5000	2256(1)	13(1)
F(1)	2209(5)	-2791(5)	7450(5)	24(1)
F(2)	1851(4)	-3149(4)	4027(4)	20(1)
O(1)	-1945(6)	-6945(6)	1074(5)	25(1)
Li(1)	5000	0	4204(2)	25(2)

[a] Equivalent isotropic *U* defined as one third of the trace of the orthogonalized $\mathbf{U}_{ij}$ tensor.

Table 3.3. Bond Lengths, Bond Valences, Long Contacts and Bond Angles in $Li^{+}TcO_2F_4^{-}$

Bond Lengths (Å) and Corresponding Bond Valences (v.u.)[a]			
	Tc(1)-F(1)	Tc(1)-F(2)	Tc(1)-O(1)
Bond valence	0.883	0.656	1.862
Bond length	1.876(3)	1.986(3)	1.660(4)
Total bond valence:	6.80		
	Li(1)-F(1)	Li(1)-F(2)	Li(1)-F(2)'
Bond valence	0.147	0.185	0.135
Bond length	2.07(1)	1.99(1)	2.10(3)
Total bond valence:	0.93		

Bond Angles (deg)			
O(1)-Tc(1)-O(1A)	102.5(3)	F(2)-Tc(1)-O(1)	90.4(2)
O(1)-Tc(1)-F(1)	94.9(1)	F(2)-Tc(1)-F(1)	83.8(1)
F(1)-Tc(1)-F(1A)	164.2(3)	F(2)-Tc(1)-F(2A)	76.7(2)
F(2)-Tc(1)-O(1A)	167.1(2)		

[a] Bond valence units (v.u.) are defined in ref. 110. R_0 = 1.89 (Tc=O), R_0 = 1.83 (Tc-F) and B = 0.37 were used; Brown, I.D. Department of Physics, McMaster University, Hamilton, Ontario L8S 4M1, Canada, private communication.

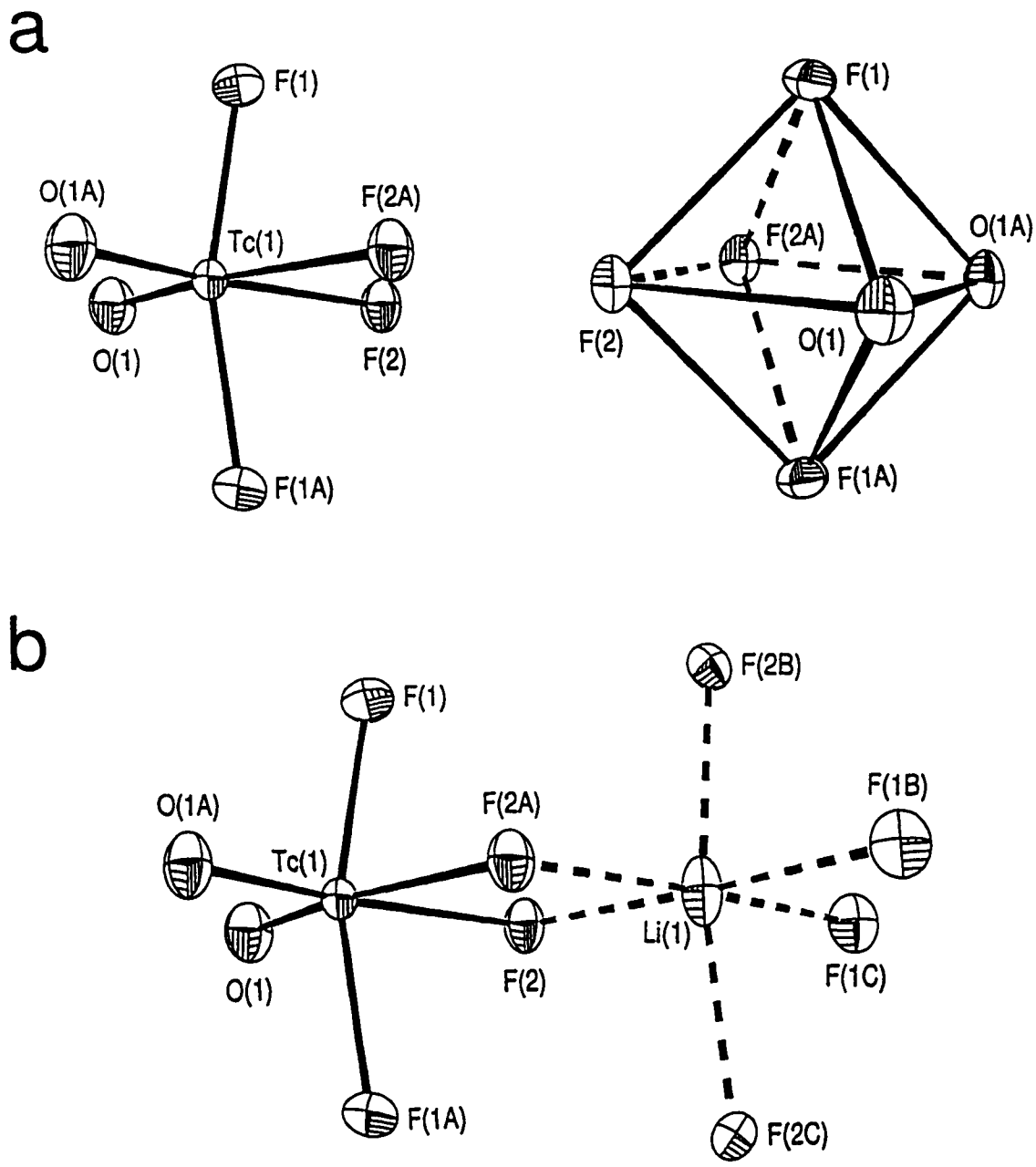

Figure 3.5. Structure of $Li^{+}TcO_2F_4^{-}$ showing thermal ellipsoids at the 50% probability level. (a) Geometry of the $TcO_2F_4^{-}$ anion and octahedron formed by the light atoms around technetium in $TcO_2F_4^{-}$, (b) arrangement of the fluorine atoms around the Li^{+} cation.

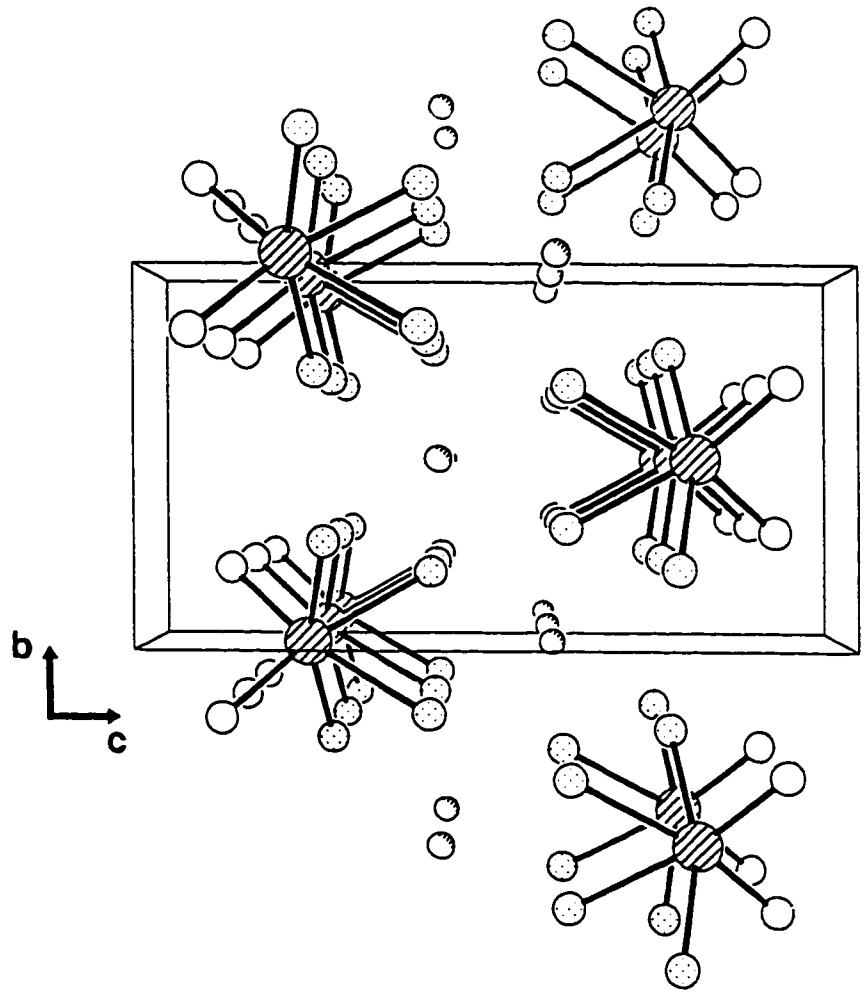

Figure 3.6. View of the $Li^{+}TcO_2F_4^{-}$ unit cell showing the packing along the *a*-axis.

compounds can be rationalized in terms of increased bond polarities anticipated because of the negative charge of the anion.

The bond valences for individual bonds, as defined by Brown,[110] are given in Table 3.3. The total bond valence for the technetium atom is 6.80 v.u. (bond valence units), with contributions of 1.86 v.u./oxygen atom, 0.88 v.u./*cis*-fluorine atom, and 0.66 v.u./*trans*-fluorine atom. The values for the Tc-O double bond and Tc-F_c bond are lower than in TcO_2F_3 (1.97 and 0.99 v.u., respectively) while the bond valence for the Tc-F_t bond is larger than for the bridging Tc-F bond in TcO_2F_3 (0.51 v.u.). Each Li^+ cation is coordinated to six fluorine atoms (Figure 3.5b), two of which are *trans*-fluorine atoms belonging to the same anion. Although the total bond valence sum for the lithium atom (0.93 v.u.) indicates it is slightly underbonded, the contributions of 0.15 v.u./*cis*-fluorine atom, 0.18 and 0.13 v.u./*trans*-fluorine atom account for the most significant contacts.

Despite considerable variations in the bond lengths and bond angles around the technetium atom in $TcO_2F_4^-$, the octahedron formed by the light atoms is relatively undistorted having $F_c\cdots F_t$, $F_t\cdots F_t$, $F_c\cdots O$, $F_t\cdots O$ and $O\cdots O$ distances of 2.580(4), 2.466(6), 2.609(5), 2.600(6) and 2.587(8) Å, respectively. The VSEPR model of molecular geometry[111] provides a satisfactory explanation for the distortion observed in the coordination sphere of the technetium atom. The greater spatial requirements of the oxygen double bond domains and their repulsive interactions with single bond pair domains at approximately right angles to them in the [O, F_c, F_c, F_t]-planes causes a bending of the F_c-Tc-F_c angle away from the oxygen atoms. This angle is 164.2(3)° in

$Li^+TcO_2F_4^-$ and represents a significantly smaller deviation from the ideal 180° angle than is found in TcO_2F_3 (154.9(3)-155.9(3)°).[41] The difference is consistent with the more polar Tc-O and Tc-F bonds of $TcO_2F_4^-$, which is reflected in their smaller bond valence values and results in weaker bond pair-bond pair repulsions in $Li^+TcO_2F_4^-$ than in TcO_2F_3. These weaker bond-pair repulsions are also reflected in the large O-Tc-O angle (102.5(3)°) and the small F_t-Tc-F_t angle (76.7(2)°), and are presumably heightened by the smaller spatial requirements of the longer Tc-F_t bond domains.

Although the VSEPR model qualitatively accounts for the irregular octahedral geometry around the technetium, it does not account for the greater stability of the *cis* arrangement of the oxygen atoms in its traditional form. The preference for the *cis*-dioxo structure can be understood in terms of the spatial relationship of the strong π-donor oxygen atoms to the approximately $d_{t_{2g}}$ orbitals of technetium required for p_π-d_π bonding. In the *trans* arrangement, the two donor p orbitals on each oxygen ligand compete for the same two $d_{t_{2g}}$ orbitals on the metal, whereas in the *cis* geometry there is less competition for bonding orbitals since all three $d_{t_{2g}}$ orbitals on the metal are available for overlap (Figure 3.7). Therefore, the bonding molecular orbitals in the *cis*-isomer have lower energies than the corresponding molecular orbitals in the *trans*-isomer, making the *cis*-isomer more stable. This *cis*-dioxo arrangement has been observed for other transition metal oxofluorides such as OsO_2F_4,[93] $ReO_2F_4^-$,[48,52] TcO_2F_3[41] and $MoO_2F_2 \cdot 2THF$.[112] This p_π-d_π bonding effect is not observed for the $IO_2F_4^-$ anion, which occurs as a kinetically determined mixture of *cis*- and *trans*-isomers.[113] Recently, the geometries of non-VSEPR molecules have been explained in terms of core electron distortions.[114] In this model, the

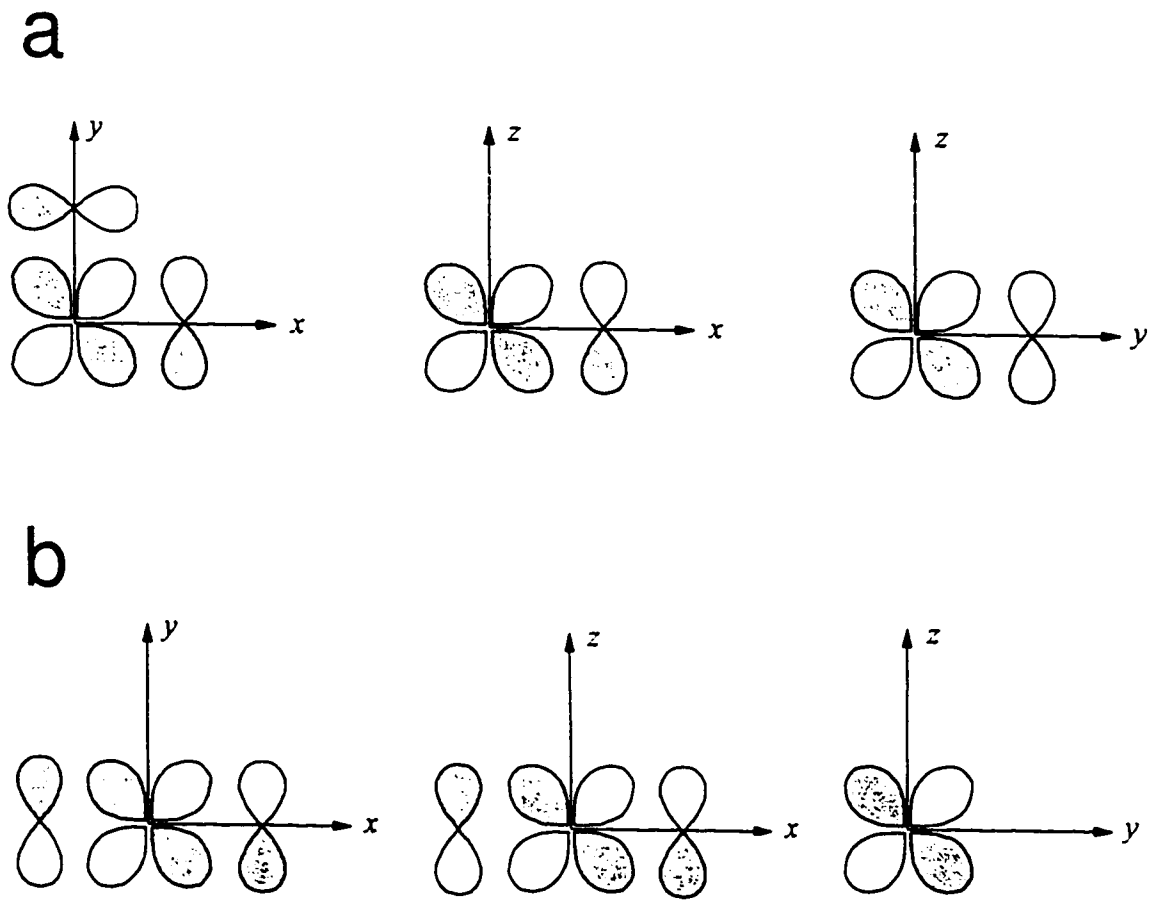

Figure 3.7. Diagram showing the overlap of the filled p orbitals of the oxygen ligands and the empty $d_{t_{2g}}$ orbitals of a transition metal in octahedral (a) *cis*-dioxo complexes and (b) *trans*-dioxo complexes.

preference for the *cis*-dioxo arrangement in d^0 transition metal complexes is attributed to nonspherical metal atom cores resulting from the distortion produced by the ligands. Calculation of the Laplacian of the electron density in these molecules reveals the formation of local concentrations of electron density in the outer shell of the core so that the geometry of a molecule is determined by the tendency of the more covalently bonded ligands to occupy sites facing regions of local charge depletion. For the dioxo d^0 transition metal complexes it was determined that the oxygen ligands face larger depletions of charge in the *cis* isomer than in the *trans* isomer, rendering the *cis*-isomer more stable.

Raman Spectroscopy and Vibrational Assignments for $M^+TcO_2F_4^-$ [M = Li, Cs, $N(CH_3)_4$]

The Raman spectra of the Li^+, Cs^+ and $N(CH_3)_4^+$ salts of $TcO_2F_4^-$ are shown in Figures 3.8, 3.9 and 3.10, respectively. The observed frequencies and their assignments for the *cis*-dioxo geometry of the $TcO_2F_4^-$ anion under C_{2v} point symmetry are listed in Table 3.4 (see **X-ray Crystal Structure of $Li^+TcO_2F_4^-$**).

The 15 vibrational modes of the $TcO_2F_4^-$ anion belong to the irreducible representations $6A_1 + 2A_2 + 4B_1 + 3B_2$ (the [O, O, Tc, F_t, F_t]-plane is taken as the $\sigma_v(xz)$-plane with *z* as the principal axis) and are all Raman active, whereas the A_1, B_1 and B_2 modes are infrared-active. The vibrational assignments were made by comparison with the calculated frequencies (see Table 3.4 and **Computational Results**) and assignments

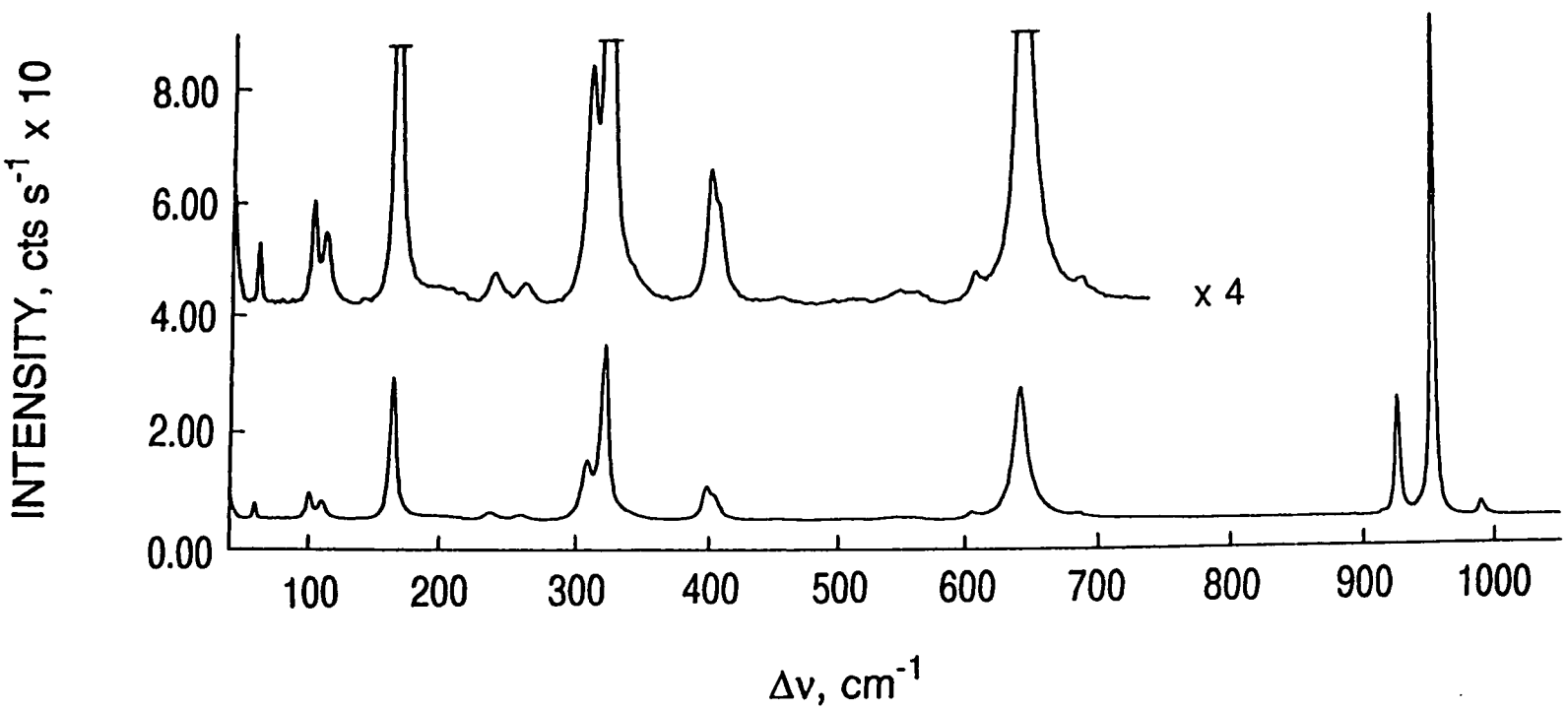

Figure 3.8. Raman spectrum of microcrystalline $Li^{+}TcO_2F_4^{-}$ recorded in a Pyrex capillary at 20 °C using 647.1-nm excitation.

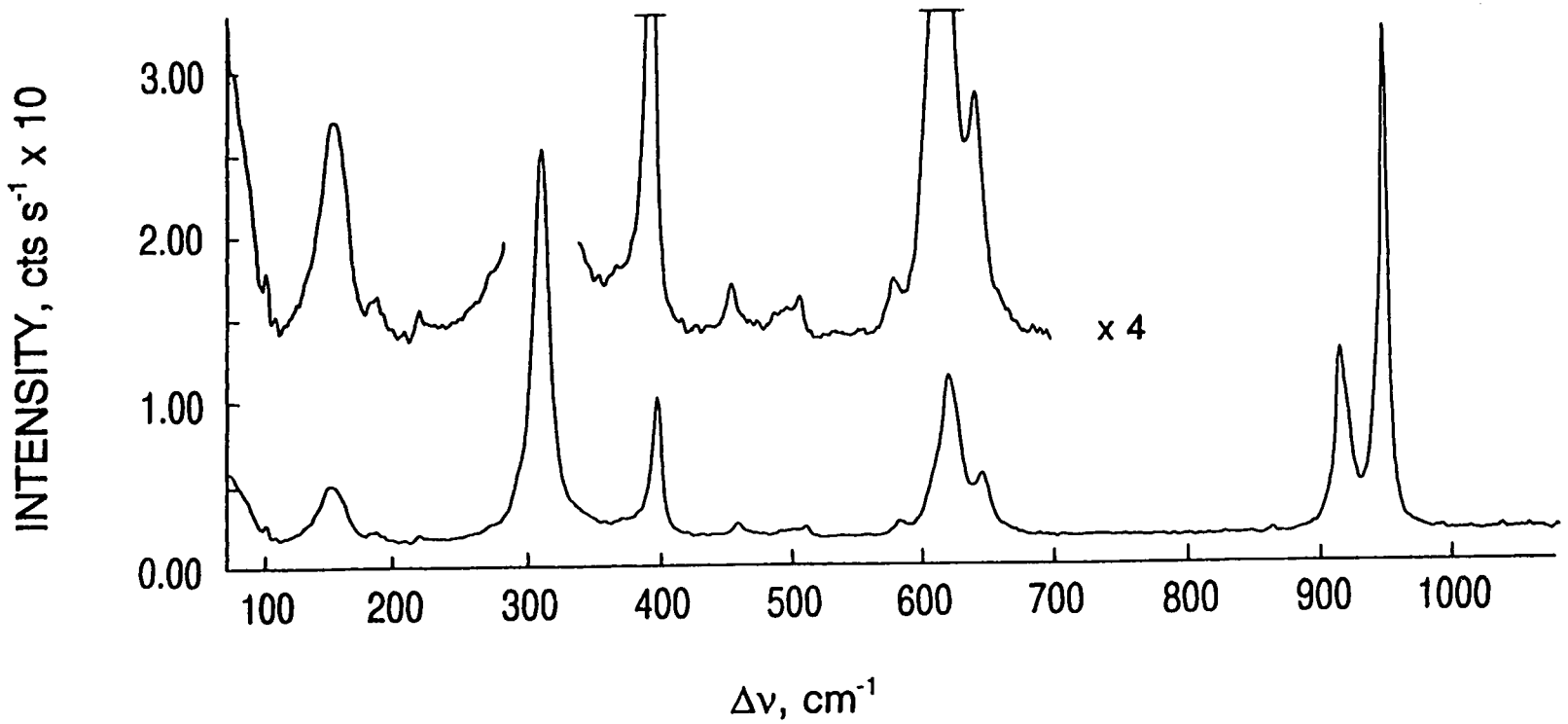

Figure 3.9. Raman spectrum of microcrystalline $Cs^{+}TcO_2F_4^{-}$ recorded in a Pyrex capillary at 20 °C using 647-1-nm excitation.

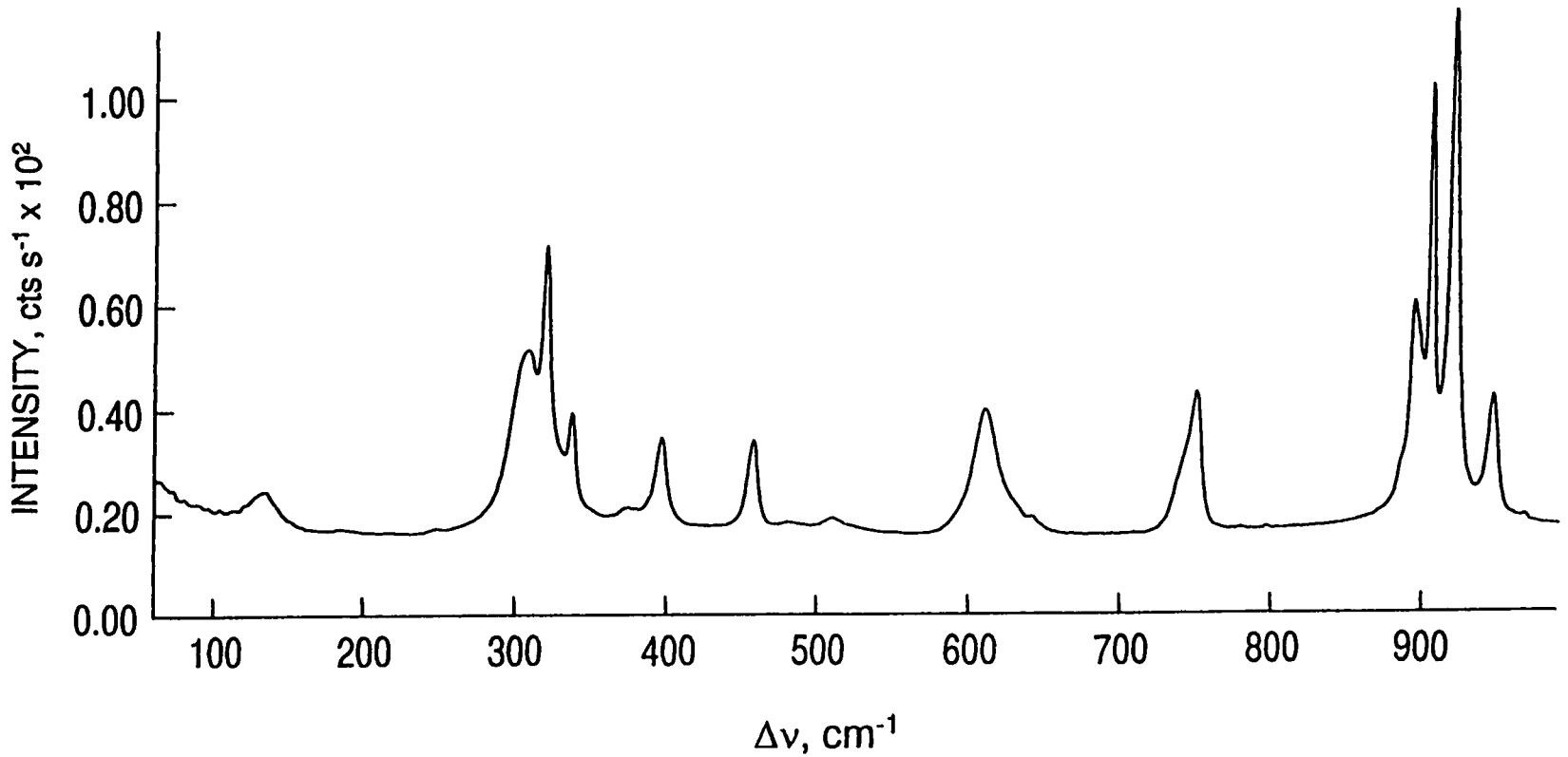

Figure 3.10. Raman spectrum of microcrystalline $N(CH_3)_4^+TcO_2F_4^-$ recorded in a Pyrex capillary at 20 °C using 647.1-nm excitation. The high frequency bands of the $N(CH_3)_4^+$ cation are not shown but are listed in Table 3.4, footnote d.

Table 3.4. Experimental Raman and Calculated Vibrational Frequencies, Assignments and Mode Descriptions for $M^+TcO_2F_4^-$ [M = Li, Cs, $N(CH_3)_4$]

Frequencies (cm^{-1})							Assignments for $TcO_2F_4^-$ C_{2v} point symmetry[c]
exp[a]			LDFT[b]		NLDFT[b]		
$LiTcO_2F_4$[d]	$CsTcO_2F_4$	$N(CH_3)_4TcO_2F_4$[e]	TZVP	DZVP	TZVP	DZVP	
954(100)	950(100)	922(100) 907(87)	935(126)	921(138)	893(120)	881(204)	$\nu_1(A_1)$, $\nu_s(TcO_2)$
927(23)	916(32)	896(44,sh)	935(201)	983(118)	890(190)	883(130)	$\nu_9(B_1)$, $\nu_{as}(TcO_2)$
641(27)	649(11)	643(3)	638(256)	645(262)	590(246)	598(248)	$\nu_{13}(B_2)$, $\nu_{as}(TcF_{2c})$
605(2)	623(30)	612(24)	628(97)	630(90)	582(92)	582(81)	$\nu_2(A_1)$, $\nu_s(TcF_{2c} + TcF_{2t})$
553(1), br	587(3)	555(4)	547(31)	551(27)	504(30)	509(29)	$\nu_3(A_1)$, $\nu_s(TcF_{2c} - TcF_{2t})$
517(<1)	515(2)	512(4)	527(70)	532(64)	486(66)	489(60)	$\nu_{10}(B_1)$, $\nu_{as}(TcF_{2t})$
453(<1)	464(2)	483(2)					f
404(5,sh) 399(7)	402(25)	398(19)	372(3)	369(2)	370(3)	363(2)	$\nu_4(A_1)$, $\delta(TcO_2)$
320(35)	315(70)	338(24) 320(56)	317(6)	307(6)	303(5)	293(5)	$\nu_5(A_1)$, $\delta(TcF_{2c} + TcF_{2t})$
			306(14)	302(16)	302(16)	297(168)	$\nu_{14}(B_2)$, $\rho_r(TcF_{2c})$

Table 3.4. continued

307(12)	298(12,sh)	309(35,sh)	293(21)	293(20)	287(22)	289(19)	$\nu_{11}(B_1)$, $\delta(OTcF_t + TcF_{2c})$
			295(0)	298(0)	290(0)	288(0)	$\nu_7(A_2)$, $\rho_t(TcO_2)$
259(1)		249(<1)					f
236(2)	227(2)	218(<1)	236(36)	235(35)	234(34)	233(31)	$\nu_{15}(B_2)$, $\rho_t(TcF_{2t})$
	194(2)	184(<1)	209(1)	203(1)	202(1)	195(1)	$\nu_6(A_1)$, $\delta(TcF_{2c} - TcF_{2t})$
162(29)	162(10,br)	135(7)	161(0)	162(0)	157(0)	162(0)	$\nu_{12}(B_1)$, $\delta(OTcF_t - TcF_{2c})$
107(3)	118(1)						lattice modes
98(5)	110(1)						
56(3)			43(0)	58(0)	53(0)	64(0)	$\nu_8(A_2)$, $\rho_t(TcF_{2t})$

[a] Spectra recorded on microcrystalline solids in Pyrex glass melting point capillaries at 20 °C using 647.1-nm excitation. Values in parentheses denote relative Raman intensities, sh a shoulder and br a broad band.

[b] Infrared intensities, in km mol^{-1}, are given in parentheses.

[c] The fluorine atom labelling scheme is given by Structure I. ν: stretching; δ: in-plane bending; ρ_r: rocking; ρ_t: twisting.

[d] Additional weak bands were observed for $Li^+TcO_2F_4^-$ at 991(2) and 685(2) cm^{-1}.

[e] Frequencies observed for $N(CH_3)_4^+$: 364(3) and 373(5), $\nu_8(E)$; 457(18), $\nu_{19}(T_2)$; 741(12,sh), 752(27), $\nu_3(A_1)$; 948(26), $\nu_{18}(T_2)$; 1178(3), $\nu_7(E)$; 1287(2), $\nu_{17}(T_2)$; 1410(2), 1418(2), $\nu_{16}(T_2)$; 1462(11), 1470(10), $\nu_2(A_1)$; 2824(3), 2879(2), 2930(4), 2964(4), 2987(4), 3032(7), $\nu_5(E)$.

[f] Unassigned bands.

for $ReO_2F_4^-$ (see Chapter 4), OsO_2F_4,[93] the TcO_2F_4-units of TcO_2F_3[41] and the *cis*-isomer of $IO_2F_4^-$.[113]

In order to evaluate the degree of vibrational coupling within the unit cell of $Li^+TcO_2F_4^-$, a factor-group analysis of the vibrational modes of the $Li^+TcO_2F_4^-$ unit cell was carried out using the correlation method[115] (Table 3.5). The symmetry of the free $TcO_2F_4^-$ anion (C_{2v}), which happens to be identical to the site symmetry, was correlated to the crystal symmetry (D_{2d}), space group $P\bar{4}2_1m$. Only the A_1 bands (ν_1-ν_6) are expected to be factor-group split in the Raman spectrum whereas no bands are predicted to be split in the infrared spectrum. In fact, no factor-group splitting could be resolved on ν_1-ν_6 in the Raman spectrum of $Li^+TcO_2F_4^-$.

The symmetric and antisymmetric TcO_2 stretching modes [Li^+: 954 and 927 cm^{-1}; Cs^+: 950 and 916 cm^{-1}; $N(CH_3)_4^+$: 922, 907 and 896 cm^{-1}] appear at lower frequencies than the TcO_2F_4-unit in the fluorine-bridged TcO_2F_3 structure (974 and 963, 958 cm^{-1}), which is expected for the more polar Tc-O bonds of the anion. The significant low frequency shift in going from the Li^+ salt to the Cs^+ salt to the $N(CH_3)_4^+$ salt is attributed to progressive lowering of the Lewis acidity over the cation series, resulting in increasing negative charge on the $TcO_2F_4^-$ anion and increasing polarization of the Tc-O bonds. The bands at 641 (Li^+), 649 (Cs^+) and 643 cm^{-1} ($N(CH_3)_4^+$) are assigned to the antisymmetric Tc-F_c stretching mode and are slightly lower than in TcO_2F_3 (632, 650 cm^{-1}) which is consistent with the trend in bond valencies that these bonds exhibit in their respective crystal structures (0.88 v.u. in $Li^+TcO_2F_4^-$ and 0.95 to 1.05 v.u. in TcO_2F_3[41]). The Tc-F_t bond valence (0.66 v.u.) is significantly lower than that of Tc-F_c (1.04 v.u.) because of

Table 3.5. Correlation Diagram[a] for the Vibrational Modes of $Li^{+}TcO_2F_4^{-}$

		free ion symmetry	site symmetry	crystal symmetry[b]		
		C_{2v}	C_{2v}	D_{2d}		
4T	$2(\nu_1 - \nu_6)$	A_1	A_1	A_1 (R)	$\nu_1 - \nu_6$	2T
2R	$2(\nu_7 - \nu_8)$	A_2	A_2	A_2 (i.a.)	ν_7, ν_8	R
				B_1 (R)	ν_7, ν_8	R
4T,2R	$2(\nu_9 - \nu_{11})$	B_1	B_1			
				B_2 (R,IR)	$\nu_1 - \nu_6$	T(-T)
4T,2R	$2(\nu_{12} - \nu_{15})$	B_2	B_2			
				E (R,IR)	$\nu_9 - \nu_{15}$	2R,3T(-T)

[a] The symbols T and R denote translatory and rotatory (external) modes, respectively, and R, IR and i.a. in parentheses denote Raman and infrared activity and inactivity, respectively.

[b] Space group $P\bar{4}2_1m$, Z = 2.

the *trans* influence of the oxo ligand, so that the antisymmetric Tc-F_t stretching mode occurs at lower frequency than the antisymmetric Tc-F_c mode. The symmetric counterparts of these modes are strongly coupled and occur at intermediate frequencies and are assigned to the bands at 553 (Li^+), 587 (Cs^+) and 555 cm^{-1} ($N(CH_3)_4^+$) (symmetric stretch) and at 517 (Li^+), 515 (Cs^+) and 512 cm^{-1} ($N(CH_3)_4^+$) (antisymmetric stretch). The TcO_2 bending mode is assigned to the band at 399, 404 (Li^+), 402 (Cs^+) and 398 cm^{-1} ($N(CH_3)_4^+$) by analogy with the Raman spectra of $N(CH_3)_4^+ReO_2F_4^-$ and TcO_2F_3, in which it occurs at 402 and 411 cm^{-1}, respectively.

The assignments of the low-frequency bands are anchored by assigning the scissoring modes $\nu_5(A_1)$, $\nu_{11}(B_1)$ and $\nu_{12}(B_1)$ to the most intense of the remaining bands. These assignments were made by comparison with those of OsO_2F_4[93] and $ReO_2F_4^-$ [48] and are supported by the theoretical values. Assignments for the remaining modes $\nu_{14}(B_2)$, $\nu_7(A_2)$, $\nu_{15}(B_2)$, $\nu_6(A_1)$ and $\nu_8(A_2)$ are more tentative and are based on the frequencies derived from the LDFT calculations.

The assignments for the $N(CH_3)_4^+$ cation of $N(CH_3)_4^+TcO_2F_4^-$ are based on those for the free cation, which belongs to the point group T_d and has 19 fundamental vibrational bands, $3A_1 + A_2 + 4E + 4T_1 + 7T_2$. Of these, the T_2 modes are infrared-active and the A_1, E and T_2 modes are Raman active. The assignments for the $N(CH_3)_4^+$ cation generally follow those previously given for other $N(CH_3)_4^+$ salts[73,116-121] and require no further comment. It can be concluded that in $N(CH_3)_4^+TcO_2F_4^-$ the distortion of the $N(CH_3)_4^+$ cation from tetrahedral symmetry is minimal.[120]

Raman Spectroscopy and Vibrational Assignments for $TcO_2F_3(CH_3CN)$

The Raman spectrum of the $TcO_2F_3(CH_3CN)$ adduct was recorded in CH_3CN solution at -44 °C. The spectrum is shown in Figure 3.11 and the frequencies and their assignments are listed in Table 3.6. Attempts to record the Raman spectrum of solid $TcO_2F_3(CH_3CN)$ at -150 °C resulted in rapid decomposition of the sample to an unidentified dark blue product. The assignments were made by comparison with calculated frequencies (see Table 3.6 and **Computational Results**) and the Raman spectra of CH_3CN,[122] TcO_2F_3,[41] $TcO_2F_4^-$ and the $ReO_2F_3(CH_3CN)$ adduct in the solid state and in CH_3CN solution (see Chapter 4). The adduct is expected to have a geometry in which CH_3CN is coordinated to the Tc atom of TcO_2F_3 in a position *trans* to one of the oxygen ligands (see **Characterization of $TcO_2F_3(CH_3CN)$ by ^{19}F, ^{99}Tc and ^{17}O NMR Spectroscopy**). Based on this assumption, the adduct would possess C_s point symmetry for which 30 Raman and infrared-active vibrational modes are predicted, belonging to the irreducible representations 19 A' + 11 A".

The Raman spectrum of $TcO_2F_3(CH_3CN)$ in CH_3CN shows three strongly polarized bands in the 900-1000 cm^{-1} region which can readily be assigned to the C-C stretch, $\nu_4(A_1)$, of free CH_3CN (920 cm^{-1}), the TcO_2 antisymmetric stretch (940 cm^{-1}) and the TcO_2 symmetric stretch (963 cm^{-1}). The band corresponding to ν(CC) of complexed CH_3CN is presumably coincident with the TcO_2 stretch at 940 cm^{-1}, and is consistent with what is observed for $ReO_2F_3(CH_3CN)$ (943 cm^{-1}). The TcO_2 stretching frequencies of $TcO_2F_3(CH_3CN)$ are intermediate between those observed for the TcO_2F_4-unit of TcO_2F_3 and the $TcO_2F_4^-$ anion, and are consistent with the formation of a Lewis acid-base adduct.

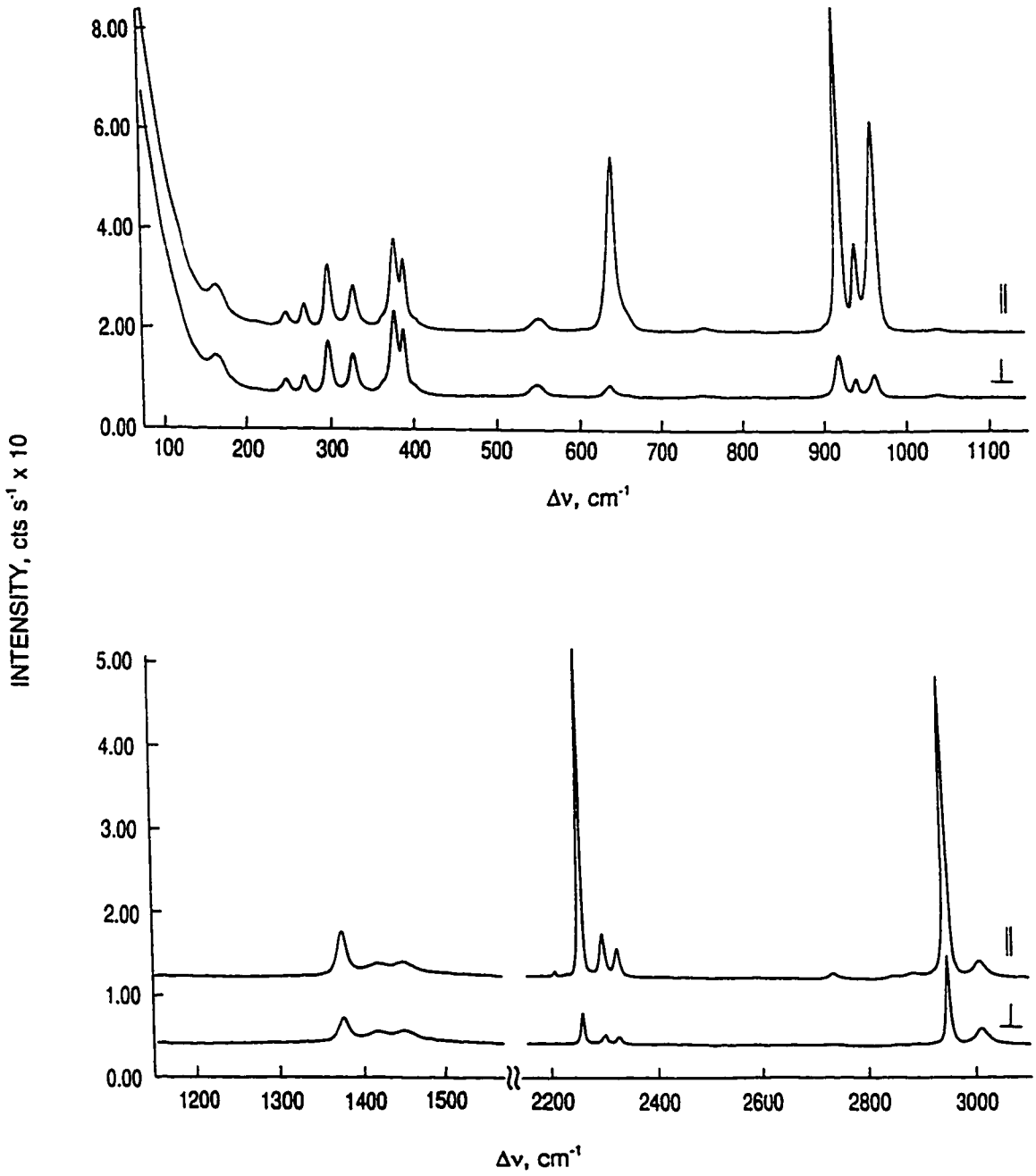

Figure 3.11. Raman spectrum of a solution of TcO_2F_3 in CH_3CN recorded in a Pyrex tube at -44 °C using 647.1-nm excitation. Upper trace and lower trace are with the analyser parallel and perpendicular to the polarization of the incident beam, respectively.

Table 3.6. Experimental Raman and Calculated Vibrational Frequencies, Assignments and Mode Descriptions for $TcO_2F_3(CH_3CN)$

Frequencies (cm^{-1})		Assignments
exp[a]	LDFT/DZVP[b]	C_s point symmetry[c]
3010(5), dp[d,e]	3092(3)	ν_{20}(A"), $\nu_{as}(CH_3)$
3010(5), dp[d,e]	3087(3)	ν_{21}(A"), $\nu_{as}(CH_3)$
2950(75), p[d]	2990(2)	ν_1(A'), $\nu_s(CH_3)$
2325(8), p		$\nu_3 + \nu_7$ (A')
2297(11), p[d]	2373(92)	ν_2(A'), ν(CN)
1416(5), dp[e]	1404(18)	ν_{22}(A"), $\delta_{as}(CH_3)$
1416(5), dp[e]	1396(17)	ν_{23}(A"), $\delta_{as}(CH_3)$
1375(15), p[d]	1347(11)	ν_3(A'), $\delta_s(CH_3)$
1039(1), dp	990(8)	ν_4(A'), $\rho_r(CH_3)$ + δ(NCC)
1020(1), dp	985(19)	ν_5(A'), $\rho_r(CH_3)$ + $\nu(TcO_t)$ + δ(NCC)
963(65), p	984(127)	ν_6(A'), $\nu(TcO_t)$ + $\rho_r(CH_3)$ + δ(NCC)
940(28), p[e]	982(41)	ν_7(A'), ν(TcN) - ν(CC)
940(28), p[e]	943(123)	ν_8(A'), $\nu(TcO_c)$
807(1), dp		$2\nu_{11}$ (A')
659(6), sh, p	658(57)	ν_9(A'), $\nu_s(TcF_{2c})$ + $\nu(TcF_t)$
637(53), p	584(27)	ν_{10}(A'), $\nu_s(TcF_{2c})$ - $\nu(TcF_t)$
549(6), dp	685(198)	ν_{24}(A"), $\nu_{as}(TcF_{2c})$
413(3), sh		
403(6), sh	405(0.5)	ν_{11}(A'), δ(TcNC) + δ(NCC)
389(35), dp	366(6)	ν_{12}(A'), $\delta(TcO_2)$
363(7), sh, dp	376(0.6)	ν_{13}(A'), δ(TcNC) + δ(NCC)
328(20), dp	325(1)	ν_{25}(A"), $\delta(O_tTcF_c)$ + $\delta(F_cTcF_t)$
	291(22)	ν_{14}(A'), $\delta(O_tTcF_t)$ - $\delta(O_cTcF_t)$ + $\delta(F_cTcF_c)$
298(28), dp	288(16)	ν_{26}(A"), oop $\delta(O_cTcF_t)$ - $\delta(O_cTcF_t)$ + $\delta(O_tTcF_t)$
270(10), p	260(12)	ν_{15}(A'), $\delta(F_tTcN)$ + $\delta(F_cTcF_c)$ - δ(NCC)
248(6), dp	228(12)	ν_{27}(A"), oop $\delta(NTcF_c)$ - $\delta(NTcF_c)$ + $\rho_w(O_tTcF_t)$
217(2), dp	208(10)	ν_{16}(A'), ν(TcN)

Table 3.6. continued

	203(2)	ν_{17}(A'), $\delta(F_cTcF_c)$ - $\delta(NTcO_c)$
165(20), dp	160(0.3)	ν_{18}(A'), $\delta(F_cTcF_c)$ - $\delta(O_tTcF_t)$
	146(1)	ν_{29}(A"), oop $\delta(O_cTcN)$ - $\rho_w(O_tTcF_t)$
	65(4)	ν_{19}(A'), ip δ(CNTc)
	44(4)	ν_{29}(A"), oop δ(CNTc)
	64i[f]	ν_{30}(A'), $\rho_w(CH_3)$

[a] Solution spectrum recorded in a Pyrex glass tube at -44 °C using 647.1-nm excitation. Values in parentheses denote relative Raman intensities, sh a shoulder, p a polarized band and dp a depolarized band. Frequencies observed for free CH_3CN (C_{3v} point symmetry): ν_5(E), 3010(5), $\nu_1(A_1)$, 2950(75), $2\nu_6$, 2886(2), $2\nu_7 + 2\nu_8$, 2848(1), $2\nu_3$, 2738(2), $\nu_3 + \nu_4(A_1)$, 2297(11), $\nu_2(A_1)$, 2257(78), $2\nu_4 + \nu_8$, 2208(1), ν_6(E), 1448(6), $\nu_3(A_1)$, 1375(15), ν_7(E), 1039(1), $\nu_4(A_1)$ 920(100), $2\nu_8$, 807(1), ν_8(E), 379(5).

[b] Infrared intensities, in km mol^{-1}, are given in parentheses.

[c] The atom labelling scheme is given by Structure II; oop and ip denote out-of-plane and in-plane, respectively; ν:stretching; δ:in-plane bending; ρr: rocking; ρw: wagging; ρt: twisting.

[d] Coincident with a mode of free CH_3CN.

[e] Coincident modes.

[f] A number of different rotomers involving the CH_3 were investigated. All gave a low imaginary frequency for the torsion. This is typical of DFT grid-based calculations.

Three bands appear in the Tc-F stretching region including a depolarized band at 549 cm^{-1}, which can only be assigned to the antisymmetric TcF_{2c} stretching mode, while the two polarized modes at 637 and 659 cm^{-1} are assigned to the symmetric TcF_{2c} stretch and the TcF_t stretch, respectively. LDFT calculations show that the symmetric TcF_{2c} stretch is strongly coupled with the TcF_t stretch. The TcO_2 scissor bend is assigned to the strong band at 389 cm^{-1} and is confirmed by the theoretical value calculated at the LDFT level. The remaining low-frequency bands are assigned to strongly coupled bending modes with the aid of frequencies calculated at the LDFT level.

The frequency shifts observed for complexed acetonitrile are comparable to those observed for the $Co(CH_3CN)_6^{2+}$ cation.[123] The ν_8 (378 cm^{-1}), ν_4 (920 cm^{-1}), ν_6 (1448 cm^{-1}), ν_2 (2257 cm^{-1}) and $\nu_3 + \nu_4$ (2297 cm^{-1}) bands of free acetonitrile are shifted to 403, 940, 1416, 2297 and 2325 cm^{-1}, respectively, in $TcO_2F_3(CH_3CN)$.

Calculated Molecular Geometries

Density functional theory has been shown to be a good method for predicting the geometries and vibrational spectra for transition metal compounds.[124] In previous studies on osmium oxofluorides,[93] it was found that the local level yielded better structural and vibrational predictions than did calculations with gradient (nonlocal) corrections.

The molecular geometries were initially optimized at the local density functional theory (LDFT) level with a polarized double zeta basis set (DZVP). The structure of monomeric TcO_2F_3 is predicted to have C_{2v} point symmetry (Table 3.7) with the oxygen atoms and a fluorine atom in the trigonal plane and is in agreement with previous

Table 3.7. Geometric Parameters for Monomeric TcO_2F_3 and $TcO_2F_3(CH_3CN)$

	TcO_2F_3 [a]					$TcO_2F_3(CH_3CN)$ [b]
	LDFT		NLDFT			LDFT
Bond Length / Angle	TZVP	DZVP	TZVP	DZVP	exp[c]	DZVP
Tc-O (Å)	1.686	1.691	1.704	1.709	1.646(9)	1.711 [1.692]
Tc-F_t (Å)	1.866	1.872	1.895	1.902		1.910
Tc-F_c (Å)	1.862	1.872	1.893	1.900	1.834(7)	1.879, 1.881
O-Tc-O (deg)	109.0	108.5	109.1	108.7		103.9
F_t-Tc-O (deg)	125.5	125.7	125.5	125.7		157.3 [98.8]
F_c-Tc-F_c (deg)	162.0	161.8	162.0	162.1		158.0
F_c-Tc-F_t (deg)	81.0	80.9	81.0	81.1		83.0, 83.0
O-Tc-F_c (deg)	95.2	95.3	95.2	95.2		93.2, 93.2 [99.5, 99.3]

[a]For simplicity, the F_{eq} and F_{ax} of the trigonal bipyramidal TcO_2F_3 monomer is also described as F_t and F_c, respectively.

[b]Values involving Tc-O *trans* to F_t are reported without brackets and values involving Tc-O *trans* to the N are reported in between brackets; other calculated values for the CH_3CN group: Tc-N, 2.308 Å; C-N, 1.162 Å; C-C, 1.439 Å; C-H, 1.104 Å; O-Tc-N, 81.6 [174.4]°; F_c-Tc-N, 80.7,79.5°; F_t-Tc-N, 75.7°; Tc-N-C, 175.8°; N-C-C, 178.9°; C-C-H, 110.1°.

[c]Experimental values are taken from polymeric TcO_2F_3 (ref. 41)

experimental and theoretical findings for the isovalent ReO_2F_3 monomer and the $OsO_2F_3^+$ cation.[63] The D_{3h} structure, with the oxygen atoms in the axial positions, is not a minimum with two imaginary frequencies and is, with a zero point energy correction, 45.3 kcal mol^{-1} higher in energy than the C_{2v} structure. The Tc-O bond distance is predicted to be 1.691 Å which is to be compared with the experimental Tc-O distances of 1.660(4) Å in $TcO_2F_4^-$ and 1.646(9) Å in the TcO_2F_3 extended chain structure.[41] The Tc-F axial and equatorial bonds are predicted to be of the same length, 1.872 Å, which is also longer than the terminal Tc-F bond of 1.834(7) Å in the TcO_2F_3 extended chain structure. The bond distances calculated using the polarized triple zeta valence basis set (TZVP) are shorter by about 0.005 Å compared to the DZVP results. The nonlocal values are longer than the local values following previously observed trends. The O-Tc-O angle is closed down from 120° to 109° as found for $OsO_2F_3^+$ and ReO_2F_3.[63] The F_c-Tc-F_c angle differs from 180° by 18° and the axial fluorines are bent away from the oxygens, toward the equatorial fluorine as in $OsO_2F_3^+$ and ReO_2F_3.

The energy-minimized structure of the $TcO_2F_3(CH_3CN)$ adduct corresponds to a *cis*-dioxo arrangement in which the CH_3CN molecule is coordinated *trans* to an oxygen. The calculated geometric parameters of the adduct differ only slightly from those calculated for monomeric TcO_2F_3 (Table 3.7). The bond distances for the Tc-O bonds differ by almost 0.02 Å with the bond *trans* to the Tc-N bond being shorter. The Tc-F bond *trans* to Tc-O is significantly lengthened by 0.03 Å as compared to the other Tc-F bonds. The bond lengths and angles for the CH_3CN moiety are essentially the same as those of the isolated molecule[125] and the long Tc-N bond distance, 2.308 Å, is consistent

with a donor-acceptor type interaction.[112] Addition of the CH_3CN ligand to trigonal bipyramidal TcO_2F_3 induces significant changes in the angles as the structure more closely approximates an octahedral structure. The O-Tc-O angle decreases by about 5° and one F_t-Tc-O angle increases by about 30° with the other F_t-Tc-O angle decreasing by a similar amount. The angle between the axial fluorines, $\angle F_c$-Tc-F_c, decreases by about 4°.

The C_{2v} structure of $TcO_2F_4^-$ (Table 3.8) has the lowest energy and is 24.1 kcal mol^{-1} more stable than the *trans*-dioxo (D_{4h}) structure which has two imaginary frequencies. The calculated C_{2v} structure Tc-O bond distance of 1.724 Å is 0.064 Å longer than that of $TcO_2F_4^-$ in the crystal. Such a difference is somewhat larger than what is expected based on LDFT calculations on OsO_2F_4,[93] which were done with pseudopotentials. The calculated values for OsO_2F_4 are 0.05 Å longer than the experimental values. The increased discrepancy between the calculated and experimental findings for $TcO_2F_4^-$ could be due to missing relativistic effects which should decrease the bond length by a few hundredths of an angstrom. Another possible source for the differences is that LDFT methods may not perform as well for anions as for neutral molecules or cations. The Tc-F_t bond length for the fluorines *trans* to oxygen is 1.946 Å and is longer than the Tc-F_c bond length of 1.910 Å. Both bond distances are longer than those of monomeric TcO_2F_3, as expected for a structure in which a fluoride ion has been added. Comparison to experiment shows that the calculated Tc-F_c bond length is 0.034 Å longer whereas the predicted Tc-F_t bond length is 0.040 Å shorter than the experimental distances. Calculations with the TZVP basis set gave similar results with bond distances shorter by about 0.01 Å than those obtained with the DZVP basis set. This

Table 3.8. Geometric Parameters for $TcO_2F_4^-$ (C_{2v})

Bond Length / Angle	LDFT		NLDFT		
	TZVP	DZVP	TZVP	DZVP	exp
Tc-O (Å)	1.715	1.724	1.734	1.724	1.660(4)
Tc-F_t (Å)	1.938	1.946	1.975	1.946	1.986(3)
Tc-F_c (Å)	1.899	1.910	1.935	1.910	1.876(3)
O-Tc-O (deg)	101.3	101.6	101.3	101.3	102.5(3)
F_t-Tc-O (deg)	89.7	89.6	89.6	89.6	90.4(2)
F_c-Tc-F_c (deg)	168.3	168.0	168.6	168.6	164.2(3)
F_c-Tc-F_t (deg)	85.5	85.4	85.6	85.6	83.8(1)
O-Tc-F_c (deg)	93.7	93.8	93.6	93.6	94.9(1)
F_t-Tc-F_t (deg)	79.5	79.5	79.2	79.3	76.7(2)

suggests that there is a strong interaction between the Li^+ and the *trans*-fluorines in the crystal (see **X-ray Crystal Structure of $Li^+TcO_2F_4^-$**). The calculated angles for $TcO_2F_4^-$ are in good agreement with the experimental values for the extended chain structure. The largest differences are for the F_c-Tc-F_c angle, which is calculated to be 4° larger than the experimental value, and for the F_t-Tc-F_t angle, which is predicted to be about 3° larger than the experimental value. These angles involve the most ionic bonds and would be expected to exhibit the largest distortions arising from the long contacts to the Li^+ cation (see **X-ray Crystal Structure of $Li^+TcO_2F_4^-$**).

Conclusion

Technetium dioxotrifluoride behaves as an electron pair acceptor toward the fluoride ion and CH_3CN, forming $TcO_2F_4^-$ and $TcO_2F_3(CH_3CN)$ which both occur as *cis*-dioxo isomers. The energy-minimized geometries determined from density functional theory calculations are in agreement with the structures determined by X-ray crystallography and by NMR and Raman spectroscopy. The energy-minimized geometry of TcO_2F_3 monomer is a trigonal bipyramid with the oxygens *cis* and in the equatorial plane as observed experimentally for the matrix-isolated ReO_2F_3[12] and the $OsO_2F_3^+$ cation in SbF_5 solution.[63]

CHAPTER 4

LEWIS ACID PROPERTIES OF ReO_2F_3*

Introduction

All of the neutral Re(VII) oxofluorides, ReO_3F, ReO_2F_3 and $ReOF_5$ have been synthesized and structurally characterized. Selig and El-Gad[126] characterized ReO_3F as the solvolysis product of ReO_4^- in anhydrous HF by Raman spectroscopy and pure solid samples were obtained by the reaction of $KReO_4$ with IF_5 in the presence of trace amounts of HF.[11] Peacock[127] first obtained $ReO_2F_4^-$ by interaction of $M^+ReO_4^-$ (M = K, Rb, Cs, Ag) with BrF_3, but the anion was not structurally characterized. A similar reaction involving Re_2O_7 with BrF_3 and KBr was subsequently used to prepare ReO_2F_3.[12] The low volatility and high melting point of ReO_2F_3 contrast with ReO_3F and $ReOF_5$ and indicate that ReO_2F_3 is polymeric in the solid state. Although the polymeric structure of TcO_2F_3 has been previously confirmed by X-ray crystallography,[41] the detailed structure of polymeric ReO_2F_3 (denoted below as $(ReO_2F_3)_\infty$) has not been determined. The ReO_2F_3 monomer has been characterized by matrix-isolation Raman and infrared spectroscopy[12] and the vibrational frequencies have been subsequently reassigned with the aid of density functional theory (DFT) calculations.[63] The vibrational spectra of the $ReO_2F_4^-$ anion have

---

* Reprinted in part with permission from Inorganic Chemistry, submitted for publication. Unpublished work © 1998 American Chemical Society.

been reported[94] and a ^{19}F NMR study of the $ReO_2F_4^-$ anion, obtained by the reaction of Re_2O_7 with HF in ethanol, has also been reported.[52] To date the most reliable preparations of ReO_2F_3 and $ReOF_5$ have involved direct fluorinations using a 4:1 molar ratio of F_2:Re_2O_7 at 200 °C for 65 h for ReO_2F_3 and a 1.1:1 molar ratio of F_2:ReO_2 at 250 °C for 12 h for $ReOF_5$.[13]

Previous work has shown that high-valent metal oxides and oxofluorides can be fluorinated in anhydrous HF using noble-gas fluorides. In anhydrous HF, XeF_6 fluorinates TcO_3F to give TcO_2F_3 [41] and KrF_2 fluorinates OsO_4 to give OsO_2F_4.[92] The present Chapter describes an improved high-yield synthesis of high-purity ReO_2F_3 using an approach analogous to that used to synthesize TcO_2F_3,[41] and the structural characterization of $(ReO_2F_3)_\infty$ by Raman spectroscopy and X-ray crystallography. The Lewis acid behaviour of ReO_2F_3 toward the fluoride ion and CH_3CN and the structural characterization of $ReO_2F_4^-$, $Re_2O_4F_7^-$, $Re_3O_6F_{10}^-$, $ReO_2F_3(CH_3CN)$ and $ReO_3F(CH_3CN)_2$ are also described.

Results and Discussion

Improved Synthesis of ReO_2F_3

Previous syntheses of ReO_2F_3 have involved time-consuming direct fluorination of Re_2O_7 or ReO_2 at elevated temperatures, followed by separation of the products by vacuum sublimation.[13,14,132] The heptoxide has also been fluorinated using BrF_3, but the tendency of the Lewis acid ReO_2F_3 to form adducts with excess BrF_3 made complete removal of this reagent difficult.[12]

An improved, high-yield synthesis for ReO_2F_3 has been achieved in the present work by the room temperature fluorination of Re_2O_7 with XeF_6 in anhydrous HF and is an extension of a general synthesis of lower oxide fluorides by solvolysis of an oxide in HF and is analogous to the preparation of TcO_2F_3.[41] Because water is also a solvolysis product, the extent of fluorination is limited to species which are stable in its presence.[133] Xenon hexafluoride readily reacts with water in HF solutions and is an aggressive fluorinator. In appropriate stoichiometries, XeF_6 also reacts with the products of the HF solvolysis of Re_2O_7, namely, H_2O and ReO_3F, to give high purity ReO_2F_3 according to equations (4.1)-(4.3). When larger ratios of XeF_6:Re_2O_7 were used, the soluble

$$Re_2O_7 + 2\ HF \longrightarrow H_2O + 2\ ReO_3F \qquad (4.1)$$

$$H_2O + XeF_6 \longrightarrow XeOF_4 + 2\ HF \qquad (4.2)$$

$$ReO_3F + XeF_6 \longrightarrow ReO_2F_3 + XeOF_4 \qquad (4.3)$$

$XeF_5^+ReO_2F_4^-$ salt was produced according to equation (4.4) and no further fluorination

$$XeF_6 + ReO_2F_3 \longrightarrow XeF_5^+ReO_2F_4^- \qquad (4.4)$$

of ReO_2F_3 to $ReOF_5$ occurred as was determined by ^{19}F NMR spectroscopy of a sample of XeF_6 and ReO_2F_3 (9:1 molar ratio) in HF (see **NMR Spectroscopy**) and is analogous in behaviour to the technetium system (see Chapter 3).

The use of three moles of XeF_6 per mole of Re_2O_7 as the upper limit ensured that only volatile $XeOF_4$ was produced, which was readily pumped off along with HF. A ratio of XeF_6:Re_2O_7 = 1.5:1 is the practical lower limit because lower ratios would likely result

in the formation of shock-sensitive and explosive XeO_3.[134] Intermediate ratios led to the formation of XeO_2F_2 (eq. (4.5)), which has a low volatility and is difficult to pump off.

$$ReO_3F + XeOF_4 \longrightarrow ReO_2F_3 + XeO_2F_2 \qquad (4.5)$$

It will be shown in Chapter 5 that $XeOF_4$ initially produced in the reaction of TcO_2F_3 with XeF_6 reacts with TcO_3F to give a volatile molecular adduct, $TcO_2F_3 \cdot XeO_2F_2$, which has been isolated and characterized by X-ray crystallography.

The present synthesis provides ReO_2F_3 in almost quantitative yield as a stable, colourless, microcrystalline solid which is essentially insoluble in anhydrous HF and has a melting point (113-116 °C) and color which are consistent with the observations of Stevie and Sunder[13] who reported an almost white solid and a similar melting point (115 °C). The purity of this material is significantly higher than that reported by Peacock et al.[14] who described ReO_2F_3 as a pale yellow solid melting at 90 °C. Unlike TcO_2F_3, ReO_2F_3 is stable in Pyrex and in CH_3CN solutions at room temperature; however, CH_3CN solutions of ReO_2F_3 produce charring when warmed to -40 °C in the presence of $N(CH_3)_4F$, and ReO_2F_3 solutions in CH_2Cl_2 undergo rapid decomposition at room temperature to give blue solutions, typical of Re(VI) species.

The pale yellow $M^+ReO_2F_4^-$ (M = Na, K, Rb, Cs, Ag) salts have been previously reported and were formed by combination of ReO_2F_3 and the alkali metal fluorides in the solid state at 120-150 °C[55] or in the reaction between $M^+ReO_4^-$ and BrF_3[127] and indicated that ReO_2F_3 is a moderately strong fluoroacid relative to BrF_3 and capable of forming stable Lewis acid-base adducts with BrF_3. Although ReO_2F_3 is insoluble in HF, it rapidly

dissolves in the presence of alkali metal fluorides to give pale yellow solutions of $M^+ReO_2F_4^-$ (M = Li, Na, K, Cs, $N(CH_3)_4$) salts whose solubilities in anhydrous HF increase with cation size. The K^+ and Cs^+ salts are too soluble for effective crystal growth, but crystals of $Li^+ReO_2F_4^-$ could be grown readily from saturated HF solutions. The $Na^+ReO_2F_4^-$ salt, prepared in a similar manner, gave a pale yellow, microcrystalline powder which was shown by X-ray powder diffraction to be isomorphous with the Li^+ salt. The Lewis acid behaviour of ReO_2F_3 in HF contrasts with that of TcO_2F_3 whose conjugate base, $TcO_2F_4^-$, undergoes solvolysis in HF according to equation (4.6) in all but very concentrated fluoro-basic solutions (see Chapter 3).

$$TcO_2F_4^- \xrightarrow{HF} TcO_2F_3 + F^-_{(solv)} \qquad (4.6)$$

When the molar ratio of ReO_2F_3:F^- is increased to 2:1 and to 3:1, the dinuclear and trinuclear rhenium anions, $Re_2O_4F_7^-$ and $Re_3O_6F_{10}^-$, are formed according to equations (7) and (8). A 1.9:1 molar ratio of KF and ReO_2F_3 in HF resulted in the cocrystallization of

$$2\ ReO_2F_3 + F^- \xrightarrow{HF} Re_2O_4F_7^- \qquad (4.7)$$

$$3\ ReO_2F_3 + F^- \xrightarrow{HF} Re_3O_6F_{10}^- \qquad (4.8)$$

$K^+Re_2O_4F_7^-$ and ReO_2F_3. The nature and concentration of the cation as well as the relative amount of ReO_2F_3 used influences the degree of anion oligomerization in solution. As can be seen from the existence of $K^+Re_2O_4F_7^-\cdot 2ReO_2F_3$, the $Re_2O_4F_7^-$ anion is the highest oligomer present in solution when KF is used as the fluorobase, even when a two-fold

molar excess of ReO_2F_3 with respect to KF is used. In contrast, the $Re_3O_6F_{10}^-$ anion can only be obtained by using the stronger fluorobase CsF. This behaviour suggests that significant ion-pairing occurs between K^+ and $Re_2O_4F_7^-$, which renders the $Re_2O_4F_7^-$ anion insufficiently fluorobasic to disrupt the ReO_2F_3 polymer and coordinate to another ReO_2F_3-unit. Conversely, the weaker Lewis acidity of Cs^+ and accompanying weaker ion-pair interactions serve to enhance the fluoride base strength of the $Re_2O_4F_7^-$ anion sufficiently to coordinate another ReO_2F_3-unit forming the $Re_3O_6F_{10}^-$ anion.

The Lewis acid character of ReO_2F_3 is also evident from its solubility in CH_3CN solvent. The complex, $ReO_2F_3(CH_3CN)$, was isolated as a white solid by removal of the solvent at 0 °C. Unlike its technetium analogue, $ReO_2F_3(CH_3CN)$ can be stored at room temperature without dissociation to ReO_2F_3 and CH_3CN, suggesting a stronger Re-N bond, which is expected based on the greater Lewis acidity of ReO_2F_3 compared to that of TcO_2F_3. When the molar ratio of ReO_2F_3 to $N(CH_3)_4^+ReO_2F_4^-$ was increased to 2:1 in CH_3CN solution, there was no evidence for the formation of $N(CH_3)_4^+Re_3O_6F_{10}^-$ in CH_3CN solution. This is attributed to the stronger Lewis base character of CH_3CN relative to $Re_2O_4F_7^-$ so that any additional ReO_2F_3 reacts with the solvent to form the $ReO_2F_3(CH_3CN)$ adduct.

^{19}F NMR Spectroscopy

$N(CH_3)_4^+ReO_2F_4^-$, $Cs^+ReO_2F_4^-$ and $XeF_5^+ReO_2F_4^-$. The ^{19}F NMR spectrum of $N(CH_3)_4^+ReO_2F_4^-$ was recorded at 30 °C in CH_3CN. The spectrum displays two triplets [$^2J(^{19}F_{c,t}\text{-}^{19}F_{c,c})$ = 87 Hz] at -53.8 and -64.2 ppm (Figure 4.1) which are assigned to the

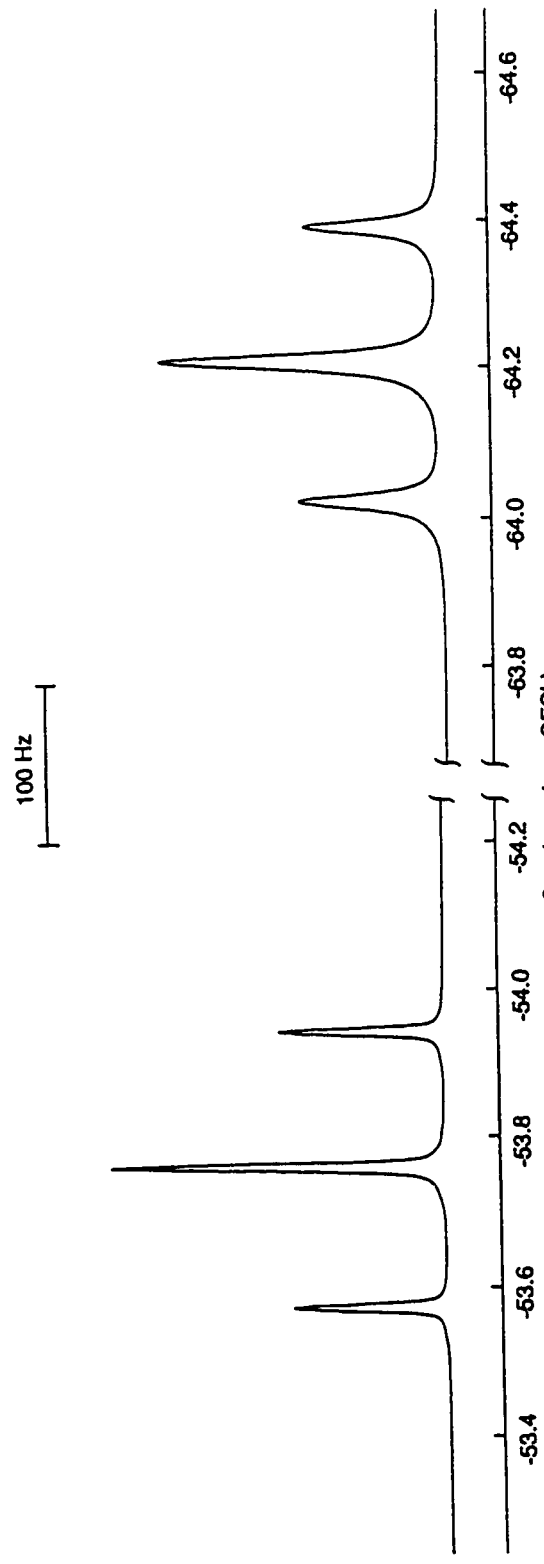

Figure 4.1. ^{19}F NMR spectrum (470.599 MHz) of $N(CH_3)_4^+ReO_2F_4^-$ in CH_3CN solvent recorded at 30 °C.

fluorine environments *trans* ($F_{c,t}$) and *cis* ($F_{c,c}$) to the oxygen ligands and establish that the *cis* geometry is adopted by $ReO_2F_4^-$ in solution (Structure I). The triplet corresponding

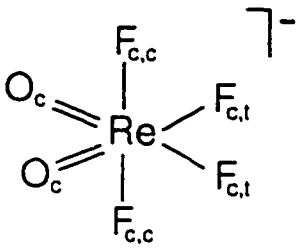

Structure I

to the $F_{c,c}$ environment is broadened ($\Delta\nu_{1/2}$ = 10.7 Hz) compared to that of $F_{c,t}$ ($\Delta\nu_{1/2}$ = 5.8 Hz). The signal broadening is attributed to residual scalar coupling of ^{19}F to the quadrupolar nuclei ^{185}Re (37.4%, $I = {}^5/_2$, $Q = 2.8 \times 10^{-28}$ m^2) and ^{187}Re (62.6%, $I = {}^5/_2$, $Q = 2.6 \times 10^{-28}$ m^2).[60] It is anticipated that $^1J(^{185,187}Re\text{-}^{19}F_{c,c}) > {}^1J(^{185,187}Re\text{-}^{19}F_{c,t})$ because the Re-$F_{c,c}$ bonds are expected to be more covalent than the Re-$F_{c,t}$ bonds, which are *trans* to oxygen. The lengthening of the Re-$F_{c,t}$ bonds was confirmed in the X-ray structure of $Li^+ReO_2F_4^-$ (see **X-ray Crystal Structures**) and the correspondingly smaller $^1J(^{19}F_{c,t}\text{-}^{185,187}Re)$ coupling constant is analogous to the trend observed in the ^{19}F NMR spectrum of $TcO_2F_4^-$ (see Chapter 3).

The ^{19}F NMR spectrum of a 1:5 molar ratio of ReO_2F_3 and CsF in HF at 30 °C consists of a singlet at -35.6 ppm ($\Delta\nu_{1/2}$ = 10 Hz) assigned to the $F_{c,c}$ environment of $ReO_2F_4^-$ (Figure 4.2). Only one other resonance was observed at -195.1 ppm ($\Delta\nu_{1/2}$ = 60 Hz) and was assigned to the $F_{c,t}$ environment of $ReO_2F_4^-$ undergoing rapid fluorine exchange with the solvent. This exchange is slowed sufficiently at -80 °C to observe two triplets at -30.7 ppm ($\Delta\nu_{1/2}$ = 65 Hz) and -135.7 ($\Delta\nu_{1/2}$ = 50 Hz), assigned to the *cis*- and

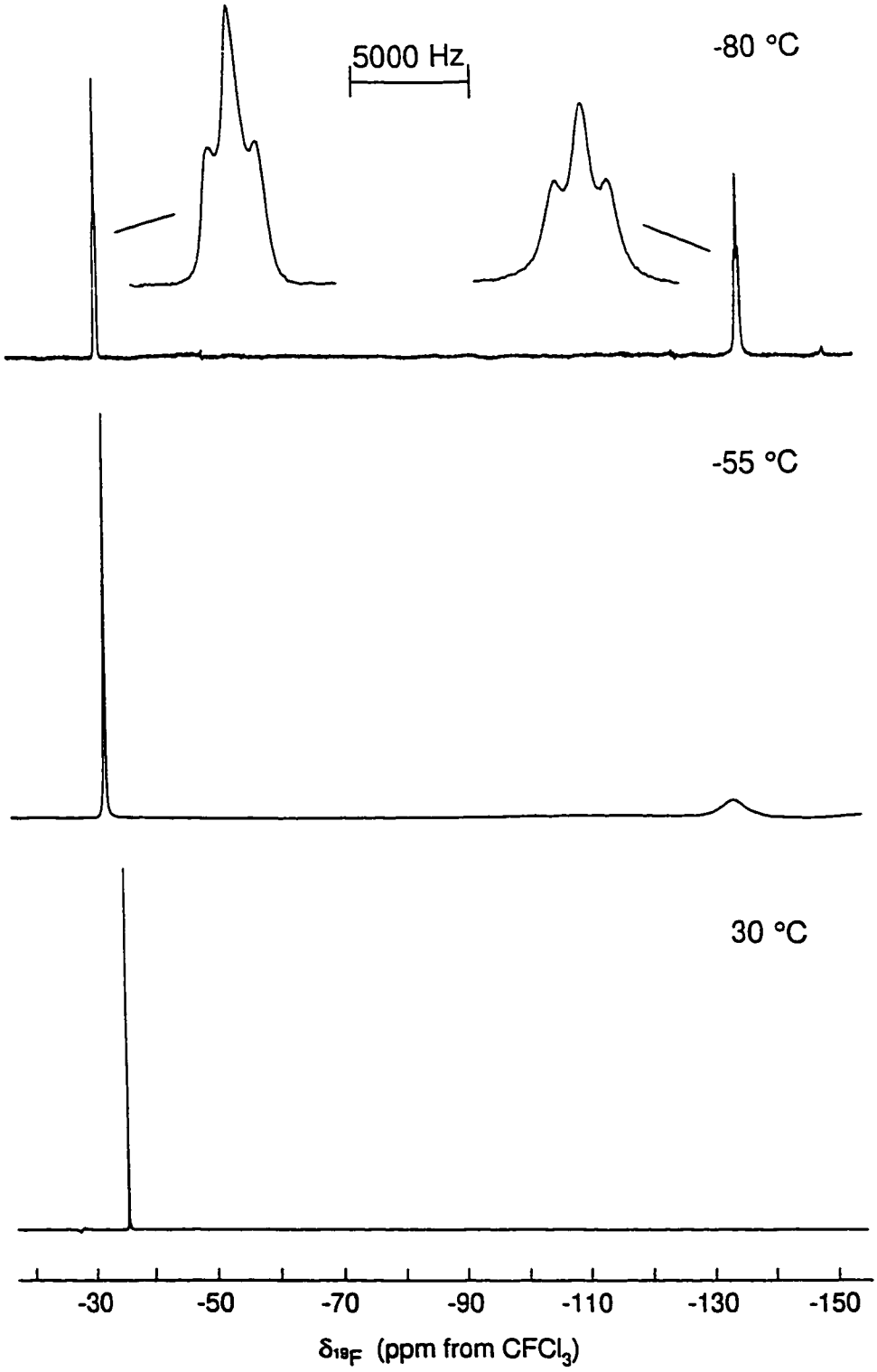

Figure 4.2. Variable-temperature ^{19}F NMR spectra (282.409 MHz) of ReO_2F_3 and CsF (1:5 molar ratio) dissolved in HF.

trans-fluorines, respectively, and the HF solvent resonance at -190.9 ppm ($\Delta\nu_{1/2}$ = 30 Hz). The exchange behaviour parallels that of $Cs^+TcO_2F_4^-$ in HF in the presence of excess CsF and confirms the assignment of the more labile fluorine environment to the fluorines *trans* to oxygen. As for $TcO_2F_4^-$, the $F_{c,t}$ environment occurs at lower frequency than that of $F_{c,c}$. The coupling constant, $^2J(^{19}F_{c,c}\text{-}^{19}F_{c,t})$ = 85 Hz, is in excellent agreement with that observed for $N(CH_3)_4^+ReO_2F_4^-$ in CH_3CN and with the value reported by Buslaev et al.[52] (89 Hz) for a solution of Re_2O_7 in 60% HF in ethanol (-32.2 ppm, triplet; -109.2 ppm, triplet). It is worth noting the remarkable solvent dependence of the ^{19}F chemical shifts for $ReO_2F_4^-$.

Further fluorination of ReO_2F_3 to $ReOF_5$ by XeF_6 does not occur in HF at room temperature as was determined from the ^{19}F NMR spectrum of a 1:9 molar ratio of ReO_2F_3 and XeF_6, which only consists of a singlet at -31.9 ppm ($\Delta\nu_{1/2}$ = 12 Hz) assigned to $F_{c,c}$ of $ReO_2F_4^-$ and a broad resonance at -120.8 ppm ($\Delta\nu_{1/2}$ = 210 Hz) assigned to the *trans*-fluorines of $ReO_2F_4^-$ undergoing rapid fluorine exchange with XeF_6, XeF_5^+ and HF.

$ReO_2F_3(CH_3CN)$. There are three isomers possible for $ReO_2F_3(CH_3CN)$, a *trans*-dioxo isomer and two *cis*-dioxo isomers in which CH_3CN is coordinated *trans* to an oxygen or *trans* to a fluorine. All three isomers would result in the same multiplicities and relative intensities in the ^{19}F NMR spectrum, namely a doublet and a triplet in the intensity ratio 2:1. The energy-minimized structure calculated by LDFT calculations for gas-phase $ReO_2F_3(CH_3CN)$ is a *cis*-dioxo isomer in which CH_3CN is coordinated *trans* to an oxygen (Structure II; see **Computational Results**), and is analogous to the energy-minimized structure predicted for $TcO_2F_3(CH_3CN)$. Moreover, no examples of pseudooctahedral

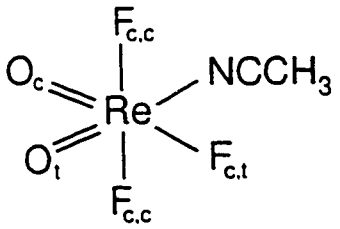

Structure II

trans-dioxo d^0 species are known. Consequently, Structure II is assumed to represent the geometry of $ReO_2F_3(CH_3CN)$ in solution and is the basis of the subsequent assignments.

The ^{19}F NMR spectrum of $ReO_2F_3(CH_3CN)$ was recorded in SO_2ClF solvent in the presence of excess CH_3CN at 30 and -80 °C (values in square brackets). The spectrum consists of an AB_2 pattern with the $F_{c,c}$ environment at -23.8 ($\Delta\nu_{1/2}$ = 18 Hz) [-24.1 ($\Delta\nu_{1/2}$ = 13 Hz)] ppm (doublet) and the $F_{c,t}$ environment at -25.8 ($\Delta\nu_{1/2}$ = 27 Hz) [-34.3 ($\Delta\nu_{1/2}$ = 15 Hz)] ppm (triplet) with relative integrated intensities of 2.0:1.0 (Structure II and Figure 4.3a) and a two-bond $^2J(^{19}F_{c,t}\text{-}^{19}F_{c,c})$ coupling constant of 119 [117] Hz. The ^{19}F NMR spectrum of $ReO_2F_3(CH_3CN)$ was also recorded in CH_3CN solvent at 30 °C (Figure 4.3b), yielding NMR parameters very similar to those obtained for the adduct in SO_2ClF solvent, i.e., -24.5 (doublet) and -31.1 (triplet) ppm, $^2J(^{19}F_{c,t}\text{-}^{19}F_{c,c})$ = 115 Hz. The ^1H NMR spectrum of $ReO_2F_3(CH_3CN)$ recorded in SO_2ClF in the presence of excess CH_3CN consists of two singlets at 2.40 and 1.81 ppm corresponding to complexed and free CH_3CN, respectively. The ^{13}C NMR spectrum of this solution shows the complexed acetonitrile signals at 1.81 (CH_3) and 119.0 (CN) ppm, whereas free CH_3CN occurs at 0.46 (CH_3) and 117.5 (CN) ppm. The ^1H and ^{13}C complexation shifts for $ReO_2F_3(CH_3CN)$

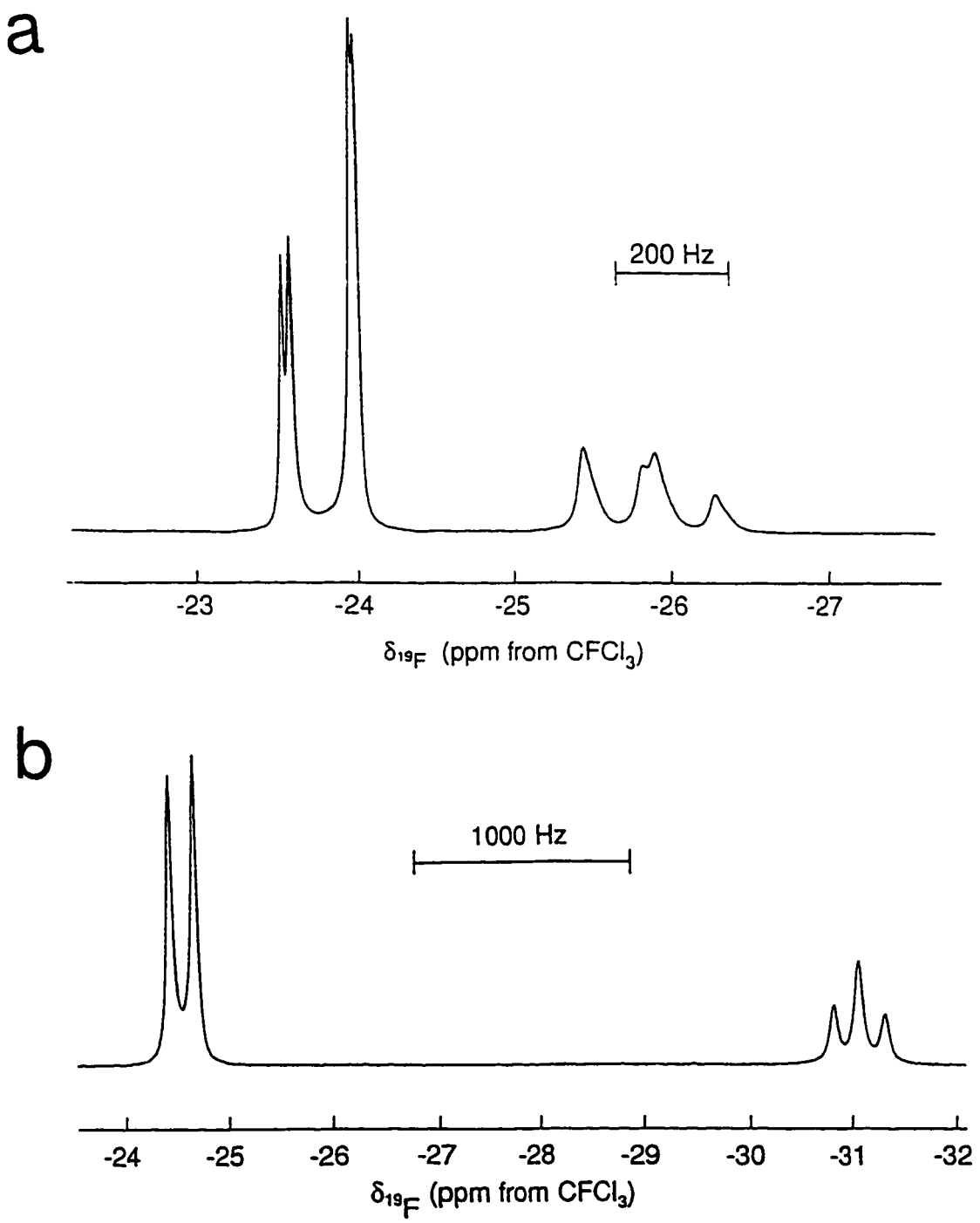

Figure 4.3. ^{19}F NMR spectra (282.409 MHz) of (a) $ReO_2F_3(CH_3CN)$ in SO_2ClF and (b) ReO_2F_3 in CH_3CN, recorded at 30 °C.

with respect to the free CH_3CN are consistent with Lewis acid-base adduct formation where CH_3CN donates electron density to ReO_2F_3. The narrow linewidths of the ^1H ($\Delta\nu_{1/2}$ = 5 Hz) and ^{13}C ($\Delta\nu_{1/2}$ = 11 Hz) resonances indicate that the rate of exchange between free and complexed CH_3CN is slow on the NMR time scale. There is a significant increase in the shielding of the $F_{c,t}$ resonance upon increasing the temperature from -80 to 30 °C, whereas the chemical shift of the $F_{c,c}$ resonance remains essentially unchanged. A similar temperature dependence was observed for $TcO_2F_3(CH_3CN)$ (see Chapter 3).

$N(CH_3)_4^+Re_2O_4F_7^-$. The ^{19}F NMR spectrum of a 1:1 molar ratio of ReO_2F_3 and $N(CH_3)_4^+ReO_2F_4^-$ recorded in CH_3CN solvent at -40 °C consists of an equilibrium mixture of three species: $ReO_2F_3(CH_3CN)$ [65 mol%; $F_{c,c}$ doublet, -24.3 ppm ($\Delta\nu_{1/2}$ = 15 Hz); $F_{c,t}$ triplet -34.7 ppm ($\Delta\nu_{1/2}$ = 15 Hz); $^2J(^{19}F_{c,t}\text{-}^{19}F_{c,c})$, 118 Hz[, $ReO_2F_4^-$ [12 mol%; $F_{c,c}$ triplet, -66.3 ppm ($\Delta\nu_{1/2}$ = 5 Hz); $F_{c,t}$ triplet -52.1 ppm ($\Delta\nu_{1/2}$ = 5 Hz); $^2J(^{19}F_c\text{-}^{19}F_t)$, 87 Hz] and $Re_2O_4F_7^-$ (23 mol%) (Figure 4.4). The ^{19}F NMR spectrum of the $Re_2O_4F_7^-$ anion (Structure III) consists of a doublet of doublets at -28.8 ppm ($\Delta\nu_{1/2}$ = 9 Hz) assigned to the terminal

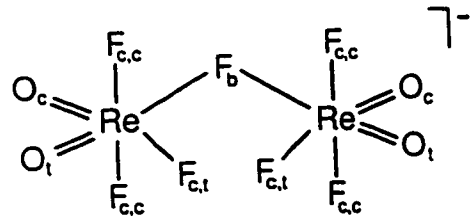

Structure III

Figure 4.4. ^{19}F NMR spectrum (282.409 MHz) of a 1:1 molar ratio of $N(CH_3)_4^+ReO_2F_4^-$ and ReO_2F_3 in CH_3CN recorded at -40 °C. Labels A, B and C denote resonances assigned to $ReO_2F_3(CH_3CN)$, $ReO_2F_4^-$ and $Re_2O_4F_7^-$, respectively, with the subscripts c, t and b corresponding to the *cis*-, *trans*-, and bridging fluorine environments, respectively. The three quintet components of the bridging fluorine resonance of $Re_2O_4F_7^-$ are identified by asterisks (*), daggers (†) and double daggers (‡).

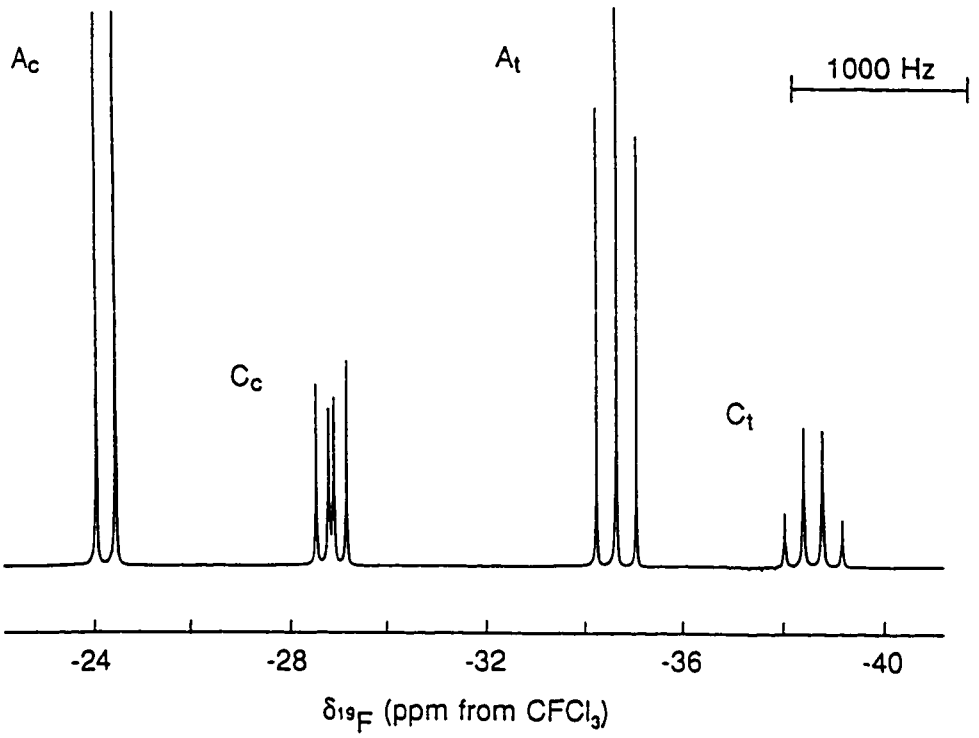
Ac
At
1000 Hz
Cc
Ct
-24
-28
-32
-36
-40
δ19F (ppm from CFCl3)

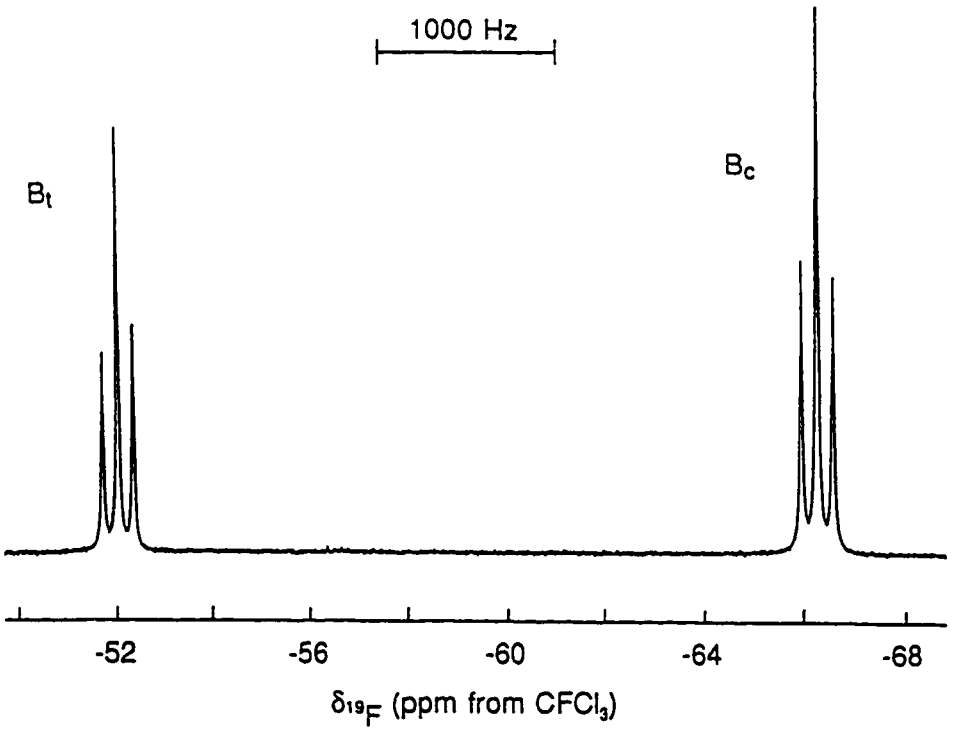
1000 Hz
Bt
Bc
-52
-56
-60
-64
-68
δ19F (ppm from CFCl3)

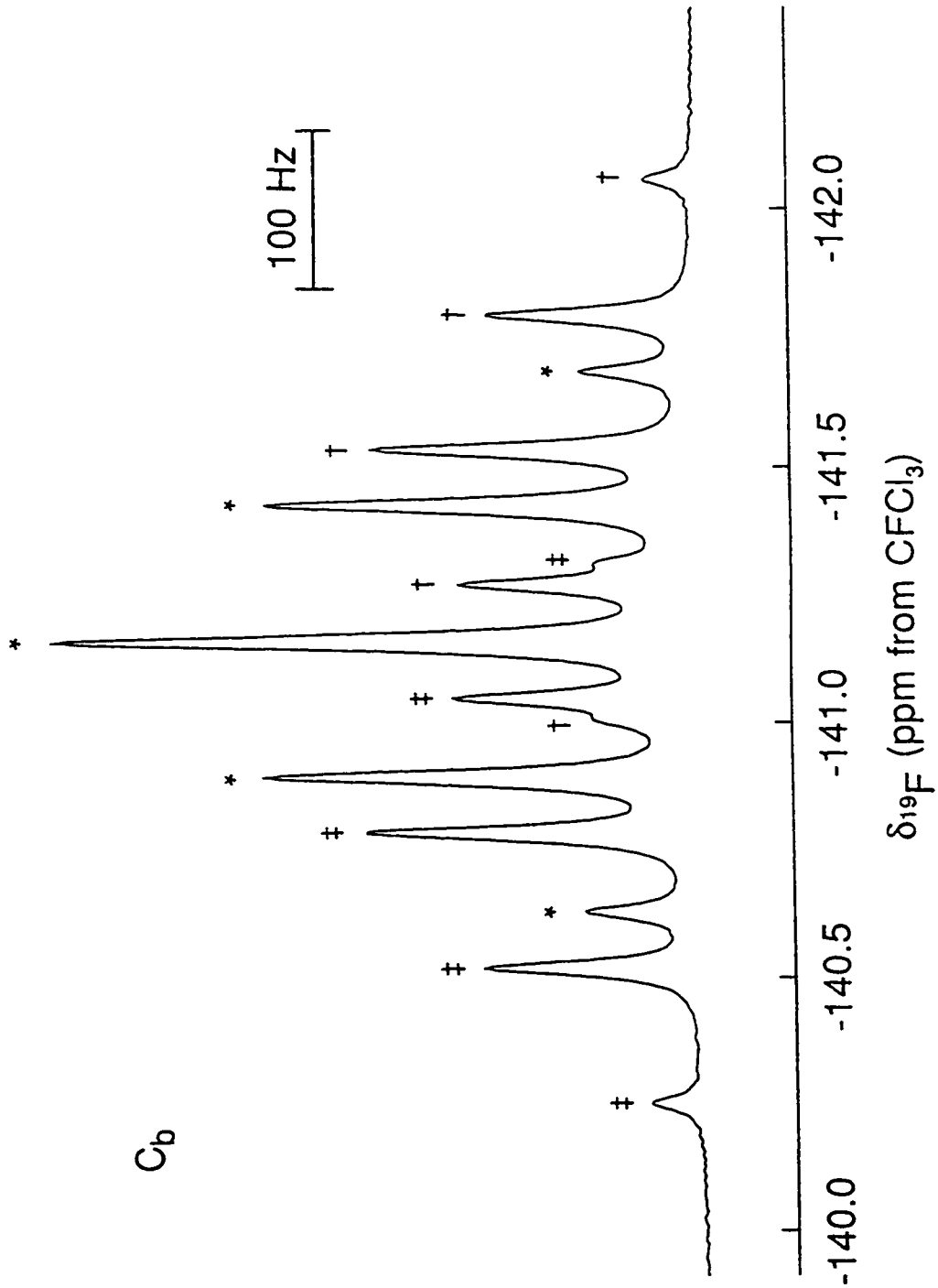
100 Hz
C_b
-140.0
-140.5
-141.0
-141.5
-142.0
$\delta_{^{19}F}$ (ppm from $CFCl_3$)

fluorines *cis* to the oxygens ($F_{c,c}$), a doublet of triplets at -38.6 ppm ($\Delta\nu_{1/2}$ = 12 Hz) assigned to the terminal fluorines *trans* to O_c ($F_{c,t}$) and a triplet of quintets at -141.2 ppm ($\Delta\nu_{1/2}$ = 12 Hz) assigned to the bridging fluorine (F_b). The strong shielding of the F_b resonance is characteristic of fluorine-bridged transition metal complexes (e.g., $Mo_2O_2F_9^-$,[105] $W_2O_2F_9^-$,[135] and isoelectronic $Os_2O_4F_7^+$)[93] and is consistent with its more ionic bonding. The coupling constants $^2J(^{19}F_{c,t}\text{-}^{19}F_{c,c})$ and $^2J(^{19}F_{c,t}\text{-}^{19}F_b)$ are identical (105 Hz), while $^2J(^{19}F_{c,c}\text{-}^{19}F_b)$ is significantly smaller (75 Hz). The coupling constant between the bridging and terminal fluorines in $Re_2O_4F_7^-$ is significantly larger than those of $Mo_2O_2F_9^-$ (56 Hz),[105] $W_2O_2F_9^-$ (59 Hz),[135] $WOF_4{\cdot}XeF_2$ (50 Hz),[136] $MoOF_4{\cdot}XeF_2$ (50 Hz),[136] $WOF_4{\cdot}KrF_2$ (48 Hz),[137] $MoOF_4{\cdot}KrF_2$ (44 Hz)[137] and $Sb_2F_{11}^-$ (60 Hz),[138] and is consistent with the more covalent M-F_b bonds that result from the higher electronegativity of Re(VII).

X-ray Crystal Structures

Details of the data collection parameters and other crystallographic information for $Li^+ReO_2F_4^-$, $K^+Re_2O_4F_7^-$, $K^+Re_2O_4F_7^-{\cdot}2ReO_2F_3$, $Cs^+Re_3O_6F_{10}^-$ and $ReO_3F(CH_3CN)_2{\cdot}CH_3CN$ are given in Tables 4.1 and 4.2. The final atomic coordinates and the equivalent thermal parameters are summarized in Tables 4.3 to 4.7. Important bond lengths, angles, significant long contacts and bond valences, as defined by Brown,[110] for individual bonds and anion-cation contacts are given in Tables 4.8 to 4.12.

Table 4.1. Summary of Crystal Data and Refinement Results for $Li^+ReO_2F_4^-$, $K^+Re_2O_4F_7^-$ and $K^+Re_2O_4F_7^-\cdot 2ReO_2F_3$

	$Li^+ReO_2F_4^-$	$K^+Re_2O_4F_7^-$	$K^+Re_2O_4F_7^-\cdot 2ReO_2F_3$
space group	$P\bar{4}2_1m$ (113)	$P2/n$ (13)	$C2$ (5)
a (Å)	4.727(3)	5.4990(11)	27.32(2)
b (Å)	4.727(3)	5.1530(10)	5.274(5)
c (Å)	8.880(7)	14.753(3)	5.355(2)
β (deg)	90.0	95.68(3)	99.53(4)
V (Å^3)	198.4(7)	416.0(1)	760.9(11)
molecules/unit cell	2	2	2
molecular wt (g mol^{-1})	301.14	608.50	1158.90
calcd density (g cm^{-3})	5.040	4.858	5.058
T (°C)	24	20	-60
colour	pale yellow	colourless	colourless
μ (mm^{-1})	16.48	15.96	32.17
wavelength (Å)	0.56086	0.56086	0.71073
final agreement factors	R^a = 0.0378	R^a = 0.0473	R^a = 0.0238
	wR_2^b = 0.1029	wR_2^b = 0.1200	wR_2^b = 0.0645

[a] $R = \Sigma||F_o|-|F_c||/\Sigma|F_o|$

[b] $wR_2 = [\Sigma[w(F_o^2-F_c^2)^2]/\Sigma[w(F_o^2)^2]]^{1/2}$

Table 4.2. Summary and Crystal Data and Refinement Results for $Cs^+Re_3O_6F_{10}^-$ and $ReO_3F(CH_3CN)_2 \cdot CH_3CN$

	$Cs^+Re_3O_6F_{10}^-$	$ReO_3F(CH_3CN)_2$
space group	$P\bar{1}$ (2)	*Pnma* (62)
a (Å)	7.011(1)	9.138(3)
b (Å)	9.773(2)	12.518(5)
c (Å)	10.331(2)	9.138(3)
α (deg)	113.73(1)	90.0
β (deg)	91.05(2)	90.0
γ (deg)	92.42(2)	90.0
V (Å^3)	647.4(2)	1045.4(7)
molecules/unit cell	2	4
molecular wt (g mol^{-1})	977.51	373.34
calcd density (g cm^{-1})	5.018	2.372
T (°C)	-118	-63
colour	colourless	colourless
μ (mm^{-1})	16.61	11.62
wavelength (Å)	0.56086	0.71073
final agreement factors	$R^a = 0.0522$	$R^a = 0.0198$
	$R_w^b = 0.0529$	$wR_2^c = 0.0605$

[a] $R = \Sigma||F_o|-|F_c||/\Sigma|F_o|$

[b] $R_w = [\Sigma[w(|F_o|-|F_c|)^2]/\Sigma w(|F_o|)^2]^{1/2}$

[c] $wR_2 = [\Sigma[w(F_o^2-F_c^2)^2]/\Sigma[w(F_o^2)^2]]^{1/2}$

Table 4.3. Final Atomic Coordinates (× 10^4) and Equivalent Isotropic Displacement Coefficients ($Å^2$ × 10^3) in $Li^+ReO_2F_4^-$

	x	*y*	*z*	U_{eq} [a]
Re(1)	0	5000	7748(1)	8(1)
F(1)	2239(11)	2761(11)	2565(10)	17(1)
F(2)	1851(9)	3149(9)	5975(8)	13(1)
O(1)	1926(13)	3074(13)	8960(10)	18(1)
Li(1)	0	5000	4148(36)	21(4)

[a] Equivalent isotropic *U* defined as one third of the trace of the orthogonalized U_{ij} tensor.

Table 4.4. Final Atomic Coordinates ($\times 10^4$) and Equivalent Isotropic Displacement Coefficients ($Å^2 \times 10^3$) in $K^+Re_2O_4F_7^-$

	x	*y*	*z*	U_{eq} [a]
Re(1)	2439(1)	7616(1)	1128(1)	16(1)
K(1)	-2500	3224(11)	2500	32(1)
O(1)	2590(18)	8697(22)	72(9)	29(3)
O(2)	-302(16)	5859(20)	984(8)	23(2)
F(1)	2500	6168(25)	2500	30(3)
F(2)	5499(14)	8840(19)	1658(7)	34(2)
F(3)	1133(16)	10389(160	1619(8)	35(2)
F(4)	4196(16)	4544(16)	1040(7)	29(2)

[a] Equivalent isotropic *U* defined as one third of the trace of the orthogonalized $\mathbf{U}_{ij}$ tensor.

Table 4.5. Final Atomic Coordinates ($\times 10^4$) and Equivalent Isotropic Displacement Coefficients ($Å^2 \times 10^3$) in $K^+Re_2O_4F_7^- \cdot 2ReO_2F_3$

	x	*y*	*z*	U_{eq} [a]
Re(1)	-756(1)	-9606(1)	-880(1)	22(1)
K(1)	0	-5112(7)	-5000	31(1)
F(1)	0	-8318(20)	0	34(2)
F(2)	-480(3)	-10955(16)	-3592(14)	39(2)
F(3)	-520(3)	-12324(16)	909(14)	42(2)
F(4)	-780(3)	-6652(13)	-2863(12)	32(2)
O(1)	-1348(3)	-10498(21)	-1754(17)	36(2)
O(2)	-815(3)	-7707(17)	1769(13)	27(2)
Re(2)	-2007(1)	-5387(1)	3827(1)	19(1)
F(5)	-2601(2)	-7248(14)	5020(14)	28(1)
F(6)	-2481(3)	-4963(14)	1009(12)	33(2)
F(7)	-1791(2)	-5464(14)	7295(12)	31(1)
O(3)	-1793(3)	-8203(16)	3090(18)	35(2)
O(4)	-1577(3)	-3396(15)	3068(17)	33(2)

[a] Equivalent isotropic *U* defined as one third of the trace of the orthogonalized $\mathbf{U}_{ij}$ tensor.

Table 4.6. Final Atomic Coordinates (× 10^4) and Equivalent Isotropic Displacement Coefficients ($Å^2$ × 10^3) in $Cs^+Re_3O_6F_{10}^-$

	x	*y*	*z*	U_{eq} [a]
Re(1)	2309(1)	6243(1)	3687(1)	12(1)
O(1)	1668(13)	4776(9)	4053(9)	22(2)
O(2)	1240(13)	7684(10)	4981(10)	26(2)
F(1)	385(10)	6015(9)	2335(9)	28(2)
F(2)	3723(11)	5241(8)	2040(7)	24(1)
F(3)	4697(11)	6663(10)	4573(8)	28(2)
F(4)	3303(10)	8066(8)	3074(7)	19(1)
Re(2)	2595(1)	10171(1)	3282(1)	11(1)
O(3)	2825(12)	10782(11)	5065(8)	24(2)
O(4)	2047(12)	11718(8)	3046(9)	20(1)
F(5)	161(10)	9275(9)	3058(8)	23(1)
F(6)	5169(9)	10258(9)	2949(8)	22(1)
F(7)	2504(14)	8990(10)	1142(6)	38(2)
Re(3)	2380(1)	7794(1)	-1121(1)	13(1)
O(5)	2389(15)	6623(12)	-2836(7)	30(2)
O(6)	1864(13)	9462(11)	-1146(9)	24(2)
F(8)	2988(10)	6294(8)	-421(7)	22(1)
F(9)	-93(10)	7322(10)	-782(9)	29(2)
F(10)	5006(10)	8256(10)	-820(8)	27(2)
Cs(1)	6957(1)	7024(1)	1197(1)	15(1)

[a] Equivalent isotropic *U* defined as one third of the trace of the orthogonalized U_{ij} tensor.

Table 4.7. Final Atomic Coordinates (× 10^4) and Equivalent Isotropic Displacement Coefficients (Å^2 × 10^3) in $ReO_3F(CH_3CN)_2 \cdot CH_3CN$

	x	*y*	*z*	U_{eq} [a]
Re(1)	127(1)	2500	220(1)	28(1)
O(1)	-710(5)	3579(3)	992(6)	38(1)
O(2)	1790(7)	2500	1250(7)	28(1)
F(1)	-900(6)	2500	-1563(7)	41(2)
N(1)	1449(5)	3652(3)	-1215(6)	30(1)
C(1)	2100(6)	4210(4)	-1949(6)	27(1)
C(2)	2949(12)	4927(4)	-2883(10)	37(1)
N(2)	4667(16)	7500	-190(19)	98(4)
C(3)	4739(15)	6548(13)	-134(21)	49(3)
C(4)	4791(15)	5642(14)	-95(21)	54(4)

[a] Equivalent isotropic *U* defined as one third of the trace of the orthogonalized $\mathbf{U}_{ij}$ tensor.

Table 4.8. Bond Lengths, Long Contacts, Bond Valences and Bond Angles in $Li^{+}ReO_2F_4^{-}$

Bond Lengths (Å) and Corresponding Bond Valences (v.u.)[a]			
	Re(1)-F(1)	Re(1)-F(2)	Re(1)-O(1)
Bond valence	0.920	0.638	1.976
Bond length	1.867(8)	2.002(7)	1.678(9)
Total bond valence: 7.07			
	Li(1)-F(1)	Li(1)-F(2)	Li(1)-F(2)'
Bond valence	0.157	0.160	0.132
Bond length	2.05(3)	2.04(3)	2.108(7)
Total bond valence: 0.90			

Bond Angles (deg)			
O(1)-Re(1)-O(1A)	100.2(7)	F(2)-Re(1)-O(1A)	168.1(4)
O(1)-Re(1)-F(1)	95.5(2)	F(2)-Re(1)-O(1)	91.7(4)
O(1A)-Re(1)-F(1)	96.1(3)	F(2)-Re(1)-F(1)	82.8(3)
F(1)-Re(1)-F(1A)	162.9(6)	F(2)-Re(1)-F(2A)	76.3(4)

[a] Bond valence units (v.u.) are defined in ref. 110. R_0 = 1.930 (Re(VII)=O), R_0 = 1.836 (Re(VII)-F), R_0 = 1.360 (Li(I)-F) and B = 0.37 were used.

Table 4.9. Bond Lengths, Bond Valences, Long Contacts and Bond Angles in $K^+Re_2O_3F_7^-$

Bond Lengths (Å) and Corresponding Bond Valences (v.u.)[a]						
Re(1)	O(1)	O(2)	F(1)	F(2)	F(3)	F(4)
Bond valence	2.058	1.613	0.422	0.857	1.148	0.922
Bond length	1.663(12)	1.753(9)	2.155(4)	1.893(8)	1.785(9)	1.866(8)
Total bond valence: 7.02						
K(1)	O(2,2A)	F(1,1A)	F(2B,2C)	F(3B,3C)	F(4B,4C)	F(4D,4E)
Bond valence	0.104	0.045	0.129	0.088	0.030	0.125
Bond length	2.97(1)	3.140(7)	2.75(1)	2.89(1)	3.295(12)	2.76(1)
Total bond valence: 1.04						

Bond Angles (deg)			
O(1)-Re(1)-O(2)	100.5(5)	O(2)-Re(1)-F(4)	160.2(5)
O(1)-Re(1)-F(1)	176.2(3)	F(1)-Re(1)-F(2)	82.2(4)
O(1)-Re(1)-F(2)	99.9(5)	F(1)-Re(1)-F(3)	79.1(4)
O(1)-Re(1)-F(3)	98.4(5)	F(1)-Re(1)-F(4)	78.2(4)
O(1)-Re(1)-F(4)	98.7(5)	F(2)-Re(1)-F(3)	159.9(5)
O(2)-Re(1)-F(1)	82.4(4)	F(2)-Re(1)-F(4)	86.7(4)
O(2)-Re(1)-F(2)	95.0(4)	F(3)-Re(1)-F(4)	82.3(4)
O(2)-Re(1)-F(3)	89.9(4)	Re(1)-F(1)-Re(1A)	139.5(6)

[a] Bond valence units (v.u.) are defined in ref. 110. R_0 = 1.930 (Re(VII)=O), R_0 = 1.836 (Re(VII)-F), R_0 = 1.992 (K(I)-F) and B = 0.37 were used.

Table 4.10. Bond Lengths, Bond Valences Long Contacts and Bond Angles in $K^+Re_2O_4F_7^-\cdot 2ReO_2F_3$

$K^+Re_2O_4F_7^-$

Bond Lengths (Å) and Corresponding Bond Valences (v.u.)[a]						
Re(1)	O(1)	O(2)	F(1)	F(2)	F(3)	F(4)
Bond valence	1.987	1.558	0.428	0.881	1.154	0.888
Bond length	1.676(7)	1.766(7)	2.150(4)	1.883(7)	1.783(8)	1.880(6)
Total bond valence: 6.90						
K(1)	O(2B,2C)	F(1,1A)	F(2B,2C)	F(3B,3C)	F(4,4A)	
Bond valence	0.117	0.042	0.138	0.107	0.145	
Bond length	2.925(8)	3.168(7)	2.724(8)	2.820(8)	2.706(7)	
Total bond valence: 1.01						

Bond Angles (deg)			
O(1)-Re(1)-O(2)	99.8(4)	O(2)-Re(1)-F(4)	89.1(3)
O(1)-Re(1)-F(1)	176.2(3)	F(1)-Re(1)-F(2)	78.2(3)
O(1)-Re(1)-F(2)	98.7(5)	F(1)-Re(1)-F(3)	83.6(4)
O(1)-Re(1)-F(3)	99.8(5)	F(1)-Re(1)-F(4)	78.8(4)
O(1)-Re(1)-F(4)	97.6(4)	F(2)-Re(1)-F(3)	87.5(4)
O(2)-Re(1)-F(1)	81.8(3)	F(2)-Re(1)-F(4)	81.9(4)
O(2)-Re(1)-F(2)	159.4(4)	F(3)-Re(1)-F(4)	160.9(4)
O(2)-Re(1)-F(3)	95.6(4)	Re(1)-F(1)-Re(1A)	143.3(6)

Table 4.10. continued

ReO_2F_3

Bond Lengths (Å) and Corresponding Bond Valences (v.u.)[a]						
Re(2)	O(3)	O(4)	F(5)	F(5A)	F(6)	F(7)
Bond valence	2.036	1.992	0.510	0.467	1.014	0.953
Bond length	1.667(8)	1.675(8)	2.085(6)	2.118(7)	1.831(6)	1.854(6)

Total bond valence: 6.97

Bond Angles (deg)			
O(3)-Re(2)-O(4)	102.3(4)	O(4)-Re(2)-F(7)	97.8(4)
O(3)-Re(2)-F(5)	88.5(4)	F(5)-Re(2)-F(5A)	79.8(1)
O(3)-Re(2)-F(5A)	168.2(4)	F(5)-Re(2)-F(6)	80.2(3)
O(3)-Re(2)-F(6)	98.1(4)	F(5)-Re(2)-F(7)	79.5(3)
O(3)-Re(2)-F(7)	98.7(4)	F(5A)-Re(2)-F(6)	79.8(3)
O(4)-Re(2)-F(5)	169.1(4)	F(5A)-Re(2)-F(7)	79.5(3)
O(4)-Re(2)-F(5A)	89.4(4)	F(6)-Re(2)-F(7)	153.2(3)
O(4)-Re(2)-F(6)	98.8(4)	Re(2)-F(5)-Re(2A)	156.0(4)

[a] Bond valence units (v.u.) are defined in ref. 110. R_0 = 1.930 (Re(VII)=O), R_0 = 1.836 (Re(VII)-F), R_0 = 1.992 (K(I)-F) and B = 0.37 were used.

Table 4.11. Bond Lengths, Bond Valences, Long Contacts and Bond Angles in $Cs^{+}Re_3O_6F_{10}^{-}$

	Bond Lengths (Å) and Corresponding Bond Valences (v.u.)[a]					
Re(1)	O(1)	O(2)	F(1)	F(2)	F(3)	F(4)
Bond valence	2.025	1.788	0.927	0.823	0.984	0.361
Bond length	1.669(8)	1.715(8)	1.864(7)	1.908(6)	1.842(6)	2.213(6)
Total bond valence: 6.91						
Re(2)	O(3)	O(4)	F(4)	F(5)	F(6)	F(7)
Bond valence	1.892	1.949	0.544	0.960	0.968	0.578
Bond length	1.694(8)	1.683(7)	2.061(8)	1.851(7)	1.848(6)	2.039(6)
Total bond valence: 6.89						
Re(3)	O(5)	O(6)	F(7)	F(8)	F(9)	F(10)
Bond valence	1.976	1.887	0.427	0.763	0.960	0.920
Bond length	1.678(7)	1.695(7)	2.151(6)	1.936(7)	1.851(7)	1.867(7)
Total bond valence: 6.93						
Cs(1)	F(1A)	F(5A)	F(8A)	F(9A)	F(10)	F(8)
Bond valence	0.152	0.125	0.158	0.155	0.119	0.118
Bond length	3.027(7)	3.099(7)	3.013(7)	3.020(7)	3.117(8)	3.122(7)
Total bond valence: 0.94						

Table 4.11. continued

Bond Angles (deg)

O(1)-Re(1)-O(2)	102.6(4)	O(2)-Re(1)-F(4)	81.9(3)
O(1)-Re(1)-F(1)	98.5(4)	F(1)-Re(1)-F(2)	82.0(4)
O(1)-Re(1)-F(2)	99.0(4)	F(1)-Re(1)-F(3)	159.2(4)
O(1)-Re(1)-F(3)	97.9(4)	F(1)-Re(1)-F(4)	81.6(3)
O(1)-Re(1)-F(4)	175.4(3)	F(2)-Re(1)-F(3)	83.0(3)
O(2)-Re(1)-F(1)	93.1(4)	F(2)-Re(1)-F(4)	76.5(3)
O(2)-Re(1)-F(2)	158.4(5)	F(3)-Re(1)-F(4)	81.0(3)
O(2)-Re(1)-F(3)	95.6(4)	Re(1)-F(4)-Re(2)	140.6(3)
O(3)-Re(2)-O(4)	103.3(4)	O(4)-Re(2)-F(7)	89.7(4)
O(3)-Re(2)-F(4)	89.7(4)	F(4)-Re(2)-F(5)	80.9(3)
O(3)-Re(2)-F(5)	97.5(4)	F(4)-Re(2)-F(6)	79.7(3)
O(3)-Re(2)-F(6)	96.9(4)	F(4)-Re(2)-F(7)	77.3(3)
O(3)-Re(2)-F(7)	167.0(4)	F(5)-Re(2)-F(6)	155.7(3)
O(4)-Re(2)-F(4)	166.9(3)	F(5)-Re(2)-F(7)	81.0(3)
O(4)-Re(2)-F(5)	98.7(4)	F(6)-Re(2)-F(7)	80.5(4)
O(4)-Re(2)-F(6)	96.9(4)	Re(2)-F(7)-Re(3)	178.5(5)
O(5)-Re(3)-O(6)	104.3(5)	O(6)-Re(3)-F(10)	94.6(4)
O(5)-Re(3)-F(7)	170.8(5)	F(7)-Re(3)-F(8)	75.9(3)
O(5)-Re(3)-F(8)	94.9(4)	F(7)-Re(3)-F(9)	81.9(4)
O(5)-Re(3)-F(9)	97.6(4)	F(7)-Re(3)-F(10)	80.4(4)
O(5)-Re(3)-F(10)	98.1(4)	F(8)-Re(3)-F(9)	82.7(3)
O(6)-Re(3)-F(7)	85.0(4)	F(8)-Re(3)-F(10)	82.4(3)
O(6)-Re(3)-F(8)	160.8(4)	F(9)-Re(3)-F(10)	159.2(3)
O(6)-Re(3)-F(9)	94.7(4)		

Table 4.11. continued

[a] Bond valence units (v.u.) are defined in ref. 110. R_0 = 1.930 (Re(VII)=O), R_0 = 1.836 (Re(VII)-F) and B = 0.37 were used.

Table 4.12. Bond Lengths and Bond Angles in $ReO_3F(CH_3CN)_2 \cdot CH_3CN$

Bond Lengths (Å) and Corresponding Bond Valences (v.u.)[a]				
Re(1)	O(1)	O(2)	F(1)	N(1)
Bond valence	1.837	1.468	0.888	0.531
Bond length	1.705(4)	1.788(5)	2.880(5)	2.294(4)
Total bond valence: 7.09				

Bond Angles (deg)			
O(1)-Re(1)-O(1A)	104.8(3)	O(2)-Re(1)-N(1)	81.5(2)
O(1)-Re(1)-O(2)	99.4(2)	F(1)-Re(1)-N(1)	76.6(2)
O(1)-Re(1)-F(1)	97.8(2)	N(1)-Re(1)-N(1A)	77.9(2)
O(1)-Re(1)-N(1)	88.5(2)	Re(1)-N(1)-C(1)	178.6(5)
O(1)-Re(1)-N(1A)	166.2(2)	N(1)-C(1)-C(2)	178.9(5)
O(2)-Re(1)-F(1)	151.7(2)		

[a] Bond valence units (v.u.) are defined in ref. 110. R_0 = 1.930 (Re(VII)=O), R_0 = 1.836 (Re(VII)-F), R_0 = 2.06 (Re-N) and B = 0.37 were used.

$Li^+ReO_2F_4^-$, $K^+Re_2O_4F_7^-$, $K^+Re_2O_4F_7^-\cdot 2ReO_2F_3$, $Cs^+Re_3O_6F_{10}^-$

(a) Crystal Packing. The $ReO_2F_4^-$ anions (Figure 4.5) and Li^+ cations are packed along the *a*- and *b*-axes, and alternatively along the *c*-axis. The interactions of the fluorine atoms, *trans* to the oxygen atoms, with the Li^+ cations result in a bilayer arrangement such that all oxygen atoms are directed away from the cation and face oxygen atoms in the adjacent layer. Each bilayer is separated from the other by a distance of 3.065 Å, which is at the limit of the sum of the van der Waals radii for two oxygen atoms (2.84 Å).[139] An identical packing arrangement is observed in isostructural $Li^+TcO_2F_4^-$ (see Chapter 3).

The crystal structure of $K^+Re_2O_4F_7^-$ consists of layers of $K^+Re_2O_4F_7^-$ stacked along the *c*-axis. The shortest interatomic distance between the layers is between O(2) and O(1) (2.998 Å) and is at the limit of the sum of the van der Waals radii. The $Re_2O_4F_7^-$ anions are connected to each other within the *ab*-plane through contacts with K^+ cations (Figure 4.6a). There are also several weak contacts between the $Re_2O_4F_7^-$ anions within the same layer (F(2)···F(5), 2.904 Å and O(2)···F(4), 3.023 Å). The crystal structure is similar to that of $K^+Re_2O_4F_7^-\cdot 2ReO_2F_3$ which consists of layers of $K^+Re_2O_4F_7^-$ and $(ReO_2F_3)_\infty$ which alternate along the *a*-axis (Figure 4.6b). The shortest interatomic distance between the two layers is between O(1) and F(7) (2.897 Å) and is also at the limit of the sum of the fluorine and oxygen van der Waals radii (2.82 Å).[139] Consequently, each component of the structure is considered distinct and will be discussed separately. In this structure, the $Re_2O_4F_7^-$ anions are connected to each other within the *bc*-plane through contacts with K^+ cations. Weak contacts between the $Re_2O_4F_7^-$ anions also occur within the same plane

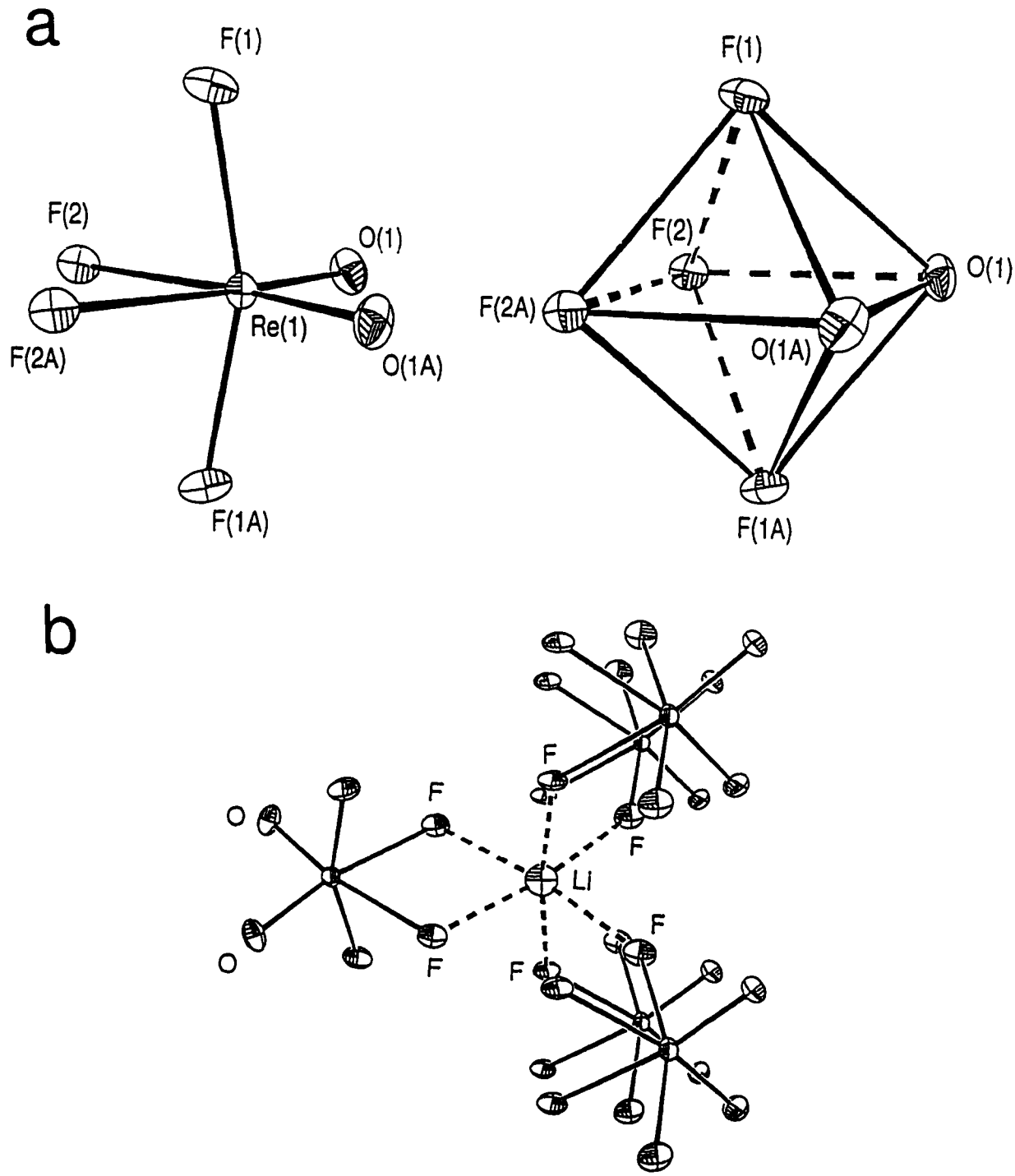

Figure 4.5. Structure of $Li^{+}ReO_2F_4^{-}$ showing thermal ellipsoids at the 50% probability level. (a) Geometry of the $ReO_2F_4^{-}$ anion and octahedron formed by the light atoms around rhenium in $ReO_2F_4^{-}$, (b) arrangement of the fluorine atoms around the Li^{+} cation.

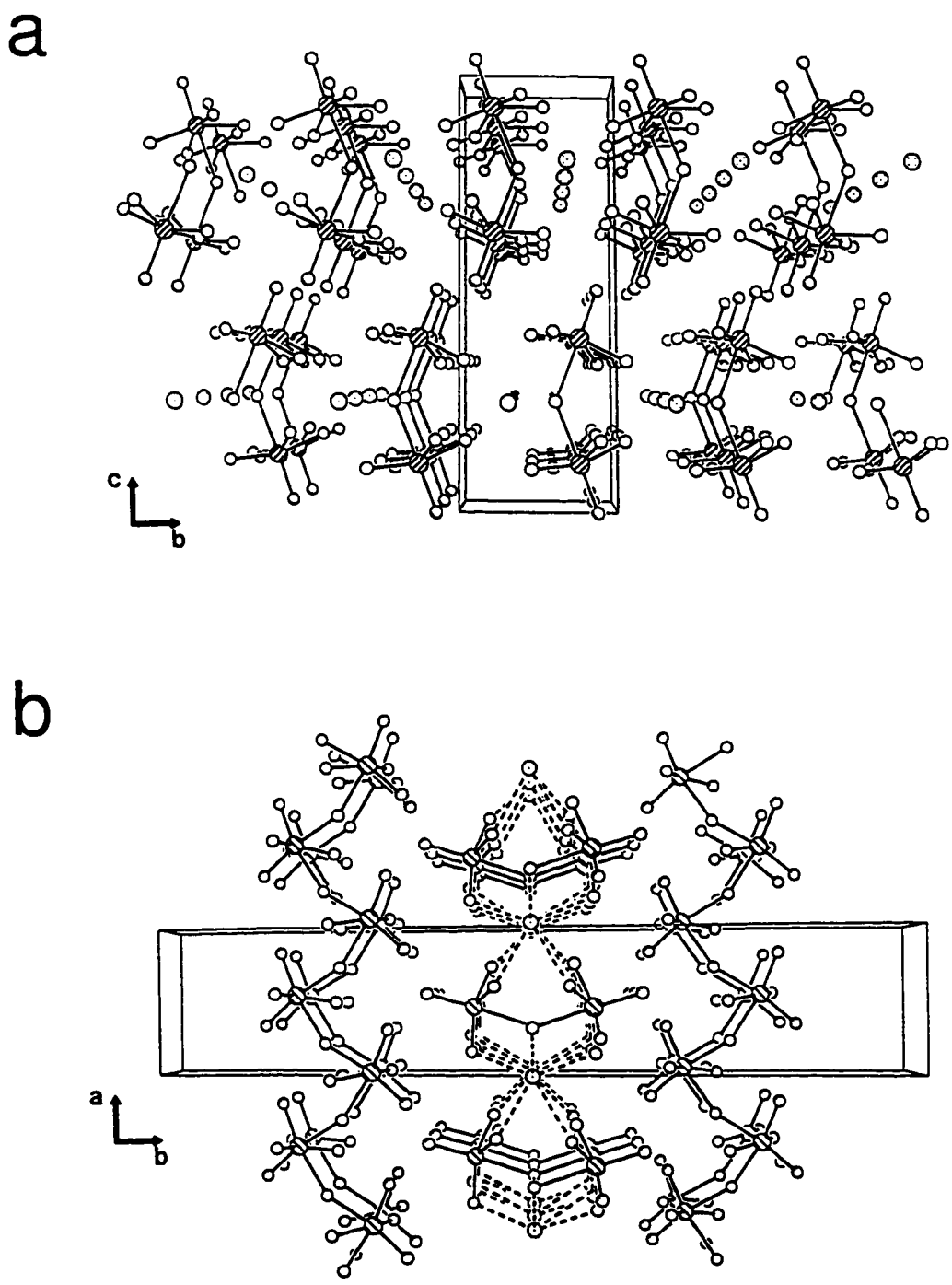

Figure 4.6. Views of (a) the $K^+Re_2O_4F_7^-$ unit cell showing the packing along the *a*-axis and (b) the $K^+Re_2O_4F_7^-\cdot 2ReO_2F_3$ unit cell showing the packing along the *c*-axis.

(O(2)···F(4), 2.910 Å and O(2)···F(3), 3.008 Å). The geometrical parameters for $K^+Re_2O_4F_7^-$ are identical in both structures and that the Re-O and Re-F bond length distortions are reproducible, confirming that they are related to cation-anion interactions or packing effects and do not result from positional disorder between F and O (see Chapter 2).

The roughly L-shaped $Re_3O_6F_{10}^-$ anions are stacked in eclipsed arrays along the *a*-axis (Figure 4.7a) and the shortest secondary contacts occur between O(1)···O(4), 2.768 Å and O(3)···F(3), 2.873 Å.

(b) Anion and Molecular Geometries and Secondary Contacts. The alkali metal cations (M^+) form long M···F contacts[140] with the anions in the crystal structures of $Li^+ReO_2F_4^-$, $K^+Re_2O_4F_7^-$, $K^+Re_2O_4F_7^-\cdot 2ReO_2F_3$ and $Cs^+Re_3O_6F_{10}^-$. The lithium cation in $Li^+ReO_2F_4^-$ has six short Li···F contacts with the fluorine atoms forming a slightly distorted octahedron. The coordination sphere of Li^+ is derived from five anions corresponding to four $F_{c,t}$ atoms at 2.04(3)-2.108(7) Å belonging to three independent $ReO_2F_4^-$ anions and to two $F_{c,c}$ atoms at 2.05(3) Å belonging to two independent $ReO_2F_4^-$ anions. Although the total bond valence around Li^+ arising from these fluorine contacts is significantly less than 1.00 (0.90 v.u.), the shortest Li···O distance (3.44(3) Å) and the next shortest Li···F distance (3.45(3) Å) are too long to be considered as contacts (the corresponding bond valences are less than 0.01).

The potassium cation in $K^+Re_2O_4F_7^-$ forms eight long contacts with two anions; six contacts with terminal fluorine atoms (2.711(8), 2.728(9) and 2.820(8) Å) and two

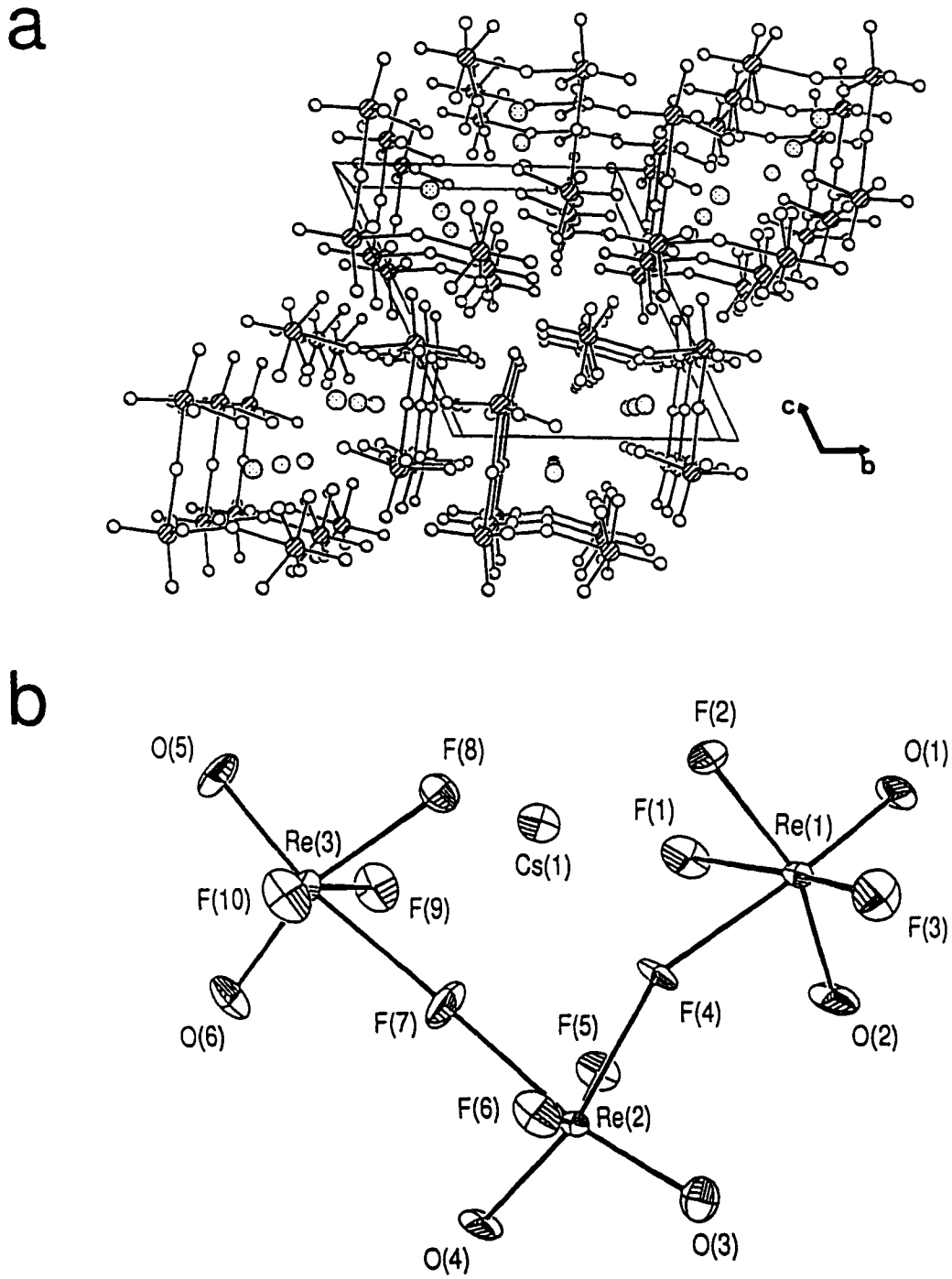

Figure 4.7. Views of (a) the $Cs^{+}Re_3O_6F_{10}^{-}$ unit cell showing the packing along the *a*-axis and (b) the $Re_3O_6F_{10}^{-}$ anion (the thermal ellipsoids are at the 50% probability level).

contacts with oxygen atoms *cis* to the fluorine bridge (2.922(9) Å). The total bond valence is 1.01 v.u. for the potassium cation. The bond valence values for the light atoms are reasonable except for F(3) (1.15 v.u.), which is slightly overbonded, and O(2) (1.55 v.u.), which is underbonded. There are two longer contacts with the bridging fluorine (3.168(7) Å).

The cesium ion in $Cs^+Re_3O_6F_{10}^-$ forms six short Cs···F contacts with the terminal fluorine atoms of three anions (3.013(7) - 3.122(7) Å) providing a total bond valence of 0.94 v.u. for Cs(1). The next longest contacts are also with terminal fluorine atoms, namely, F(2), 3.194(7) and F(2A), 3.145(8) Å and with one of the bridging fluorine atoms, F(4), 3.190(7) Å. The F(7)-Cs(1) distance (3.746(10) Å) shows that there is no contact between the second bridging fluorine atom and the cation (0.022 v.u.).

The central Re atoms in all four compounds are coordinated to two oxygen atoms and four fluorine atoms in which the oxygen atoms are *cis* to one another providing a distorted octahedral environment around the Re atom that is similar to the coordination in other *cis*-dioxo species, namely, isoelectronic $WO_2F_4^{2-}$ [141] and OsO_2F_4,[92] the [*cis*-OsO_2F_3]-units in the $Os_2O_4F_7^+$ [63] cation, the $TcO_2F_4^-$, $MoO_2F_4^{2-}$,[99] $VO_2F_4^{3-}$ [101] and $ReO_2(OTeF_5)_4^-$ [128] anions, the [*cis*-MO_2F_4]-units of the infinite chain species TcO_2F_3 [41], $MoO_2F_3^-$,[94] $VO_2F_3^-$ [101] and MoO_2F_2(bpy)[142] and WO_2F_2(bpy).[143] The preference for the *cis*-dioxo bonded structure has been discussed in Chapter 3.

The $Re_2O_4F_7^-$ anion consists of two symmetry-related, fluorine-bridged [ReO_2F_4]-units (Figure 4.8a), while the structure of the $Re_3O_6F_{10}^-$ anion is an open chain with the central bridging *cis*-ReO_2F_4-unit linked to the Re atom of two terminal ReO_2F_3 groups by

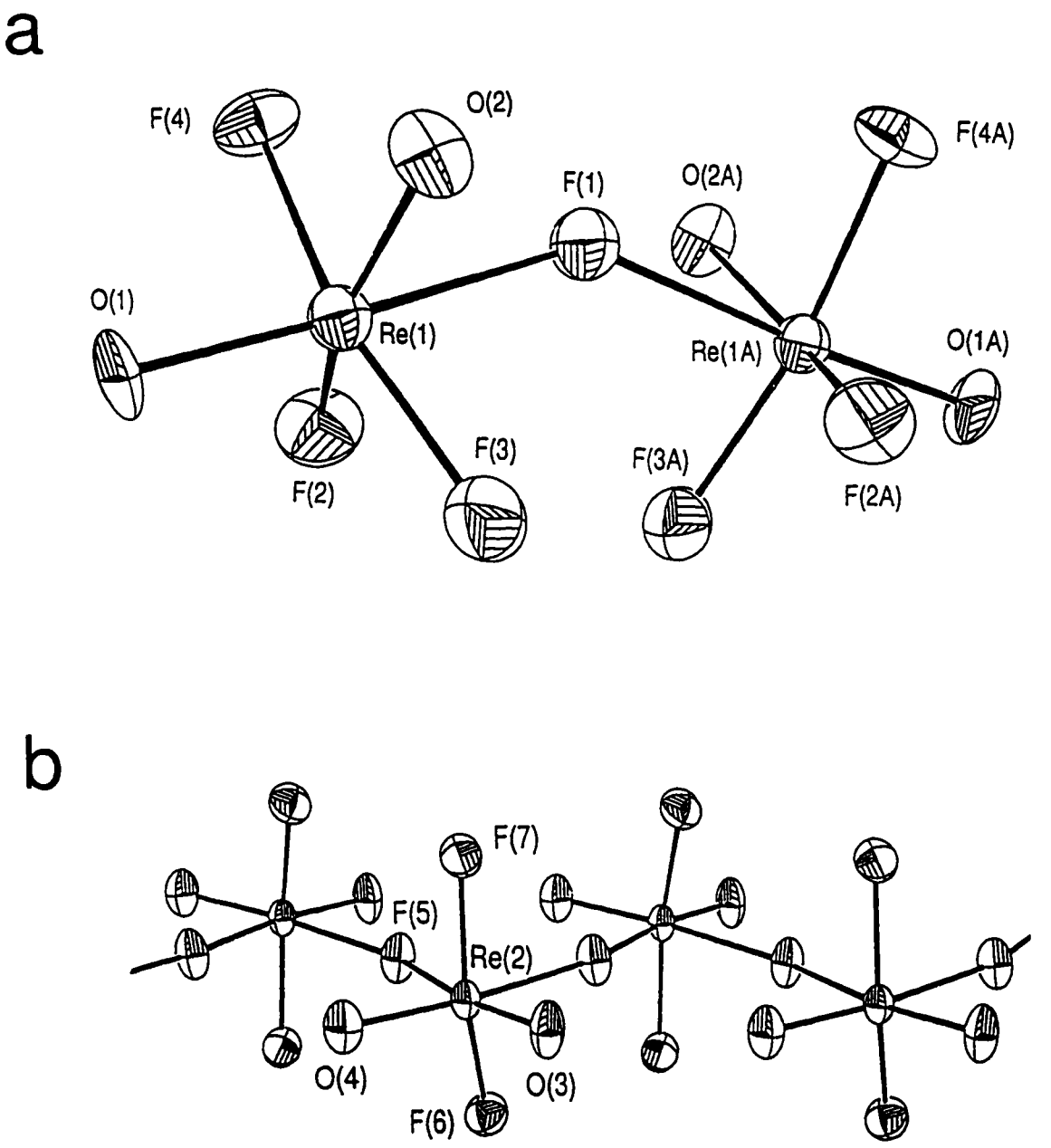

Figure 4.8. Geometries of (a) the $Re_2O_4F_7^-$ anion and (b) the $(ReO_2F_3)_\infty$ infinite chain in $K^+Re_2O_4F_7^-\cdot 2ReO_2F_3$. Thermal ellipsoids are at the 50% probability level.

bridging fluorine atoms that are *cis* to one another (Figure 4.7b). The structure of ReO_2F_3 consists of an infinite chain of *cis*-fluorine bridged $[ReO_2F_4]$-units running parallel to the *b*-axis (Figure 4.8b).

The bond lengths of all three anions can be classified into five groups: Re-O_t bonds, *trans* to Re-F_b bridging bonds; Re-O_c bonds, *cis* to Re-O_t bonds and *trans* to terminal fluorines, $F_{c,t}$; Re-$F_{c,c}$ bonds, *cis* to Re-O_t and Re-O_c bonds and *trans* to one another; terminal Re-$F_{c,t}$ bonds, *cis* to Re-O_t bonds and *trans* to Re-O_c bonds; and bridging Re-F_b bonds, *trans* to Re-O_t bonds.

The Re-O bond lengths are comparable to those in other pseudooctahedral Re(VII) compounds, i.e., $ReOF_5$ (1.64(4) Å),[17] $ReO(OTeF_5)_5$ (1.68(1) Å),[144] Re_2O_7 (1.65(3)-1.73(3) Å),[145] $ReO_2(OTeF_5)_4$ (1.664(9) Å),[128] $ReO_3Cl_3^{2-}$ (1.704(17) Å)[49] and to that of the pentagonal bipyramidal $ReOF_6^-$ anion (1.629(14)-1.671(7) Å);[54] and are longer than the Re(VII)-O bonds in the $Re_2O_2F_9^+$ cation (1.63(2) Å)[46] and the Re(VI)-O double bond in $ReO(OTeF_5)_4{\cdot}F_2Te(OTeF_5)_2$ (1.63(7) Å).[144] In $Re_2O_4F_7^-$, the Re-O_c bond length (1.767(8) Å) is found to be considerably longer than the Re-O_t bond length (1.670(8) Å). This trend has also been observed in and discussed for the isoelectronic $Os_2O_4F_7^+$ cation (Os-O_c (1.750 Å) > Os-O_t (1.676 Å)).[63] The difference is presumably enhanced in the present structure by significant interaction with K^+ at 2.922(9) Å and long contacts with F atoms of neighbouring anions with the O_c atom, whereas no such interactions exist for the O_t atom. This trend is clearly observed in $Re_3O_6F_{10}^-$ for the two Re-O_t and Re-O_c bond lengths associated with the terminal rhenium atoms (Table 4.11), whereas the two central Re-O_t bond lengths are equal within experimental error.

The Re-$F_{c,c}$ and Re-$F_{c,t}$ bond distances of all three anions and of polymeric ReO_2F_3 are generally in good agreement with the terminal Re-F bond distances in ReO_3F (1.859(8) Å),[9] $ReOF_6^-$ (ax: 1.894(11) - 1.927(10) and eq: 1.862(2) - 1.917(7) Å),[54] $ReOF_5$ (1.810(7) Å),[17] ReO_2F_3 (calculated, ax: 1.876 and eq: 1.894 Å),[63] $(ReOF_4{\cdot}SbF_5)_2$ (1.841(15) Å)[146] and in $ReOF_4$ (1.86(4) Å);[25] except in $ReO_2F_4^-$ where the Re-$F_{c,t}$ bond distance is in better agreement with the Re-F_b bond distances in $ReOF_4$ (2.14(4) Å, range: 1.99(4) - 2.28(4) Å),[25] and in $Re_2O_2F_9^+$ (2.060(4) Å).[46] In both $ReO_2F_4^-$ and $Re_3O_6F_{10}^-$, the Re-$F_{c,t}$ bonds *trans* to the oxygen atoms are significantly longer than the Re-$F_{c,c}$ bonds *trans* to fluorine atoms, a feature in common with OsO_2F_4,[92] $TcO_2F_4^-$, the $[OsO_3F_3]$-, $[TcO_2F_4]$- and $[MoOF_5]$-units of the infinite chain polymers OsO_3F_2,[147] TcO_2F_3 [41] and $MoOF_4$,[129] the $[TcOF_5]$-unit of trimeric $TcOF_4$ [37] and the [*cis*-OsO_2F_4]-unit of $Os_2O_4F_7^+$.[63] The difference has been attributed to the *trans* influence of the M-O double bonds of the d^0 metal, for which there are significant $p_\pi \rightarrow d_\pi$ interactions. As a consequence, the M-$F_{c,t}$ bond lengths resemble those of M-F_b bonds.

The Re-F_b bond distance in $Re_2O_4F_7^-$ (2.150(3) Å) is comparable to those in $Cs^+Re_3O_6F_{10}^-$ (2.213(9) - 2.148(8) Å) and the bridging angle of 143.3(6)° is very similar to that in $H_3O^+W_2O_2F_9^-$ [131] (144(2)°) and approaches the ideal value for hexagonal close packing of the light atoms (132°).[130]

The Re-F_b bond distances in $Re_3O_6F_{10}^-$ are asymmetric with average Re-F_b bond distances around the central rhenium Re(2) (2.061(8) - 2.042(6) Å) comparable to those observed in the $ReO_2F_4^-$ anion (2.001(6) Å) and in $(ReOF_4{\cdot}SbF_5)_2$ (2.079(15) Å; Re-F_b *trans* to a terminal fluorine),[146] but shorter than those around the terminal rhenium atoms,

Re(1) and Re(3) (2.213(9) - 2.148(8) Å). The Re-F_b bond lengths associated with the terminal rhenium atoms are similar to the Re-F_b bond (2.231(15) Å) in $(ReOF_4 \cdot SbF_5)_2$ [146] which is *trans* to the Re-O bond. The asymmetry among the Re-F_b bond lengths is reflected in their bond valence values (Table 4.11). As the number of terminal fluorine atoms varies from two for the central rhenium atom to three for the terminal rhenium atoms, the rhenium bond valence sum must remain constant at or near 7 v.u. so that the bridge must elongate to partially compensate for the bond valence contribution of the additional terminal fluorine on each terminal rhenium atom. The difference between the two bridging bond lengths, Re(1)-F(4) and Re(3)-F(7), is attributed to the long F(4)···Cs(1) contact which serves to elongate the Re(1)-F(4) bond.

The terminal Re-$F_{c,c}$ bond distances in $(ReO_2F_3)_\infty$ (average: 1.844(7) Å) are slightly shorter than in $Li^+ReO_2F_4^-$ and the Re-F_b (average: 2.102(6) Å) is longer than Re-$F_{c,c}$, as expected for a bridging fluorine. The bridging angle between each ReO_2F_4-unit is 156.0(4)° and is slightly larger than that observed in TcO_2F_3 (148.8(3)°).[41]

The bond valence sum for each rhenium atom is very close to 7.00 v.u. in all four structures, indicating that all significant contacts to the rhenium atoms have been accounted for. The bond valence values of the Re-O and Re-F in $(ReO_2F_3)_\infty$ are very close to the ideal values of 1.00 for the terminal fluorines, 2.00 for the oxygens and 0.50 for the bridging fluorine atom. The differences observed among the anions result from long contacts between selected F or O atoms and the alkali metals which contribute to the bond valence sum to the extent required to fulfil the valence requirements of each Re atom. This is supported by the two Re-F_b-Re bond angles in $Re_3O_6F_{10}^-$, Re(1)-F(4)-Re(2)

and Re(2)-F(7)-Re(3), which differ by almost 40°. The Re(2)-F(7)-Re(3) angle is essentially linear (178.7(6)°), close to the ideal angle for cubic close packing (180°),[130] and the corresponding long contact to F(7) is Cs(1) - F(7), 3.749(11) Å, whereas the Re(1)-F(4)-Re(2) angle is 140.5(4)°, approaching the ideal value for hexagonal close packing (132°).[130] The Cs(1)-F(4) contact is shorter, 3.189(7) Å and, in this case, the distortion permits a contact between Cs(1) and F(4) which allows the ideal bond valence for F(4) to be achieved.

Although there is considerable variation in the bond lengths around the rhenium atom, the octahedra formed by the light atoms are relatively undistorted, as shown by the average interligand atom distances which are all within the range 2.47(1) - 2.72(1) Å. The average values of the angles in $Re_2O_4F_7^-$, $Re_3O_6F_{10}^-$ and $(ReO_2F_3)_\infty$ are very similar to those found in $ReO_2F_4^-$. The asymmetry of the distortion is also reflected in the angles the light atoms subtend with the rhenium atom(s) and has been rationalized in terms of the VSEPR model of molecular geometry[111] in the infinite chain polymer TcO_2F_3 [41] and the structurally related $Os_2O_4F_7^+$ cation[63] and $TcO_2F_4^-$ anion. The greater spatial requirements of the oxygen double bond domains and their repulsive interactions with single bond domains at approximately right angles to them in the $[O,F_{c,c},F_{c,c},F_{c,t}]$- or $[O,F_{c,c},F_{c,c},F_b]$-planes causes a bending of the $F_{c,c}$-Re-$F_{c,c}$ angle away from the oxygen atoms and toward the terminal and/or bridging fluorine atoms [$ReO_2F_4^-$, 162.9(6)°; $Re_2O_4F_7^-$, 159.9(5)°; $Re_3O_6F_{10}^-$, av. 158.0(5)° and $(ReO_2F_3)_\infty$, 153.2(3)°]. These weaker bond-pair repulsions are also reflected in the angles subtended at the rhenium atoms by the *trans* (terminal and/or bridging) fluorine atoms, namely, $F_{c,t}$-Re-$F_{c,t}$, $F_{c,t}$-Re-F_b and F_b-Re-F_b which are

significantly smaller than 90° [$ReO_2F_4^-$, 76.3(4)°; $Re_2O_4F_7^-$, 78.2(4)°; $Re_3O_6F_{10}^-$, av. 76.6(4)° and $(ReO_2F_3)_\infty$, 79.8(1)°] and by the oxygen atoms, namely, O_c-Re-O_t, O_c-Re-O_c and O_t-Re-O_t, which are significantly larger than 90° [$ReO_2F_4^-$, 100.2(7)°; $Re_2O_4F_7^-$, 100.5(4)°; $Re_3O_6F_{10}^-$, av. 103.4(5)° and $(ReO_2F_3)_\infty$, 102.3(4)°]. These angles are also similar to their counterparts in $ReO_2(OTeF_5)_4^-$ [77.1(3) and 163.2(8)°].[128] It is noteworthy that the angles $F_{c,t}$-Re-$F_{c,t}$ ($ReO_2F_4^-$), $F_{c,t}$-Re-F_b($Re_2O_4F_7^-$ or $Re_3O_6F_{10}^-$) and F_b-Re-F_b ($Re_3O_6F_{10}^-$ or ReO_2F_3) and all O-Re-O angles increase while the $F_{c,c}$-Re-$F_{c,c}$ angles in all four species decrease as the nuclearity of the anion increases.

$ReO_3F(CH_3CN)_2\cdot CH_3CN$

In an attempt to grow crystals of $ReO_2F_3(CH_3CN)$, single crystals of the hydrolysis product, $ReO_3F(CH_3CN)_2\cdot CH_3CN$, were obtained. The coordination around the Re atom consists of a pseudooctahedral arrangement of three oxygen atoms, a fluorine atom and two nitrogen-coordinated CH_3CN molecules (Figure 4.9a). The oxygen atoms adopt a facial arrangement, which results in the coordination of the fluorine atom and each CH_3CN ligand *trans* to an oxygen atom. The *fac*-isomer is expected to be more stable than the *mer*-isomer because each filled p orbital on an oxygen competes equally for the three available empty $d_{t_{2g}}$ orbitals on the rhenium in the *fac*-isomer rendering it more stable. Other examples of octahedral oxohalide anions that have facial arrangements include $MoO_3F_3^{3-}$,[148] $ReO_3Cl_3^{2-}$ [49] and $OsO_3F_3^-$.[149]

The Re atom lies below the [O(1), O(1A), N(1), N(1A)]-plane by 0.054 Å toward F(1) as a result of the greater repulsion between the larger Re=O bond pair domains and

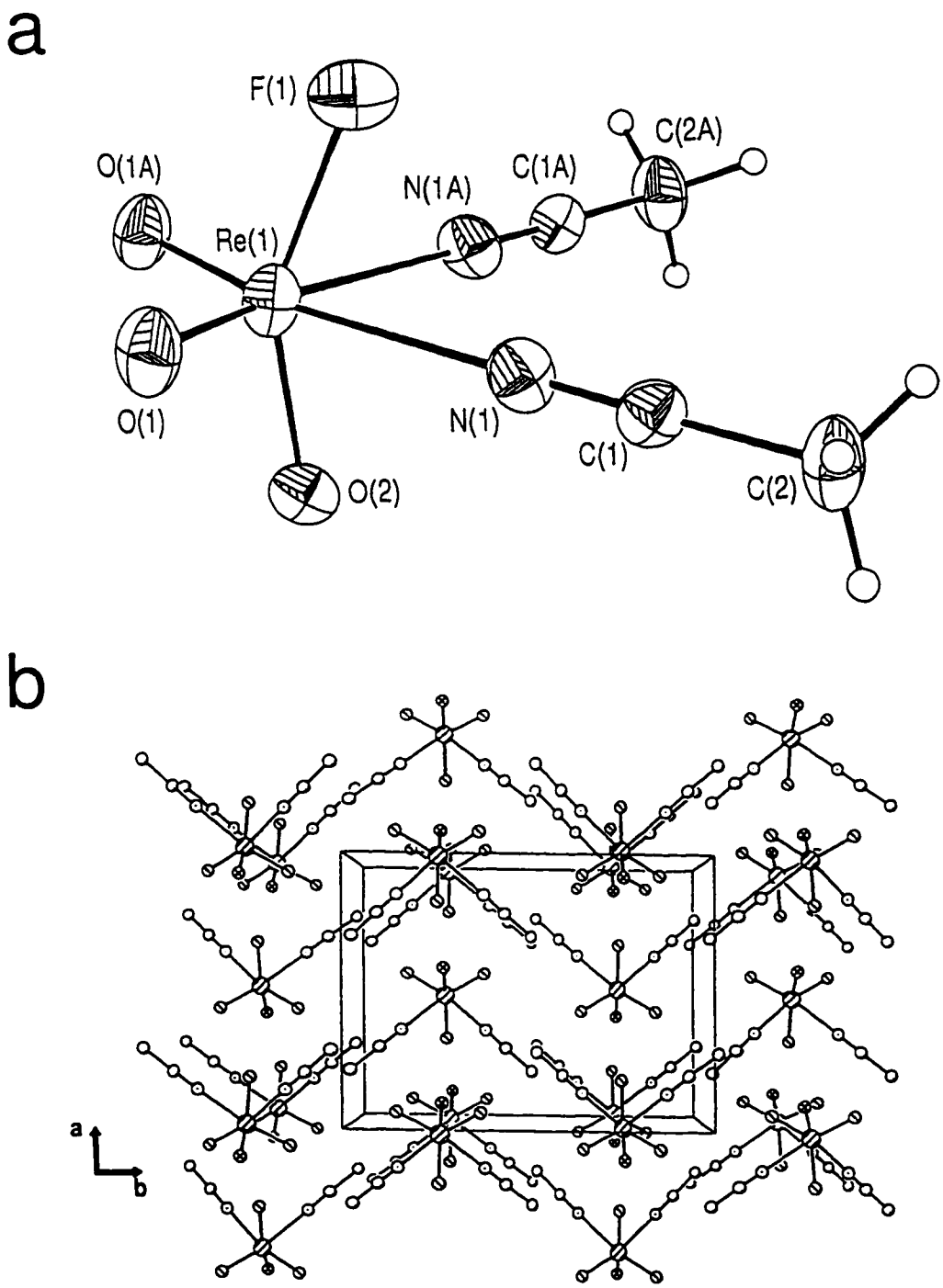

Figure 4.9. (a) Geometry of the $ReO_3F(CH_3CN)_2$ adduct (thermal ellipsoids are at the 50% probability level) and (b) the unit cell of $ReO_3F(CH_3CN)_2 \cdot CH_3CN$ showing the packing along the *c*-axis.

the bond pair domain of the neighbouring ligands. The lengths of the Re-O bonds *trans* to the CH_3CN ligands (1.704(3) Å) are comparable to other Re(VII)-O bonds. The Re-O_t bond *trans* to the F atom is significantly longer (1.801(6) Å) than the Re-O_c bond and is even longer than the Re-O_c bond in $K^+Re_2O_4F_7^-$. The Re-F(1) bond length (1.883(5) Å) is also affected by the *trans* influence of the oxo ligand, and is intermediate between the Re-$F_{c,c}$ and Re-$F_{c,t}$ bond lengths observed in the related oxo-compounds (*vide supra*). The Re-N bond length and the geometric parameters for CH_3CN are similar to those of other d^0 transition metal complexes with CH_3CN (e.g., $ReO_2(CH_3CN)_3^+ReO_4^-$,[150] Re-N, 2.267(2)-2.289(3) Å and $(\eta^2\text{-}CH_3CO_2)ReO_3(CH_3CN)$, Re-N, 2.331(5) Å; N-C, 1.111(8) Å and C-C, 1.452(9) Å). The O-Re-O angle (104.8(3)°) is significantly larger than 90° while the N-Re-N (77.9(2)°) angle is smaller, and is presumably the result of the larger oxygen bond-pair domains.

When viewed along the *b*-axis, the extended structure of $ReO_3F(CH_3CN)_2$ shows that within an *ab*-plane each molecule is rotated 90° with respect to its nearest neighbour, and each molecule is rotated 180° relative to its nearest neighbour in an adjacent plane (Figure 4.9b). This arrangement results in large channels that run in the *b*-direction and which contain disordered CH_3CN solvent molecules.

Raman Spectroscopy

With the exception of $Cs^+Re_3O_6F_{10}^-$ and $(ReO_2F_3)_\infty$, the assignments of the observed Raman vibrational frequencies were aided by LDFT and NLDFT calculations and are summarized in Tables 4.13 to 4.15 along with their theoretical values. The experimental

Table 4.13. Experimental and Calculated Raman Frequencies, Assignments and Mode Descriptions for $ReO_2F_4^-$

Frequencies (cm^{-1})[a]							
exp					LDFT[b]	NLDFT[b]	Assignments
Li	Na	K [c]	Cs	$N(CH_3)_4$	DZVP2	DZVP2	C_{2v} point symmetry[d]
1011(100) 1004(4),sh 998(2),sh 984(3)	1011(100) 1005(4),sh 997(1),sh 983(9) 981(8),sh	987,s	973(100)	972(100)	945(106)	936(111)	$\nu_1(A_1)$, $\nu_s(ReO_2)$
973(20) 962(2)	973(25) 964(>0)	951,m	949(16),sh 939(16)	947(20) 939(19)	920(203)	917(200)	$\nu_9(B_1)$, $\nu_{as}(ReO_2)$
661(10)	664(8)	649,m	649(5),sh	636(8)	630(81)	584(93)	$\nu_2(A_1)$, $\nu_s(ReF_{2c,c} + ReF_{2c,t})$
640(1)	648(1)	606,vvw	634(8)	605(1),sh	619(246)	552(221)	$\nu_{13}(B_2)$, $\nu_{as}(ReF_{2c,c})$
523(1)	525(1)	525,s	535(1),br	538(1)	565(75)	506(43)	$\nu_3(A_1)$, $\nu_s(ReF_{2c,c} - ReF_{2c,t})$
		489,s	503(>0),br	502(1)	546(88)	502(80)	$\nu_{10}(B_1)$, $\nu_{as}(ReF_{2c,t})$
406(7) 400(4),sh	407(7) 392(1),sh	410,m	405(8),sh 398(11) 381(3)	419(2),sh 402(8)	363(8)	361(2)	$\nu_4(A_1)$, $\delta(ReO_2)$
344(3),sh 332(41)	340(2),sh 326(12)	325,s	326(28)	344(4),sh 318(16)	264(13)	310(18)	$\nu_5(A_1)$, $\delta(ReF_{2c,c} + ReF_{2c,t}$

Table 4.13. continued

320(6)			318(13)	309(9),sh	273(31)	287(31)	$\nu_{11}(B_1)$, $\delta(OReF_{c,t} + ReF_{2c,c})$
	280(1)	278,m	292(1),sh	293(2),sh	333(34)	334(14)	$\nu_{14}(B_2)$, $\rho_r(ReF_{2c,c} + ReO_2)$
253(1)	258(1)		229(1),br	223(>0)	324(0)	321(0)	$\nu_7(A_2)$, $\rho_t(ReF_{2c,t} + ReO_2)$
245(2)			203(1),br	192(1)	287(29)	242(58)	$\nu_{15}(B_2)$, $\rho_t(ReF_{2c,t})$
177(23)	184(2),sh 173(5)	180,m	157(4),br	164(2)	183(0)	220(12)	$\nu_6(A_1)$, $\delta(ReF_{2c,c} - ReF_{2c,t})$
115(1)	97(2)	115,vvw		145(5)	165(0)	83(0)	$\nu_{12}(B_1)$, $\delta(ReOF_{c,t} - ReF_{2c,c})$
110(2)							
83(2)	79(3)			75(>0),sh	167(0)	109(0)	$\nu_8(A_2)$, $\rho_t(ReF_{2c,t}$-$ReO_2)$
76(1)				47(2)			lattice vibration

[a] Spectra recorded on microcrystalline solid in a rotating Pyrex glass capillary at 23 °C using 514.5-nm excitation. Values in parentheses denote relative intensities; sh: shoulder; br: broad; s: strong; m: medium; w: weak; vvw: very very weak. Values given in parentheses are Raman intensities. Other weak peaks were observed for $Li^+ReO_2F_4^-$ at 947(1), 937(1) and 917(1) cm^{-1}, $Na^+ReO_2F_4^-$ at 945(8), 937(7) and 914(>0) cm^{-1}, $Cs^+ReO_2F_4^-$ at 766(>0), 884(2), 902(2) and 1010(>0) cm^{-1}, $N(CH_3)_4^+ReO_2F_4^-$ at 837(1) and 779(2) cm^{-1} and at 374(4); 459(8); 742(8),sh; 752(13) cm^{-1} which are cation modes.

[b] Infrared intensities, in km mol^{-1}, are given in parentheses.

[c] Values reported are Raman frequencies from ref. 94.

[d] ν: stretching; δ: in-plane bending; ρ_r: rocking; ρ_t: twisting.

Table 4.14. Experimental Raman Frequencies, Assignments and Mode Descriptions for $K^+Re_2O_4F_7^-$ and Calculated Frequencies for $Re_2O_4F_7^-$

Frequency, cm^{-1}			Assignment
exp[a,b]	exp[a,c]	calc[d]	C_2 point symmetry[e]
1028(4) 1018(100)	985(xx)	983(10) 977(218)	A, $\nu_s[(ReO_t + ReO_c) + (Re'O_t + Re'O_c)]$ B, $\nu_s[(ReO_t + ReO_c) - (Re'O_t + Re'O_c)]$
991(3),sh 982(12)	965(24)	948(178)	A, $\nu_{as}[(ReO_t - ReO_c) + (Re'O_t - Re'O_c)]$
961(35) 949(3)	961(16),sh	944(157)	B, $\nu_{as}[(ReO_t - ReO_c) - (Re'O_t - Re'O_c)]$
677(3),sh 658(9)	663(8) 654(4),sh	662 (77) 659 (115)	B, $\nu_s[(ReF_{2c,c} + ReF_{c,t}) - (Re'F_{2c,c} + Re'F_{c,t})]$ A, $\nu_s[(ReF_{2c,c} + ReF_{c,t}) + (Re'F_{2c,c} + Re'F_{c,t})]$
658(9) 639(3),sh	 638(1),br	655 (321) 644 (19)	B, $\nu_{as}[(ReF_{2c,c}) + (Re'F_{2c,c})]$ A, $\nu_{as}[(ReF_{2c,c}) - (Re'F_{2c,c})]$
		582 (79) 582 (30)	A, $\nu(ReF_{c,t} + Re'F_{c,t}) - \nu_s(ReF_{2c,c} + Re'F_{2c,c})$ B, $\nu(ReF_{c,t} - Re'F_{c,t}) - \nu_s(Re'F_{2c,c} - Re'F_{2c,c})$
556(1)	554(x),br	512 (270)	B, $\nu_{as}(ReF_bRe')$
416(2),sh 407(9),sh	405(5),sh	383 (1)	A, $\delta(ReO_2 + Re'O_2)$
402(15)	400(6)	380 (13)	B, $\delta(ReO_2 - Re'O_2)$
352(32)	351(13)	354 (5) 352 (5)	A, $\delta[(O_cReF_{c,c} + F_{c,c}ReF_{c,t}) + (O_cRe'F_{c,c} + F_{c,c}Re'F_{c,t})]$ B, $\delta[(O_cReF_{c,c} + F_{c,c}ReF_{c,t}) - (O_cRe'F_{c,c} + F_{c,c}Re'F_{c,t})]$
333(7) 327(7)	 326(9)	335 (2) 331 (0) 323 (17)	B, $\delta(F_{c,c}ReF_b - F_{c,c}Re'F_b + ReF_bRe')$ A, $\delta(F_{c,c}ReF_b + F_{c,c}Re'F_b + ReF_bRe')$ A, $\delta(F_bReO_t + F_bRe'O_t + ReF_bRe')$
311(15)	313(9),sh	319 (58)	B, $\delta(F_bReO_t - F_bRe'O_t + ReF_bRe')$
	305(11) 298(4),sh	314 (7)	A, $O_cF_{2c,c}F_{c,t}Re$(inversion) + $O_cF_{2c,c}F_{c,t}Re'$(inversion)
285(2)	280(1)	281 (44)	B, $\delta(F_{c,c}ReF_{c,c} - F_{c,c}Re'F_{c,c} + ReF_bRe')$
269(2)	268(1) 258(1)	261 (9) 259 (77)	A, $\delta(F_{c,c}ReF_{c,t} + F_{c,c}Re'F_{c,t} + ReF_bRe')$ B, $\delta(F_{c,c}ReF_{c,t} - F_{c,c}Re'F_{c,t} + ReF_bRe')$

Table 4.14. continued

238(2),sh	237(1),br	223 (8)	B, $\delta[(F_{c,t}ReF_{c,c} + F_{c,t}Re'F_{c,c}) + (F_{c,c}ReO_c + F_{c,c}Re'O_c)]$
229(3)		222 (8)	A, $\delta[(F_{c,t}ReF_{c,c} - F_{c,t}Re'F_{c,c}) - (ReF_bRe' + F_{c,c}Re'O_t)]$
213(2)			
205(2)		196 (5)	A, $\delta_{oop}(ReOF_3 - Re'OF_3)$
192(2)	193(1)	187 (8)	B, $\delta(F_{c,t}ReO_c - F_{c,t}Re'O_c)$
154(1)		139 (0)	A, $\rho_r(ReO_2F_3)$
115(2)	123(9)	128 (0)	A, $\rho_t(ReO_2F_3)$
		123 (1)	A, $\delta(O_tReF_b + O_tRe'F_b)$
		117 (2)	B, ρ_r(Re group - Re' group)[f]
	112(9)	108 (0)	A, $\nu_s(ReF_bRe')$
75(4)		70 (0)	A, ρ_r(Re group + Re' group)[g]
55(5)			

[a] Values in parentheses denote relative Raman intensities; sh: shoulder; br: broad.

[b] Spectrum recorded on microcrystalline solid in Lindemann glass capillary at 22 °C using 514.5-nm excitation.

[c] Spectrum recorded on single crystal in a Pyrex capillary at 22 °C using 514.5-nm excitation. A broad peak was also observed at 800(>0) cm^{-1}, but was not assigned.

[d] Infrared intensities, in km mol^{-1}, are given in parentheses.

[e] The labels Re_t and Re_c refer to the terminal and central rhenium atoms, respectively, of $Re_3O_6F_{10}$.

[f] $\delta(O_tReF_b - O_tRe'F_b)$.

[g] $\delta(O_tReF_b + O_tRe'F_b)$.

Table 4.15. Experimental Raman Frequencies, Assignments and Mode Descriptions for Polymeric ReO_2F_3 and $Cs^+Re_3O_6F_{10}^-$

Frequencies (cm^{-1})			Assignments
ReO_2F_3 [a,b]	$K^+Re_2O_4F_7^-{\cdot}2ReO_2F_3$ [a,c]	$Cs^+Re_3O_6F_{10}^-$ [a,d]	C_{2v} point symmetry[e]
1025(100)	1028(65) 1021(100) 1017(38),sh	1024(100),Re_c 1016(11),Re_c	A_1, $\nu_s(ReO_2)$
		972(16),Re_t	
994(33) 990(11)	992(29)	990(9),Re_c 968(6),sh,Re_t	B_1, $\nu_{as}(ReO_2)$
713(2) 700(14)	690(6)	688(>0),Re_c 655(1),Re_t	A_1, $\nu_s(ReF_{2c,c})$
670(1),sh 664(4)	677(2),sh 663(8)	665(4),Re_c 641(>0),Re_t	B_2, $\nu_{as}(ReF_{2c,c})$
		568(>0),Re_c 553(>0),Re_t	ν_{as}(ReFRe)
432(>0) 412(17)	445(>0) 417(12)	405(3),sh,Re_c 400(6),Re_t 396(5)	A_1, $\delta(ReO_2)$
349(6)	351(13)	363(>0)	A_1, $\delta(ReF_{2c,c} + ReF_{2b})$
332(11) 326(6),sh 319(5)	326(9) 312(9),sh	336(>0),sh 321(>0),sh 313(4) 307(3) 298(>0),sh	B_1, $\delta(OReF_b + ReF_{2c,c})$
288(1)	280(1)	285(>0)	B_2, $\rho_r(ReF_{2c,c})$
276(2),sh 270(x) 251(3)		271(>0) 255(>0) 250(x) 238(1)	
223(>0)	229(1)	228(>0)	A_2, $\rho_t(ReO_2)$

Table 4.15. continued

213(>0)		218(>0),Re_c	
204(>0)		205(>0),Re_c	
		188(1),Re_t	
159(1)		153(>0)	
136(4)		138(>0)	
114(>0)	112(9)	114(>0)	ν_s(ReFRe)
101(2)		99(>0)	
87(>0)			
75(1)			
55(4)			

[a] Values in parentheses denote relative Raman intensities; sh: shoulder; br: broad.

[b] Spectrum recorded on microcrystalline solid in a Pyrex capillary at 22 °C using 514.5-nm excitation. Few weak peaks were also observed at 957(>0) and 952(>0) cm^{-1} but were not assigned.

[c] Spectrum recorded on single crystal in a Pyrex capillary at 22 °C using 514.5-nm excitation. A broad peak was also observed at 800(>0) cm^{-1}, but was not assigned.

[d] Spectrum recorded on microcrystalline solid in a Pyrex capillary at 22 °C using 514.5-nm excitation. Broad peaks were also observed at 947(>0), 934(>0), 923(>0), 862(>0), 822(>0) and 793(>0) cm^{-1} but were not assigned.

[e] The labels Re_t and Re_c refer to the terminal and central rhenium atoms, respectively, of $Re_3O_9F_{10}^-$. ν: stretching; δ: in-plane bending; ρ_r: rocking; ρ_t: twisting.

and calculated vibrational frequencies for monomeric ReO_2F_3 and their assignments have been previously discussed[63] and were also used to aid in the vibrational assignments of the related anions, adducts and $(ReO_2F_3)_\infty$.

Vibrational activities of the anions in $Li^+ReO_2F_4^-$, $K^+Re_2O_4F_7^-$, $K^+Re_2O_4F_7^-\cdot 2ReO_2F_3$, $Cs^+Re_3O_6F_{10}^-$ and of $(ReO_2F_3)_\infty$ in $K^+Re_2O_4F_7^-\cdot 2ReO_2F_3$ have been determined in their respective unit cells by correlation of the gas-phase symmetries to the crystallographic anion site and unit cell symmetries.[115] The $ReO_2F_4^-$ anion (C_{2v}), when correlated with the anion site symmetry C_{2v} and the crystal symmetry D_{2d} is predicted to have all modes Raman and infrared-active with only ν_1-ν_6 split into A_1 and B_2 components in the Raman spectrum (correlation diagram identical to that of $Li^+TcO_2F_4^-$, Table 3.5). All modes are both Raman and infrared-active for $Re_2O_4F_7^-$ (C_2) but no factor-group splitting is predicted when correlated to the anion site symmetry C_2 and the unit cell symmetry C_{2h} of $K^+Re_2O_4F_7^-$ (Table 4.16). All the bands are Raman and infrared-active and are expected to be split in both the Raman (ν_1-ν_{18} split into two A components) and infrared spectra (ν_{19}-ν_{33} split into two B components) when correlated to the anion site symmetry C_2 and the unit cell symmetry C_2 of $K^+Re_2O_4F_7^-\cdot 2ReO_2F_3$ (Table 4.17). Correlation of the free molecule symmetry of $(ReO_2F_3)_\infty$ (C_{2v}) to the molecule site symmetry (C_1) and the unit cell symmetry (C_2) of $K^+Re_2O_4F_7^-\cdot 2ReO_2F_3$ reveals that all the bands are expected to be active and split in both the Raman and infrared spectra into A and B components. Correlation of the free anion symmetry of $Re_3O_6F_{10}^-$ (C_{2v}) to the anion site symmetry (C_1) and the unit cell symmetry (C_i) reveals that all of the bands are Raman and infrared-active but are not split (Table 4.18).

Table 4.16. Correlation Diagram for the Vibrational Modes of $K^+Re_2O_4F_7^-$ [a]

	ion local symmetry	site symmetry	crystal symmetry[b]		
	C_2	C_2	C_{2h}		
			A_g (Ra)	$(\nu_1 - \nu_{18})$	R,2T
4T,2R $2(\nu_1 - \nu_{18})$	A	A	B_g (Ra)	$(\nu_{19} - \nu_{33})$	2R,4T
8T,4R $2(\nu_{19} - \nu_{33})$	A	B	A_u (IR)	$(\nu_1 - \nu_{18})$	R,T(-T)
			B_u (IR)	$(\nu_{19} - \nu_{33})$	2R,2T(-2T)

[a] The symbols T and R denote translatory and rotatory (external) modes, repectively, and R and IR in parentheses denote Raman and infrared activity, respectively.
[b] Space group *P2/n*, Z = 2.

Table 4.17. Correlation Diagram for the Vibrational Modes of $K^+Re_2O_4F_7^-\cdot 2ReO_2F_3$ [a]

	$K^+Re_2O_4F_7^-$				
	ion local symmetry	site symmetry	crystal symmetry[b]		
	C_2	C_2	C_2		
4T,2R $2(\nu_1 - \nu_{18})$	A ———	A ———	A (Ra,IR)	$(\nu_1 - \nu_{18})$	2R,3T(-T)
8T,4R $2(\nu_{19} - \nu_{33})$	A ———	B ———	B (Ra,IR)	$(\nu_{19} - \nu_{33})$	4R,6T(-2T)

Table 4.17. continued

ReO_2F_3

		ion local symmetry	site symmetry	crystal symmetry[b]		
		C_{2v}	C_1	C_2		
4T	$2(\nu_1 - \nu_6)$	A_1				
2R	$2(\nu_7, \nu_8)$	A_2	A	A (Ra,IR)	$(\nu_1 - \nu_{15})$	3R,5T(-T)
4T,2R	$2(\nu_9 - \nu_{11})$	B_1		B (Ra,IR)	$(\nu_1 - \nu_{15})$	3R,4T(-2T)
4T,2R	$2(\nu_{12} - \nu_{15})$	B_2				

[a] The symbols T and R denote translatory and rotatory (external) modes, repectively, and R and IR in parentheses denote Raman and infrared activity, respectively.
[b] Space group *C2*, Z = 2.

Table 4.18. Correlation Diagram for the Vibrational Modes of $Cs^{+}Re_3O_6F_{10}^{-}$ [a]

		ion local symmetry	site symmetry	crystal symmetry[b]		
		C_{2v}	C_1	C_i		
4T	$2(\nu_1 - \nu_{17})$	A_1				
2R	$2(\nu_{18} - \nu_{26})$	A_2	A	A_g (Ra)	$(\nu_1 - \nu_{51})$	6R
2R,4T	$2(\nu_{27} - \nu_{41})$	B_1		A_u (IR)	$(\nu_1 - \nu_{51})$	9T(-3T)
2R,4T	$2(\nu_{42} - \nu_{51})$	B_2				

[a] The symbols T and R denote translatory and rotatory (external) modes, repectively, and R and IR in parentheses denote Raman and infrared activity, respectively.
[b] Space group $P\bar{1}$, Z = 2.

$M^+ReO_2F_4^-$ [M = Li, Na, Cs, $N(CH_3)_4$]. The Raman spectra of the $ReO_2F_4^-$ salts are shown in Figures 4.10 and 4.11. Assignments are given in Table 4.13 and were based on a *cis*-$ReO_2F_4^-$ anion having C_{2v} symmetry (see **X-ray Crystal Structures** and Structure I). All 15 vibrational modes having the symmetries $6A_1 + 2A_2 + 4B_1 + 3B_2$ (the [O_c, O_c, Re, $F_{c,t}$, $F_{c,t}$]-plane is taken as the $\sigma_v(xz)$-plane with the *z*-axis as the principal axis) are expected to be Raman and infrared-active. Assignments were confirmed by LDFT and NLDFT calculations on the anion and by comparison with $TcO_2F_4^-$ and OsO_2F_4 [92] for which there are also calculated frequencies.

The present assignments for the $M^+ReO_2F_4^-$ [M = Li, Na, Cs, $N(CH_3)_4$] are in agreement with those reported by Yagodin et al.[151] who only reported the six highest infrared frequencies for the Na^+, K^+, Rb^+ and Cs^+ salts. Kuhlmann and Sawodny[94] reported 14 vibrational modes from a Raman and infrared vibrational study of $K^+ReO_2F_4^-$, and their assignments for the first seven modes, ν_1-ν_4, ν_9, ν_{12}, and ν_{13}, agree with the present assignments. The low-frequency modes have been reassigned in this work and are reported in Table 4.13. Since no polarization measurements have been reported previously, the present work also reports polarization measurements for $Cs^+ReO_2F_4^-$ in HF solution.

The splittings observed for the A_1 modes, ν_1, ν_4, ν_5 and ν_6, of the Li^+ and Na^+ salts are in agreement with the factor-group analyses. The additional splitting observed for $\nu_1(A_1)$ likely result from Fermi resonance between a combination of $\nu_2(A_1)$ and $\nu_3(A_1)$ with $\nu_1(A_1)$ (Li^+: 332 + 661 = 993 cm^{-1}; Na^+: 326 + 664 = 990 cm^{-1}) giving rise to two

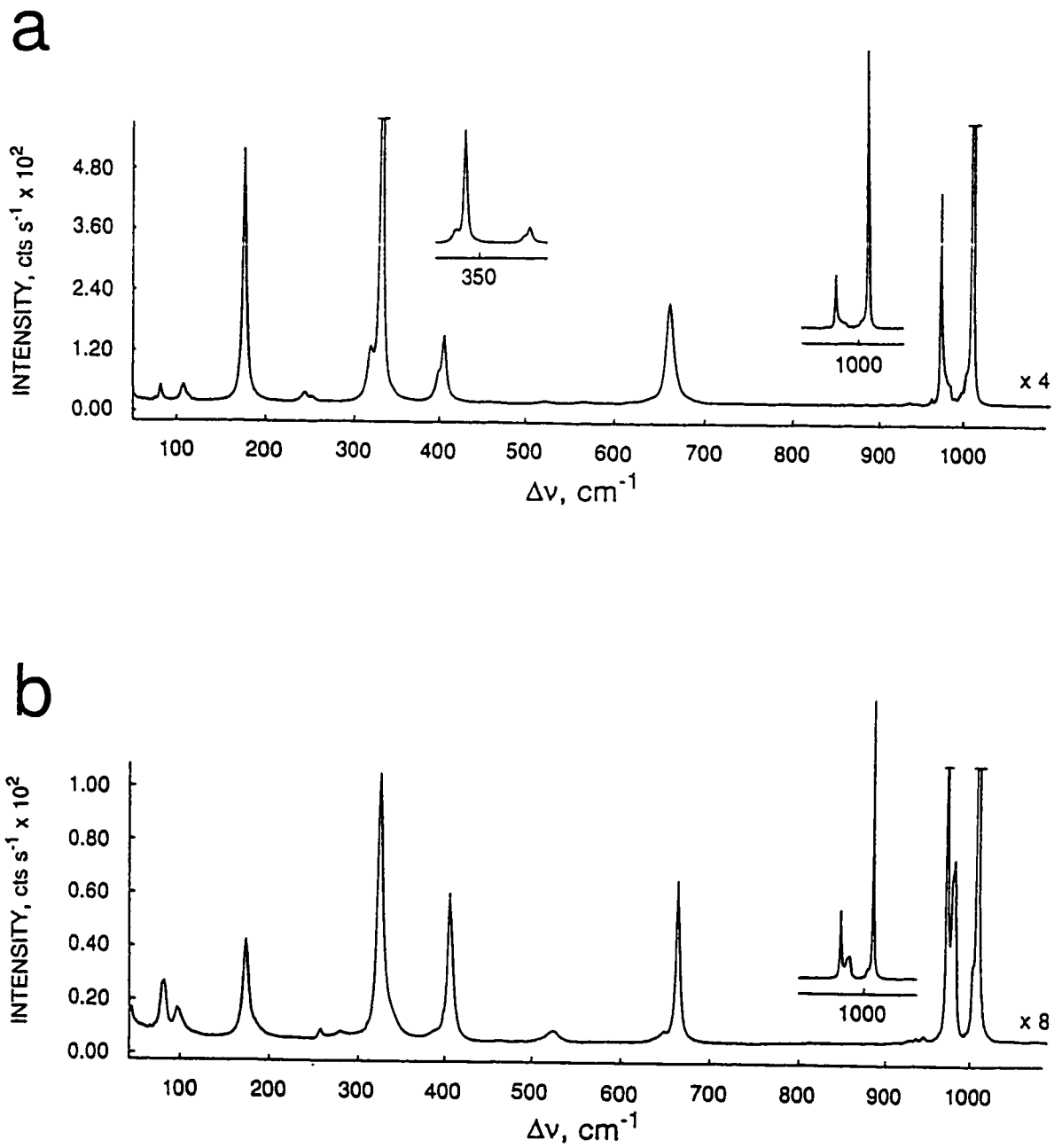

Figure 4.10. Raman spectra of microcrystalline (a) $Li^{+}ReO_2F_4^{-}$ and (b) $Na^{+}ReO_2F_4^{-}$ recorded in Pyrex capillaries at 22 °C using 514.5-nm excitation.

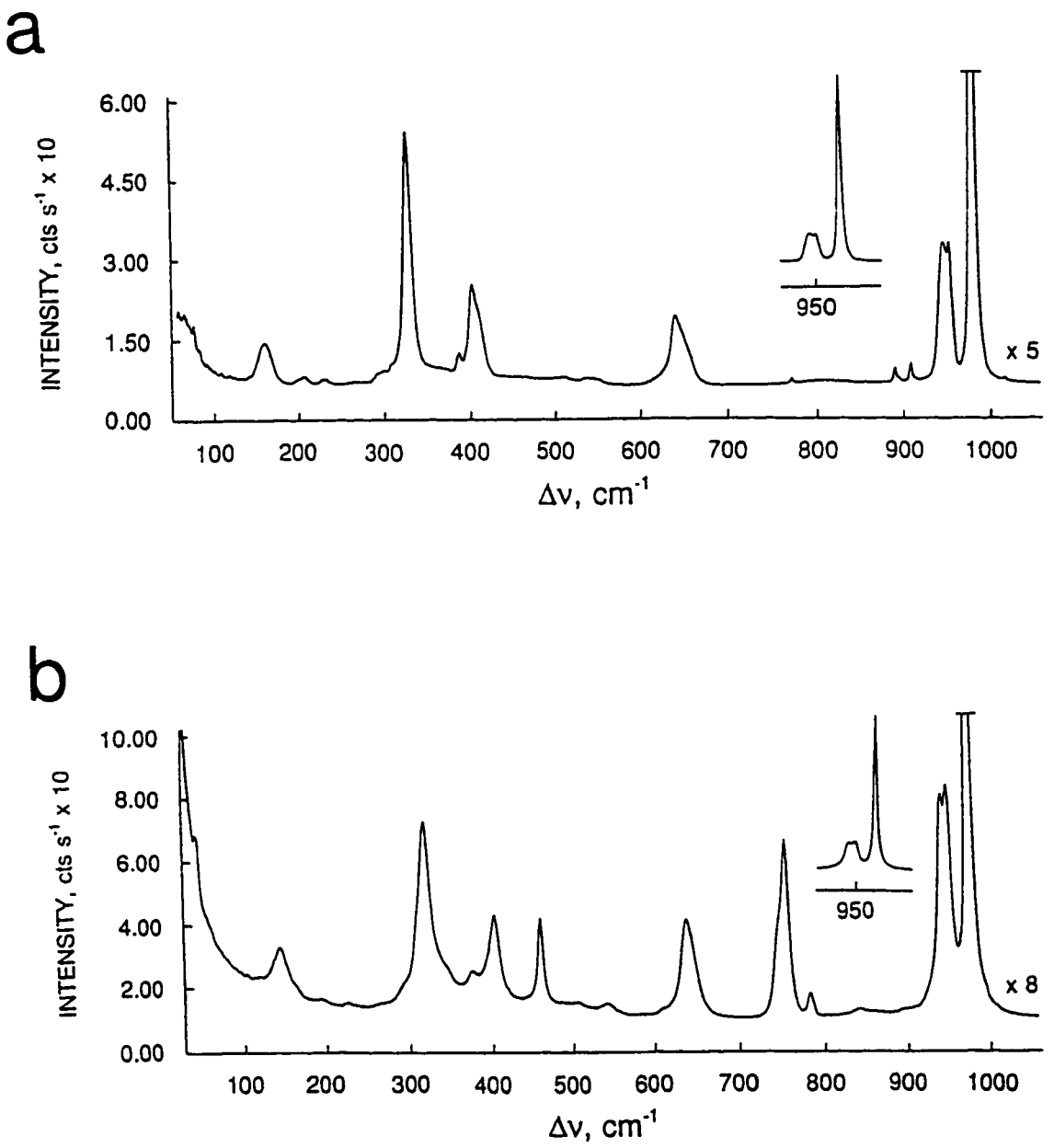

Figure 4.11. Raman spectra of microcrystalline (a) $Cs^{+}ReO_2F_4^{-}$ and (b) $N(CH_3)_4^{+}ReO_2F_4^{-}$ recorded in Pyrex capillaries at 22 °C using 514.5-nm excitation.

groups of bands centered each at 1008 (Li^+ and Na^+) and 991 (Li^+), 986 (Na^+) cm^{-1}. These lines are themselves each factor-group split into A_1 and B_2 components.

The two highest frequency bands are assigned to the Re-O stretches. The band(s) at 1004, 1011 (Li^+), 1005, 1011 (Na^+), 973 (Cs^+), 972 ($N(CH_3)_4^+$) cm^{-1} are assigned to $\nu_s(ReO_2)$ because it is the most intense band in the spectrum and is strongly polarized in the spectrum of $Cs^+ReO_2F_4^-$ in HF solution. The bands at 973, 984 (Li^+), 973, 981 (Na^+), 939, 949 (Cs^+), 939, 947 ($N(CH_3)_4^+$) cm^{-1} are depolarized in solution and are assigned to the antisymmetric ReO_2 stretching mode.

The Re-F stretching region with bands at (500-650 cm^{-1}) spans a broader frequency range than observed in ReO_2F_3 because the anion contains two types of "terminal" fluorine ligands. The two higher frequency bands [640, 661 (Li^+), 648, 664 (Na^+), 634, 649 (Cs^+), 605, 636 ($N(CH_3)_4^+$) cm^{-1}] are assigned to the $\nu_s(ReF_2)$ and $\nu_{as}(ReF_2)$ modes, respectively, for the terminal fluorines which are *cis* to the two oxygen ligands. The symmetries are assigned on the basis of their relative Raman intensities. The two remaining terminal fluorine atoms are each *trans* to oxygen ligands and their bonds to rhenium are weaker than those *trans* to fluorine because of the *trans* influence of the oxo ligands. Consequently, the bands at 523 (Li^+), 525 (Na^+), 503, 535 (Cs^+), 502, 538 ($N(CH_3)_4^+$) cm^{-1} are assigned to the symmetric and antisymmetric stretches of these more weakly bonded terminal fluorines (see **X-ray Crystal Structures**). The same frequency ordering was observed for the $TcO_2F_4^-$ anion, and as noted for this anion, it is consistent with a lower bond valence for the Re-$F_{c,t}$ bond (0.638 u.v.) than for the Re-$F_{c,c}$ bond (0.920 v.u.). The ReO_2 bending mode is assigned to the bands at 406 (Li^+), 407 (Na^+),

398 (Cs^+) and 402 ($N(CH_3)_4^+$) cm^{-1} by analogy with OsO_2F_4 [92] and $TcO_2F_4^-$. The assignments of the low-frequency bands were made by analogy with $TcO_2F_4^-$ and are supported by the theoretical values. The three most intense low-frequency bands in the $N(CH_3)_4^+$ salt are assigned to $\nu_5(A_1)$, 318; $\nu_{11}(B_1)$, 309 and $\nu_6(A_1)$, 164 cm^{-1} of the cation.[116] The remaining bands are assigned to $\nu_{14}(B_2)$, $\nu_7(A_2)$, $\nu_{15}(B_2)$, $\nu_{12}(B_1)$ and $\nu_8(A_2)$.

$K^+Re_2O_4F_7^-$. The Raman spectrum of solid $K^+Re_2O_4F_7^-\cdot 2ReO_2F_3$ is shown in Figure 4.12. The observed frequencies for $Re_2O_4F_7^-$ in $K^+Re_2O_4F_7^-$ and $K^+Re_2O_4F_7^-\cdot 2ReO_2F_3$, along with their assignments, are given in Table 4.14. Vibrational assignments of the anion were made under C_s symmetry (Structure III) for which a total of 33 vibrational modes are predicted (18A + 15B), all of which are Raman and infrared-active. Assignments of the anion modes were made by comparison with the isoelectronic $Os_2O_4F_7^+$ cation[63] and were assisted by density functional theory calculations.

Three bands are observed in the Re-O stretching region, which are assigned to symmetric (983 cm^{-1}) and antisymmetric (966, 960 cm^{-1}) combinations of ReO_2 stretches on the two ReO_2F_3-groups of the anion. These stretches appear at significantly higher frequencies than in the $K^+ReO_2F_4^-$ salt, which is consistent with a decrease in the polarity of the Re-O bonds resulting from the delocalization of the negative charge over a larger number of atoms in $Re_2O_4F_7^-$. The band at 653 cm^{-1} is assigned to a symmetric combination of the Re-$F_{2c,c}$ and $ReF_{c,t}$ bonds while the band at 639 cm^{-1} is assigned to the asymmetric of Re-$F_{2c,c}$ stretches. The broad band at 554 cm^{-1} is tentatively assigned to $\nu_{as}(ReF_bRe')$. The asymmetric bridging stretching mode in $Os_2O_4F_7^+$ [63] was assigned to a

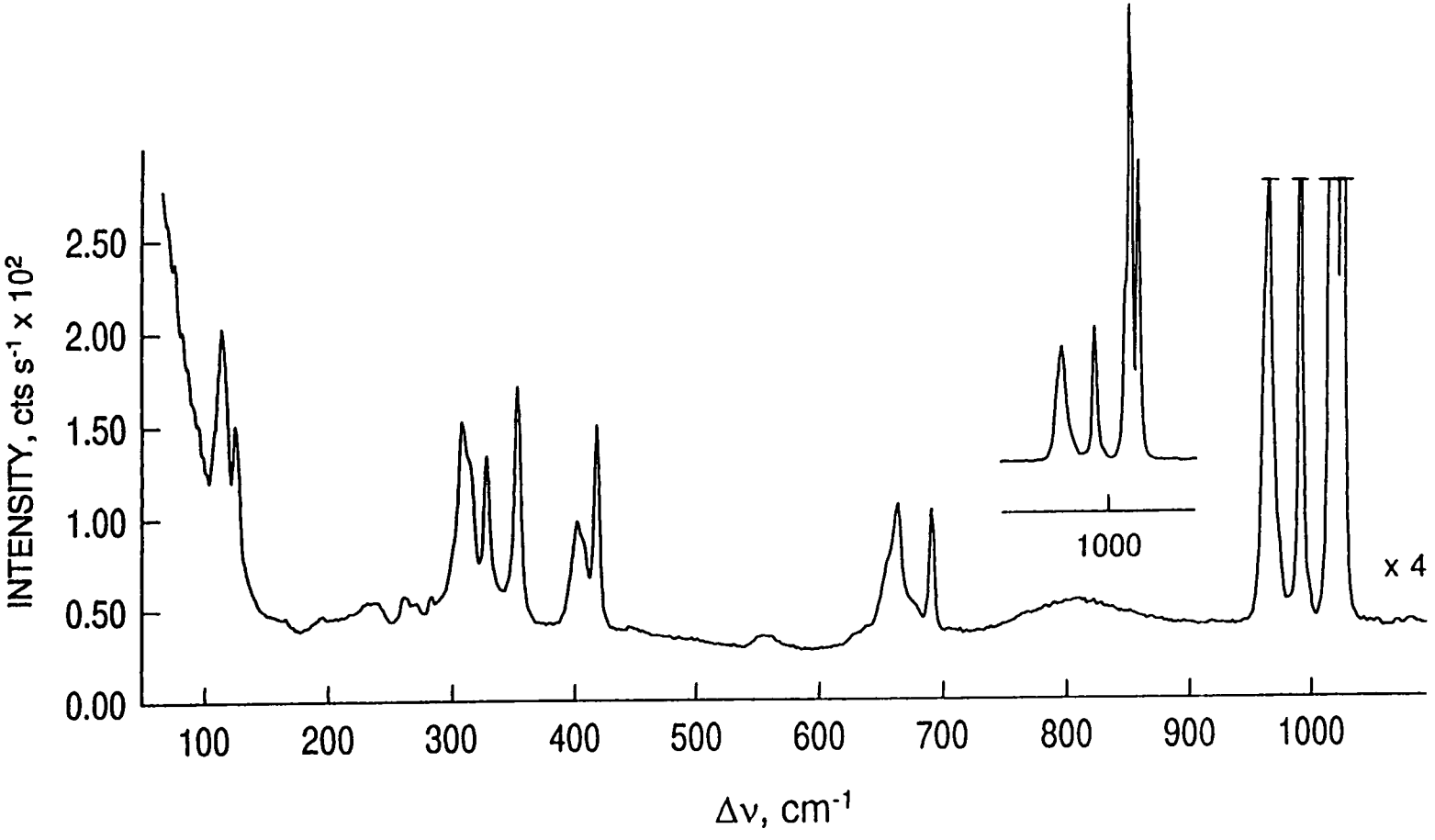

Figure 4.12. Raman spectrum of a single crystal of $K^+Re_2O_4F_7^-\cdot 2ReO_2F_3$ recorded in a Lindemann capillary at 22 °C using 647.1-nm excitation.

very broad peak at 492 (AsF_6^-) and 495 ($Sb_2F_{11}^-$) cm^{-1}. Among oligomeric fluorine-bridged systems which preserve octahedral coordination about the central metal atoms, the $Sb_2F_{11}^-$ anion has the lowest assigned stretching frequency for an Sb-F_b-Sb bridging stretching mode occurring at 332 cm^{-1}.[122] The relatively high intensity bands at 388 and 398 cm^{-1} correspond to the symmetric and antisymmetric combinations of the ReO_2 scissoring motion. The assignments of the lowest frequency bands are tentative and are based on the frequencies calculated at the LDFT level.

ReO_2F_3. The solid state Raman spectrum of $(ReO_2F_3)_\infty$ is shown in Figure 4.13a. No vibrational spectrum of $(ReO_2F_3)_\infty$ has been reported previously. Assignments are given in Table 4.15 for $(ReO_2F_3)_\infty$ and for $(ReO_2F_3)_\infty$ in $K^+Re_2O_4F_7^-{\cdot}2ReO_2F_3$ and are primarily based on those for monomeric ReO_2F_3 [12] and for $ReO_2F_4^-$ in which the environment around Re is very similar to that in $(ReO_2F_3)_\infty$. Moreover, the Re-$F_{c,t}$ bond lengths in $ReO_2F_4^-$ are very similar to the Re-F_b bond lengths in the polymer. Coupling between different ReO_2F_4-units in the chains was initially assumed to be weak. For an uncoupled *cis*-ReO_2F_4 unit of C_{2v} point symmetry, all 15 vibrational modes having the symmetries $6A_1 + 2A_2 + 4B_1 + 3B_2$, with the [$O_t$, O_t, Re, F_b, F_b]-plane taken as the $\sigma(xz)$ plane (Structure IV), are expected to be Raman active. Additional modes associated with Re-F_b-Re bridges are not accounted for in this analysis. Moreover, their expected low frequencies and intensities make their observation and assignment difficult.

The splitting observed for several bands of the spectrum of $(ReO_2F_3)_\infty$ in $K^+Re_2O_4F_7^-{\cdot}2ReO_2F_3$ is in good agreement with the factor-group analysis. A further

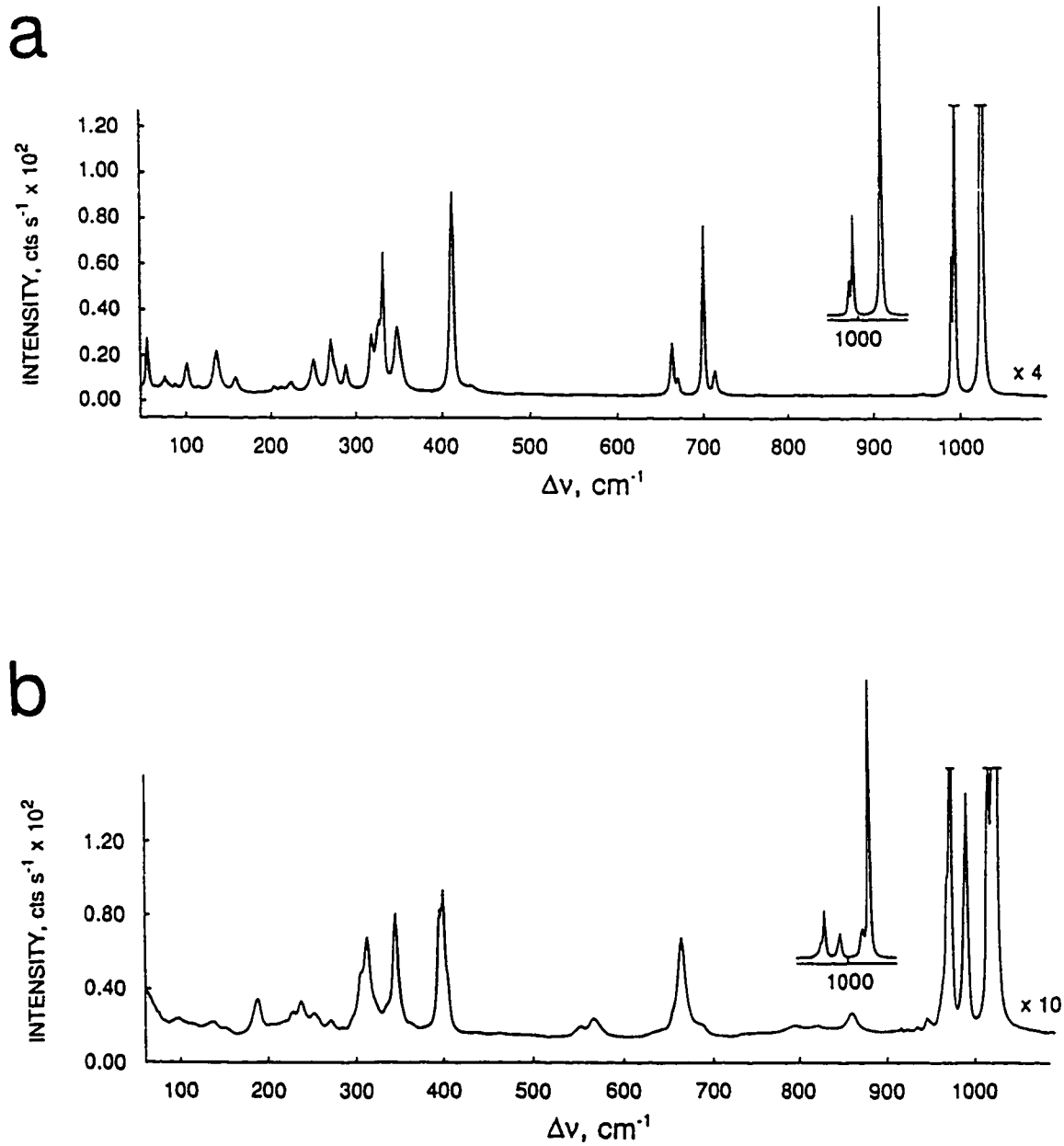

Figure 4.13. Raman spectra of (a) microcrystalline ReO_2F_3 and recorded in a Pyrex capillary and (b) a single crystal of $Cs^+Re_3O_6F_{10}^-$ recorded in a Lindemann capillary at 22 °C using 514.5-nm excitation.

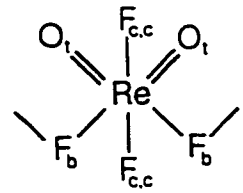

Structure IV

splitting is observed for the high-frequency band centered at 1021 cm^{-1} and may arise from coupling of the ReO_2F_4-units within the polymer chains.

The assignments for the four highest frequency modes are identical to those in $ReO_2F_4^-$ and monomeric ReO_2F_3,[12] the values being larger in $(ReO_2F_3)_\infty$ than in the $ReO_2F_4^-$ anion. The highest frequency bands occur at 990, 994 and 1025 cm^{-1} are assigned to the antisymmetric and symmetric Re-O stretches, respectively. The band at 1025 cm^{-1} is much more intense than those at 990, 994 cm^{-1} and is assigned as the symmetric stretch. The bands at 664, 670 and 700, 713 cm^{-1} are characteristic of stretching modes involving a metal bonded to a terminal fluorine ligand. These split bands are assigned to the symmetric and antisymmetric $ReF_{2c,c}$ stretches, respectively, based on the greater intensity of the higher frequency bands.

The relatively intense band at 412 cm^{-1} has a counterpart in every other *cis*-dioxo complex reported to date and is assigned by analogy with these systems to the ReO_2 scissoring mode. As expected, this value is similar to the one in $ReO_2F_4^-$ ($N(CH_3)_4^+$: 401, 419 cm^{-1}), and is significantly different from that of monomeric ReO_2F_3.[12] The difference is likely related to the difference in the O-Re-O angles, with $\delta(ReO_2)$ occurring at lower

frequency in ReO_2F_3 monomer, where the O-Re-O angle is more open (110°) than in $(ReO_2F_3)_\infty$ (102°). The pairs of bands at 332, 349 cm^{-1} and 319, 326 cm^{-1} in $(ReO_2F_3)_\infty$ are assigned by direct analogy with $ReO_2F_4^-$ to scissoring deformation modes involving $OReF_b$ and $ReF_{2c,c}$. The mode at 288 cm^{-1} can be assigned with confidence to $\rho_r(ReF_{2c,c})$. Since this mode only involves $F_{c,c}$ atoms, it is expected to be similar to that of $ReO_2F_4^-$. The modes at 223 and 101 cm^{-1} are tentatively assigned to ReO_2 torsion and $\nu_s(ReF_bRe')$ stretch by analogy with $ReO_2F_4^-$ and $Re_2O_4F_7^-$, respectively.

$Cs^+Re_3O_6F_{10}^-$. The solid state Raman spectrum of $Cs^+Re_3O_6F_{10}^-$ is shown in Figure 4.13b. Assignments are given in Table 4.15 and are based on those for $(ReO_2F_3)_\infty$ and the $ReO_2F_4^-$ anion. The $Re_3O_6F_{10}^-$ anion contains a C_{2v} ReO_2F_4-unit bridging two ReO_2F_3-units, each having C_s symmetry and not related to each other by crystal symmetry (Structure V).

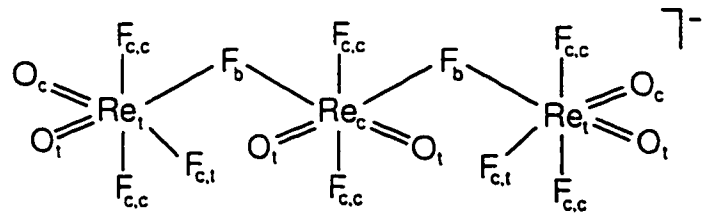

Structure V

The point symmetry of the anion is C_{2v}, all 51 vibrational modes having the symmetries $17A_1 + 9A_2 + 15B_1 + 10B_2$ with the [Re_t, Re_c, Re_t]-plane taken as the $\sigma(xz)$ plane, are expected to be Raman active. In general, the frequencies are found to be higher than those of the corresponding modes in $ReO_2F_4^-$, and is attributed to the greater charge delocalization in the $Re_3O_6F_{10}^-$ anion. Moreover, the vibrational modes associated with the

central rhenium atom occur at higher frequencies than those associated with the terminal rhenium atoms, and is consistent with more localization of the anion charge on the terminal ReO_2F_3-groups.

Five bands are observed in the Re-O stretching region, ranging from 968 to 1024 cm^{-1}. The bridging ReO_2F_4-group is in approximately the same environment as it is in $(ReO_2F_3)_\infty$. The most intense bands at 1016, 1024 cm^{-1} and the band at 990 cm^{-1} are assigned to the symmetric and antisymmetric ReO_2 stretches of the central ReO_2F_4-group, respectively, and are nearly identical to those observed for the corresponding modes in $(ReO_2F_3)_\infty$. The two remaining high-frequency bands at 968 and 972 cm^{-1} can be related to the antisymmetric and symmetric combinations of ReO_2 stretches of the two terminal ReO_2F_4-groups of the anion and are assigned based on their realtive Raman intensities. The bands at 665 and 688 cm^{-1} are assigned to the antisymmetric and symmetric $Re\text{-}F_{2c,c}$ stretches, respectively, of the central ReO_2F_3-group while the bands at 641 and 655 cm^{-1} are related to antisymmetric $Re\text{-}F_{2c,c}$ stretch and symmetric combinations of the $Re\text{-}F_{2c,c}$ and $ReF_{c,t}$ bonds, respectively, of the terminal ReO_2F_4-groups. Two weak bands are observed at 553 and 568 cm^{-1} and are tentatively assigned to the antisymmetric ReF_bRe' stretch by analogy with the weak band observed at 554 cm^{-1} in $Re_2O_4F_7^-$. By analogy with other *cis*-dioxo systems the bands at 405, 400 and 396 cm^{-1} are assigned to the scissoring deformation modes of the three ReO_2 groups in the anion. The group of bands around 298-336 cm^{-1} are assigned to combinations of ReF and OReF scissors by analogy with $ReO_2F_4^-$. The band at 285 cm^{-1} is assigned with confidence to $\rho_r(ReF_{2c,c})$ which appears at almost the same frequency for all related anions and molecules. Similarly the band at

228 cm^{-1} is assigned to the ReO_2 torsion. The very low frequency weak band at 114 cm^{-1} is assigned to the symmetric ReF_bRe' stretch by analogy with $Re_2O_4F_7^-$.

$ReO_2F_3(CH_3CN)$. The Raman spectrum of $ReO_2F_3(CH_3CN)$ was recorded in the solid state and in CH_3CN solution at 20 °C. The spectrum was assigned on the basis of the energy-minimized structure determined by LDFT calculations (Structure II). The spectrum of the solid is shown in Figure 4.14 and the frequencies and their assignments are listed in Table 4.19. The assignments were made by comparison with the Raman spectra of CH_3CN,[123] monomeric ReO_2F_3,[12] $ReO_2F_4^-$ and $TcO_2F_3(CH_3CN)$. The adduct is expected to possess C_s symmetry for which 30 Raman and infrared-active vibrational modes are predicted (19A' + 11A").

The most prominent feature in the Raman spectrum of $ReO_2F_3(CH_3CN)$ is a very intense band at 1001 cm^{-1} which appears at low frequency with respect to the corresponding band in monomeric ReO_2F_3 [12] and at high frequency with respect to that of $N(CH_3)_4^+ReO_2F_4^-$, and is consistent with the lower base strength of CH_3CN with respect to that of the fluoride ion. The bands occuring at 944-974 cm^{-1} and at 1001 cm^{-1} are similar to the antisymmetric and symmetric ReO_2 stretching modes observed in related *cis*-dioxo anions discussed in this Chapter. Their mode descriptions are complicated by coupling with the C-C and Re-N stretches as well as CCN and CH_3 deformations. Only three bands are found in the Re-F stretching region of the spectrum. The two high-frequency bands at 659 and 679 cm^{-1} are assigned to the symmetric and antisymmetric stretching modes involving the more strongly bonded *cis*-fluorine atoms, respectively. The

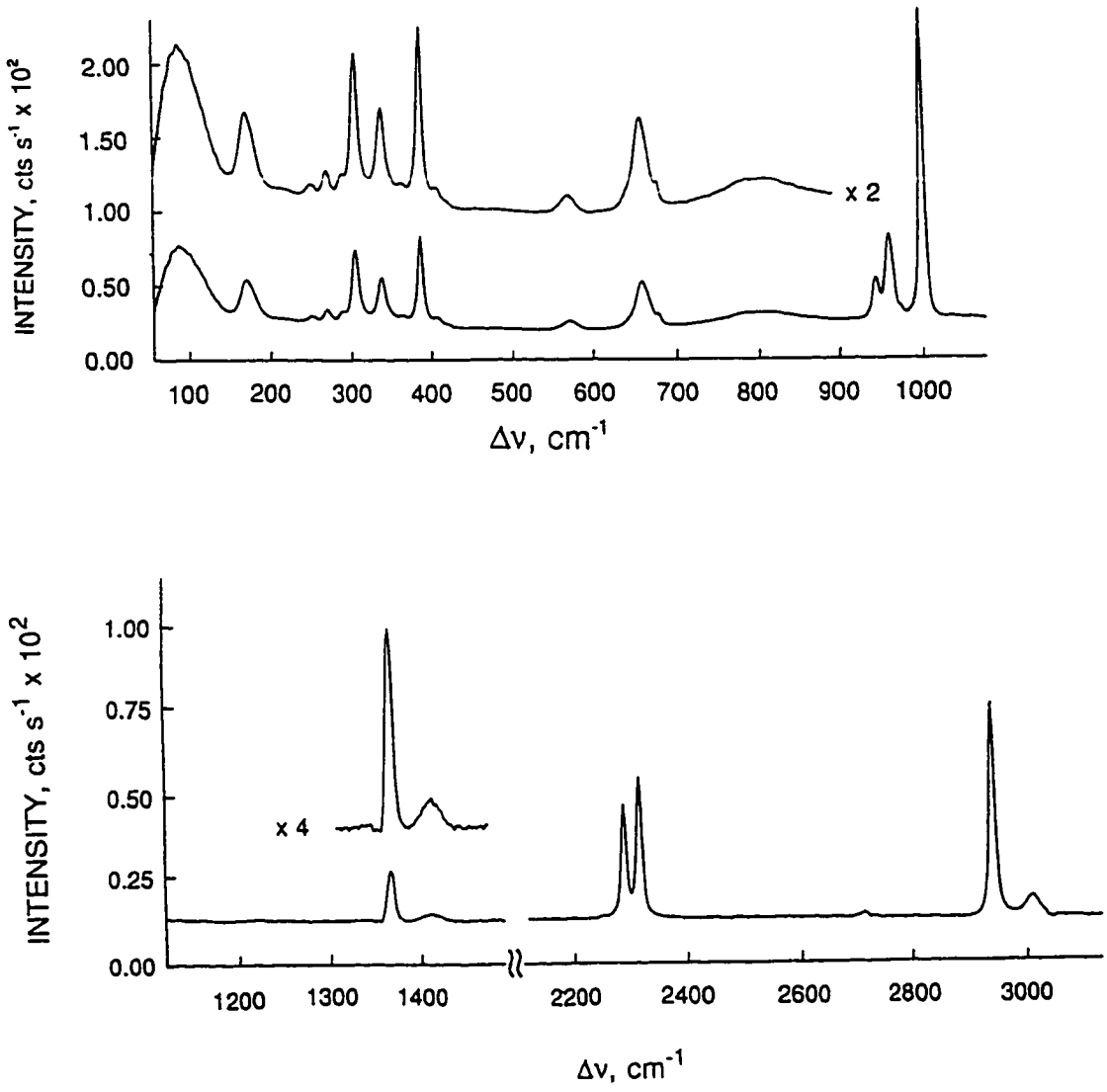

Figure 4.14. Raman spectrum of microcrystalline $ReO_2F_3(CH_3CN)$ recorded in a Pyrex capillary at 23 °C using 514.5-nm excitation.

Table 4.19. Experimental and Calculated Raman Frequencies, Assignments and Mode Descriptions for $ReO_2F_3 \cdot CH_3CN$

Frequencies (cm^{-1})			Assignments [c]
solid[a]	soln[a,b]	calc[c]	
3016(3)	d	3082(3)	$\nu_{as}(CH_3)$
		3077(3)	$\nu_{as}(CH_3)$
2947(33)	d	2989(5)	$\nu_s(CH_3)$
2323(22)	2324(14),p		$\nu_3 + \nu_7$
2297(18)	d	2373(113)	$\nu(CN)$
1412(1)	d	1387(19)	$\delta_{as}(CH_3)$
	d	1381(20)	$\delta_{as}(CH_3)$
1367(6)	1366(7),sh,p	1340(15)	$\delta_s(CH_3)$
	1041(1),dp	1028(118)	$\nu(ReO_t) + \nu(ReO_c)$
1001(100)	1002(100),p	1006(117)	$\nu(ReO_t) - \nu(ReO_c) + \rho_r(CH_3)$
974(2),sh	974(4),sh,p	987(17)	$\rho_r(CH_3) + \nu(ReO_c) + \delta(CCN)$
960(26)	962(25),p	976(19)	$\nu(ReO_c) - \nu(ReN) + \nu(CC) + \rho_r(CH_3)$
944(13)	943(15),p	986(17)	$\rho_r(CH_3) + \nu(CC)$
679(5),sh		676(53)	$\nu_s(ReF_{2c,c}) + \nu(ReF_{c,t})$
659(15)	660(22),p	667(155)	$\nu(ReF_{c,t}) - \nu(ReF_{c,c})$
572(3)	571(2),dp	560(57)	$\nu(ReF_{c,t}) - \nu(ReF_{2c,c})$
423(1)		449(14)	$\delta(ReO_2) + \delta(CNRe)$
408(4)	406(3),sh,dp	408(6)	$\delta(ReO_2) - \delta(CNRe)$
389(30)	388(16),p	401(8)	$\delta(O_tReN) - \delta(CNRe)$
366(3)	d	383(3)	$\delta(O_tReF_{c,c}) + \delta(CNRe)$
340(15)	341(7),dp	347(1)	$\delta(O_cReF_{c,c}) + \delta(F_{c,c}ReF_{c,t})$
307(24)	307(10),dp	322(16)	$\delta(F_{c,c}ReO_t) + \delta(F_{c,t}ReF_{c,c}) + \delta(O_cReN)$
292(4)	290(2),p		
278(2), sh			
272(4)	272(3),p	262(17)	$\delta(F_{c,c}ReO_c) + \delta(F_{c,c}ReO_c) - \delta(F_{c,t}ReN)$
257(2)	253(2),dp	257(23)	$\delta(F_{c,c}ReN) + \delta(OcReF_{c,t})$
252(2)			

Table 4.19. continued

		221(6)	$\nu(ReN) + \delta(F_{c,c}ReF_{c,c})$ toward $F_{c,t}$
		212(10)	$\nu(ReN) + \delta(F_{c,c}ReF_{c,c})$ toward $F_{c,t}$
188(8), sh		202(5)	$\delta(F_{c,c}ReF_{c,c})$ toward N
182(10), sh		183(2)	$\delta(NReF_{c,c} - NReF_{c,c})$
174(11)	171(7),dp	130(1)	$\delta(CH_3)$-N-(ReO_2F_3) plane 1
154(<1)		114(2)	$\delta(CH_3)$-N-(ReO_2F_3) plane 2
90(23)		81(6)	$\rho_t(CH_3)$

[a] Spectrum recorded on microcrystalline solid in a rotating Pyrex capillary and in CH_3CN solution in 3-mm o.d. Pyrex tube at 23 °C using 514.5-nm excitation. Values in parentheses denote relative intensities; sh: shoulder; br: broad; p: polarized; dp: depolarized.

[b] Frequency values observed for free CH_3CN: 3004(3), 2945(100), 2735(2), 2294(4), 2254(67), 1447(<1), 1375(3), 918(16), 379(5).

[c] Infrared intensities, in $kmol^{-1}$, are given in parentheses.

[d] Obscured by a band of free CH_3CN.

[e] ν: stretching; δ: in-plane bending; ρ_r: rocking; ρ_t: twisting.

remaining band at 572 cm^{-1} is assigned to the Re-$F_{c,t}$ stretching mode. However, LDFT calculations for $TcO_2F_3(CH_3CN)$ show that the antisymmetric $TcF_{2c,c}$ stretch is strongly coupled with the $TcF_{c,t}$ stretch. The ReO_2 bending mode is assigned to the strong band at 389 cm^{-1}, which is consistent with what is observed in the model compounds. The remaining low-frequency bands are assigned to strongly coupled bending modes from the frequencies calculated at the LDFT level but also by analogy with the frequencies calculated for $TcO_2F_3(CH_3CN)$.

The frequency shifts observed for complexed CH_3CN are comparable to those observed for $TcO_2F_3(CH_3CN)$ and for the $Co(CH_3CN)_6^{2+}$ cation.[152] The bands assigned to ν_8 (378 cm^{-1}), ν_4 (920 cm^{-1}), ν_6 (1448 cm^{-1}), ν_2 (2257 cm^{-1}), $\nu_3 + \nu_4$ (2297 cm^{-1}) of free CH_3CN are shifted to 408, 944, 1412, 2297 and 2323 cm^{-1}, respectively, in $ReO_2F_3(CH_3CN)$.

Calculated Molecular Geometries

The molecular geometries were initially optimized at the local density functional theory (LDFT) level with a polarized double-ζ basis set (DZVP) (Table 4.20). Unless specified, the results discussed are at the LDFT level. In general, and as previously observed for related systems, the NLDFT values for the geometrical parameters are longer than the LDFT values.

The calculated geometric parameters for monomeric ReO_2F_3 [63] (Structure VI) have been reported previously along with those of the isoelectronic $OsO_2F_3^+$ cation. The structure was predicted to have C_{2v} point symmetry with the two oxygen atoms and one

Table 4.20. Geometric Parameters for $ReO_2F_4^-$, $Re_2O_4F_7^-$, $Re_3O_6F_{10}^-$ and $ReO_2F_3(CH_3CN)$

$ReO_2F_4^-$

Bond Lengths (Å)				Bond Angles (deg)			
	exp	LDFT	NLDFT		exp	LDFT	NLDFT
Re-$F_{c,c}$	1.867(8)	1.913	1.936	O-Re-O	100.2(7)	100.6	102.6
Re-$F_{c,t}$	2.002(7)	1.965	1.996	$F_{c,c}$-Re-$F_{c,c}$	162.9(6)	171.8	167.7
Re-O	1.678(9)	1.737	1.740	$F_{c,t}$-Re-$F_{c,t}$	76.3(4)	82.4	78.5

$Re_2O_4F_7^-$

Bond Lengths (Å)				Bond Angles (deg)			
	exp[a]	exp[b]	LDFT		exp[a]	exp[b]	LDFT
Re-F_b	2.155(4)	2.150(4)	2.125	O-Re-O	100.5(5)	99.8(4)	101.9
Re-$F_{c,c}$	1.785(9) 1.866(8)	1.783(8) 1.880(6)	1.885 1.892	$F_{c,c}$-Re-$F_{c,c}$	159.9(5)	160.9(4)	161.9
Re-$F_{c,t}$	1.893(8)	1.883(7)	1.935	$F_{c,t}$-Re-F_b	78.2(4)	78.2(3)	78.1
Re-O_t	1.663(12)	1.676(7)	1.715	Re-F_b-Re	139.5(6)	143.3(6)	179.8
Re-O_c	1.766(7)	1.753(9)	1.724				

[a] Values for $K^+Re_2O_4F_7^-$.

[b] Values for $K^+Re_2O_4F_7^-$ in $K^+Re_2O_4F_7^-\cdot 2ReO_2F_3$.

Table 4.20. continued

$Re_3O_6F_{10}^-$

Bond Lengths (Å)			Bond Angles (deg)		
	exp	LDFT/DZPV		exp	LDFT/DZPV
Re_t-F_b	2.213(6), 2.151(6)	2.166, 2.163	O_c-Re_t-O_t	102.6(4), 104.3(5)	101.4, 103.0
Re_t-$F_{c,c}$	1.864(7), 1.842(6) 1.851(7), 1.867(7)	1.886, 1.868 1.880, 1.887	$F_{c,c}$-Re_t-$F_{c,c}$	159.2(4), 159.2(3)	161.7, 161.2
Re_t-$F_{c,t}$	1.908(6), 1.936(7)	1.922, 1.918	$F_{c,t}$-Re_t-F_b	76.5(3), 75.9(3)	77.6, 77.3
Re_t-O_t	1.669(8), 1.678(7)	1.711, 1.710	Re_t-F_b-Re_c	140.6(3), 178.5(5)	177.1, 169.3
Re_t-O_c	1.715(8), 1.695(9)	1.728, 1.724	O_t-Re_c-O_t	103.3(4)	101.8
Re_c-F_b	2.064(7), 2.039(6)	2.064, 2.080	$F_{c,c}$-Re_c-$F_{c,c}$	155.7(3)	160.6
Re_c-$F_{c,c}$	1.851(7), 1.848(6)	1.865, 1.873	F_b-Re_c-F_b	77.3(3)	79.8
Re_c-O_t	1.694(8), 1.683(7)	1.705, 1.711			

$ReO_2F_3(CH_3CN)$

Bond Lengths (Å)		Bond Angles (deg)	
	LDFT/DZVP		LDFT/DZVP
Re-O_t	1.715	O_t-Re-O_c	105.5
Re-O_c	1.723	$F_{c,c}$-Re-$F_{c,c}$	157.9
Re-$F_{c,c}$	1.880, 1.873	$F_{c,t}$-Re-N	74.2
Re-$F_{c,t}$	1.949	Re-N-C	171.8
Re-N	2.316	N-C-C	178.9
N-C	1.164		

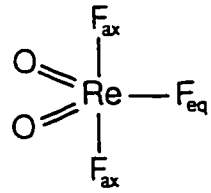

Structure VI

fluorine atom (F_{eq}) in the equatorial plane of the trigonal bipyramid. These calculated values can now be compared with the observed values for $ReO_2F_4^-$ and those of $(ReO_2F_3)_\infty$. The Re-O bond distance in ReO_2F_3 is predicted to be 1.705 Å in contrast with the shorter experimental Re-O bond distances in $ReO_2F_4^-$ (1.678(8) Å) and $(ReO_2F_3)_\infty$ (1.676(8) Å). Unlike monomeric TcO_2F_3, where the Tc-F_{eq} and Tc-F_{ax} bond lengths were predicted to be the same, in ReO_2F_3 the Re-F_{eq} bond (1.894 Å) is predicted to be longer than the Re-F_{ax} bonds (1.876 Å). The Re-F_{eq} bond is comparable to the Re-$F_{c,c}$ bonds in $ReO_2F_4^-$ (1.867(8) Å) and in $(ReO_2F_3)_\infty$ (1.834(7) and 1.854(7) Å) while, as expected, the Re-F_{ax} bond is found to be shorter than the Re-$F_{c,t}$ and Re-F_b bond distances in $ReO_2F_4^-$ (2.002(7) Å) and in $(ReO_2F_3)_\infty$ (2.102(6) Å). The O-Re-O and F_{ax}-Re-F_{ax} angles differ from the ideal 120 and 180° angles by 10 and 22°, respectively, showing that the O-Re-O angle is closing down, and that the axial fluorines are bent away from the oxygens, toward the equatorial fluorine as in $ReO_2F_4^-$ and $(ReO_2F_3)_\infty$. The F_{eq}-Re-F_{ax}, O-Re-F_{ax} and O-Re-F_{eq} angle values are the averages of their counterparts in the experimental structures of $ReO_2F_4^-$ and $(ReO_2F_3)_\infty$. Attempts to optimize the D_{3h} structure of monomeric ReO_2F_3 led to the C_{2v} structure. An approximately optimized D_{3h} structure with an Re-O bond

length of 1.78 Å and an Re-F bond length of 1.85 Å is 54.5 kcal mol^{-1} above the C_{2v} structure at the LDFT level.

The lowest energy structure for $ReO_2F_4^-$ is the *cis*-dioxo structure (C_{2v} point symmetry) and is 32.2 kcal mol^{-1} more stable than the *trans*-dioxo structure (D_{4h} point symmetry) which has three imaginary frequencies. The calculated Re-O bond distance (1.913 Å) is 0.06 Å longer than that of $ReO_2F_4^-$ in the crystal structure. A similar difference has been found for the $TcO_2F_4^-$ anion and the origin of the differences has been previously discussed. The calculated Re-$F_{c,t}$ bond lengths (1.965 Å) are longer than the Re-$F_{c,c}$ bond lengths (1.913 Å) following the experimental trend, even though the calculated values for the Re-$F_{c,c}$ and Re-$F_{c,t}$ bond lengths are 0.046 Å longer and 0.037 Å shorter, respectively, than the experimental values. This suggests that there is a strong interaction between Li^+ and the $F_{c,t}$ atoms *trans* to the O atoms in the crystal. As expected for a structure to which a fluoride ion has been added, all Re-F bond distances are longer than those in monomeric ReO_2F_3. There is good agreement between the calculated and the observed angles, and, as noted for $TcO_2F_4^-$, the largest differences occur for the angles involving the most ionic bonds, i.e., the fluorines *trans* to the oxygens, namely, $F_{c,t}$-Re-$F_{c,t}$ and $F_{c,t}$-Re-$F_{c,c}$.

As previously observed for the $TcO_2F_3(CH_3CN)$ adduct, the energy-minimized structure for $ReO_2F_3(CH_3CN)$ corresponds to a *cis*-dioxo arrangement in which the coordination sphere of the Re is expanded to six and the CH_3CN molecule is coordinated *trans* to an oxygen. The geometrical parameters calculated for the $ReO_2F_3(CH_3CN)$ adduct are very similar to those observed for $(ReO_2F_3)_\infty$ with few changes. The bond distances

for the Re-O bonds differ by 0.008 Å with the Re-O_t bond *trans* to the Re-N bond being shorter. The Re-$F_{c,t}$ bond *trans* to Re-O_c is significantly lengthened (1.949 Å) when compared to the other Re-$F_{c,c}$ bonds (1.872 and 1.880 Å). The CH_3CN moiety is essentially the same as that of the isolated molecule with R(C-C), 1.440 Å and R(C-N), 1.164 Å. The long Re-N bond (2.316 Å) is consistent with a weaker donor-acceptor type interaction as compared to the more ionic interactions of O and F with Re. A similar trend was calculated for the Tc-N bond in $TcO_2F_3(CH_3CN)$. The O_c-Re-O_t angle decreases by about 3° and one $F_{c,t}$-Re-O_c angle (154.3°) decreases by about 15° with the other $F_{c,t}$-Re-O_t angle (93.4°) increasing by a similar amount and the $F_{c,c}$-Re-$F_{c,c}$ angle decreases by only 1°.

The calculated geometry for $Re_2O_4F_7^-$ shows some significant differences when compared to the experimental crystal structure. As expected, the calculated Re-O_t bond is longer than the experimental value by 0.05 Å. However, the calculated value for the Re-O_c bond is shorter than the experimental one by 0.03 Å suggesting that the K^+ counterion is strongly interacting with these oxygens. The calculated value for the Re-$F_{c,c}$ bond is characteristic of other Re(VII)-F bond lengths, on the order of 1.9 Å, and is ~0.1 Å longer than the experimental Re(1)-F(3) value (1.783(8) Å, see **X-ray Crystal Structures**). Within the calculated Re-$F_{c,c}$ and Re-$F_{c,t}$ bonds, the expected trend, i.e., Re-$F_{c,c}$ < Re-$F_{c,t}$, is followed. The calculated value for the Re-F_b distance (2.125 Å) is in good agreement with the experimental value of 2.155(4) Å indicating that the bridging fluoride ion has a significant covalent interaction with both Re atoms. The calculated angles are in reasonable agreement with the experimental values except for the Re-F_b-Re

angle where the calculated value is near linear (179.8°) whereas the experimental value is 143.3°. This discrepancy most likely arises from the fact that within the crystal the anions and cations are not isolated but, rather, there are significant electrostatic interactions between the cation and various O and F atoms of the anion. This could easily lead to a distortion of the bridge bond angle to maximize these interactions.

The calculated geometry for $Re_3O_6F_{10}^-$ is in very good agreement with the experimental crystal structure. As observed for all other related systems, the calculated Re-O and Re-F bond distances are slightly longer than the experimental values, except for Re(1)-F(4) and Re(3)-F(8). The largest discrepancies for the angles are observed for the two Re-F_b-Re angles which are found to be larger by 37° (Re(1)-F(4)-Re(2)) and smaller by 10° (Re(2)-F(7)-Re(3)), respectively. As noted for $Re_2O_4F_7^-$, these discrepancies most likely reflect the fact that the anion is not isolated in the crystal structure. This point is substantiated by the observation that the largest discrepancies occur for the Re(1)-F(4)-Re(2) bridge angle which is most affected by anion-cation contacts (see **X-ray Crystal Structures**).

Conclusion

A new high-yield, high-purity synthesis of ReO_2F_3 was developed and involves the fluorination of ReO_3F in anhydrous HF using XeF_6. The structure of ReO_2F_3 consists of fluorine-bridged ReO_2F_4-units and is analogous to that of TcO_2F_3. The Lewis acid properties of ReO_2F_3 toward the fluoride ion and CH_3CN was investigated and resulted in the syntheses of several $M^+ReO_2F_4^-$ salts (M = Li, Na, K, Cs, $N(CH_3)_4$) and the

$ReO_2F_3(CH_3CN)$ adduct. Spectroscopic data are consistent with the fact that ReO_2F_3 is a stronger Lewis acid than TcO_2F_3. The $ReO_2F_4^-$ anion reacts with excess ReO_2F_3 to form the fluorine-bridged $Re_2O_4F_7^-$ and $Re_3O_6F_{10}^-$ anions, the higher oligomer only forms when more acidic solvents and cations are used. These oligomers were shown to exist in solution and in the solid state by X-ray crystallography, NMR and Raman spectroscopy. The *cis*-dioxo arrangement adopted by these compounds is consistent with what is observed for all other dioxo complexes of d^0 transition metals. The *trans* influence of the oxo ligands is significant in these compounds and results in a lengthening and weakening of the bonds *trans* to the oxygens. The energy-minimized geometries determined from density functional theory calculations are in agreement with the structures determined by X-ray crystallography and by NMR and Raman spectroscopy.

CHAPTER 5

FLUORIDE-ION DONOR PROPERTIES OF TcO_2F_3 AND ReO_2F_3

Introduction

It was demonstrated in Chapters 3 and 4 that TcO_2F_3 and ReO_2F_3 behave as Lewis acids and possess significant fluoride-ion affinities. The neutral $MO_2F_3(CH_3CN)$ adducts and the $MO_2F_4^-$ anions (M = Tc, Re) were spectroscopically characterized and the X-ray structures of $Li^+MO_2F_4^-$ (M = Tc, Re), $K^+Re_2O_4F_7^-$, $K^+Re_2O_4F_7^-\cdot 2ReO_2F_3$, and $Cs^+Re_3O_6F_{10}^-$ were determined. The *cis*-dioxo arrangement was observed in these and all other six-coordinate d^0 transition metal dioxofluorides (e.g., OsO_2F_4, $MoO_2F_4^{2-}$, $VO_2F_4^{3-}$, and $Os_2O_4F_7^+$).

The present Chapter describes the fluoride-ion donor properties of TcO_2F_3 and ReO_2F_3 toward SbF_5, AsF_5 and XeO_2F_2, the characterization of $TcO_2F_3\cdot SbF_5$, $ReO_2F_3\cdot SbF_5$ and $TcO_2F_3\cdot XeO_2F_2$ by X-ray crystallography, and the spectroscopic characterization of $TcO_2F_3\cdot AsF_5$, $ReO_2F_3\cdot AsF_5$, $Re_2O_4F_5^+Sb_2F_{11}^-$ and $[ReO_2F_2(CH_3CN)_2]^+SbF_6^-$.

Results and Discussion

The Interaction of MO_2F_3 (M = Tc, Re) with AsF_5 and SbF_5

Solution ^{19}F and ^{99}Tc NMR Studies of the Reactions of MO_2F_3 with AsF_5 and SbF_5; the $TcO_2F_2^+$ and $ReO_2F_2^+$ Moieties. Both TcO_2F_3 and ReO_2F_3 are essentially insoluble in

anhydrous HF at room temperature, but dissolve readily in HF solutions acidified with the strong Lewis acids AsF_5 and SbF_5. A combining ratio of 1:1 was found when the solvent was removed from solutions containing a five-fold or greater molar excess of AsF_5 or SbF_5. The pale yellow TcO_2F_3 and colourless ReO_2F_3 adducts with SbF_5 were isolated and stored at room temperature without decomposition. In contrast, the compounds formed with AsF_5 had to be isolated and maintained at temperatures below -40 °C because they have significant dissociation vapour pressures of AsF_5 above that temperature and slowly revert to the starting materials.

The high solubilities of $MO_2F_3{\cdot}SbF_5$ and $MO_2F_3{\cdot}AsF_5$ (M = Tc, Re) in anhydrous HF apparently result from dissociation of the adduct into $MO_2F_2^+$ cations (Structure I) and

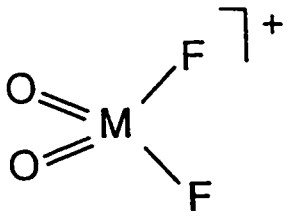

Structure I

AsF_6^- and SbF_6^- anions (eq. (5.1)). However, the $MO_2F_2^+$ cations are expected to be strong

$$MO_2F_3{\cdot}PnF_5 \overset{HF}{\rightleftharpoons} MO_2F_2^+PnF_6^- \quad (M = Tc, Re;\ Pn = As, Sb) \qquad (5.1)$$

Lewis acids and likely interact with Lewis bases in solution, possibly forming soluble adducts with SbF_6^-, HF_2^-, HF and MO_2F_3. Because the existence of the isolated $MO_2F_2^+$ cations could not be unequivocally proven by NMR or Raman spectroscopy, the species

observed in HF solutions of $MO_2F_2 \cdot PnF_5$ will be referred as "the $MO_2F_2^+$ moiety". The ^{19}F NMR spectrum of $TcO_2F_3 \cdot AsF_5/5AsF_5$ in HF at -84 °C consists of a broad singlet at 109.2 ppm ($\Delta\nu_{1/2}$ = 438 Hz), which is significantly deshielded compared to the fluorine resonances in $TcO_2F_3(CH_3CN)$ (25.3 and 37.3 ppm in CH_3CN at 30 °C) and $TcO_2F_4^-$ (-14.1 and -18.7 ppm in CH_3CN; 23.0 ppm in HF), and is consistent with the formation of a cationic $TcO_2F_2^+$ moiety. Broad resonances at -67.9 ($\Delta\nu_{1/2}$ = 3500 Hz) and -124.9 ppm ($\Delta\nu_{1/2}$ = 2500 Hz) are assigned to AsF_6^- and exchange averaged AsF_5 and HF, respectively. The ^{19}F NMR spectrum recorded at 30 °C consists of a singlet at -134.7 ppm ($\Delta\nu_{1/2}$ = 1675 Hz) and is the result of rapid fluorine exchange between HF, AsF_5, AsF_6^- and the $TcO_2F_2^+$ moiety. The ^{99}Tc NMR spectrum of $TcO_2F_3 \cdot AsF_5/5AsF_5$ in HF at -54 °C is a singlet at 140.3 ppm ($\Delta\nu_{1/2}$ = 2500 Hz) which is broadened by fast quadrupolar relaxation of the ^{99}Tc nucleus. Sharpening of the signal occurred at higher temperature ($\Delta\nu_{1/2}$ = 793 Hz, 30 °C), although not sufficiently to observe ^{99}Tc-^{19}F coupling. The ^{99}Tc resonance is deshielded relative to TcO_3F in HF (43.7 ppm) but is similar to that of TcO_3^+ in HF (160.7 ppm).[40] The ^{19}F NMR spectrum of $TcO_2F_3 \cdot SbF_5$ in HF recorded at -80 °C consists of two broad resonances at 106.8 ppm ($\Delta\nu_{1/2}$ = 1000 Hz), -127.8 ppm ($\Delta\nu_{1/2}$ = 2350 Hz) and a sharp singlet at -193.7 ppm ($\Delta\nu_{1/2}$ = 30 Hz), which are assigned to the $TcO_2F_2^+$ moiety, SbF_6^- and HF, respectively. An attempt was made to slow the fluorine exchange by dissolving TcO_2F_3 in neat SbF_5, but the high viscosity of SbF_5 increased the quadrupolar relaxation rate of ^{99}Tc resulting in a very broad ^{99}Tc resonance, even at 64 °C (128.4 ppm; $\Delta\nu_{1/2}$ = 18 600 Hz). The ^{19}F NMR spectrum of this solution recorded at

30 °C yielded a singlet at 137.5 ppm ($\Delta\nu_{1/2}$ = 106 Hz) and a broad resonance at -114.1 ppm ($\Delta\nu_{1/2}$ = 4700 Hz) assigned to SbF_5 exchange-averaged with $Sb_nF_{5n+1}^-$.

The ^{19}F NMR spectra of $ReO_2F_3 \cdot AsF_5/5AsF_5$ and $ReO_2F_3SbF_5/5SbF_5$ in HF at 30 °C each displays a singlet in the fluorine-on-rhenium region of the spectrum. The resonances are broadened because of fluorine exchange with the solvent and occur at 19.8 ($\Delta\nu_{1/2}$ = 1625 Hz) and 24.4 ppm ($\Delta\nu_{1/2}$ = 1550 Hz) for HF solutions of $ReO_2F_3 \cdot AsF_5$ and $ReO_2F_3 \cdot Sb_nF_{5n+1}^-$, respectively. The spectrum of $ReO_2F_3 \cdot AsF_5/5AsF_5$ also displays an intense singlet at -163.5 ppm ($\Delta\nu_{1/2}$ = 210 Hz) assigned to HF, AsF_5 and AsF_6^- undergoing rapid fluorine exchange. The spectrum of $ReO_2F_3 \cdot SbF_5/5SbF_5$ displays two additional resonances at -125.3 ppm ($\Delta\nu_{1/2}$ = 2380 Hz) in the F-on-Sb(V) region of the spectrum assigned to SbF_5 exchange averaged with SbF_6^- and a resonance at -193.0 ppm ($\Delta\nu_{1/2}$ = 400 Hz) assigned to HF. Dissolution of ReO_2F_3 in neat SbF_5 slowed intermolecular fluorine exchange sufficiently at 30 °C to give a singlet at 37.4 ppm ($\Delta\nu_{1/2}$ = 200 Hz) in the F-on-Re(VII) region on the spectrum. The intense, broad ^{19}F resonances arising from polymeric $(SbF_5)_n/Sb_nF_{5n+1}^-$ were also observed at -86.2 ($\Delta\nu_{1/2}$ = 1500 Hz), -104.7 ($\Delta\nu_{1/2}$ = 1100 Hz) and -132.0 ppm ($\Delta\nu_{1/2}$ = 1350 Hz).

Solution ^{19}F NMR Characterization of the $Re_2O_4F_5^+$ Cation. The $ReO_2F_3 \cdot SbF_5$ adduct undergoes self-dissociation in SO_2ClF to form the fluorine-bridged $Re_2O_4F_5^+$ cation (Structure II) according to equation (5.2). Similar fluorine-bridged cations have been observed when $ReOF_5$ and *cis*-OsO_2F_4 were allowed to react with AsF_5 or SbF_5, forming the $Re_2O_2F_9^+$ [46] and $Os_2O_4F_7^+$ [63] cations, respectively. The $Re_2O_4F_5^+$ cation has been

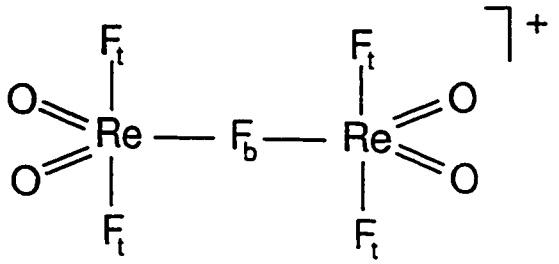

Structure II

$$2\ ReO_2F_3{\cdot}SbF_5 \xrightarrow{SO_2ClF} Re_2O_4F_5^+Sb_2F_{11}^- \qquad (5.2)$$

previously detected as a minor species (2% of the maximum intensity) in the mass spectrum of ReO_2F_3, along with $ReO_2F_2^+$ (100%), $ReO_2F_3^+$ (2%) and other $ReO_xF_y^+$ cations.

The ^{19}F NMR spectrum of this solution at 30 °C (Figure 5.1) consists of a doublet and quintet, with a terminal to bridging fluorine coupling constant $^2J(^{19}F_t\text{-}^{19}F_b)$ = 105 Hz and relative integrated intensities of 4.0:1.0, consistent with the fluorine-bridged $Re_2O_4F_5^+$ cation. An exchange-averaged resonance was also observed at -117.8 ppm ($\Delta\nu_{1/2}$ = 3750 Hz) and was assigned to the $Sb_2F_{11}^-$ anion. The insolubility of $ReO_2F_3{\cdot}SbF_5$ precluded the acquisition of NMR spectra at lower temperatures. The chemical shift of the four equivalent fluorines in the ^{19}F NMR spectrum of $Re_2O_4F_5^+$ (23.3 ppm; doublet) is very similar to the chemical shift of the $ReO_2F_2^+$ moiety observed for HF solutions of ReO_2F_3 acidified with AsF_5 or SbF_5 (*vide supra*). The bridging fluorine environment (-152.2 ppm; quintet) is highly shielded which is a feature in common with other fluorine-

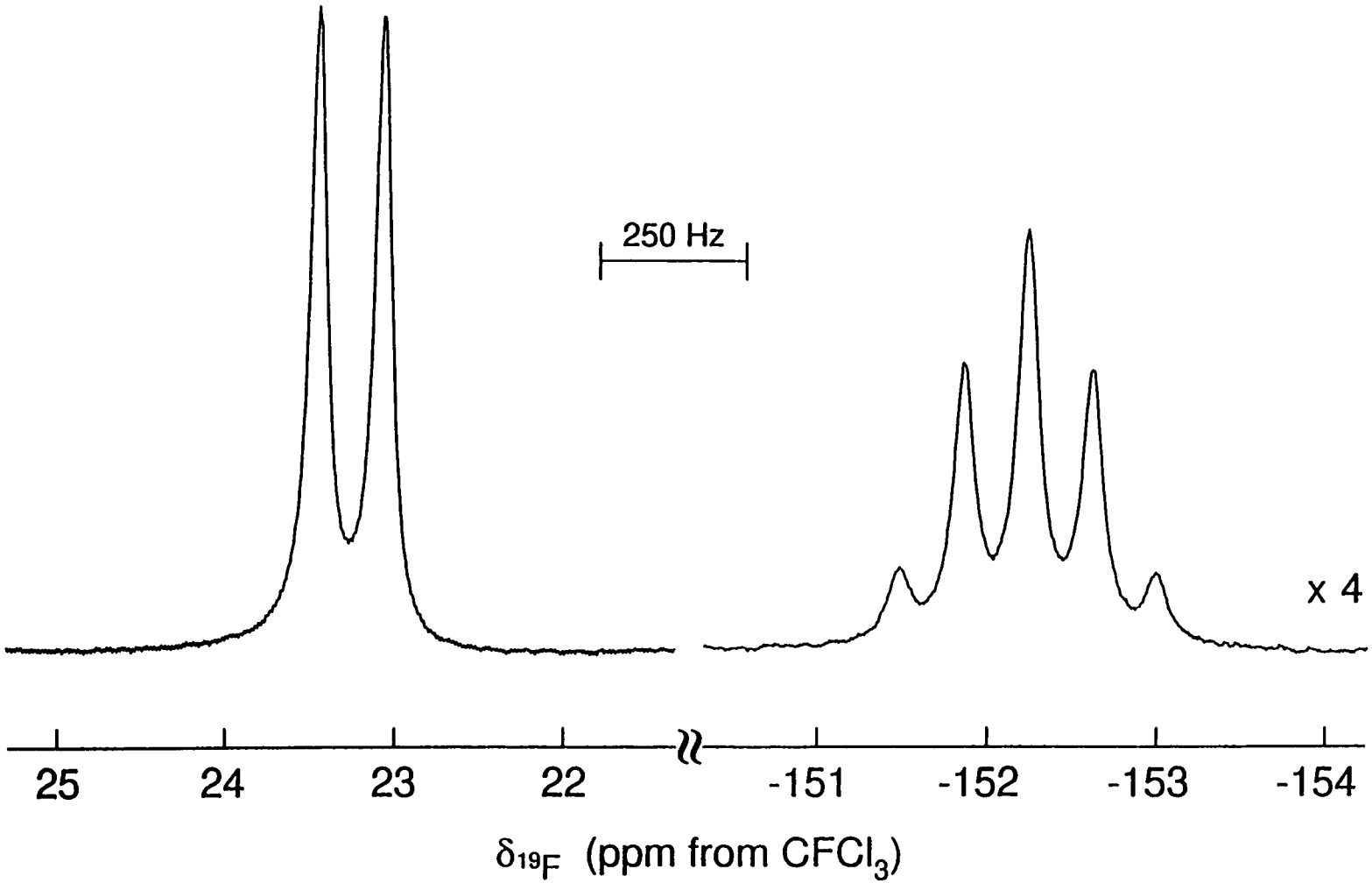

Figure 5.1. ^{19}F NMR spectrum (282.409 MHz) of $ReO_2F_3 \cdot SbF_5$ dissolved in SO_2ClF solvent recorded at 30 °C.

bridged transition metal oxofluoro-species, e.g., $W_2O_2F_9^-$,[105] $Mo_2O_2F_9^-$,[135] $Os_2O_4F_7^+$,[63] and $Re_2O_4F_7^-$ (see Chapter 4). Although $ReOF_5$ would result in the same relative signal integrations and multiplicities, this interpretation can be rejected because the fluorine-fluorine spin-coupling (105 Hz) is significantly larger than that reported for $ReOF_5$ (69 Hz)[15] and the chemical shifts of $ReOF_5$ occur at significantly higher frequencies (183.4 and -36.0 ppm in HF[53]; 199.0 and -3.7 ppm in WF_6 [15]). The $^2J(^{19}F_t\text{-}^{19}F_b)$ coupling constant in $Re_2O_4F_5^+$ is larger in $Re_2O_4F_7^-$ (75 Hz) and $Os_2O_4F_7^+$ (72 Hz), which is attributed to the different ligand geometry around the metal atoms, i.e., pseudotrigonal bipyramidal for $Re_2O_4F_5^+$ versus pseudooctahedral for $Re_2O_4F_7^-$ and $Os_2O_4F_7^+$. No other oxofluorides of the type $M_2O_4F_5$ or $M_2O_2F_7$ have been characterized by NMR spectroscopy but the structures of the $V_2O_4F_5^{3-}$ and $V_2O_2F_7^{3-}$ anions[155] have been determined by X-ray crystallography and consist of face-sharing VO_2F_4 and VOF_5 octahedra, respectively, having three bridging fluorine ligands. The $U_2O_4F_5^-$ anion has also been reported[156] but no detailed structural data is available other than an infrared spectrum consistent with the linear geometry adopted by the UO_2 group, as observed in all other U(VI) dioxo complexes. The $Re_2O_4F_5^+$ cation, which was only observed in SO_2ClF solution, forms the polymeric adduct $ReO_2F_3{\cdot}SbF_5$ upon crystallization (see ***X-ray Crystal Structures of $TcO_2F_3{\cdot}SbF_5$ and $ReO_2F_3{\cdot}SbF_5$***) and recovery from SO_2ClF as determined by Raman spectroscopy. The Tc analog of the dinuclear cation, $Tc_2O_4F_5^+$, was not observed because of the insolubility of $TcO_2F_3{\cdot}SbF_5$ in SO_2ClF.

X-ray Crystal Structures of $TcO_2F_3 \cdot SbF_5$ and $ReO_2F_3 \cdot SbF_5$. Details of the data collection parameters and other crystallographic information are given in Table 5.1. The final atomic coordinates and the equivalent thermal parameters for $TcO_2F_3 \cdot SbF_5$ and $ReO_2F_3 \cdot SbF_5$ are summarized in Tables 5.2 and 5.3, respectively. Important bond lengths, corresponding bond valences and bond angles for $TcO_2F_3 \cdot SbF_5$ and $ReO_2F_3 \cdot SbF_5$ are listed in Tables 5.4 and 5.5.

The structures of $TcO_2F_3 \cdot SbF_5$ and $ReO_2F_3 \cdot SbF_5$ consist of infinite chains of MO_2F_4- and SbF_6-units alternating along the *b*-axis of the unit cell (Figures 5.2 and 5.3). The oxygen atoms are *cis* to each other and *trans* to the bridging fluorine atoms, whereas the bridging fluorine atoms on antimony are *trans* to each other. Both structures are closely related to that of the $MoOF_4 \cdot SbF_5$ adduct[146] which also consists of infinite chains of alternating $MoOF_5$- and SbF_6-units in which the oxygen atom is *trans* to a fluorine bridge and the bridging fluorines on antimony are *trans* to each other. The rhenium analog consists of two $ReOF_4 \cdot SbF_5$ units linked by fluorine bridges forming a distorted eight-membered ring.[146]

The Tc-O bond lengths (1.640(6) and 1.643(5) Å) in $TcO_2F_3 \cdot SbF_5$ are characteristic of a Tc-O double bond and are similar in length to the Tc-O bonds found in TcO_2F_3 (1.646(9) Å)[41] but slightly shorter than the Tc-O bond lengths in $Li^+TcO_2F_4^-$ (1.660(4) Å), Tc_2O_7 (1.672(8) Å, terminal)[108] and $N(CH_3)_4^+TcO_4^-$ (1.676(8) Å).[109] The Tc-F_t bond lengths (1.800(5) and 1.804(5) Å) are shorter than the terminal Tc-F bond lengths in TcO_2F_3 (1.834(7) Å)[41] and $Li^+TcO_2F_4^-$ (1.876(3) Å). The Tc-F_b bond lengths (2.217(4) and 2.222(4) Å) are significantly longer than the Tc-F bridging bonds in TcO_2F_3 (average,

Table 5.1. Summary of Crystal Data and Refinement Results for $TcO_2F_3 \cdot SbF_5$, $ReO_2F_3 \cdot SbF_5$ and $TcO_2F_3 \cdot XeO_2F_2$

	$TcO_2F_3 \cdot SbF_5$	$ReO_2F_3 \cdot SbF_5$	$TcO_2F_3 \cdot XeO_2F_2$
space group	$P2_1/n$ (14)	$P2_1/c$ (14)	$Cmc2_1$ (36)
a (Å)	7.366(2)	5.479(1)	7.895(2)
b (Å)	10.441(2)	10.040(2)	16.204(3)
c (Å)	9.398(2)	12.426(2)	5.198(1)
β (°)	93.32(3)	99.01(3)	90.0
V (Å^3)	721.6(3)	675.1(2)	665.0(2)
molecules/unit cell	4	4	4
molecular wt (g mol^{-1})	404.64	491.94	389.19
calcd density (g cm^{-3})	3.717	4.840	3.878
T (°C)	24	-50	-100
colour	yellow	colourless	yellow
μ (mm^{-1})	8.01	11.83	9.22
wavelength (Å)	0.56086	0.56086	0.56086
final agreement factors	R^a = 0.0649	R^a = 0.0533	R^a = 0.0402
	wR_2 [b] = 0.1112	wR_2 [b] = 0.1158	wR_2 [b] = 0.0822

[a] $R = \Sigma||F_o|-|F_c||/\Sigma|F_o|$

[b] $wR_2 = [\Sigma[w(F_o^2-F_c^2)^2]/\Sigma[w(F_o^2)^2]]^{1/2}$

Table 5.2. Final Atomic Coordinates ($\times 10^4$) and Equivalent Isotropic Displacement Coefficients ($Å^2 \times 10^3$) for $TcO_2F_3 \cdot SbF_5$

	x	*y*	*z*	U_{eq}[a]
Tc(1)	-1310.9(7)	-1725.3(5)	3371.6(6)	26.2(1)
Sb(1)	2836.4(6)	217.7(4)	1873.7(5)	26.5(1)
O(1)	-2153(7)	-286(6)	3098(6)	40(1)
O(2)	-2870(8)	-2446(6)	4262(7)	50(2)
F(1)	-1720(7)	-2447(5)	1644(5)	44(1)
F(2)	342(6)	-1381(5)	4813(5)	41(1)
F(3)	4595(6)	1524(4)	1499(6)	42(1)
F(4)	1090(6)	-1101(4)	2235(5)	39(1)
F(5)	1081(8)	1436(6)	2117(9)	74(2)
F(6)	3508(9)	312(8)	3784(6)	74(2)
F(7)	4572(6)	-1017(5)	1628(7)	51(1)
F(8)	2164(7)	124(5)	-48(5)	51(1)

[a] Equivalent isotropic *U* defined as one third of the trace of the orthogonalized $\mathbf{U}_{ij}$ tensor.

Table 5.3. Final Atomic Coordinates ($\times 10^4$) and Equivalent Isotropic Displacement Coefficients ($Å^2 \times 10^3$) for $ReO_2F_3 \cdot SbF_5$

	x	*y*	*z*	U_{eq}[a]
Re(1)	3383.2(5)	2388.4(2)	7172.7(2)	8.65(6)
Sb(1)	0	0	5000	8.7(1)
Sb(2)	0	5000	5000	8.2(1)
O(1)	4118(12)	3289(6)	8300(5)	16(1)
O(2)	4822(12)	962(6)	7486(5)	15.1(9)
F(1)	245(9)	1894(5)	7316(4)	14.5(8)
F(2)	5440(10)	3144(5)	6327(4)	16.5(8)
F(3)	-1935(9)	-1548(5)	4445(4)	12.6(7)
F(4)	-1149(9)	5989(5)	3666(4)	14.0(8)
F(5)	2554(10)	4302(6)	4358(4)	16.1(8)
F(6)	-759(10)	794(5)	3637(4)	14.6(8)
F(7)	2776(9)	-748(5)	4588(4)	15.3(8)
F(8)	-1933(10)	3565(5)	4474(4)	16.6(8)

[a] Equivalent isotropic *U* defined as one third of the trace of the orthogonalized U_{ij} tensor.

Table 5.4. Bond Lengths (Å), Bond Valences (v.u.) and Bond Angles (deg) in $TcO_2F_3 \cdot SbF_5$

Bond Lengths (Å) and Corresponding Bond Valences (v.u.)[a]						
Tc(1)	O(1)	O(2)	F(1)	F(2)	F(3)	F(4)
Bond valence	1.965	1.949	1.084	1.073	0.351	0.347
Bond length	1.640(6)	1.643(5)	1.800(5)	1.804(5)	2.217(4)	2.222(4)
Total bond valence: 6.77						
Sb(1)	F(3)	F(4)	F(5)	F(6)	F(7)	F(8)
Bond valence	0.704	0.702	0.895	0.898	0.890	0.871
Bond length	1.927(4)	1.928(4)	1.838(5)	1.837(5)	1.840(5)	1.848(5)
Total bond valence: 4.96						

Bond Angles (deg)			
O(1)-Tc(1)-O(2)	103.3(3)	F(3)-Sb(1)-F(4)	179.4(2)
O(1)-Tc(1)-F(1)	101.6(3)	F(3)-Sb(1)-F(5)	91.0(2)
O(1)-Tc(1)-F(2)	99.6(3)	F(3)-Sb(1)-F(6)	89.7(3)
O(1)-Tc(1)-F(3)	166.2(2)	F(3)-Sb(1)-F(7)	89.6(2)
O(1)-Tc(1)-F(4)	87.7(2)	F(3)-Sb(1)-F(8)	90.2(2)
O(2)-Tc(1)-F(1)	100.5(3)	F(4)-Sb(1)-F(5)	89.5(2)
O(2)-Tc(1)-F(2)	99.8(3)	F(4)-Sb(1)-F(6)	90.6(2)
O(2)-Tc(1)-F(3)	90.4(2)	F(4)-Sb(1)-F(7)	89.8(2)
O(2)-Tc(1)-F(4)	169.0(3)	F(4)-Sb(1)-F(8)	89.4(2)
F(1)-Tc(1)-F(2)	146.2(2)	F(5)-Sb(1)-F(6)	89.6(4)

Table 5.4. continued

F(1)-Tc(1)-F(3)	76.7(2)	F(5)-Sb(1)-F(7)	179.3(2)
F(1)-Tc(1)-F(4)	77.6(2)	F(5)-Sb(1)-F(8)	90.4(3)
F(2)-Tc(1)-F(3)	76.5(2)	F(6)-Sb(1)-F(7)	90.6(3)
F(2)-Tc(1)-F(4)	77.4(2)	F(6)-Sb(1)-F(8)	179.9(3)
F(3)-Tc(1)-F(4)	78.5(2)	F(7)-Sb(1)-F(8)	89.4(3)
Tc(1A)-F(3)-Sb(1)	163.4(3)	Tc(1)-F(4)-Sb(1)	148.6(3)

[a]Bond valence units (v.u.) are defined in ref. 110. R_0 = 1.89 (Tc(VII)=O), R_0 = 1.83 (Tc(VII)-F), R_0 = 1.797 (Sb(V)-F) were used along with B = 0.37; Brown, I.D. Department of Physics, McMaster University, Hamilton, Ontario L8S 4M1, Canada, private communication.

Table 5.5. Bond Lengths (Å), Bond Valences (v.u.) and Bond Angles (deg) in $ReO_2F_3 \cdot SbF_5$

Bond Lengths (Å) and Corresponding Bond Valences (v.u.)[a]						
Re(1)	O(1)	O(2)	F(1)	F(2)	F(3)	F(4)
Bond valence	2.126	2.063	1.030	1.036	0.364	0.374
Bond length	1.651(6)	1.662(6)	1.825(5)	1.823(5)	2.210(5)	2.200(5)
Total bond valence: 6.99						
Sb(1)		F(3,3A)	F(6,6A)	F(7,7A)		
Bond valence		0.670	0.846	0.893		
Bond length		1.945(4)	1.859(5)	1.839(5)		
Total bond valence: 4.82						
Sb(2)		F(4,4A)	F(5,5A)	F(8,8A)		
Bond valence		0.661	0.860	0.878		
Bond length		1.950(5)	1.853(5)	1.846(5)		
Total bond valence: 4.80						

Bond Angles (deg)			
O(1)-Re(1)-O(2)	103.2(3)	F(2)-Re(1)-F(3)	78.5(2)
O(1)-Re(1)-F(1)	100.0(3)	F(2)-Re(1)-F(4)	76.5(2)
O(1)-Re(1)-F(2)	99.8(3)	F(3)-Re(1)-F(4)	76.0(2)
O(1)-Re(1)-F(3)	168.2(2)	F(3)-Sb(1)-F(6)	89.3(2)

Table 5.5. continued

O(1)-Re(1)-F(4)	92.3(2)	F(3)-Sb(1)-F(7)	90.2(2)
O(2)-Re(1)-F(1)	99.4(3)	F(6)-Sb(1)-F(7)	89.9(3)
O(2)-Re(1)-F(2)	100.5(3)	F(4)-Sb(2)-F(5)	89.5(2)
O(2)-Re(1)-F(3)	88.5(2)	F(4)-Sb(2)-F(8)	90.3(2)
O(2)-Re(1)-F(4)	164.5(2)	F(5)-Sb(2)-F(8)	89.0(2)
F(1)-Re(1)-F(2)	147.8(2)	Re(1)-F(3)-Sb(1)	136.5(2)
F(1)-Re(1)-F(3)	77.0(2)	Re(1)-F(4)-Sb(2)	149.5(3)
F(1)-Re(1)-F(4)	77.6(2)		

[a]Bond valence units (v.u.) are defined in ref. 110. R_0 = 1.930 (Re(VII)=O), R_0 = 1.836 (Re(VII)-F), R_0 = 1.797 (Sb(V)-F) were used along with B = 0.37.

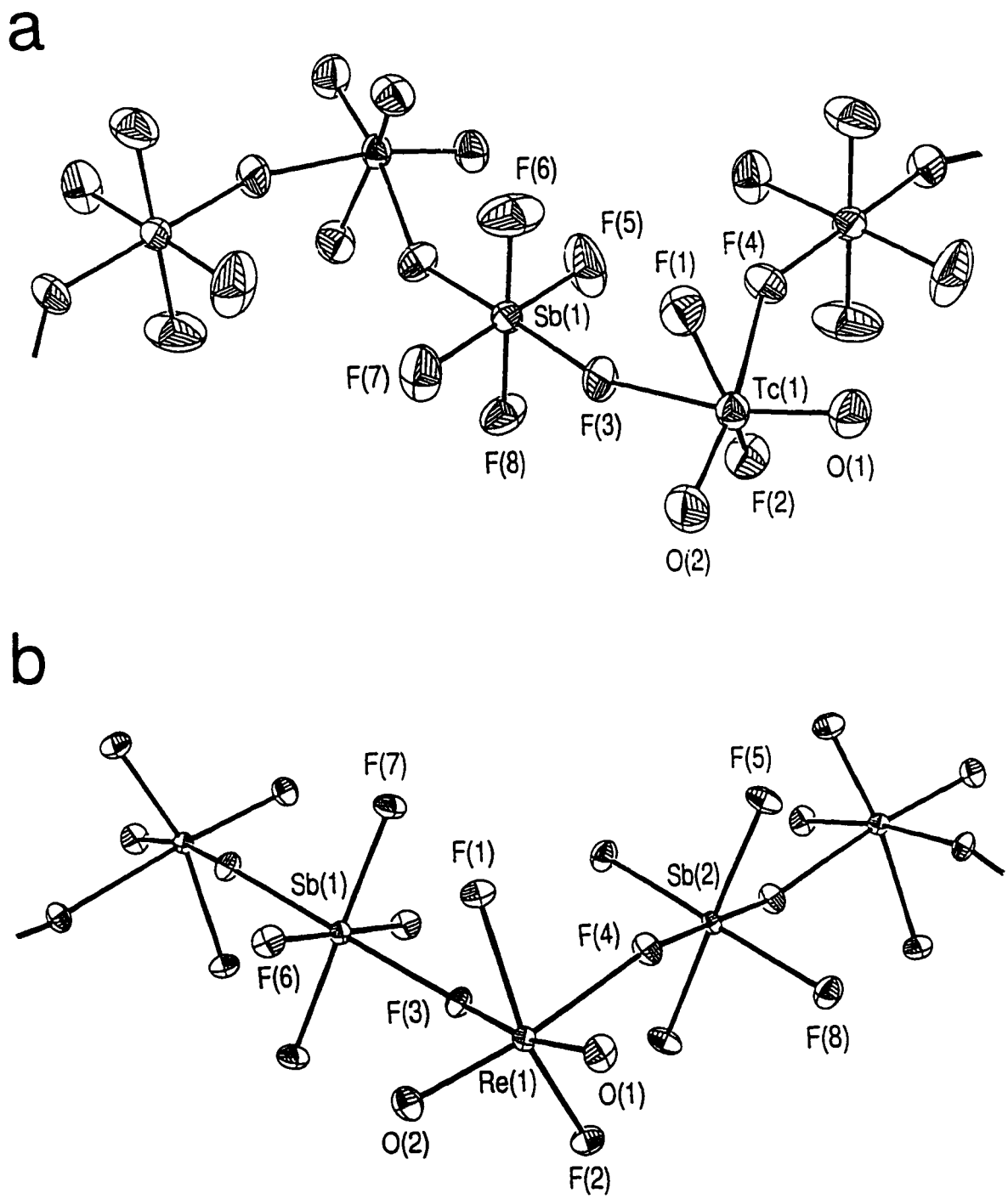

Figure 5.2. Structures of (a) $TcO_2F_3 \cdot SbF_5$ and (b) $ReO_2F_3 \cdot SbF_5$ with thermal ellipsoids at the 50% probability level.

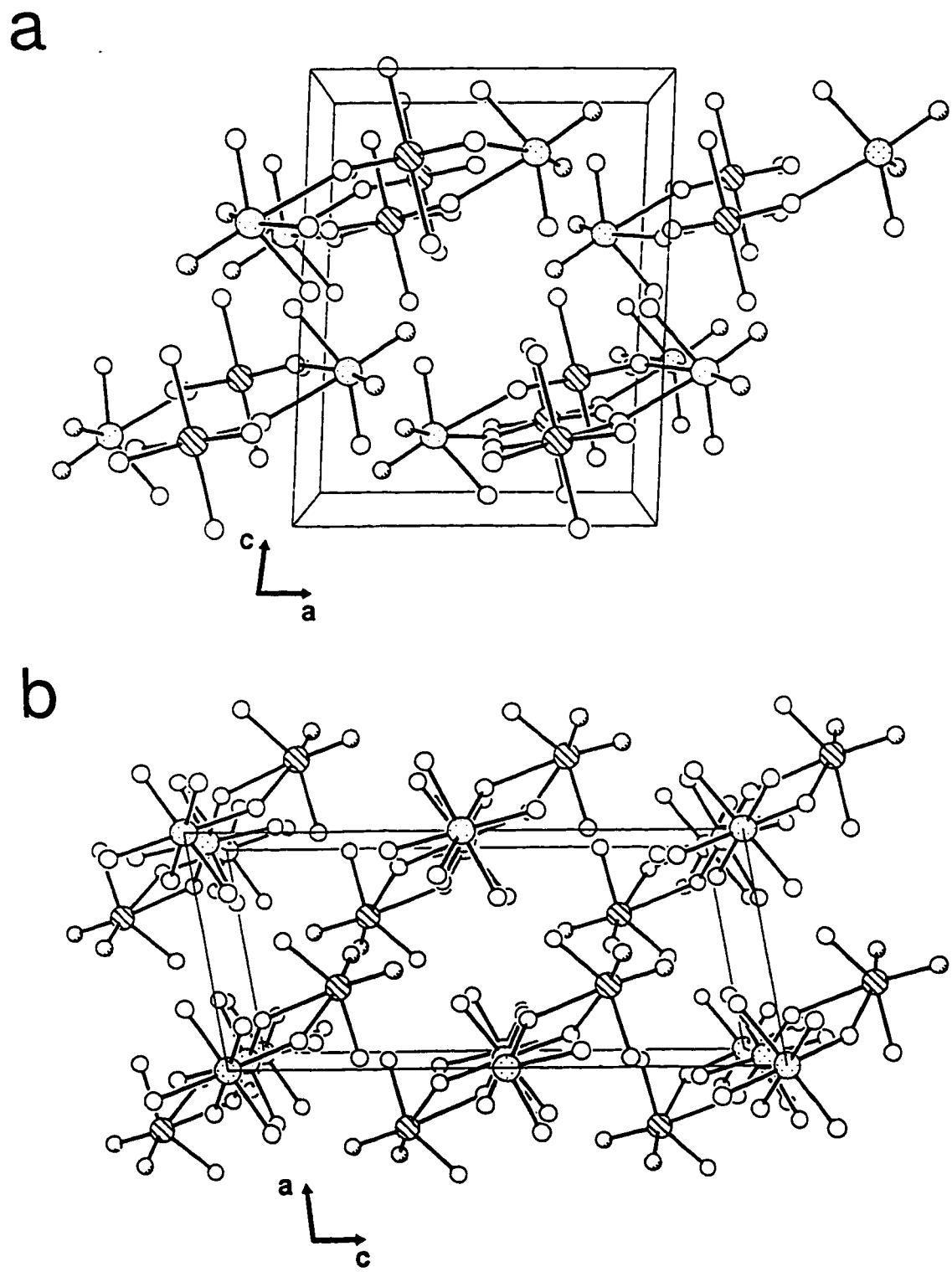

Figure 5.3. View of unit cells of (a) $TcO_2F_3 \cdot SbF_5$ and (b) $ReO_2F_3 \cdot SbF_5$ showing the packing along the *b*-axis.

2.080(5) Å). The decrease in the Tc-F_t and Tc-O bond lengths in the $TcO_2F_3 \cdot SbF_5$ adduct relative to the model compounds is consistent with the expected increase in covalent character of these bonds resulting from the formal removal of a fluoride ion from TcO_2F_3 by SbF_5. The terminal Sb-F_t bond lengths (average, 1.842(6) Å) are slightly longer that the terminal Sb-F bond lengths in $MoOF_4 \cdot SbF_5$ (average, 1.817(7))[146] and the Sb-F_b bond lengths (1.927(4) and 1.928(4) Å) are similar to the bridging Sb-F bond lengths in $MoOF_4 \cdot SbF_5$ (average 1.936(6) Å).

The Re-O bond lengths in $ReO_2F_3 \cdot SbF_5$ (1.651(6) and 1.662(6) Å) are characteristic of a Re-O double bond and similar to the Re-O bond lengths found in $Li^+ReO_2F_4^-$ (1.678(9) Å), ReO_2F_3 in $K^+Re_2O_4F_7^- \cdot 2ReO_2F_3$ (1.672(9) and 1.680(9) Å), $Cs^+Re_3O_6F_{10}^-$ (1.672(11)-1.708(9) Å), Re_2O_7 (1.65(3)-1.73(3) Å)[145] and $Re_2O_2F_9^+Sb_2F_{11}^-$ (1.63(2) Å).[46] The Re-F_t bond lengths in $ReO_2F_3 \cdot SbF_5$ (1.823(5) and 1.825(5) Å) are shorter than the terminal Re-F bond lengths in $Li^+ReO_2F_4^-$ (1.867(8) Å), ReO_3F (1.859(8) Å)[9] and $ReOF_4 \cdot SbF_5$ (1.841(15) Å).[146] The Re-F_b bond lengths (2.200(5) and 2.210(5) Å) are comparable to the Re-F bridging bond in $ReOF_4 \cdot SbF_5$ (*trans* to O, 2.231(15) Å),[146] but longer than in ReO_2F_3 in $K^+Re_2O_4F_7^- \cdot 2ReO_2F_3$ (2.085(6) and 2.119(7) Å) and in $Re_2O_2F_9^+$ (2.060(4) Å).[46] The Sb-F_t bond lengths (average, 1.849(5) Å) are equal to those in $TcO_2F_3 \cdot SbF_5$ (*vide supra*) but the Sb-F_b bond lengths (1.945(4) and 1.950(5) Å) are slightly longer than those in $TcO_2F_3 \cdot SbF_5$, consistent with the stronger Lewis acid character of ReO_2F_3 relative to that of TcO_2F_3 as evident from the solvolytic behaviour of $ReO_2F_4^-$ and $TcO_2F_4^-$ in HF.

The bond valences for individual bonds, as defined by Brown,[110] are given in Tables 5.4 and 5.5 for $TcO_2F_3 \cdot SbF_5$ and $ReO_2F_3 \cdot SbF_5$, respectively. The total bond valence for the technetium atom is 6.77 v.u. (bond valence units), with contributions of 1.96 v.u./oxygen atom, 1.08 v.u./terminal fluorine atom and 0.35 v.u./bridging fluorine atom. The values for the Tc-O double bond and the Tc-F_t bond are slightly higher than in TcO_2F_3 (1.94 and 0.99 v.u., respectively).[41] On the other hand, the bond valence for the Tc-F_b bond is significantly smaller than in TcO_2F_3 (0.51 v.u.)[41] and is consistent with a Lewis acid-base adduct in which TcO_2F_3 acts as the Lewis base. The total bond valence for the rhenium atom in $ReO_2F_3 \cdot SbF_5$ is 6.99 v.u., with contributions of 2.09 v.u./oxygen atom, 1.03 v.u./terminal fluorine atom and 0.37 v.u./bridging fluorine atom. These values are comparable to those for $TcO_2F_3 \cdot SbF_5$.

The octahedra formed by the light atoms in $TcO_2F_3 \cdot SbF_5$ and $ReO_2F_3 \cdot SbF_5$ are relatively undistorted having average $F_t \cdots F_b$, $F_b \cdots F_b$, $F_t \cdots O$, $F_b \cdots O$ and $O \cdots O$ distances of 2.525(7), 2.809(6), 2.647(8), 2.738(7) and 2.575(9) Å, respectively, for $TcO_2F_3 \cdot SbF_5$ and 2.536(7), 2.714(7), 2.667(8), 2.767(8) and 2.598(9), respectively, for $ReO_2F_3 \cdot SbF_5$. The VSEPR model of molecular geometry[111] provides a satisfactory explanation for the distortion observed for the coordination sphere of the metal atom. The greater spatial requirement of the oxygen double bond domains and their repulsive interactions with single bond pair domains at approximately right angles to them in the [O, F_t, F_t, F_b]-planes causes a bending of the F_t-M-F_t angle away from the oxygen atoms. This angle is 146.2(2)° in $TcO_2F_3 \cdot SbF_5$ and 147.8(2)° in $ReO_2F_3 \cdot SbF_5$ and represents a significantly larger deviation from the ideal 180° angle than is found in TcO_2F_3 (154.9(3)-155.9(3)°),[41]

$Li^+TcO_2F_4^-$ (164.2(3)°), ReO_2F_3 in $K^+Re_2O_4F_7^-2ReO_2F_3$ (153.0(3)°) and $Li^+ReO_2F_4^-$ (162.9(6)°). The difference is consistent with the shorter, more covalent M-O bonds of $TcO_2F_3{\cdot}SbF_5$ and $ReO_2F_3{\cdot}SbF_5$, which is reflected in their larger bond valence values and results in stronger bond-pair bond-pair repulsions than in TcO_2F_3 and $Li^+ReO_2F_4^-$.

The significant variation in the M-F_b-M bridging angles within and between the two structures is noteworthy: 163.4(3) and 148.6(3)° for $TcO_2F_3{\cdot}SbF_5$; 149.5(3) and 136.5(2)° for $ReO_2F_3{\cdot}SbF_5$. These bridging angles, which are intermediate between those predicted for hexagonal (132°) and cubic (180°) closest packing of the fluorine atoms,[130] were also observed to vary widely in similar structures such as TcO_2F_3 (range: 140.5(3)-153.8(3)°) and $Cs^+Re_3O_6F_{10}^-$ (178.7(6) and 140.5(4)°) and seem to be mainly the result of packing effects.

Raman Spectra of $TcO_2F_3{\cdot}PnF_5$ and $ReO_2F_3{\cdot}PnF_5$. The Raman spectra of $TcO_2F_3{\cdot}PnF_5$ and $ReO_2F_3{\cdot}PnF_5$ (Pn = As, Sb) are shown in Figures 5.4 and 5.5. The observed frequencies and their assignments are listed in Table 5.6. In accordance with the crystal structures of $TcO_2F_3{\cdot}SbF_5$ and $ReO_2F_3{\cdot}SbF_5$, in which the bridging fluorines are *cis* to each other on the transition metal and *trans* to each other on the Sb, the spectra were interpreted in terms of the local symmetries of the MO_2F_4-units (C_{2v} point symmetry) and the PnF_6-units (D_{4h} point symmetry). The 15 vibrational modes of the MO_2F_4-units belong to the irreducible representation $6A_1 + 2A_2 + 4B_1 + 3B_2$ (the [O, O, M, F, F]-plane is taken as the $\sigma_v(xz)$-plane with the z-axis as the principal axis) and are all Raman-active and the A_1, B_1 and B_2 modes are infrared-active. The vibrational modes for the PnF_6-units

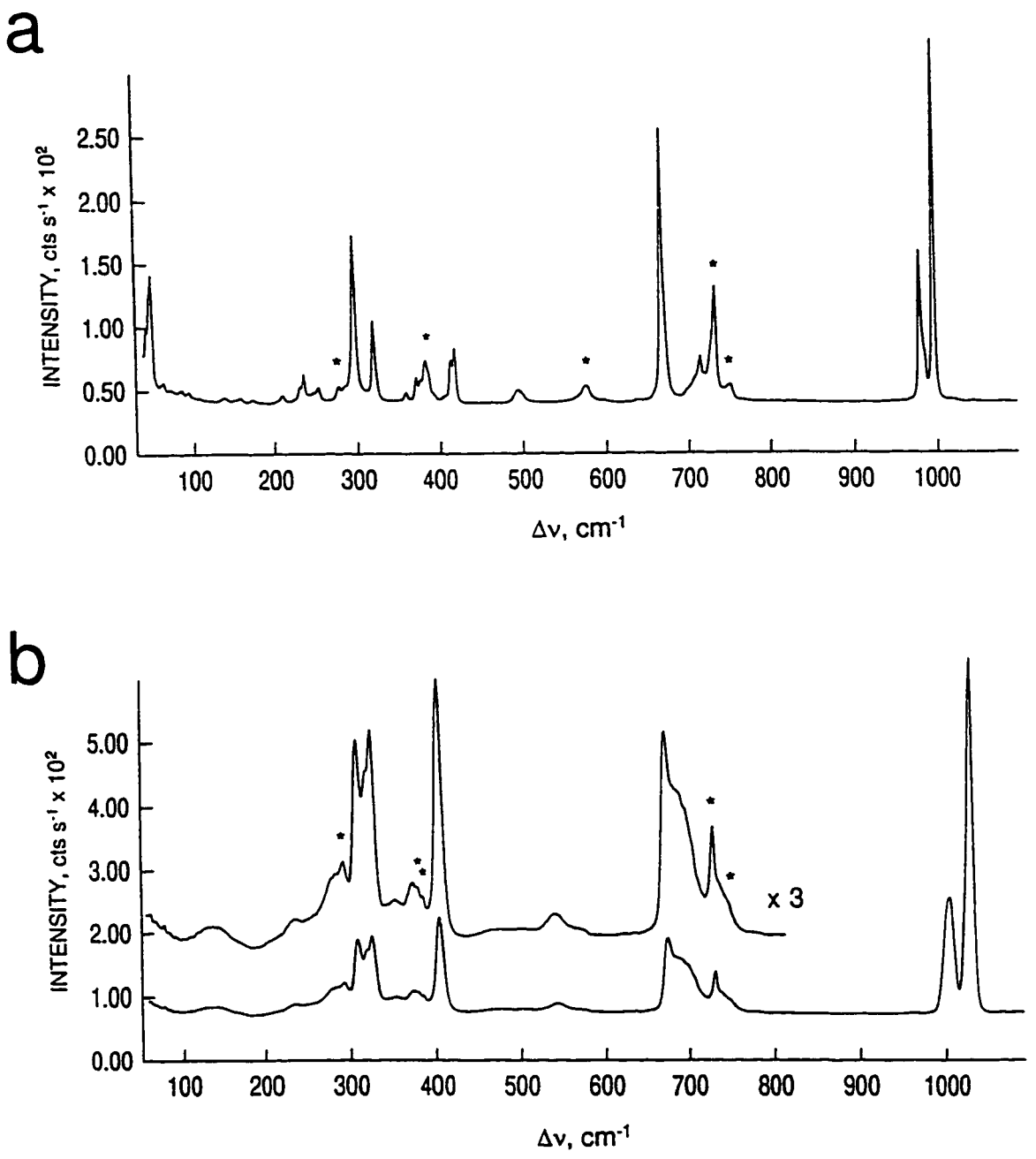

Figure 5.4. Raman spectra of microcrystalline (a) $TcO_2F_3 \cdot AsF_5$ and (b) $ReO_2F_3 \cdot AsF_5$ recorded in FEP at -150 °C using 514.5-nm excitation. Asterisks (*) denote FEP lines.

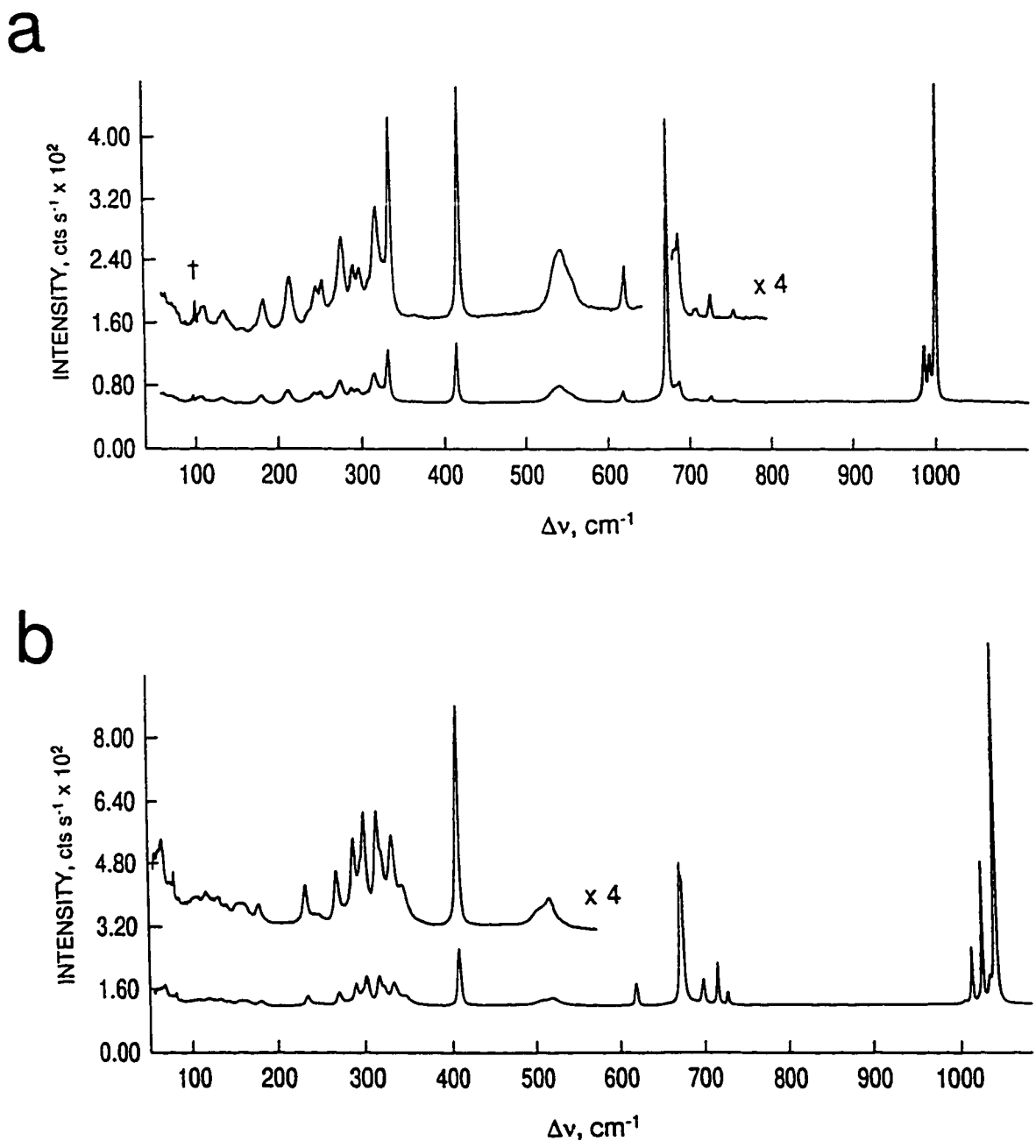

Figure 5.5. Raman spectra of microcrystalline (a) $TcO_2F_3 \cdot SbF_5$ (647.1-nm excitation) and (b) $ReO_2F_3 \cdot SbF_5$ (514.5-nm excitation) recorded in Pyrex melting point capillaries at 20 °C. Dagger (†) denotes a plasma line.

Table 5.6. Raman Frequencies, Assignments and Mode Descriptions for $TcO_2F_3 \cdot PnF_5$ and $ReO_2F_3 \cdot PnF_5$ (Pn = As, Sb)

Frequencies (cm^{-1})[a]				Assignments[b]	
$TcO_2F_3 \cdot AsF_5$[c]	$TcO_2F_3 \cdot SbF_5$[d]	$ReO_2F_3 \cdot AsF_5$[c]	$ReO_2F_3 \cdot SbF_5$[d]	MO_2F_4 (C_{2v})	PnF_6 (D_{4h})
997(100)	995(100)	1035(100)	1040(100)	A_1, $\nu_s(MO_2)$	
972(23),sh	982(14) 972(17)	1009(32)	1025(39) 1013(16)	B_1, $\nu_{as}(MO_2)$	
	746(>0)[e]				
714(15)	721(2)	727(10)	724(4) 713(11)	A_1, $\nu_s(MF_{2t})$	
	699(>0)[e]				
	682(6) 678(5),sh	694(14),sh	696(6) 672(6)	B_2, $\nu_{as}(MF_{2t})$	
669(80)	668(89)	671(20)	670(39)		A_{1g}, $\nu_s(PnF_{4t})$
640(25),sh	613(3)		616(6)		B_{1g}, $\nu_{as}(PnF_{4t})$
576(5)	552(2),sh	570(1),sh	517(2),br	B_1, $\nu_{as}(MF_{2b})$	
492(4)	541(5)	542(2),br	503(1),br	A_1, $\nu_s(MF_{2b})$	A_{1g}, $\nu_s(PnF_{2b})$

Table 5.6. continued

416(21) 413(12),sh	410(19)	411(27)	407(15)	A_1, $\delta(MO_2)$	
370(7)		372(6)			B_{2g}, $\delta(AsF_{4t})$
357(2)	351(4)	342(2)			
319(25)	328(16)	325(21) 318(17),sh	330(6) 318(6),sh	A_1, $\delta(MF_{2t})$	
	312(9)	307(20)	313(8)	B_2, $\rho_w(MO_2)$	
	301(3),sh		298(8)	B_1, $\delta(MF_{2t})$	
295(51)	291(4)	291(8)	294(6),sh	A_2, $\rho_t(MO_2)$	
	286(4)		286(6)		B_{2g}, $\delta(SbF_{4t})$
276(4) 252(4) 246(3),sh	270(6) 248(3) 241(3)	277(6),sh 240(2)	266(4) 245(>0)		
234(9) 230(5),sh	230(1),sh	232(3)	229(3)	B_2, $\rho_w(MF_{2b})$	
208(3)	207(4)	201(1)			

Table 5.6. continued

171(1)	178(3)		176(1)	A_1, $\delta(MF_{2b})$
157(1)			158(1) 151(1)	
136(1)			137(>0)	
120(>0)	127(2)	132(3),br	129(1) 126(>0)	B_1, $\rho_r(MO_2)$
104(>0)	105(2)		114(1) 105(>0) 98(>0)	
92(2) 83(2) 48(42)			89(2) 81(4)	A_2, $\rho_t(MF_{2b})$

[a] Values in parentheses denote relative intensities; sh: shoulder; br: broad.

[b] ν: stretching; δ: in-plane bending; ρ_t: twisting; ρ_r: rocking; ρ_w: wagging. F_t and F_b denote terminal and bridging fluorines, respectively.

[c] Spectrum recorded on microcrystalline solid in FEP at -150 °C using 514.5-nm excitation.

[d] Spectrum recorded on microcrystalline solid in rotating Pyrex glass capillary at 23 °C using 514.5-nm excitation.

[e] These bands may be assigned to formally inactive Raman stretches (E_u and A_{2u}) which are visible because of factor group splitting within the unit cell.

belong to the irreducible representations $2A_{1g} + B_{1g} + B_{2g} + 2A_{2u} + B_{2u} + 2E_u$ of which the A_{1g}, B_{1g} and B_{2g} modes are Raman active and the A_{2u} and E_u modes are infrared-active.

In order to evaluate the degree of vibrational coupling within the unit cells of $TcO_2F_3 \cdot SbF_5$ and $ReO_2F_3 \cdot SbF_5$, factor-group analyses[115] of the vibrational modes of the unit cells were carried out by correlation of the vibrational modes of the MO_2F_4- and SbF_6-units to the crystal symmetries of $TcO_2F_3 \cdot SbF_5$ ($P2_1/n$, C_{2h}) and $ReO_2F_3 \cdot SbF_5$ ($P2_1/c$, C_{2h}) as shown in Tables 5.7 and 5.8. The vibrational modes of the isolated MO_2F_4-units (C_{2v}), when correlated to their site symmetries (C_1) and to the unit cell symmetry (C_{2h}), are each split into Raman active A_g and B_g components and infrared-active A_u and B_u components. The analysis of the SbF_6 modes are more complex. All vibrational modes of the SbF_6-unit in $TcO_2F_3 \cdot SbF_5$ (D_{4h}), when correlated to the site symmetry of SbF_6 (C_1) and the unit cell symmetry (C_{2h}), are active and split into A_g and B_g components in the Raman spectrum and into A_u and B_u components in the infrared spectrum. In addition, ν_5 and ν_9-ν_{11} are further split into two A_g, B_g, A_u and B_u components. The vibrational modes of the SbF_6-unit in $ReO_2F_3 \cdot SbF_5$ (D_{4h}) were correlated to its site symmetry (C_1) and the unit cell symmetry (C_{2h}). The ν_1-ν_4 modes are each expected to split into two A_g components and two B_g components, whereas ν_5 is split into four A_g and four B_g components. In addition, ν_6-ν_8 each split into two A_u and B_u components whereas ν_9-ν_{11} are expected to split into four A_u and B_u components.

The Raman spectra of $TcO_2F_3 \cdot PnF_5$ and $ReO_2F_3 \cdot PnF_5$ were assigned by comparison with the spectra of polymeric TcO_2F_3 and ReO_2F_3 as well as by comparison with $TcO_2F_4^-$

Table 5.7. Correlation Diagrams[a] for the Vibrational Modes of $TcO_2F_3 \cdot SbF_5$

		TcO_2F_4-unit				
		molecule local symmetry	site symmetry	crystal symmetry[b]		
		C_{2v}	C_1	C_{2h}		
4T	$4(\nu_1 - \nu_6)$	A_1	A	A_g (Ra)	$\nu_1 - \nu_{15}$	3R,3T
4R	$4(\nu_7 - \nu_8)$	A_2		B_g (Ra)	$\nu_1 - \nu_{15}$	3R,3T
4T,4R	$4(\nu_9 - \nu_{11})$	B_1		A_u (IR)	$\nu_1 - \nu_{15}$	3R,2T(-T)
4T,4R	$4(\nu_{12} - \nu_{15})$	B_2		B_u (IR)	$\nu_1 - \nu_{15}$	3R,T(-2T)

Table 5.7. continued

SbF_6-unit

		molecule local symmetry	site symmetry	crystal symmetry[b]		
		D_{4h}	C_1	C_{2h}		
	$4(\nu_1 - \nu_2)$	A_{1g}		A_g (Ra)	$\nu_1 - \nu_4, 2\nu_5, \nu_6 - \nu_8, 2(\nu_9 - \nu_{11})$	3R,3T
4R		A_{2g}				
	$4(\nu_3)$	B_{1g}		B_g (Ra)	$\nu_1 - \nu_4, 2\nu_5, \nu_6 - \nu_8, 2(\nu_9 - \nu_{11})$	3R,3T
	$4(\nu_4)$	B_{2g}	A			
4R	$4(\nu_5)$	E_g		A_u (IR)	$\nu_1 - \nu_4, 2\nu_5, \nu_6 - \nu_8, 2(\nu_9 - \nu_{11})$	3R,2T(-T)
4T	$4(\nu_6 - \nu_7)$	A_{2u}				
	$4(\nu_8)$	B_{2u}		B_u (IR)	$\nu_1 - \nu_4, 2\nu_5, \nu_6 - \nu_8, 2(\nu_9 - \nu_{11})$	3R,T(-2T)
4T	$4(\nu_9 - \nu_{11})$	E_u				

[a] The symbols T and R denote translatory and rotatory (external) modes, respectively, and R and IR in parentheses denote Raman and infrared activity, respectively.

[b] Space group $P2_1/n$, Z = 4.

Table 5.8. Correlation Diagrams[a] for the Vibrational Modes of $ReO_2F_3 \cdot SbF_5$

ReO_2F_4-unit

		molecule local symmetry	site symmetry	crystal symmetry[b]		
		C_{2v}	C_1	C_{2h}		
4T	$4(\nu_1 - \nu_6)$	A_1	A	A_g (Ra)	$\nu_1 - \nu_{15}$	3R,3T
4R	$4(\nu_7 - \nu_8)$	A_2		B_g (Ra)	$\nu_1 - \nu_{15}$	3R,3T
4T,4R	$4(\nu_9 - \nu_{11})$	B_1		A_u (IR)	$\nu_1 - \nu_{15}$	3R,2T(-T)
4T,4R	$4(\nu_{12} - \nu_{15})$	B_2		B_u (IR)	$\nu_1 - \nu_{15}$	3R,T(-2T)

Table 5.8. continued

SbF_6-unit

		molecule local symmetry	site symmetry	crystal symmetry[b]		
		D_{4h}	C_i	C_{2h}		
	$4(\nu_1 - \nu_2)$	A_{1g}		A_g (Ra)	$2(\nu_1 - \nu_4),4\nu_5$	6R
4R		A_{2g}				
	$4(\nu_3)$	B_{1g}	A_g	B_g (Ra)	$2(\nu_1 - \nu_4),4\nu_5$	6R
	$4(\nu_4)$	B_{2g}				
4R	$4(\nu_5)$	E_g		A_u (IR)	$2(\nu_6 - \nu_8),4(\nu_9 - \nu_{11})$	5T(-T)
4T	$4(\nu_6 - \nu_7)$	A_{2u}	A_u			
	$4(\nu_8)$	B_{2u}		B_u (IR)	$2(\nu_6 - \nu_8),4(\nu_9 - \nu_{11})$	4T(-2T)
4T	$4(\nu_9 - \nu_{11})$	E_u				

[a] The symbols T and R denote translatory and rotatory (external) modes, respectively, and R and IR in parentheses denote Raman and infrared activity, respectively.

[b] Space group $P2_1/c$, Z = 4.

and $ReO_2F_4^-$ for which the assignments are based on calculated frequencies. The MO_2 symmetric stretching modes are found at 997 and 995 [1035 and 1040] cm^{-1} ($TcO_2F_3 \cdot AsF_5$ and $TcO_2F_3 \cdot SbF_5$ frequencies given with $ReO_2F_3 \cdot AsF_5$ and $ReO_2F_3 \cdot SbF_5$ frequencies in square brackets), whereas the corresponding antisymmetric modes occur at 972 and 972/982 [1009 and 1013/1025] cm^{-1}. The assignment of the symmetric and antisymmetric modes was based upon the relative intensities of the bands. These modes are shifted to significantly higher frequencies compared to their parent compounds TcO_2F_3 (974 and 963 cm^{-1})[41] and ReO_2F_3 (1025 and 994 cm^{-1}). The symmetric terminal MF_{2t} stretches were assigned to the bands at 714 and 721 [727 and 713/724] cm^{-1} and the corresponding antisymmetric modes occur at 678/682 [694 and 672/696] cm^{-1}. These assignments are based on the fact that an increase in frequency is expected with respect to TcO_2F_3 (632, 650, 670 and 685 cm^{-1})[41] and ReO_2F_3 (664, 670, 700 and 713 cm^{-1}) because of the enhanced covalent character of the M-F_t and M-O bonds resulting from the formal removal of a fluoride ion. The antisymmetric and symmetric bridging MF_{2b} stretching modes were assigned to the bands at 576 and 552 [517 and 570] cm^{-1} and 492 and 541 [542 and 503] cm^{-1}, respectively, based on their broad, weak peak profiles, which is a typical feature in the spectra of other fluorine-bridged species. The MO_2 scissoring modes occur at 413/416 and 410 [411 and 407] cm^{-1} which is consistent with the corresponding mode in TcO_2F_3 (411 cm^{-1}) and ReO_2F_3 (412 cm^{-1}). The assignment of the remaining deformation modes are tentative and were based on a comparison with those obtained from local density functional calculations for TcO_2F_3 monomer, $TcO_2F_4^-$, ReO_2F_3 monomer[63] and $ReO_2F_4^-$ as well as the experimental frequencies for matrix-isolated

ReO_2F_3.[112] The symmetric terminal fluorine bond stretching modes for the AsF_6^- and SbF_6^--units were assigned to the high-intensity bands at 669 and 668 [671 and 670] cm^{-1}, respectively. The corresponding antisymmetric modes for the AsF_6^- and SbF_6^--units occur at lower frequency and are assigned to the bands at 640 and 613 [616] cm^{-1}, respectively. The in-plane bending modes of the terminal fluorines in the AsF_6 and SbF_6^--units are found at 370 [372] cm^{-1} and 286 [286] cm^{-1}, respectively, and are in good agreement with the previously reported values.[157]

The Raman spectra of $TcO_2F_3 \cdot PnF_5$ and $ReO_2F_3 \cdot PnF_5$ in anhydrous HF are shown in Figure 5.6 and 5.7. The observed frequencies and their assignments are listed in Table 5.9. Although the high solubilities of the adducts in this solvent suggest ionization into $MO_2F_2^+$ and PnF_6^- anions, strong interactions between the cations and the Lewis bases in solution are likely to occur based on the expected strong Lewis acid character of $TcO_2F_2^+$ and $ReO_2F_2^+$. Consequently, the Raman spectra were interpreted in terms of solvated $MO_2F_2^+$ moieties and PnF_6^- anions. The vibrational modes of $MO_2F_2^+$ (C_{2v} point symmetry) belong to the irreducible representations $4A_1 + A_2 + 2B_1 + 2B_2$, all of which are Raman and infrared-active except A_2 which is only Raman active. The vibrational modes for the PnF_6^- anions (O_h point symmetry) belong to the irreducible representations $A_{1g} + E_g + 2T_{1u} + T_{2g} + T_{2u}$ of which A_{1g}, E_g and T_{2g} are Raman active and T_{1u} and T_{2u} are infrared-active.

The symmetric MO_2 stretching modes were assigned to the polarized bands at 992 and 993 [1037 and 1035] cm^{-1} and the corresponding antisymmetric modes were assigned to the depolarized bands at 972 and 981 [1012 and 1011] cm^{-1}. The polarized bands at

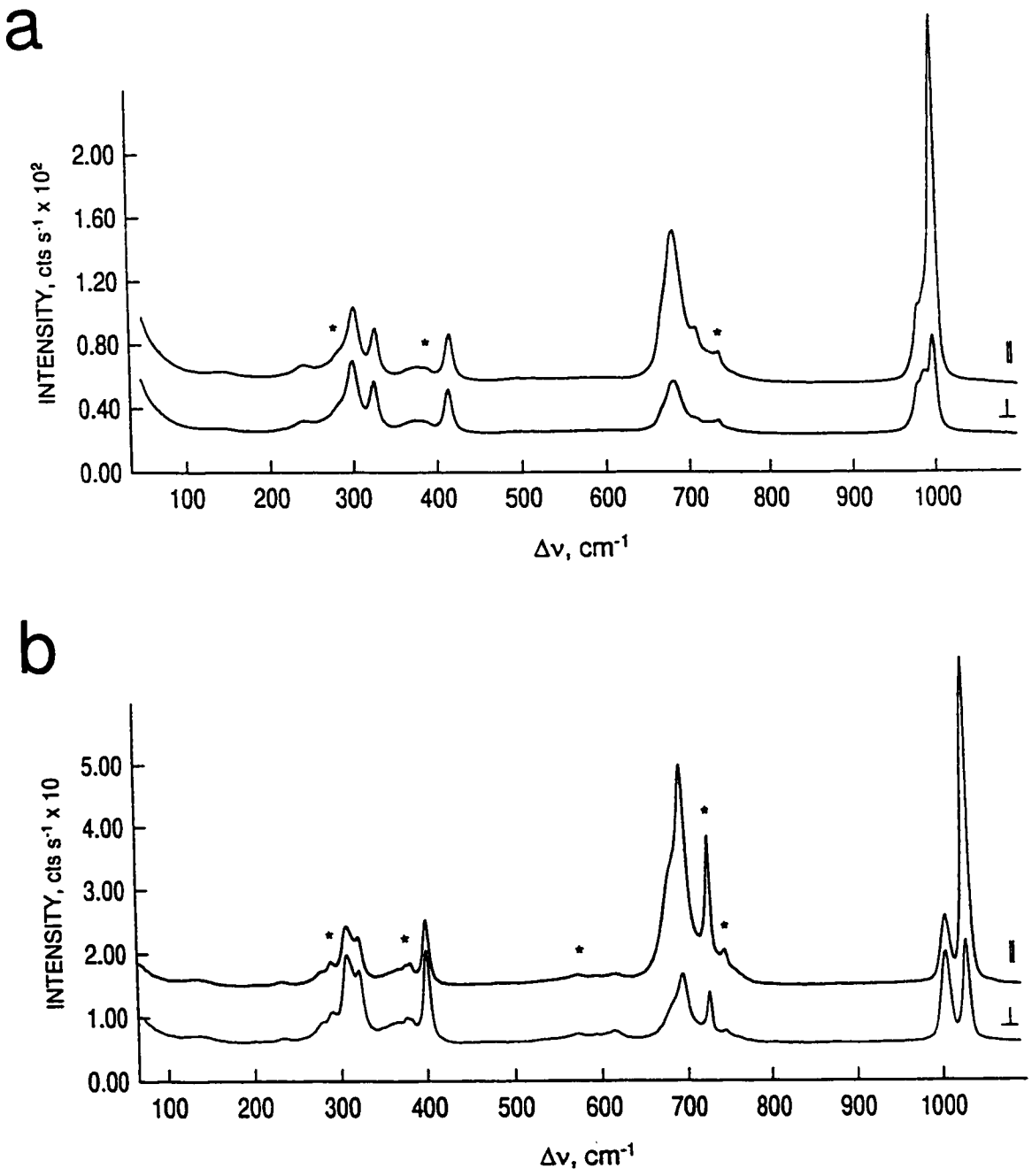

Figure 5.6. Raman spectra of HF solutions of (a) $TcO_2F_3 \cdot AsF_5$ and (b) $ReO_2F_3 \cdot AsF_5$ recorded in FEP at 20 °C using 514.5-nm excitation, with the analyzer oriented parallel (∥) and perpendicular (⊥) to the polarization of the incident beam. Asterisks (*) denote FEP lines.

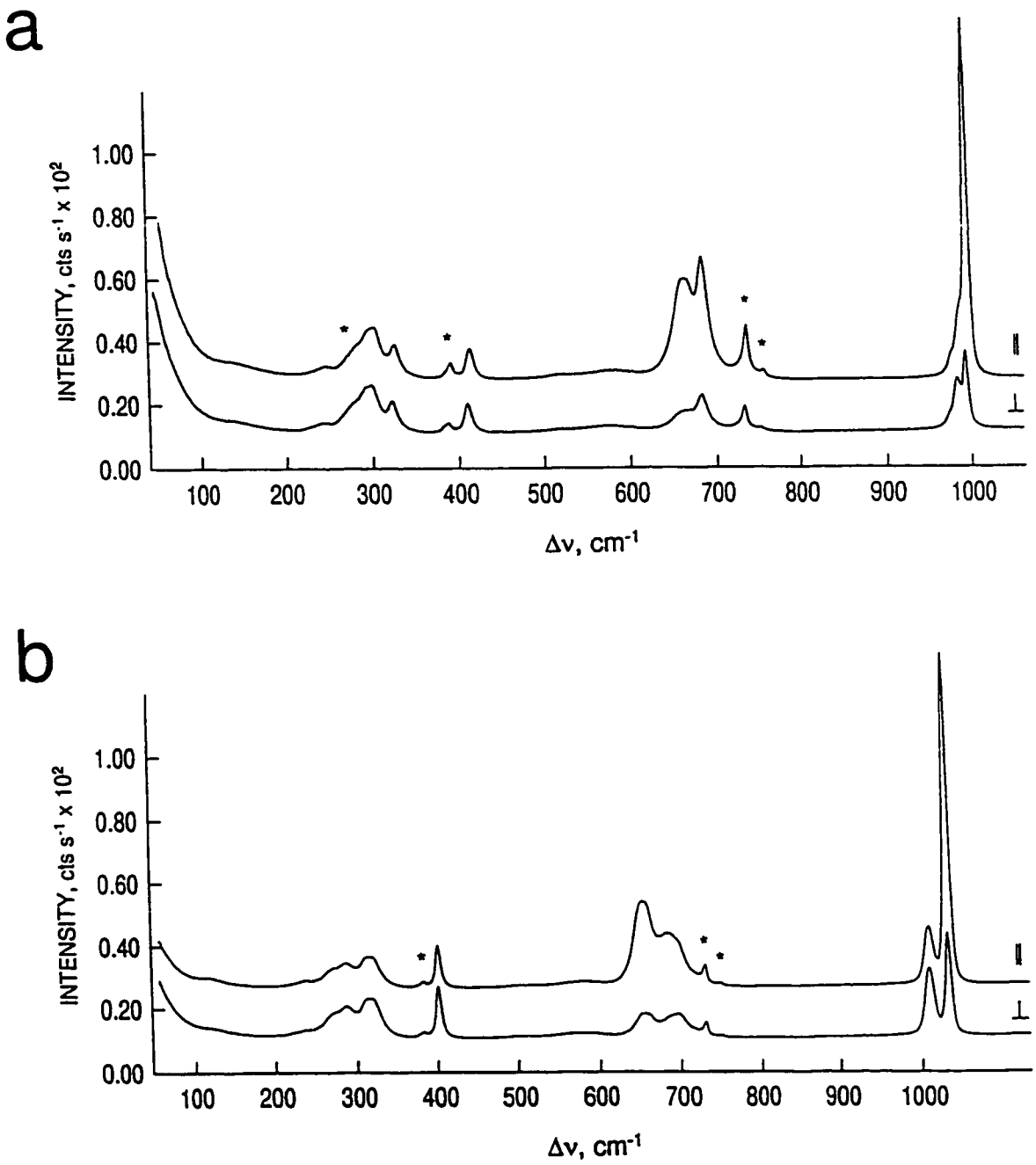

Figure 5.7. Raman spectra of HF solutions of (a) $TcO_2F_3 \cdot SbF_5$ and (b) $ReO_2F_3 \cdot SbF_5$ recorded in FEP at 20 °C using 514.5-nm excitation, with the analyzer oriented parallel (∥) and perpendicular (⊥) to the polarization of the incident beam. Asterisks (*) denote FEP lines.

Table 5.9. Raman Frequencies, Assignments and Mode Descriptions for $TcO_2F_3 \cdot PnF_5$ and $ReO_2F_3 \cdot PnF_5$ (Pn = As, Sb) in HF Solution[a]

Frequencies (cm^{-1})[b]				Assignments[c]	
$TcO_2F_3 \cdot AsF_5$	$TcO_2F_3SbF_5$	$ReO_2F_3AsF_5$	$ReO_2F_3SbF_5$	MO_2F_2 (C_{2v})	PnF_6 (O_h)
992(100),p	993(100),p	1037(100),p	1035(100),p	A_1, $\nu_s(MO_2)$	
972(23),sh,dp	981(18),sh,dp	1012(22),dp	1011(20),dp	B_1, $\nu_{as}(MO_2)$	
701(15)	680(34),p	701(54),p	689(16),p	A_1, $\nu_s(MF_2)$	
676(42),p	655(30),p	687(31),sh,p	658(26),p		A_{1g}, $\nu_s(PnF_6)$
664(25),sh,dp	662(30),sh,dp	620(2),dp		B_2, $\nu_{as}(MF_2)$	
	507(>0),dp		503(>0),dp		E_g, $\nu_{as}(SbF_6)$
409(15),dp	407(10),dp	404(18),dp	403(20),dp	A_1, $\delta(MO_2)$	
375(6),dp		371(5),sh,dp			T_{2g}, $\delta(AsF_4)$
321(17),dp	321(1),dp	325(13),dp	321(12),dp	B_2, $\rho_w(MF_2)$	
295(24),dp	296(15),dp	311(16),dp	321(12),dp	A_1, $\delta(MF_2)$	
	290(15),sh,dp		289(8),dp		T_{2g}, $\delta(SbF_4)$

Table 5.9. continued

	274(10),sh,dp	293(6),dp	277(7),sh,dp	B_1, $\rho_r(MF_2)$
		280(3),dp	239(3),dp	A_2, $\rho_t(MF_2)$
234(6),dp	239(4),dp	236(1),dp	223(2),dp	
132(4),dp		134(2),dp	122(2),dp	

[a] Spectrum of HF solution recorded in FEP at 23 °C using 514.5-nm excitation.

[b] Values in parentheses denote relative intensities; sh: shoulder; br: broad; p: polarized; dp: depolarized.

[c] ν: stretching; δ: in-plane bending; ρ_t: twisting; ρ_r: rocking; ρ_w: wagging. F_t and F_b denote terminal and bridging fluorines, respectively.

701 and 680 [701 and 689] cm^{-1} were assigned to the symmetric MF_2 stretching modes, whereas the corresponding antisymmetric modes were partially obscured by the intense A_{1g} modes of the anions and were assigned to the bands at 664 and 662 [620] cm^{-1}. The MO_2 scissoring modes were assigned to the intense bands at 409 and 407 [404 and 403] cm^{-1} and are a consistent feature in the Raman spectra of *cis*-dioxo transition metal complexes. The remaining MF_2 deformation modes, i.e., wagging, bending, rocking and twisting modes are tentative and were assigned based on the ordering of the frequencies observed and calculated for valence isoelectronic CrO_2F_2, MoO_2F_2, and WO_2F_2.[158] The symmetric stretching modes of the anions occur at 676 [687] cm^{-1} for AsF_6^- and at 655 [658] cm^{-1} for SbF_6^-, and agree well with the previously reported values.[157] The corresponding antisymmetric stretching modes were not observed for AsF_6^- and only occur as weak features at 507 [503] cm^{-1} for SbF_6^-. The T_{2g} bending modes of AsF_6^- and SbF_6^- were assigned to the depolarized bands at 375 [371] and 290 [289] cm^{-1}, respectively, in accordance with the literature values.[157]

The $ReO_2F_2(CH_3CN)_2^+$ Cation

NMR Spectroscopy. The ^{19}F NMR spectrum of $ReO_2F_3 \cdot SbF_5$ dissolved in CH_3CN at 0 °C consists of a singlet at 7.2 ppm ($\Delta\nu_{1/2}$ = 15 Hz) and a multiplet at -122.8 ppm resulting from the superposition of an equi-intense sextet and an equi-intense octet (Figure 5.8) (relative integrated intensities 1.00:2.85) arising from the SbF_6^- anion [$^1J(^{19}F\text{-}^{121}Sb)$ = 1932 Hz; $^1J(^{19}F\text{-}^{123}Sb)$ = 1044 Hz], in excellent agreement with the literature values for $Ag^+SbF_6^-$ in CH_3CN [-123 ppm; $^1J(^{19}F\text{-}^{121}Sb)$ = 1934 Hz; $^1J(^{19}F\text{-}^{121}Sb)$ = 1047)].[159] The

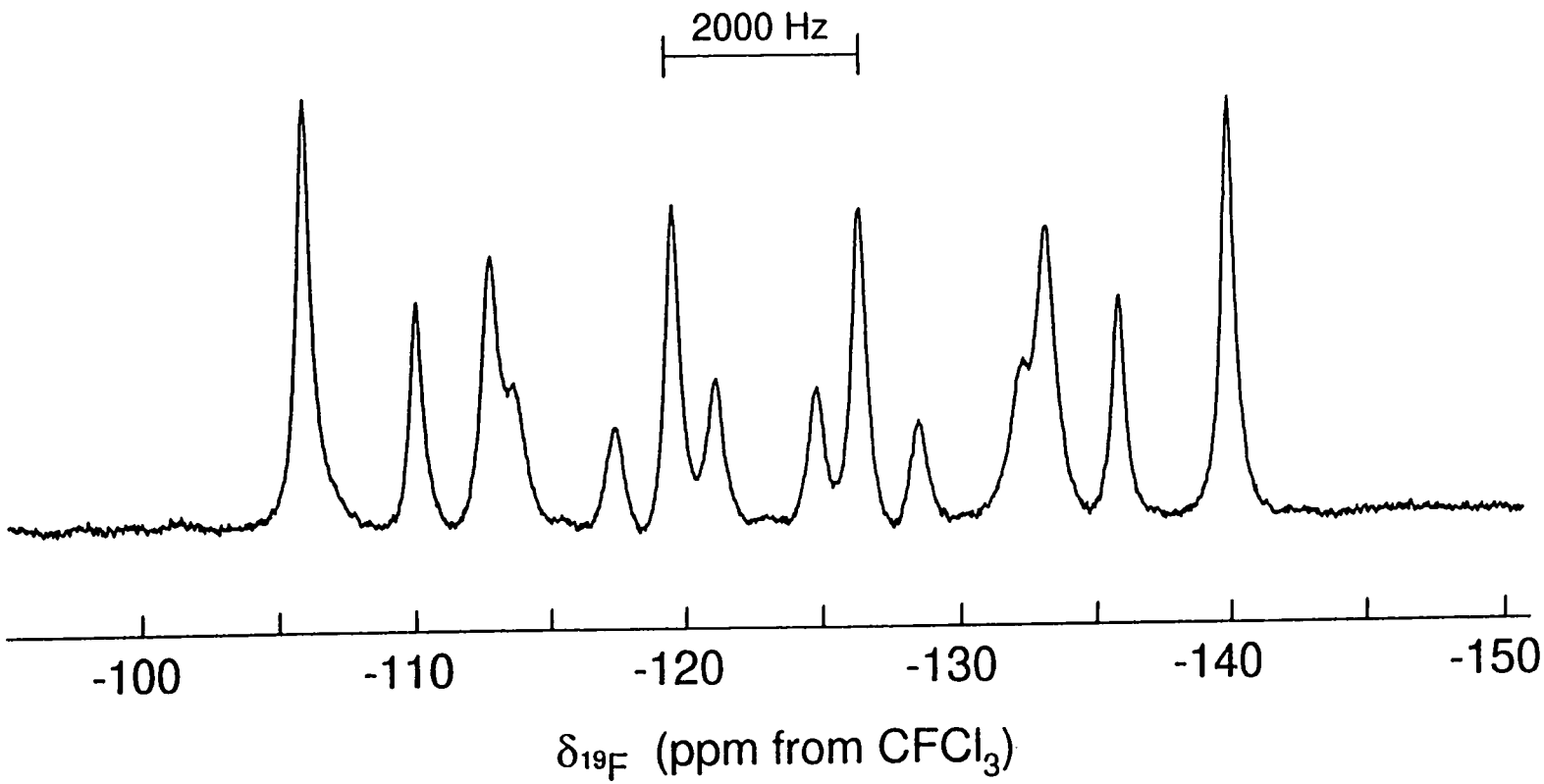

Figure 5.8. ^{19}F NMR spectrum (282.409 MHz) of $ReO_2F_3 \cdot SbF_5$ dissolved in CH_3CN recorded at 0 °C, showing the SbF_6^- resonance.

well-resolved spin-spin coupling between ^{19}F and the quadrupolar ^{121}Sb and ^{123}Sb nuclei indicate dissociation of the adduct into distinct cations and anions. The $ReO_2F_2^+$ cation is expected to be highly acidic and likely coordinates to two solvent molecules in order to achieve a coordination number of six. The arrangement of the oxygens in the complex is expected to be *cis* as in all d^0 transition metal complexes, whereas the CH_3CN ligands are predicted to coordinate to the positions *trans* to the oxo ligands as observed for $MoO_2F_2(THF)_2$,[112] $MOF_4(CH_3CN)$ (M = Mo, W),[160] $MO_2F_3(CH_3CN)$ (M = Tc, Re) and $ReO_3F(CH_3CN)_2$. Furthermore, the occurrence of a sharp singlet in the ^{19}F NMR spectrum indicates that the fluorine ligands are symmetrically equivalent. The resulting ligand arrangement in the $[ReO_2F_2(CH_3CN)_2]^+$ cation is shown in Structure III. The ^1H NMR

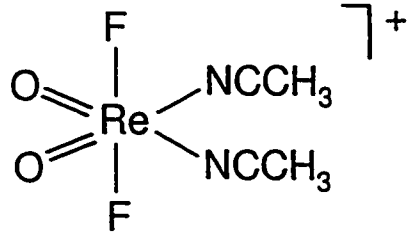

Structure III

spectrum of this solution consists of two singlets at 2.00 and 2.64 ppm, corresponding to the solvent and the complexed CH_3CN, respectively. The ^{13}C NMR spectrum also shows the complexed CH_3CN at 125.4 (CN) and 3.10 ppm (CH_3), as well as the solvent at 117.4 (CN) and 0.48 (CH_3) ppm. The complexation shifts in $[ReO_2F_2(CH_3CN)_2]^+SbF_6^-CH_3$ ($\Delta\delta(^1H)$ = 0.64 ppm; $\Delta\delta(^{13}CH_3)$ = 2.62 ppm; $\Delta\delta(^{13}CN)$ = 8.00 ppm) are significantly larger than those observed for $ReO_2F_3(CH_3CN)$ ($\Delta\delta(^1H)$ = 0.46 ppm; $\Delta\delta(^{13}CH_3)$ = 1.08 ppm;

$\Delta\delta(^{13}CN)$ = 1.54 ppm). These observations are consistent with the anticipated greater Lewis acidity of the $ReO_2F_2^+$ cation. At 0 °C, the sample slowly decomposes and the original colourless solution turns dark red within ca. 20 min. As the decomposition proceeds, a doublet and a triplet [$^1J(^{19}F\text{-}^{19}F)$ = 117 Hz] appear at -24.6 and -33.1 ppm, respectively, which arise from to the colourless $ReO_2F_3(CH_3CN)$ adduct. The low solubility of the $[ReO_2F_2(CH_3CN)_2]^+SbF_6^-$ salt in CH_3CN prevented the acquisition of NMR spectra at temperatures lower than 0 °C. No attempt was made to identify the species responsible for the intense dark red colour of the solution. Attempts to prepare the $TcO_2F_2(CH_3CN)_2^+$ cation by dissolution of $TcO_2F_3 \cdot SbF_5$ in CH_3CN at 0 °C resulted in rapid decomposition, evident from gas evolution and the formation of a dark blue solution.

Raman Spectroscopy. The Raman spectrum of the $[ReO_2F_2(CH_3CN)_2]^+SbF_6^-$ salt isolated from CH_3CN solution is shown in Figure 5.9. The observed frequencies and their assignments for the cation (C_{2v} point symmetry) and the anion (O_h point symmetry) are listed in Table 5.10. The vibrational assignments were made by comparison with the Raman spectra of polymeric ReO_2F_3, $ReO_2F_3(CH_3CN)$, CH_3CN[122] and $ReO_2F_4^-$.

The bands arising from complexed CH_3CN have been assigned by comparison with those of the $ReO_2F_3(CH_3CN)$ adduct and those of free CH_3CN. The antisymmetric and symmetric ReO_2 stretching modes are readily assigned to 998 and 1012 cm^{-1}, respectively, and their presence confirms the cis-dioxo arrangement predicted for the cation (see ***NMR Spectroscopy***). The ReO_2 symmetric stretch appears at higher frequency than in

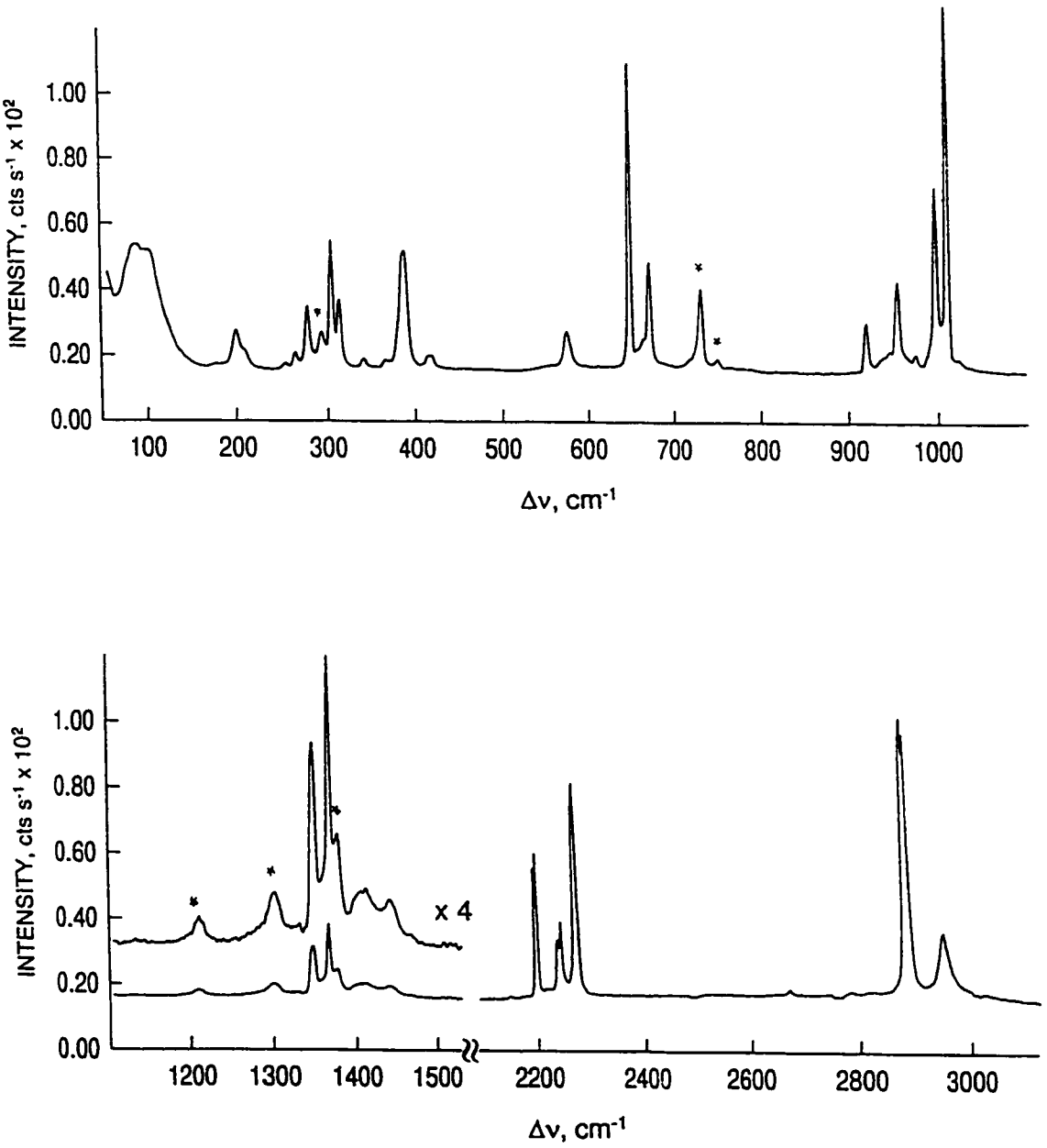

Figure 5.9. Raman spectrum of $[ReO_2F_2(CH_3CN)_2]^+SbF_6^-$ recorded in FEP at -150 °C using 514.5-nm excitation. Asterisks (*) denote FEP lines.

Table 5.10. Raman Frequencies, Assignments and Mode Descriptions for $[ReO_2F_2(CH_3CN)_2]^+SbF_6^-$ [a]

Frequencies (cm^{-1})[b]	Assignments[c]	
	$[ReO_2F_2(CH_3CN)_2]^+$ (C_{2v})	SbF_6^- (O_h)
3012(21)	$\nu_{as}(CH_3)$	
2950(86),sh	$\nu_s(CH_3)$	
2330(71) 2327(66),sh	$\nu(CN)$	
1448(3)	$\delta_{as}(CH_3)$	
1411(3)	$\delta_{as}(CH_3)$	
1355(13)	$\delta_s(CH_3)$	
1012(100)	A_1, $\nu_s(ReO_2)$	
998(49)	B_1, $\nu_{as}(ReO_2)$	
956(24)	$\nu(CC)$	
672(29)		A_{1g}, $\nu_s(SbF_6)$
648(82)	A_1, $\nu_s(ReF_2)$	
574(10)	B_2, $\nu_{as}(ReF_2)$	
558(1)		E_g, $\nu_{as}(SbF_4)$
419(4) 414(4)	$\delta(CCN)$ $\delta(CCN)$	
388(32)	A_1, $\delta(ReO_2)$	
365(3)		
340(3)		
313(19)	A_1, $\delta(ReF_2)$	
304(35)	B_2, $\rho_w(ReO_2)$	
293(15)	B_1, $\delta(ReF_2)$	
277(17)	A_2, $\rho_t(ReO_2)$	T_{2g}, $\delta_s(SbF_4)$

Table 5.10. continued

264(5)	A_1, $\nu_s(ReN_2)$
253(2)	B_1, $\nu_{as}(ReN_2)$
209(5),sh	
199(10)	B_2, $\rho_w(ReN_2)$
177(1)	
101(22)	A_1, $\delta(ReN_2)$
86(19)	B_1, $\rho_r(ReO_2)$
54(5)	A_2, $\rho_t(ReN_2)$

[a] Spectrum recorded on microcrystalline solid in FEP at -150 °C using 514.5-nm excitation.

[b] Values in parentheses denote relative intensities; sh: shoulder. Bands assigned to residual CH_3CN solvent (C_{3v} point symmetry): $\nu_1(A_1)$, 2945(90), $2\nu_3$, 2730(1), $\nu_3 + \nu_4$, 2293(21)/2300(24), $\nu_2(A_1)$, 2252(45)/2256(48), $\nu_3(A_1)$, 1374(16), $\nu_4(A_1)$, 919(12).

[c] ν: stretching; δ: in-plane bending; ρ_t: twisting; ρ_r: rocking; ρ_w: wagging.

$ReO_2F_3(CH_3CN)$ (1001 cm^{-1}), but at lower frequency than in ReO_2F_3 (1025 cm^{-1}) and $ReO_2F_3{\cdot}SbF_5$ (1040 cm^{-1}) whereas the ReO_2 antisymmetric stretch is at higher frequency than in $ReO_2F_3(CH_3CN)$ (944 cm^{-1}) and ReO_2F_3 (990, 994 cm^{-1}), but at lower frequency than in $ReO_2F_3{\cdot}SbF_5$ (1025 cm^{-1}). The antisymmetric and symmetric ReF_2 stretching modes occur at 574 and 648 cm^{-1}, respectively. The band at 388 cm^{-1} was assigned to the ReO_2 scissoring motion, which is at lower frequency than in ReO_2F_3 (412 cm^{-1}), $ReO_2F_3{\cdot}SbF_5$ (407 cm^{-1}) and $ReO_2F_3(CH_3CN)$ (389 cm^{-1}). The remaining low-frequency bands are very similar to those in the $ReO_2F_3{\cdot}SbF_5$ spectrum and were tentatively assigned to ReF_2 bending motions as well as to ReO_2 and ReN_2 wagging, twisting and rocking motions. The antisymmetric and symmetric ReN_2 stretching modes are expected to occur in the 200-300 cm^{-1} region of the spectrum as was observed for other transition metal complexes with CH_3CN[161] and are tentatively assigned to the bands at 253 and 264 cm^{-1}, respectively. The Raman-active modes associated with the octahedral SbF_6^- anion $\nu_1(A_g)$, $\nu_2(E_g)$ and $\nu_5(T_{2g})$ appear at 672, 558 and 277 cm^{-1}, respectively, and are in good agreement with the values previously reported in the literature[157] and consistent with an SbF_6^- anion that is not significantly distorted from O_h symmetry.

The $TcO_2F_3{\cdot}XeO_2F_2$ Adduct

Xenon hexafluoride is used in the preparation of TcO_2F_3 to scavenge water produced by the solvolysis of Tc_2O_7 in HF and to fluorinate TcO_3F to TcO_2F_3 (eq. (5.3)-(5.5)). The stoichiometry for the complete conversion of Tc_2O_7 to TcO_2F_3 and formation of $XeOF_4$ corresponds to the molar ratio XeF_6:Tc_2O_7 = 3:1. When smaller quantities of

$$Tc_2O_7 + 4\ HF \longrightarrow 2\ TcO_3F + H_3O^+HF_2^- \quad (5.3)$$

$$XeF_6 + H_3O^+HF_2^- \longrightarrow XeOF_4 + 4\ HF \quad (5.4)$$

$$TcO_3F + XeF_6 \longrightarrow TcO_2F_3 + XeOF_4 \quad (5.5)$$

XeF_6 are used (a 1.5:1 molar ration was used in this experiment), $XeOF_4$ acts as a fluorinating agent and XeO_2F_2 is formed (eq. (6)). The pale yellow adduct $TcO_2F_3 \cdot XeO_2F_2$

$$TcO_3F + XeOF_4 \longrightarrow TcO_2F_3 + XeO_2F_2 \quad (5.6)$$

can then be sublimed out of the reaction mixture under static vacuum at 45 °C and shows no sign of decomposition when stored under dry nitrogen at room temperature for at least two weeks.

X-ray Crystal Structure of $TcO_2F_3 \cdot XeO_2F_2$. Details of the data collection parameters and other crystallographic information are given in Table 5.1. The final atomic coordinates and the equivalent thermal parameters are summarized in Table 5.11. Important bond lengths, angles and significant long contacts are listed in Table 5.12.

The structure of $TcO_2F_3 \cdot XeO_2F_2$ consists of infinite chains of TcO_2F_3 running parallel to the *c*-axis and bridged to XeO_2F_2 chains by long Tc-F···Xe contacts (Figure 5.10). The Tc atoms in the TcO_2F_3 chains are bonded to two oxygens that are *cis* to each other (Figure 5.11a) and *trans* to the bridging fluorines and two fluorine atoms that are *cis* to the oxygens and *trans* to each other, as was observed in the crystal structure of

Table 5.11. Final Atomic Coordinates ($\times 10^4$) and Equivalent Isotropic Displacement Coefficients ($Å^2 \times 10^3$) for $TcO_2F_3 \cdot XeO_2F_2$

	x	*y*	*z*	U_{eq}[a]
Tc(1)	0	5958(1)	18978(3)	10.5(3)
Xe(1)	0	11241.5(8)	5619(1)	15.0(3)
O(1)	0	6733(8)	17032(27)	16(3)
O(2)	0	6422(10)	21770(29)	26(4)
O(3)	1747(10)	11740(6)	4338(22)	28(2)
F(1)	0	5171(7)	15786(27)	20(2)
F(2)	-2270(9)	5708(5)	18793(17)	23(2)
F(3)	0	11945(10)	8525(22)	34(3)
F(4)	0	10458(8)	2838(26)	30(3)

[a] Equivalent isotropic *U* defined as one third of the trace of the orthogonalized $\mathbf{U}_{ij}$ tensor.

Table 5.12. Bond Lengths (Å), Bond Valences (v.u.), Long Contacts (Å) and Bond Angles (deg) in $TcO_2F_3 \cdot XeO_2F_2$

Bond Lengths (Å) and Corresponding Bond Valences (v.u.)[a]					
Tc(1)	O(1)	O(2)	F(1)	F(1A)	F(2,2A)
Bond valence	2.120	1.992	0.491	0.541	0.970
Bond length	1.612(13)	1.635(15)	2.093(13)	2.057(11)	1.840(7)
Total bond valence: 7.08					
Xe(1)	O(3,3A)	F(3)	F(4)	F(2,2A)	F(4A)
Bond valence	1.794	0.908	0.857	0.233	0.199
Bond length	1.731(9)	1.892(13)	1.925(13)	2.848(8)	2.985(13)
Total bond valence: 6.02					

Bond Angles (deg)			
O(1)-Tc(1)-O(2)	101.5(8)	F(1)-Tc(1)-F(2)	79.9(3)
O(1)-Tc(1)-F(1)	88.7(6)	F(1A)-Tc(1)-F(2)	80.1(3)
O(1)-Tc(1)-F(1A)	168.3(6)	F(2)-Tc(1)-F(2A)	153.8(5)
O(1)-Tc(1)-F(2)	98.0(3)	O(3)-Xe(1)-O(3A)	105.6(6)
O(2)-Tc(1)-F(1)	169.8(7)	O(3)-Xe(1)-F(3)	91.5(4)
O(2)-Tc(1)-F(1A)	90.2(7)	O(3)-Xe(1)-F(4)	91.1(4)
O(2)-Tc(1)-F(2)	98.5(3)	F(3)-Xe(1)-F(4)	175.7(6)
F(1)-Tc(1)-F(1A)	79.6(2)		

Table 5.12. continued

[a]Bond valence units (v.u.) are defined in ref. 110. R_0 = 1.89 (Tc(VII)=O), R_0 = 1.83 (Tc(VII)-F), R_0 = 1.971 (Xe(VI)=O), R_0 = 1.838 (Xe(VI)-F) were used along with N = 3.33 for Xe and B = 0.37 for Tc; Brown, I.D. Department of Physics, McMaster University, Hamilton, Ontario L8S 4M1, Canada, private communication.

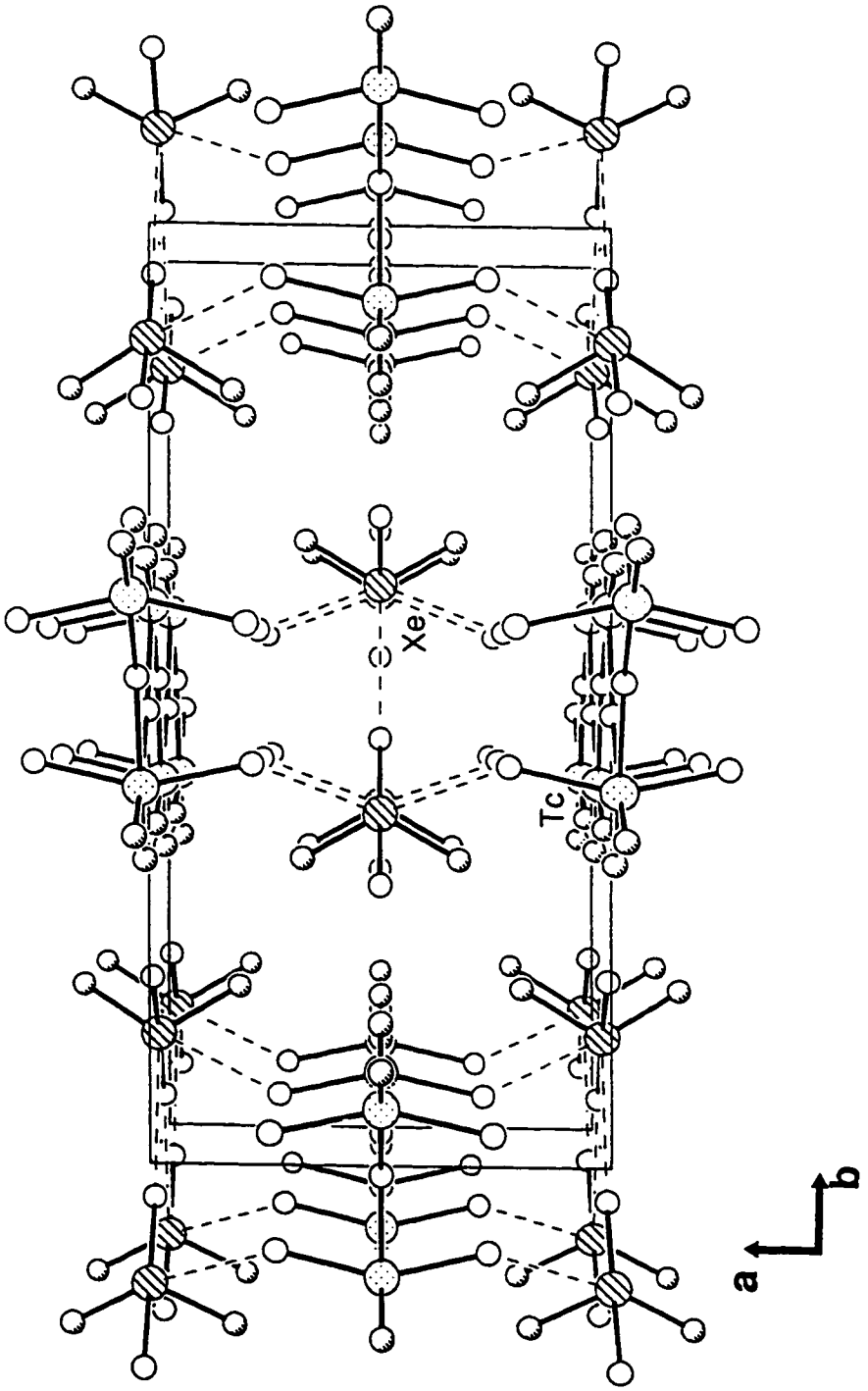

Figure 5.10. View of the $TcO_2F_3 \cdot XeO_2F_2$ unit cell showing the packing along the *c*-axis.

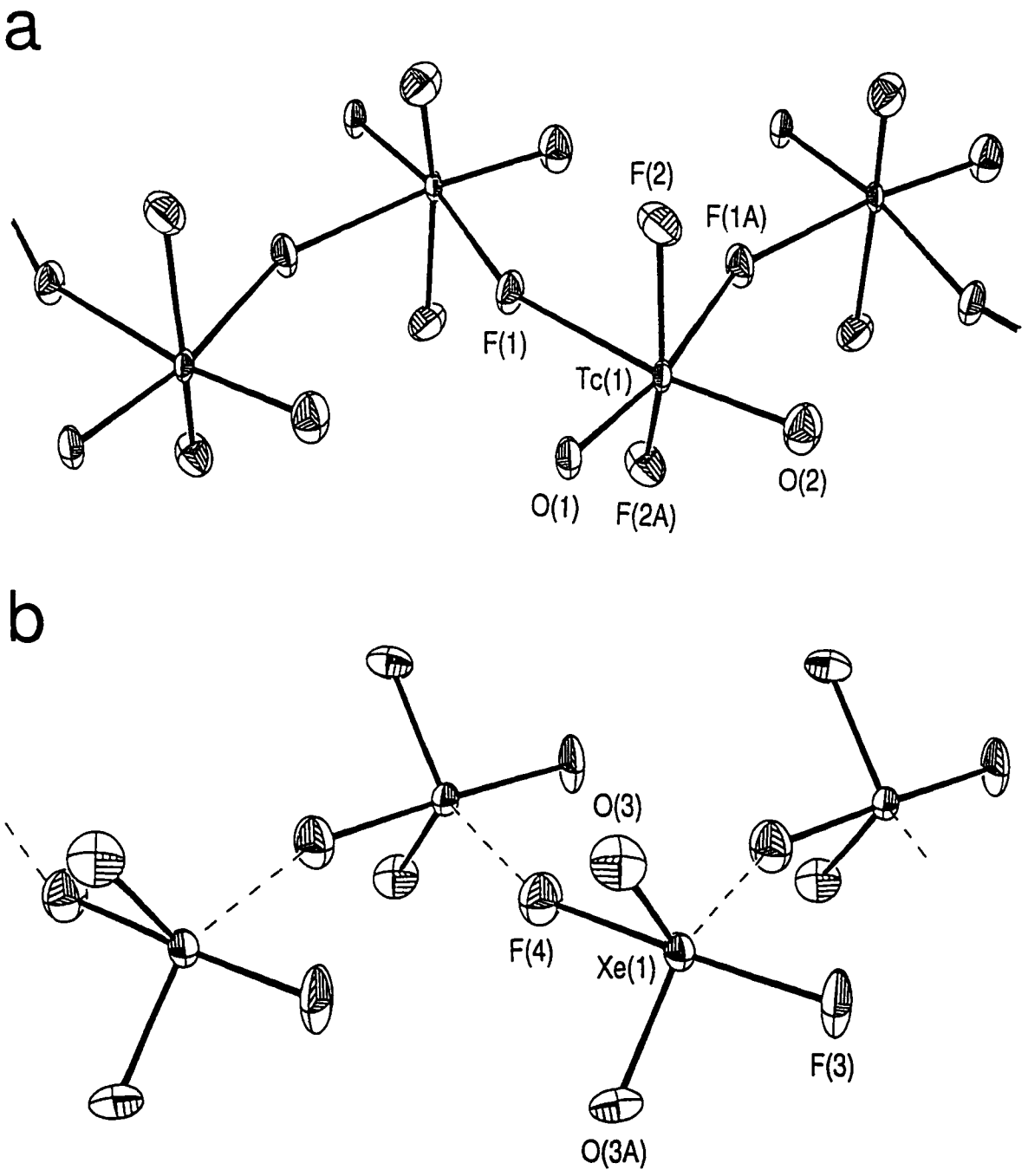

Figure 5.11. Structures of (a) the TcO_2F_3 infinite chain and (b) the XeO_2F_2 infinite chain in the $TcO_2F_3 \cdot XeO_2F_2$ adduct. Thermal ellipsoids are at the 50% probability level.

TcO_2F_3. The arrangement of the light atoms around Xe is similar to what was observed in the structure of XeO_2F_2 [162] and is consistent with the disphenoidal geometry predicted by the VSEPR model.[111] The double-bonded oxygen atoms and the lone pair occupy the equatorial plane whereas the fluorine atoms lie in axial positions. An interesting aspect of this structure is that the XeO_2F_2 molecules have secondary contacts to Xe through fluorine-bridging within the XeO_2F_2 chains (Figure 5.11b) and contrasts with the structure of XeO_2F_2 which exhibits secondary Xe···O contacts.[162]

The Tc-O distance (1.62(1) Å) is characteristic of a Tc-O double bond. It is slightly shorter than the Tc-O bond length found in TcO_2F_3 (1.646(9) Å)[41] and significantly shorter than that found in $Li^+TcO_2F_4^-$. The Tc-F bridging bond lengths (2.06(1) and 2.09(1) Å) are very similar to those found in TcO_2F_3 (average, 2.080(5) Å).[41] The terminal Tc-F bond lengths (1.840(7) Å) are also very similar to those found in TcO_2F_3 (average, 1.834(7) Å).[41] The important bond angles for the TcO_2F_3 chain in the adduct are almost identical with those of TcO_2F_3.[41] The only difference is in the F_t-Tc-F_t angle (153.8(5)°) which is slightly smaller than that in TcO_2F_3 (average, 155.3(3)°) and may arise from the larger electron pair domains of the shorter Tc-O double bonds in the adduct.

The Xe-O distance (1.734(9) Å) is slightly longer than in XeO_2F_2 (1.714(4) Å)[162] and intermediate between the Xe=O bond lengths of $XeOF_4$ (1.703(15) Å)[163] and XeO_3 (1.76(3) Å).[164] There are two types of axial Xe-F bonds in the present structure. One is slightly longer (1.925(13) Å) than the other (1.892(13) Å) as a result of a secondary fluorine bridge contact with Xe in a neighbouring XeO_2F_2 molecule, and both compare

well with the Xe(VI)-F bond lengths of XeO_2F_2 (1.899(3) Å)[162] and $XeOF_4$ (1.900(5) Å).[163] The O-Xe-O bond angle in this structure (105.6(6)°) and in XeO_2F_2 (105.7(3)°) are identical, the F-Xe-F bond angle in the adduct (175.7(6)°) is slightly more open than that in XeO_2F_2 (174.7(4)°). It is important to note that, contrary to the VSEPR model prediction,[111] this F-Xe-F angle is bent *toward* the nonbonding electron pair on xenon. This feature was also observed in the structures of XeO_2F_2 [162] and $XeO_2(OTeF_5)_2$,[165] as well as in $XeOF_4$.[163] Huston and coworkers[162] explained this feature in the structure of XeO_2F_2 by assuming that the Xe-O double bond repels the Xe-F bonds more effectively than the Xe lone pair, whereas the small O-Xe-O angle results from an inherent preference of the oxygens for bonding to the Xe p orbitals than to the s orbitals, and not because of repulsion from the lone valence electron pair on Xe. Gillespie and Robinson[166] explain these apparent inconsistencies by assuming that the lone-pair domain exerts directional repulsive effects (i.e., a lone pair domain in an equatorial position spreads out more in the equatorial direction than in the axial direction). However, this argument is not consistent with the structure of $XeOF_4$ [163] in which the fluorine ligands are also bent *toward* the valence electron lone pair.

The variations in the Tc-O and Xe-O bond lengths in the adduct relative to those of TcO_2F_3 and XeO_2F_2 can be rationalized in terms of Lewis acid-base interactions. There is some electron density transferred from TcO_2F_3 to XeO_2F_2 which increases the bond polarity of Xe-O and decreases that of Tc-O, resulting in longer and shorter bond lengths, respectively.

The bond valences for individual bonds are given in Table 5.12. The total bond valence for the technetium atom is 7.08 v.u., with contributions of 2.06 v.u./oxygen atom, 0.97 v.u./terminal fluorine atom and 0.52 v.u./bridging fluorine atom. The values for the Tc-O double bond are slightly higher than in TcO_2F_3 (1.97 v.u.)[41] whereas those for the Tc-F_t and Tc-F_b bonds are similar to those in TcO_2F_3 (0.99 and 0.51 v.u., respectively).[41] The long contacts between Xe and the terminal fluorine atoms on Tc (2.848(8) Å) are significantly shorter than the sum of the van der Waals radii (3.45 Å)[139] as indicated by their bond valence (0.23 v.u.) and clearly indicates that XeO_2F_2 is acting as a fluoride-ion acceptor toward TcO_2F_3. However, this Lewis acid-base interaction in which the TcO_2F_3 chain is only slightly perturbed is significantly weaker than in the $TcO_2F_3 \cdot SbF_5$ adduct in which the SbF_5 is intercalated directly into the TcO_2F_3 chain. This behaviour is consistent with the stronger Lewis acid character of SbF_5 over XeO_2F_2. The total bond valence for the xenon atom is 6.02 v.u., with contributions of 1.79 v.u./oxygen atom and 1.91 v.u./terminal fluorine atom. The coordination sphere around Xe is completed by one long contact with a terminal fluorine of another XeO_2F_2-unit (2.985(13) Å, 0.20 v.u.) and two with the TcO_2F_3 chain (*vide supra*). These three Xe-F long contacts are directed so that they avoid the valence lone pair of the xenon atom, as observed in the structures of XeF_3^+,[168] XeF_5^+ [169] and $XeOF_3^+$.[69a]

Raman Spectrum of $TcO_2F_3 \cdot XeO_2F_2$. The Raman spectrum of the $TcO_2F_3 \cdot XeO_2F_2$ adduct is shown in Figure 5.12. The observed frequencies and their assignments are listed in Table 5.13. The spectrum of the adduct was assigned by comparison with the Raman

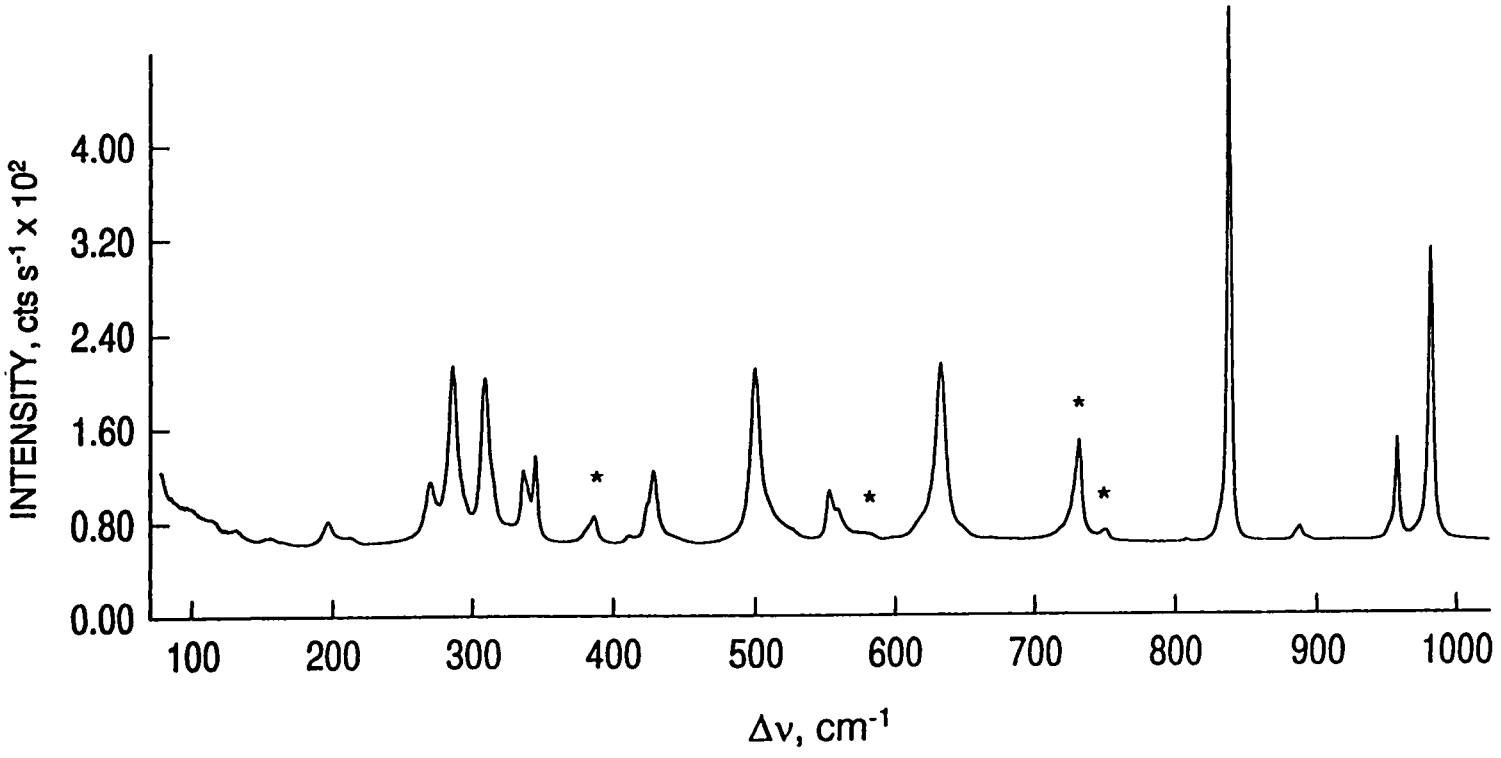

Figure 5.12. Raman spectrum of $TcO_2F_3 \cdot XeO_2F_2$ recorded in FEP at 20 °C using 514.5-nm excitation. Asterisks (*) denote FEP lines.

Table 5.13. Raman Frequencies, Assignments and Mode Descriptions for the $TcO_2F_3 \cdot XeO_2F_2$ Adduct[a]

Frequencies (cm^{-1})[b]	Assignments[c]	
	TcO_2F_4 (C_{2v})	XeO_2F_2 (C_{2v})
984(84)	A_1, $\nu_s(TcO_2)$	
959(26)	B_1, $\nu_{as}(TcO_2)$	
889(3)		B_1, $\nu_{as}(XeO_2)$
840(100)		A_1, $\nu_s(XeO_2)$
633(30)	A_1, $\nu_s(TcF_{2t})$	
620(5),sh	B_2, $\nu_{as}(TcF_{2t})$	
580(2),br	A_1, $\nu_s(TcF_{2b})$	
559(5),sh	B_1, $\nu_{as}(TcF_{2b})$	
553(8)		B_2, $\nu_{as}(XeF_2)$
499(28)		A_1, $\nu_s(XeF_2)$
426(11) 422(6),sh	A_1, $\delta(TcO_2)$	
343(17)		A_1, $\delta(XeO_2)$
336(10),sh	A_1, $\delta(TcF_{2t})$	
334(12)	B_2, $\rho_w(TcO_2)$	
307(28)	B_1, $\delta(TcF_{2t})$	
284(32)	A_2, $\rho_t(TcO_2)$	
268(10)	B_2, $\rho_w(TcF_{2b})$	
209(1)		A_1, $\delta(XeF_2)$
195(3)	A_1, $\delta(TcF_{2b})$	
152(1)		
129(2)	B_1, $\rho_r(TcF_{2b})$	
111(2)		

Table 5.13. continued

94(>0)		
74(3)		A_2, $\rho_t(TcF_{2b})$

[a] Spectrum recorded on microcrystalline solid in FEP at 23 °C using 514.5-nm excitation.

[b] Values in parentheses denote relative intensities; sh: shoulder; br: broad.

[c] ν: stretching; δ: in-plane bending; ρ_t: twisting; ρ_r: rocking; ρ_w: wagging.

spectra of polymeric TcO_2F_3,[41] matrix-isolated XeO_2F_2 [167] and XeO_2F_3.[167] The TcO_2F_4-units (point symmetry C_{2v}) belong to the irreducible representations $6A_1 + 2A_2 + 4B_1 + 3B_2$ (the [O, O, Tc, F, F]-plane is taken as the $\sigma_v(xz)$-plane with the z-axis as the principal axis) and are Raman active whereas only the A_1, B_1 and B_2 modes are infrared-active. The vibrational modes of the XeO_2F_2-units (point symmetry C_{2v}) belong to the irreducible representations $4A_1 + A_2 + 2B_1 + 2B_2$ and are all Raman active and the A_1, B_1 and B_2 modes are infrared-active.

In order to evaluate the degree of vibrational coupling within the unit cell of $TcO_2F_3 \cdot XeO_2F_2$, a factor-group analysis of the vibrational modes of the unit cells was carried out using the correlation method.[115] Correlation of the vibrational modes of the TcO_2F_4-unit (C_{2v}) and the XeO_2F_2-unit (C_{2v}) to their site symmetry ($C_s(yz)$) and to the crystal symmetry (C_{2v}), space group $Cmc2_1$, results in the splitting of the modes into Raman active A_1 components, inactive A_2 components and Raman and infrared-active B_1 and B_2 components (Table 5.14). The ν_1-ν_6 and ν_{12}-ν_{15} modes of the TcO_2F_4-unit are each expected to split into two A_1 and two B_2 components, whereas ν_7-ν_{11} split into two A_2 and two B_1 components. The ν_1-ν_4 and ν_8-ν_9 modes of the XeO_2F_2-unit each split into two A_1 and two B_2 components, whereas ν_5-ν_7 are expected to split into two A_2 and two B_1 components.

The symmetric and antisymmetric Tc-O stretches were assigned to the bands at 984 and 959 cm^{-1}, respectively, and occur at higher frequency compared to the corresponding stretches for polymeric TcO_2F_3 (974 and 963 cm^{-1}),[41] which is consistent with the increased valence bond order observed in the crystal structure of $TcO_2F_3 \cdot XeO_2F_2$.

Table 5.14. Correlation Diagram for the Vibrational Modes of $TcO_2F_3 \cdot XeO_2F_2$

		TcO_2F_4-unit				
		molecule local symmetry	site symmetry	crystal symmetry[b]		
		C_{2v}	$C_s(yz)$	C_{2v}		
4T	$4(\nu_1 - \nu_6)$	A_1	A'	A_1 (Ra)	$2(\nu_1 - \nu_6),2(\nu_{12} - \nu_{15})$	2R,3T(-T)
4R	$4(\nu_7 - \nu_8)$	A_2	A"	A_2 (i.a.)	$2(\nu_7 - \nu_{11})$	4R,2T
4T,4R	$4(\nu_9 - \nu_{11})$	B_1		B_1 (R,IR)	$2(\nu_7 - \nu_{11})$	4R,T(-T)
4T,4R	$4(\nu_{12} - \nu_{15})$	B_2		B_2 (R,IR)	$2(\nu_1 - \nu_6),2(\nu_{12} - \nu_{15})$	2R,3T(-T)

Table 5.14. continued

		XeO_2F_2-unit				
		molecule local symmetry	site symmetry	crystal symmetry[b]		
		C_{2v}	$C_s(yz)$	C_{2v}		
4T	$4(\nu_1 - \nu_4)$	A_1	A'	A_1 (Ra)	$2(\nu_1 - \nu_4),2(\nu_8 - \nu_9)$	2R,3T(-T)
4R	$4\nu_5$	A_2	A"	A_2 (i.a.)	$2(\nu_5 - \nu_7)$	4R,2T
4T,4R	$4(\nu_6 - \nu_7)$	B_1		B_1 (R,IR)	$2(\nu_5 - \nu_7)$	4R,T(-T)
4T,4R	$4(\nu_8 - \nu_9)$	B_2		B_2 (R,IR)	$2(\nu_1 - \nu_4),2(\nu_8 - \nu_9)$	2R,3T(-T)

[a] The symbols T and R denote translatory and rotatory (external) modes, respectively, and R, IR and i.a. in parentheses denote Raman and infrared activity and inactivity, respectively.

[b] Space group $Cmc2_1$, Z = 4.

The symmetric and antisymmetric Xe-O stretches occur at 840 and 889 cm^{-1}, respectively, and are shifted to lower frequency relative to the matrix-isolated XeO_2F_2 (849 and 906 cm^{-1}).[167] The terminal Tc-F symmetric stretch at 633 cm^{-1} is significantly lower in frequency than in TcO_2F_3 (650 cm^{-1}).[41] The symmetric and antisymmetric Xe-F stretches at 499 and 553 cm^{-1} are shifted to lower frequency relative to XeO_2F_2 (537 and 585 cm^{-1}).[167] The stretching frequencies for XeO_2F_2 in the adduct are intermediate between those of pure XeO_2F_2 and the $XeO_2F_3^-$ anion and clearly reflects the more polar nature of the XeO_2F_2 bonding in the adduct and the Lewis acid character of XeO_2F_2 toward TcO_2F_3.

The TcO_2 scissoring mode occurs at 422, 426 cm^{-1} and is shifted to higher frequency from that in TcO_2F_3 (411 cm^{-1}).[41] The band at 343 cm^{-1} can be assigned to the XeO_2 bend and is shifted to high frequency relative to the value of 331 cm^{-1} observed in XeO_2F_2.[167] The assignments for the remaining bands in the spectrum are tentative and were based on frequencies obtained from local density calculations for $TcO_2F_4^-$ and TcO_2F_3. The remaining deformation modes associated with XeO_2F_2 (XeO_2 twist, XeO_2 wag and out-of-plane XeF_2 bend) were not observed but are expected to be quite weak based on the intensities reported for XeO_2F_2.[167]

Conclusion

Both TcO_2F_3 and ReO_2F_3 were shown to behave as fluoride-ion donors toward AsF_5, SbF_5 and XeO_2F_2. Although the $TcO_2F_2^+$ and $ReO_2F_2^+$ cations could not be definitely identified in HF solution by NMR and Raman spectroscopy, it is reasonable to assume their existence (at least as part of an equilibrium) based on the high solubilities of the

$MO_2F_3 \cdot PnF_5$ adducts in HF and the characterization of the $[ReO_2F_2(CH_3CN)_2]^+$ cation in CH_3CN. In the solid state, the $MO_2F_3 \cdot PnF_5$ adducts show strong Lewis acid-base interactions and the structures of the SbF_5 adducts consist of chains of alternating fluorine-bridged MO_2F_4- and SbF_6-units. In contrast, the $TcO_2F_3 \cdot XeO_2F_2$ only shows weak interaction in the form of long contacts between XeO_2F_2 and the TcO_2F_3 chains. In each case, the *cis*-dioxo arrangement around the transition metal is maintained and bridging always occurs *trans* to the oxygen ligands. The preference for the *cis*-dioxo arrangement in these structures results from the optimum overlap between the strong π-donor oxygen atoms to the approximately $d_{t_{2g}}$ orbitals of the metal (see Chapter 3). Alternatively, the preference for the *cis*-dioxo arrangement in d^0 transition metal complexes can be attributed to the nonspherical metal atom core resulting from the distortion produced by the ligands.[114] The fluorine-bridged dinuclear $Re_2O_4F_5^+$ cation was also identified in SO_2ClF solution and is a rare example of five-coordinate transition metal oxofluoride.

CHAPTER 6

SOLUTION STRUCTURES OF TcO_2F_3 AND ReO_2F_3

Introduction

The transition metal pentafluorides, oxotetrafluorides and dioxotrifluorides all complete their six-coordination in the solid state by the formation of *cis*-fluorine bridges, and can be classified in four distinct structural types.[170] The VF_5-type, which includes CrF_5, TcF_5 and ReF_5, consists of infinite chains of MF_6-units linked by *cis*-fluorine bridges. The oxofluorides $MoOF_4$,[171] $TcOF_4$,[37] $ReOF_4$,[25] TcO_2F_3[41] and ReO_2F_3 (see Chapter 4) also adopt VF_5-type structures in which the oxygen atoms are always *trans* to a fluorine bridge. The NbF_5-type is adopted by TaF_5, MoF_5 and WF_5, and consists of cyclic tetramers with near linear fluorine bridges.[170] Crystal data indicate that WOF_4 also adopts a cyclic tetrameric structure with bridging W-F-W angles of 173°.[130] The RuF_5-type includes OsF_5, RhF_5, IrF_5 and PtF_5 and is a variation of the NbF_5 type consisting of a rhombus shape with nonlinear bridging angles.[170] Trimeric structures are less common, but metastable modifications based on a cyclic trimeric unit were characterized for $TcOF_4$, $ReOF_4$ and $MoOF_4$.[170] Although these fluorides and oxofluorides are well characterized in the solid state, their solution structures in nonionizing solvents have been considerably less studied. A ^{19}F NMR study of WOF_4 dissolved in toluene at -93 °C confirmed the cyclic tetrameric arrangement observed in the solid state but also indicated the presence

of polymeric species resulting from the rupture of the tetramers.[172] The high solubility of $MoOF_4$ in SO_2ClF,[136,137] even at very low temperature, suggests that the open-chain $MoOF_4$ polymer rearranges to the presumably more soluble trimeric or tetrameric species; however, a study of this system has not yet been published.

Additional examples of cyclic fluorides and oxofluorides include SbF_5, which exists as a polymeric liquid[138] but crystallizes as a cyclic tetramer,[173] $(SbOF_4)_3^{3-}$ consisting of an oxygen-bridged cyclic trimer in the solid state,[174] and the $V_3O_3F_{12}^{3-}$ [175] and $Mo_3O_6F_9^{3-}$ [176] anions which both adopt fluorine-bridged trimeric structures.

This Chapter describes how NMR spectroscopy and spectral simulation were used to determine the structures adopted by ReO_2F_3 and TcO_2F_3 in SO_2ClF solvent.

Results and Discussion

The solubilities of ReO_2F_3 and TcO_2F_3 in SO_2ClF are low at room temperature and are consistent with the polymeric nature of the compounds. However, some of the initially insoluble solid dissolves upon heating the mixtures to ca. 50 °C for 15 min to form colourless and pale yellow solutions for ReO_2F_3 and TcO_2F_3, respectively.

The ^{19}F NMR Spectrum of ReO_2F_3 in SO_2ClF

Solutions of ReO_2F_3 in SO_2ClF at -120 °C consist of an equilibrium mixture of the cyclic trimer (Structure I) and cyclic tetramer (Structure II) in a molar ratio of 5.0:1.0, as determined from the relative integrated intensities of their ^{19}F NMR resonances (Figure 6.1). This ratio remains relatively constant with increasing temperature, with a value of

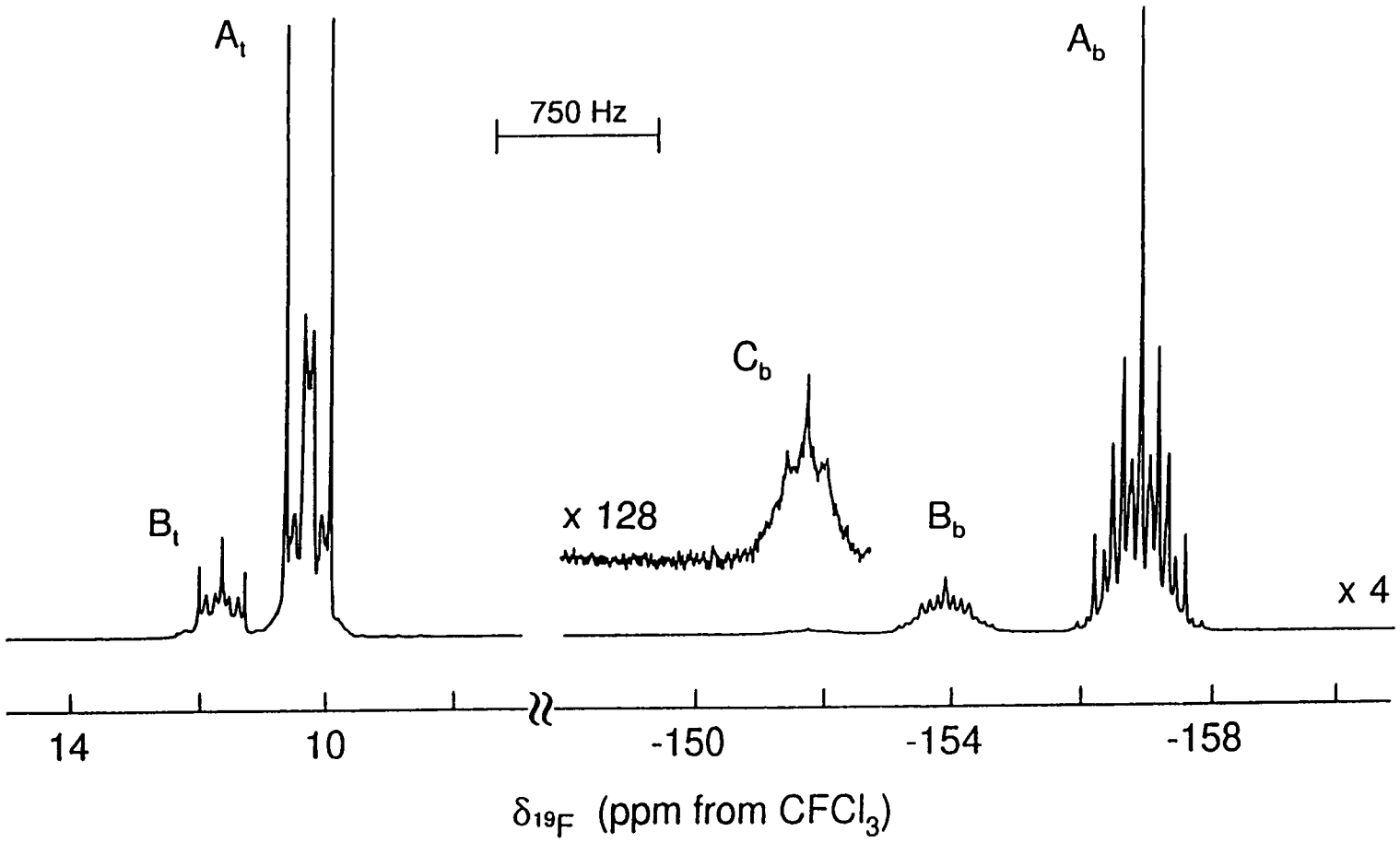

Figure 6.1. ^{19}F NMR spectum (282.409 MHz) of ReO_2F_3 in SO_2ClF recorded at -120 °C. Labels A, B and C denote the resonances of $(ReO_2F_3)_3$, $(ReO_2F_3)_4$ and $(ReO_2F_3)_5$, respectively, with the subscripts t and b corresponding to the terminal and bridging environments, respectively.

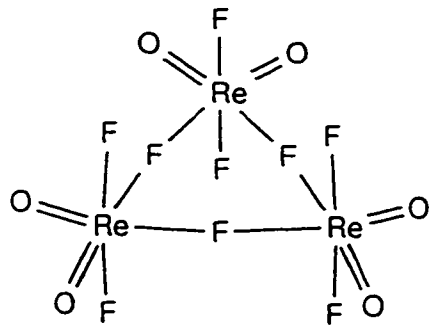

Structure I

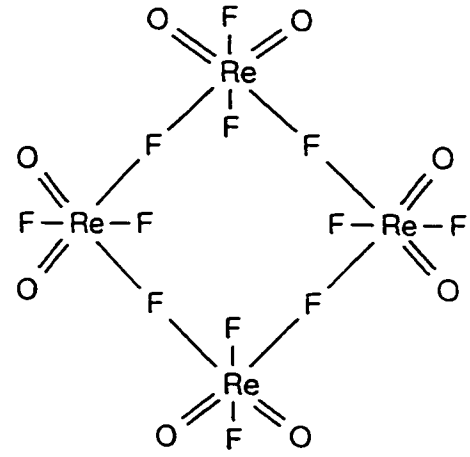

Structure II

5.3:1.0 at -40 °C. The ^{19}F NMR spectrum of $(ReO_2F_3)_3$ consists of two resonances at 10.3 and -156.9 ppm with relative integrated intensities of 2.0:1.0 which were assigned to the terminal and bridging fluorines, respectively. The other set of resonances, which also have relative integrated intensities of 2.0:1.0, occur at 11.7 and -153.9 ppm and were assigned to the terminal and bridging environments of $(ReO_2F_3)_4$, respectively. A very weak resonance at -151.9 ppm was also observed and was tentatively assigned to the bridging fluorine environment in a cyclic pentamer although a corresponding terminal fluorine resonance was not detected. The chemical shift of the terminal fluorines is significantly deshielded compared to that of $ReO_2F_3(CH_3CN)$ in SO_2ClF (-23.8 and -25.8 ppm) (see Chapter 4) whereas the chemical shift of the bridging fluorines is highly shielded as is observed for other fluorine-bridge oxofluoro-species, e.g., $W_2O_2F_9^-$,[105] $Mo_2O_2F_9^-$,[135] $Os_2O_4F_7^+$,[63] $Re_2O_4F_7^-$ and $Re_2O_4F_5^+$ (see Chapter 5).

The apparent complexity of the spectrum arises from the magnetic nonequivalence of the fluorine nuclei. This phenomenon occurs when a nucleus is coupled to two or more chemically equivalent nuclei with different coupling constants and is usually observed in cyclic systems as well as in systems with hindered rotation.[177] A typical example of magnetic nonequivalence that is closely related to the present system is 1,3,5-trifluorobenzene (Structure III), which is an $(AX)_3$ spin system (or AA'A"XX'X")

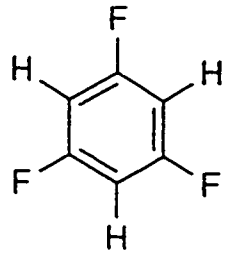

Structure III

consisting of two sets of three chemically equivalent but magnetically nonequivalent nuclei (three H and three F) interacting through four coupling constants: $^4J(^1H\text{-}^1H)$, $^4J(^{19}F\text{-}^{19}F)$, $^3J(^1H\text{-}^{19}F)$ and $^5J(^1H\text{-}^{19}F)$.[178] The resulting ^1H and ^{19}F NMR spectra each consist of 56 distinct transitions with the ^{19}F spectrum having features similar to the terminal fluorine resonance in the spectrum of $(ReO_2F_3)_3$.

Simulation of the ^{19}F NMR spectrum of $(ReO_2F_3)_3$, an $(AX_2)_3$ spin system, was achieved using nine magnetically nonequivalent fluorines (six terminal (F_t) and three bridging (F_b)) and required two chemical shifts and five coupling constants (Figure 6.2). The dominant features of the spectrum were first simulated by refining the larger two-bond coupling constants to $^2J(^{19}F_t\text{-}^{19}F_b) = 98$ Hz and $^2J(^{19}F_b\text{-}^{19}F_b) = 65$ Hz. The secondary features of the spectrum were simulated by the introduction and refinement of the three-

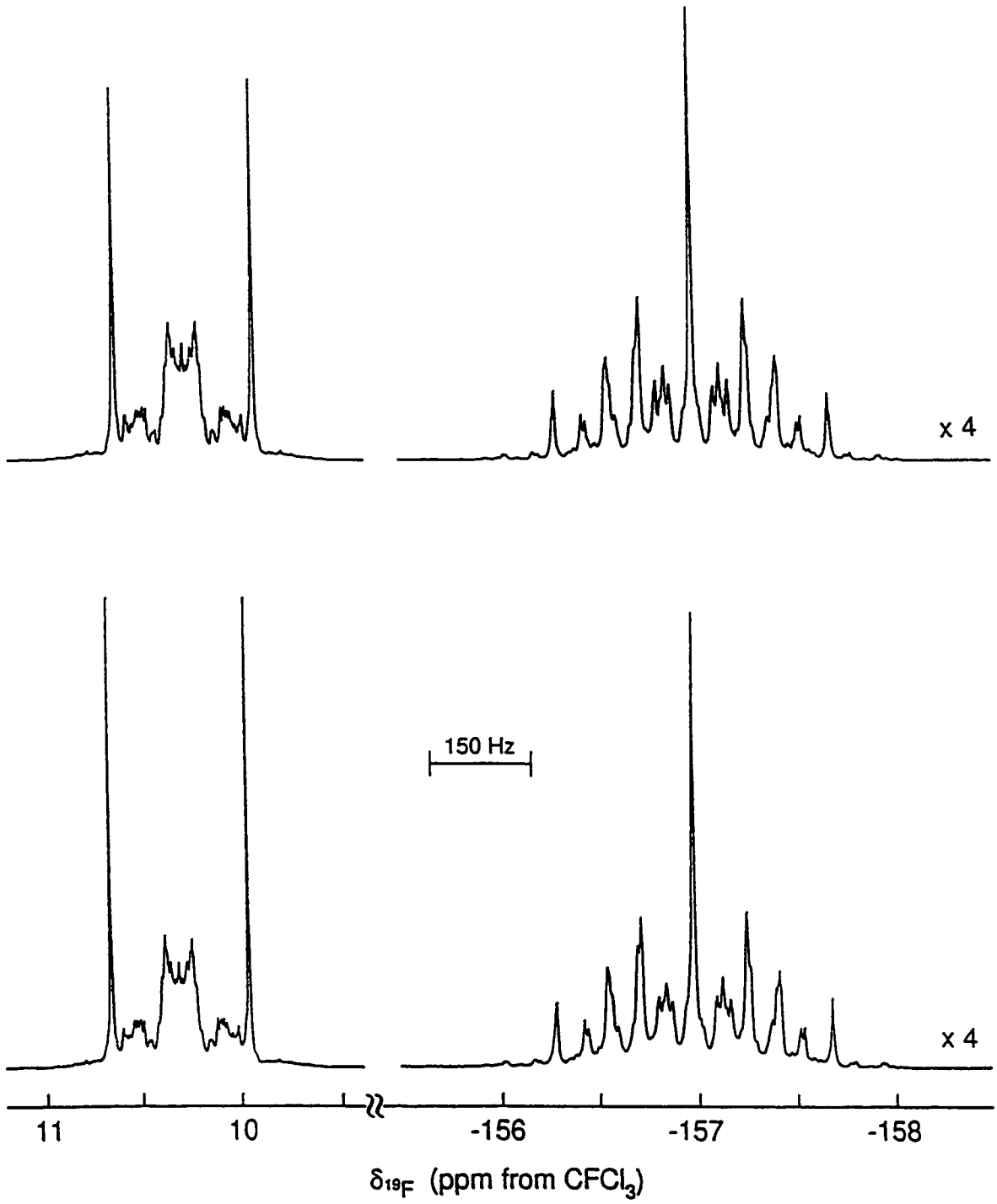

Figure 6.2. The simulated (upper trace) and observed (lower trace) ^{19}F NMR spectra (282.409 MHz) of ReO_2F_3 in SO_2ClF recorded at -120 °C showing the terminal and bridging fluorine environments of the cyclic trimer $(ReO_2F_3)_3$.

bond coupling constants $^3J(^{19}F_t\text{-}^{19}F_t) = 12$ Hz and $^3J(^{19}F_t\text{-}^{19}F_t') = 2$ Hz (coupling between fluorines *cis* and *trans* with respect to a fluorine bridge, respectively). The exact value of the last coupling constant introduced, $^2J(^{19}F_t\text{-}^{19}F_t)$, could not be determined with certainty because acceptable simulated spectra were obtained for any value above 15 Hz, but was set to 15 Hz based on the results obtained for the simulations of $(ReO_2F_3)_4$ and $(TcO_2F_3)_3$.

The ^{19}F NMR spectrum of $(ReO_2F_3)_4$, an $(AX_2)_4$ spin system, was simulated with a similar procedure, which required twelve magnetically nonequivalent fluorine nuclei (eight terminal and four bridging) (Figure 6.3). The final coupling constants were $^2J(^{19}F_t\text{-}^{19}F_b) = 102$ Hz, $^2J(^{19}F_b\text{-}^{19}F_b) = 105$ Hz, $^3J(^{19}F_t\text{-}^{19}F_t) = 12$ Hz, $^3J(^{19}F_t\text{-}^{19}F_t') = 2$ Hz and $^2J(^{19}F_t\text{-}F_t) = 15$ Hz. The significant increase in the magnitude of $^2J(^{19}F_b\text{-}^{19}F_b)$ in going from the trimer to the tetramer may be the result of a different F_b-Re-F_b angle in the cycles.[179] This angle is likely to be more acute in the trimer as a result of the smaller ring size, whereas it is expected to be more open in the tetramer.

The ^{19}F and ^{99}Tc NMR Spectra of TcO_2F_3 in SO_2ClF

The ^{19}F NMR spectrum of TcO_2F_3 in SO_2ClF recorded at -120 °C is shown in Figure 6.4 and consists of two resonances at 76.2 and -148.6 ppm having relative integrated intensities of 2.0:1.0. The spectrum was simulated as a $(AX_2)_3$ spin system with the method used for $(ReO_2F_3)_3$ and $(ReO_2F_3)_4$, resulting in the coupling constants $^2J(^{19}F_b\text{-}^{19}F_t) = 105$ Hz, $^2J(^{19}F_b\text{-}^{19}F_b) = 48$ Hz and $^2J(^{19}F_t\text{-}^{19}F_t) = 15$ Hz. The broadness of the resonances in the experimental spectrum resulting from residual scalar coupling of the fluorine to the quadrupolar ^{99}Tc nucleus precluded the refinement of additional coupling

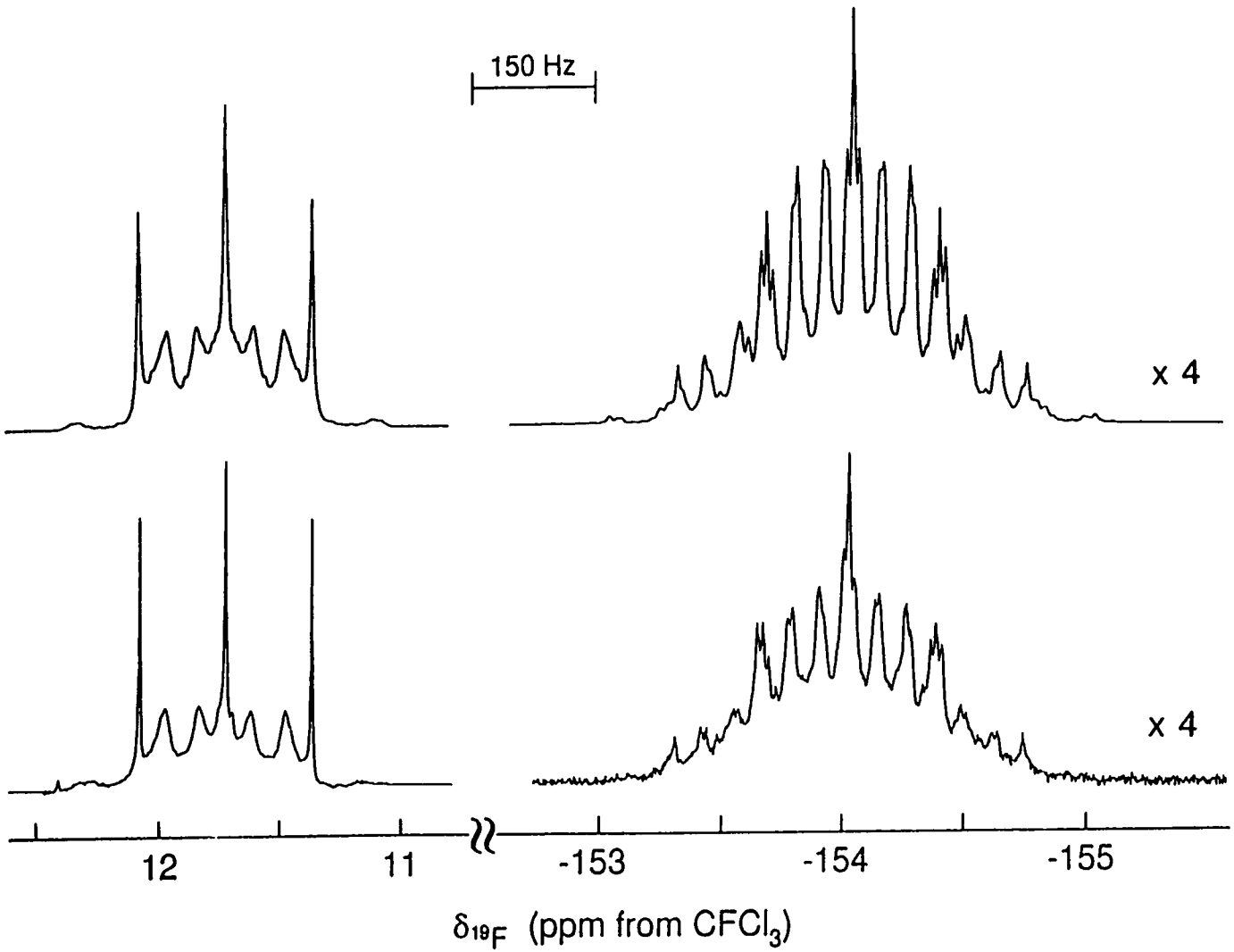

Figure 6.3. The simulated (upper trace) and observed (lower trace) ^{19}F NMR spectra (282.409 MHz) of ReO_2F_3 in SO_2ClF recorded at -120 °C showing the terminal and bridging fluorine environments of the cyclic tetramer $(ReO_2F_3)_4$.

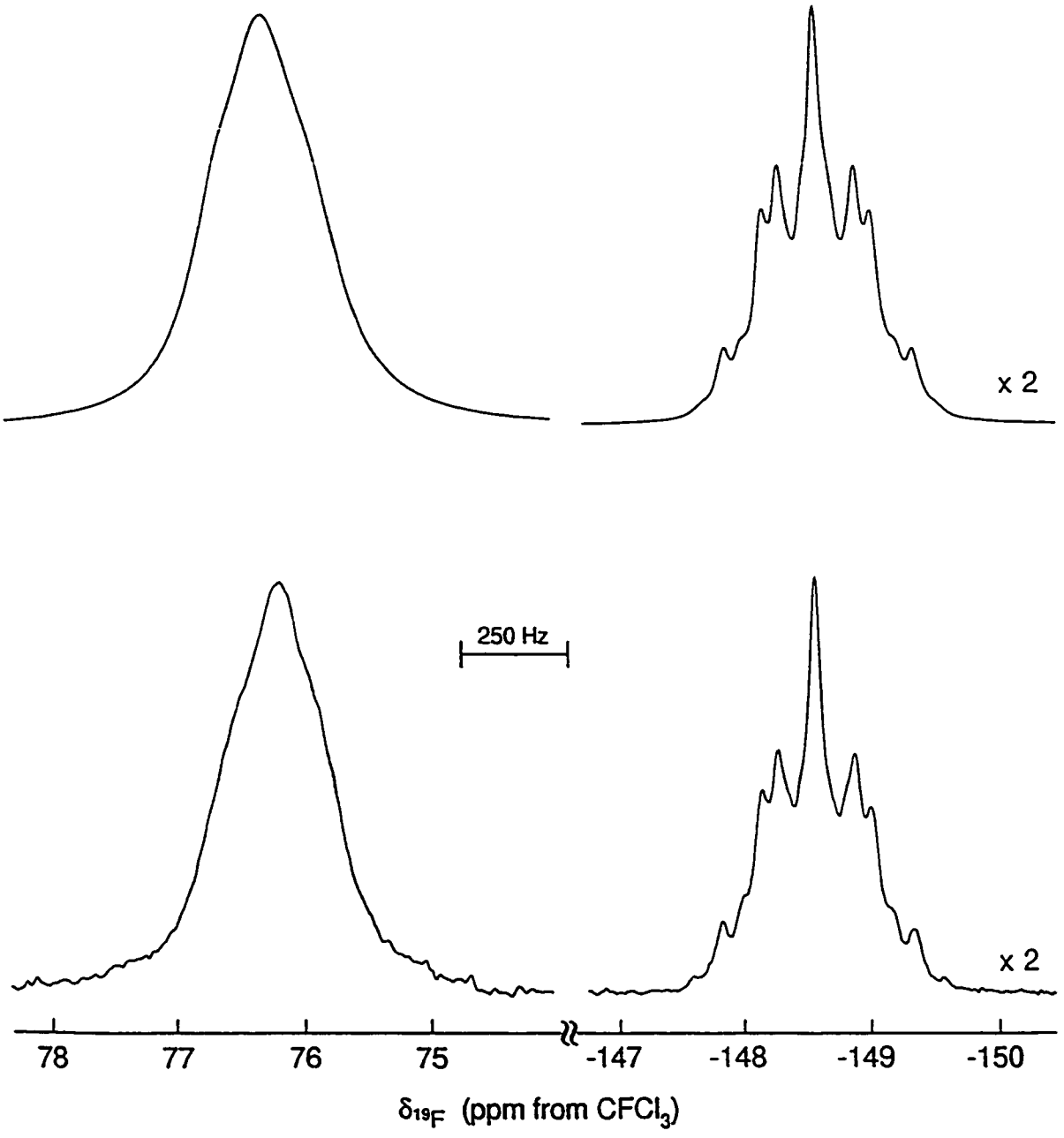

Figure 6.4. The simulated (upper trace) and observed (lower trace) ^{19}F NMR spectra (282.409 MHz) of TcO_2F_3 in SO_2ClF recorded at -120 °C showing the terminal and bridging fluorine environments of the cyclic trimer $(TcO_2F_3)_3$.

constants of lower magnitude. Line-broadening factors of 130 Hz and 30 Hz in the simulation of the terminal and bridging resonances, respectively, were required in order to account for the residual coupling between ^{99}Tc and the fluorine nuclei which is expected to follow the order $^1J(^{19}F_t\text{-}^{99}Tc) > {}^1J(^{19}F_b\text{-}^{99}Tc)$ (see Chapter 3). The ^{19}F NMR spectrum at 30 °C (Figure 6.5a) shows the partially quadrupole-collapsed saddle-shaped resonance of the terminal fluorines at 85.1 ppm ($\Delta\nu_{1/2}$ = 1570 Hz), and is consistent with the larger coupling between ^{99}Tc and the terminal fluorines. The bridging fluorine resonance could not be observed at this temperature presumably because of its low intensity and quadrupolar broadening.

The ^{99}Tc NMR spectrum of TcO_2F_3 in SO_2ClF recorded at 30 °C shows a single resonance at 211.0 ppm ($\Delta\nu_{1/2}$ = 500 Hz) with partly resolved coupling to the terminal fluorines of $(TcO_2F_3)_3$. After resolution enhancement by Gaussian multiplication of the free-induction decay (Figure 6.5b) , the one-bond $^{99}Tc\text{-}^{19}F_t$ coupling constant was estimated at $^1J(^{99}Tc\text{-}^{19}F_t) \approx 160$ Hz, which is significantly smaller than the value of 235 Hz observed for $N(CH_3)_4^+TcO_2F_4^-$ in CH_3CN (see Chapter 3). The ^{99}Tc chemical shift of $(TcO_2F_3)_3$ in SO_2ClF is more shielded than that of TcO_2F_3 in CH_3CN (267.4 ppm at 30 °C), $N(CH_3)_4^+TcO_2F_4^-$ in CH_3CN (343.2 ppm at 45 °C) and $Cs^+TcO_2F_4^-$ in HF (247.4 ppm at 30 °C).

Raman Spectroscopy

Attempts to grow crystals of $(ReO_2F_3)_3$ and $(ReO_2F_3)_4$ from SO_2ClF solutions were unsuccessful. However, the Raman spectrum of the colourless material recovered from

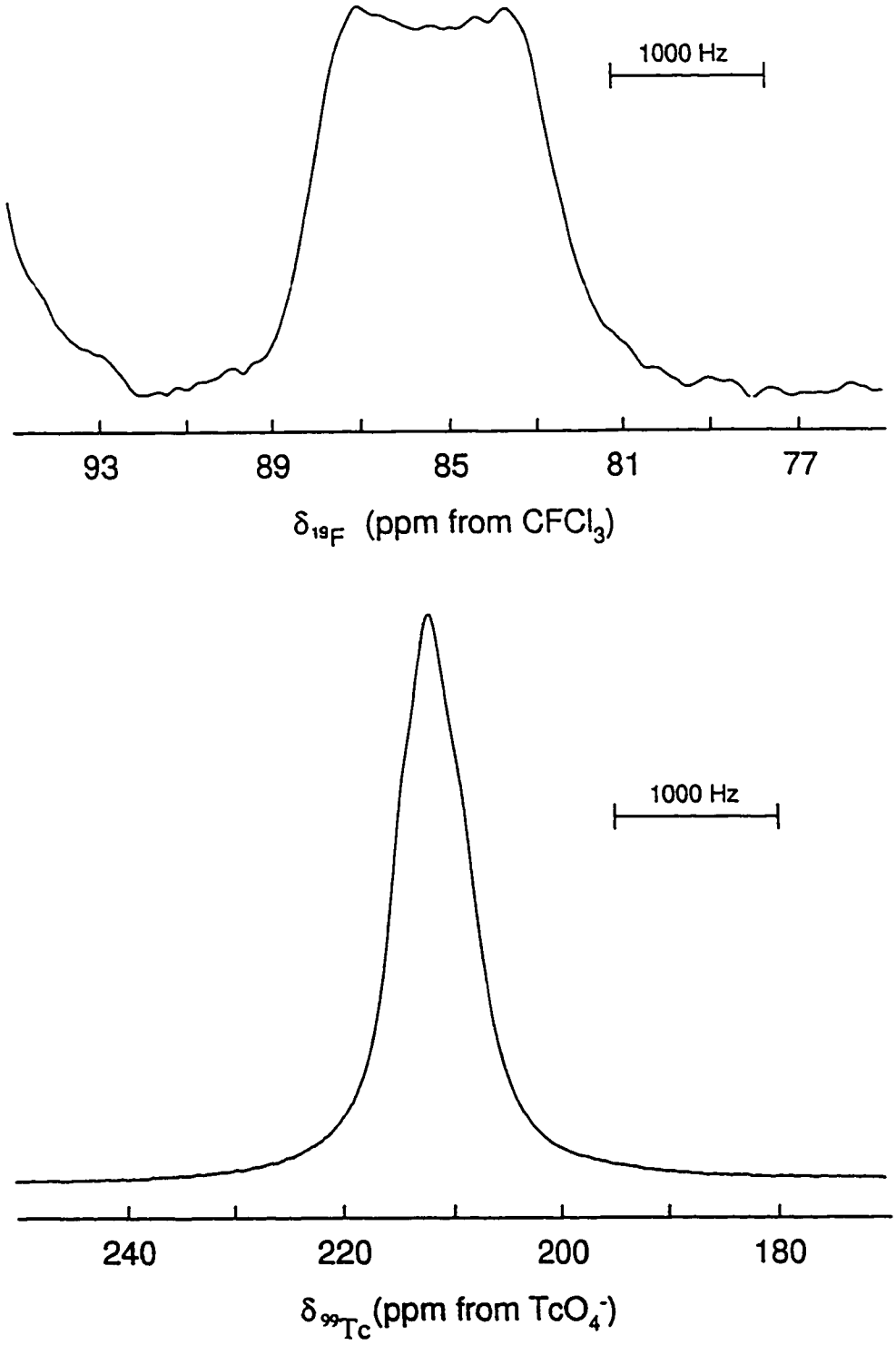

Figure 6.5. NMR spectra of TcO_2F_3 in SO_2ClF recorded at 30 °C showing coupling between the terminal fluorine environments and ^{99}Tc in $(TcO_2F_3)_3$: (a) ^{19}F (282.409 MHz) spectrum and (b) ^{99}Tc (67.555 MHz) spectrum.

these solutions (Figure 6.6a) shows significant shifts in a number of bands compared to the spectrum of polymeric ReO_2F_3 (Table 6.1). The bands assigned to the antisymmetric Re-O stretching mode are shifted from 990 and 994 cm^{-1} in polymeric ReO_2F_3 to 997 and 1001 cm^{-1}, the bands assigned to the symmetric terminal Re-F stretching mode are shifted from 700 and 713 cm^{-1} to 688 cm^{-1}, and the band assigned to the ReO_2 bending mode is shifted from 412 cm^{-1} to 404 cm^{-1}. Although the exact origin of these frequency shifts is not clear, they indicate that the material recovered from SO_2ClF is a different structural phase than polymeric ReO_2F_3 (see Chapter 4). The Raman frequencies and intensities of the material recovered from a solution of TcO_2F_3 in SO_2ClF (Figure 6.6b) are not shifted significantly from those of polymeric TcO_2F_3.[41]

Conclusion

In this Chapter, it was shown by simulation of the ^{19}F NMR spectrum of ReO_2F_3 in SO_2ClF that the solution contains an equilibrium mixture of a cyclic trimer, a cyclic tetramer and possibly a cyclic pentamer. In contrast, TcO_2F_3 exists in SO_2ClF solution exclusively as the cyclic trimer.

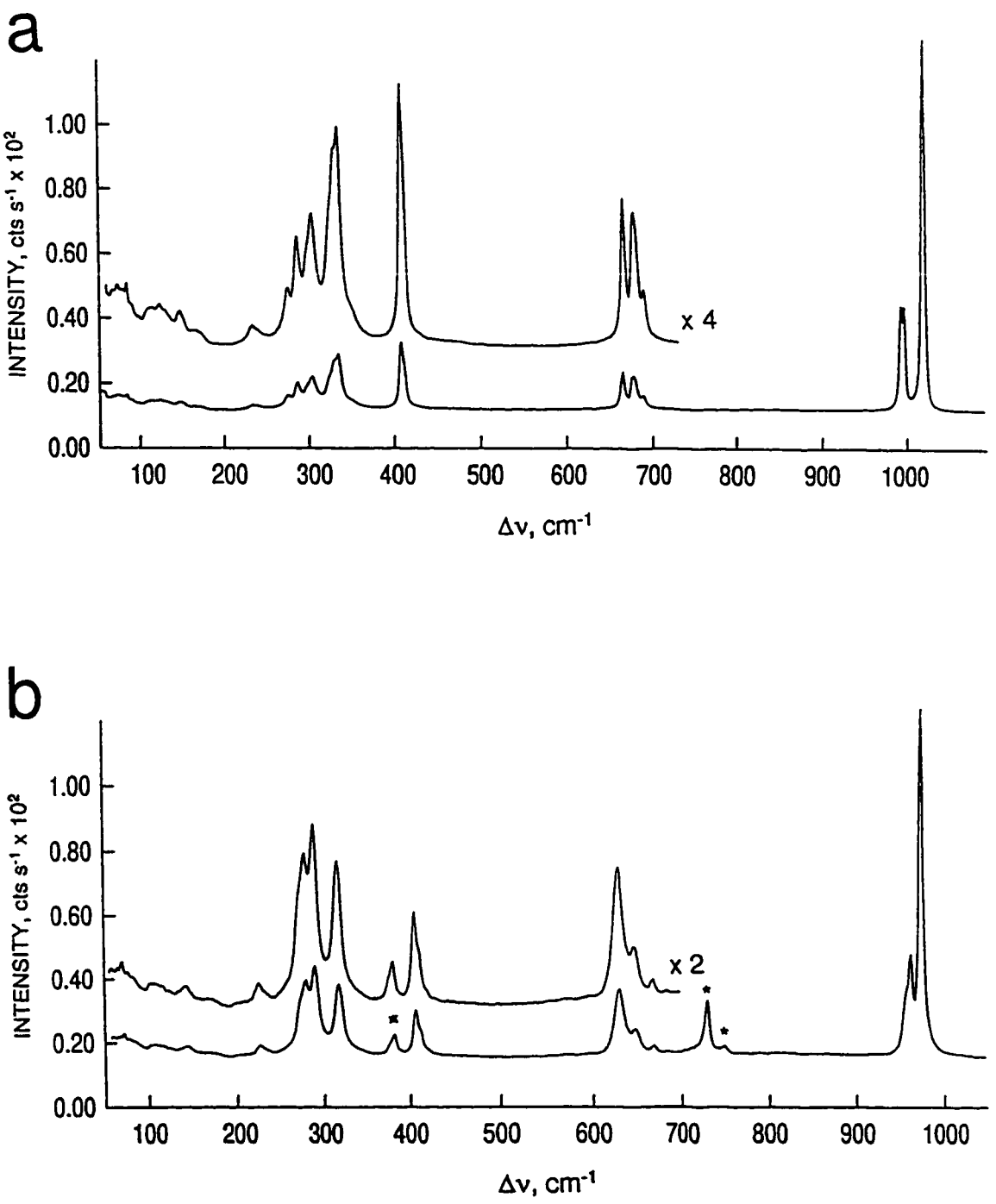

Figure 6.6. Raman spectra of microcrystalline material recovered from a solution of (a) ReO_2F_3 in SO_2ClF and (b) TcO_2F_3 in SO_2ClF recorded at 22 °C using 514.5-nm excitation. Asterisks (*) denote FEP lines.

Table 6.1. Raman Frequencies, Assignments and Mode Descriptions for ReO_2F_3 and TcO_2F_3 Recovered from an SO_2ClF Solution Compared to their Polymeric Phases

Frequencies (cm^{-1})[a]				Assignments[b]
ReO_2F_3 from SO_2ClF[c]	ReO_2F_3 polymer[d]	TcO_2F_3 from SO_2ClF[c]	TcO_2F_3 polymer[d]	C_{2v} point symmetry
1025(100)	1026(100)	973(100)	974(100)	A_1, $\nu_s(ReO_2)$
1001(29) 997(29)	994(33) 990(11)	961(29) 958(17),sh	963(27) 956,sh	B_1, $\nu_{as}(ReO_2)$
688(5),sh	713(2) 700(14)	685(1) 669(2)	685(3) 670(7)	A_1, $\nu_s(ReF_{2t})$
677(10) 665(11)	670(1),sh 664(4)	648(7) 631(19)	650(16) 632(36)	B_2, $\nu_{as}(ReF_{2t})$
404(19)	412(17)	414(8),sh 409(13)	416,sh 411(19)	A_1, $\delta(ReO_2)$
345(4),sh 328(16)	349(6) 332(11)			A_1, $\delta(ReF_{2t})$
323(15),sh 318(10),sh	326(6),sh 319(5)	319(19)	320(22)	B_2, $\rho_w(ReO_2)$

Table 6.1. continued

298(10) 292(8),sh	288(1)	292(25)	295(30)	B_1, $\delta(ReF_{2t})$
280(9)	276(2)	281(21)	284(24)	A_2, $\rho_t(ReO_2)$
268(5)	270(4)	275(15),sh	278,sh	
	251(3)		264(2)	
226(3)	223(>0)	228(4)	231(3)	B_2, $\rho_w(ReF_{2b})$
	213(>0) 204(>0)		215(>0)	
158(3)	159(1)	172(2)	175(>0)	A_1, $\delta(ReF_{2b})$
139(4)	136(4)	146(4)	148(2)	B_1, $\rho_t(ReO_2)$
114(4)	114(>0)		122(2)	
106(4) 81(4)	101(2) 87(>0)	110(3)	111(2)	
75(6)	75(1)	75(8)		A_2, $\rho_t(ReF_{2b})$
	55(4)			

Table 6.1. continued

[a] Values in parentheses denote relative intensities; sh: shoulder.

[b] ν: stretching; δ: in-plane bending; ρ_t: twisting; ρ_r: rocking; ρ_w: wagging. F_t and F_b denote terminal and bridging fluorines, respectively.

[c] Spectrum recorded on microcrystalline solid in Pyrex glass capillary at 23 °C using 514.4-nm excitation.

[d] From Chapter 4.

[e] Spectrum recorded on microcrystalline solid in FEP at 23 °C.

[f] From ref. 41, with new assignments based on those of ReO_2F_3.

CHAPTER 7

SYNTHESIS, CHARACTERIZATION AND CHEMICAL BEHAVIOUR OF $TcOF_5$

Introduction

As noted in Chapter 1, $ReOF_5$ can be prepared relatively easily by high temperature fluorination of ReO_2 with elemental fluorine. Under similar conditions, TcO_2 is only fluorinated to TcO_3F. The relative resistance of the Tc metal centre to further fluorination follows the trend of increased oxophilicity in going from Re(VII) to Tc(VII) to Mn(VII). This phenomenon also dominates Os(VIII) and Ru(VIII) oxofluoride chemistry. When OsO_4 is allowed to react with KrF_2 in HF, the fluorination does not proceed beyond OsO_2F_4 [eq. (7.1)].[63] In an attempt to prepare $OsOF_5^+$ and $OsOF_6$, the reaction of OsO_2F_4 with $KrF^+AsF_6^-$ was carried out in HF but only resulted in the formation of the dinuclear $Os_2O_4F_7^+$ cation [eq. (7.2)].[63] No oxofluorides of Ru(VIII) have

$$OsO_4 + 2\ KrF_2 \xrightarrow{HF} OsO_2F_4 + 2\ Kr + O_2 \qquad (7.1)$$

$$2\ OsO_2F_4 + KrF^+AsF_6^- \xrightarrow{HF} Os_2O_4F_7^+AsF_6^- + Kr + F_2 \qquad (7.2)$$

yet been prepared. Ruthenium tetroxide is unreactive toward fluorine gas at room temperature, but reacts with KrF_2 in HF yielding $RuOF_4$ in which ruthenium has been

reduced to the +6 oxidation state [eq. (7.3)].[180] Fluorination of RuO_4 with ClF_3 at room temperature results in the formation of $ClO_2^+RuF_6^-$.[181]

$$RuO_4 + 2\ KrF_2 \xrightarrow{HF} RuOF_4 + {}^3/_2\ O_2 + 2\ Kr \qquad (7.3)$$

Detailed structures of the transition metal oxopentafluorides have not yet been determined. A gas phase electron diffraction study[17] confirmed the expected C_{4v} geometry of $ReOF_5$ but the axial and equatorial Re-F bond lengths were refined as one parameter and therefore could not be differentiated. The difference in axial and equatorial M-F bond lengths is of particular interest because it is not clear if the *trans* influence of the oxo ligand plays an important role in the structures of oxopentafluorides. Single crystals of $OsOF_5$ have been examined by X-ray crystallography[182] but the analysis of the data was complicated by absorption problems and possible disorder of the structure. As a result, some of the reported bond lengths (more specifically, the axial Os-F bond length of 1.72 ± 0.03 Å and Os-O bond length of 1.74 ± 0.03 Å) are probably not reliable. Normal coordinate treatments[183] of the vibrational spectra of $ReOF_5$ and $OsOF_5$ concluded that the axial M-F bond is significantly more covalent than the equatorial bonds, which contrasts with the lengthening of the axial bond anticipated as a result of the *trans* influence of the oxo ligand.

The fluoride-ion donor behaviour of $ReOF_5$ toward the strong Lewis acids AsF_5 and SbF_5 has been studied,[184] resulting in the synthesis of cationic species. The structure of the dinuclear $Re_2O_2F_9^+$ cation was determined by X-ray crystallography as its $Sb_2F_{11}^-$ salt and consists of two fluorine-bridged $ReOF_5$-units with the oxo ligands *trans* to the

bridging fluorine (Figure 1.3b). The nature of the compound resulting from the combination of $ReOF_5$ and AsF_5 was described as discrete $ReOF_4^+$ cations and AsF_6^- anions based on the 1:1 combining ratio of $ReOF_5$ and AsF_5, although the bands attributed to the cation in the Raman spectrum of $ReOF_5 \cdot AsF_5$ were identical in frequencies and relative intensities to those of $Re_2O_2F_9^+Sb_2F_{11}^-$.[184]

The fluoride-ion affinity of $ReOF_5$ was investigated using KF, RbF, CsF, NOF and NO_2F as the fluoride sources.[53,55] The structure of the $ReOF_6^-$ anion was determined by X-ray crystallography as its NO_2^+ and Cs^+ salts which were obtained by slow hydrolysis of CH_3CN solutions of $NO_2^+ReF_8^-$ and $Cs^+ReF_8^-$, and consists of a pentagonal bipyramidal arrangement of the ligands around the Re atom, with the doubly-bonded oxygen occupying an axial position (Figure 1.4b).[54]

This Chapter describes the synthesis of the last member of the Tc(VII) oxofluoride series, $TcOF_5$, and its characterization by ^{19}F and ^{99}Tc NMR spectroscopy and by vibrational spectroscopy. The fluoride-ion donor behaviour of $TcOF_5$ toward AsF_5 and SbF_5 is also described as well as attempts to prepare the $TcOF_6^-$ anion and the TcF_6^+ cation.

Results and Discussion

The Synthesis of $TcOF_5$ and its Characterization by NMR and Vibrational Spectroscopy

When TcO_3F is fluorinated to TcO_2F_3 by XeF_6 in anhydrous HF, no evidence was found for further fluorination to $TcOF_5$. Instead, any excess XeF_6 present acts as a

fluoride-ion donor, solubilizing TcO_2F_3 to form $XeF_5^+TcO_2F_4^-$ (see Chapter 3). A similar behaviour was observed for the rhenium system (see Chapter 4). In an attempt to produce a stronger fluorinating medium, TcO_2F_3 was dissolved in liquid XeF_6 at 40 °C forming a yellow solution but no indication of $TcOF_5$ formation was detected by Raman spectroscopy.

As can be seen from the previous results, a fluorinating agent stronger than XeF_6 is needed to remove one of the two remaining oxygens of TcO_2F_3. Krypton difluoride was found to be a strong enough fluorinating agent to generate $TcOF_5$ from TcO_2F_3, although a ten-fold excess of KrF_2 is needed because of the competing autodecomposition of the KrF_2 at room temperature over the 48 h required for complete reaction [eq. (7.4)]. The

$$TcO_2F_3 + KrF_2 \xrightarrow{HF} TcOF_5 + Kr + {}^1/_2\ O_2 \qquad (7.4)$$

unfavourable kinetics are thought to be the result of the strong Tc-O double bond and also the fact that TcO_2F_3 is insoluble in HF. Consequently, the reaction was attempted with the HF-soluble $TcO_2F_4^-$ for which the negative charge should weaken the Tc-O bonds [eq. (7.5)]. Unfortunately, the reaction rate did not increase significantly. Periodic sonication

$$Cs^+TcO_2F_4^- + KrF_2 \xrightarrow{HF} TcOF_5 + Kr + {}^1/_2\ O_2 + Cs^+(HF)_xF^- \qquad (7.5)$$

of a mixture of TcO_2F_3 and a five-fold excess of KrF_2 in HF was determined to be the most efficient method for the preparation of $TcOF_5$.

The resulting volatile orange solid melts reversibly and without decomposition at 57-58 °C and is deep red-orange in the liquid state. The solid is stable for at least two

weeks at room temperature when kept under anhydrous conditions, but eventually decomposes to a dark red uncharacterized compound after two months, even when kept at -78 °C.

NMR Spectroscopy. The gross structure of $TcOF_5$ was unambiguously established by ^{19}F NMR spectroscopy. At -110 °C in SO_2ClF solvent, the ^{99}Tc-^{19}F scalar couplings are quadrupole collapsed as a result of the long rotational correlation time of the $TcOF_5$ at this temperature. The spectrum (Figure 7.1a) consists of a doublet at 364.1 ppm and a quintet at 62.0 ppm having relative integrated intensities of 4.0:1.0, and were assigned to the equatorial (F_e) and the axial fluorines (F_a), respectively, confirming the pseudooctahedral geometry expected for the $TcOF_5$ molecule (Structure I). The two-bond

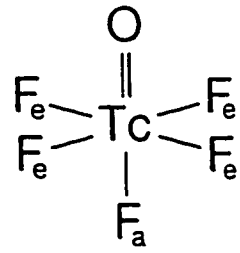

Structure I

fluorine-fluorine scalar coupling, $^2J(^{19}F_a$-$^{19}F_e) = 75$ Hz, is very similar in magnitude to that of $ReOF_5$ (69 Hz).[15] The ^{19}F resonances of $TcOF_5$ occur at 371.7 ppm ($\Delta\nu_{1/2} = 4930$ Hz) and 45.0 ppm ($\Delta\nu_{1/2} = 1840$ Hz), respectively, at 35 °C in HF solvent (Figure 7.1b) but are broadened by partially quadrupole-collapsed spin-spin coupling to the ^{99}Tc nucleus as a result of a shorter rotational correlation time. The ^{99}Tc NMR spectrum (67.520 MHz)

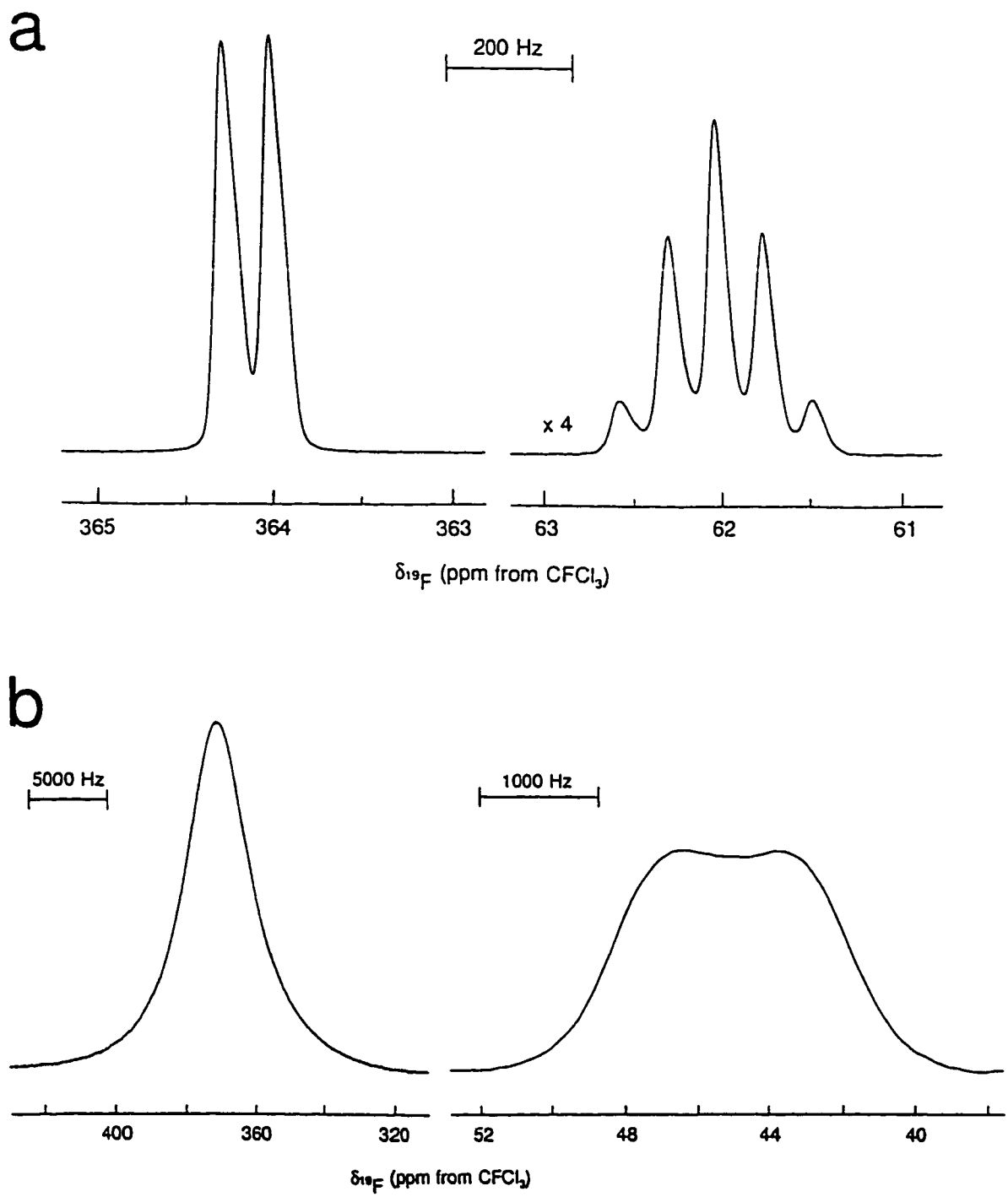

Figure 7.1. ^{19}F NMR spectra (282.409 MHz) of (a) $TcOF_5$ dissolved in SO_2ClF solvent at -110 °C and (b) $TcOF_5$ dissolved in HF at 30 °C.

of $TcOF_5$ recorded at 35 °C in HF and at 30 °C in SO_2ClF shows broad resonances at 394.5 ($\Delta\nu_{1/2}$ = 440 Hz) and 433.8 ppm ($\Delta\nu_{1/2}$ = 6680 Hz), respectively. No $^1J(^{99}Tc\text{-}^{19}F)$ couplings could be resolved in either the ^{19}F or ^{99}Tc NMR spectrum because of quadrupolar broadening resulting from the fast relaxation rate of the ^{99}Tc nucleus. These results are consistent with a previous study[40] of the reaction between TcO_3F and KrF_2 in HF, in which no products were isolated and the new ^{99}Tc resonance was wrongly attributed to TcO_2F_3, mainly because of the failure to observe the equatorial fluorine resonance at high frequency in the ^{19}F NMR spectrum.

The Trans Influence. There have been several theoretical discussions of the *trans* influence and effect.[191] As early as 1935, Grinberg[185] proposed an explanation based on polarization theory. An easily polarizable ligand induces a build-up of negative charge on the metal which is directed toward the *trans* position and an incoming ligand at the *trans* position is repelled by the dipole of the metal. The electrostatic viewpoint was improved upon by Syrkin,[186] who included hybridization at the metal to explain the *trans* effect. Chatt et al.[187] and Orgel[188] have interpreted the *trans* effect as being the result of a strong π interaction between the *trans*-directing ligand and the metal. When two ligands are located *trans* to each other, they compete for the same metal valence orbitals. If one ligand has a larger overlap with these orbitals then there is a diminution in the overlap between the metal and the *trans* ligand.

The lengthening of the M-F bond (where M is a d^0 transition metal) *trans* to an oxo ligand was also rationalized by Gillespie et al.[114] who performed SCF calculations on

a number of Cr(VII) oxofluoride complexes. The geometries adopted by these complexes, some of which do not agree with the VSEPR model predictions, were accounted for in terms of core electron distortions. For example, in $CrOF_5^-$ the strong covalent interaction of the oxo ligand with the metal causes a distortion of the outer electronic shell of the metal core resulting in a large charge concentration opposite to the Cr-O bond. Weaker interactions between the equatorial fluorine ligands and the metal result in four smaller charge concentrations opposite each fluorine ligand, for a total of five charge concentrations with an overall square pyramidal arrangement (Figure 7.2a). Consequently, the axial Cr-F bond is longer than the equatorial Cr-F bonds because it is facing a larger charge concentration. The geometric parameters calculated for $CrOF_5^-$ in the gas phase show an axial Cr-F bond (1.8318 Å) significantly longer than the equatorial bonds (1.7530 Å). This model also predicts longer *trans*-to-oxygen Cr-F bonds in *cis*-$CrO_2F_4^{2-}$ (1.9467 Å versus 1.8736 Å) based on a similar build-up of charge concentrations *trans* to the oxo ligands (Figure 7.2b).

Vibrational Spectroscopy. The Raman spectrum of $TcOF_5$ in the solid state and in HF solution at 22 °C are shown in Figure 7.3. The observed frequencies and their assignments are listed in Table 7.1 and the vibrational modes are shown in Figure 7.4. The 15 vibrational modes of $TcOF_5$ (C_{4v} point symmetry) belong to the irreducible representations $4A_1 + 2B_1 + B_2 + 4E$ which are all Raman active and the A_1 and E modes are infrared-active.

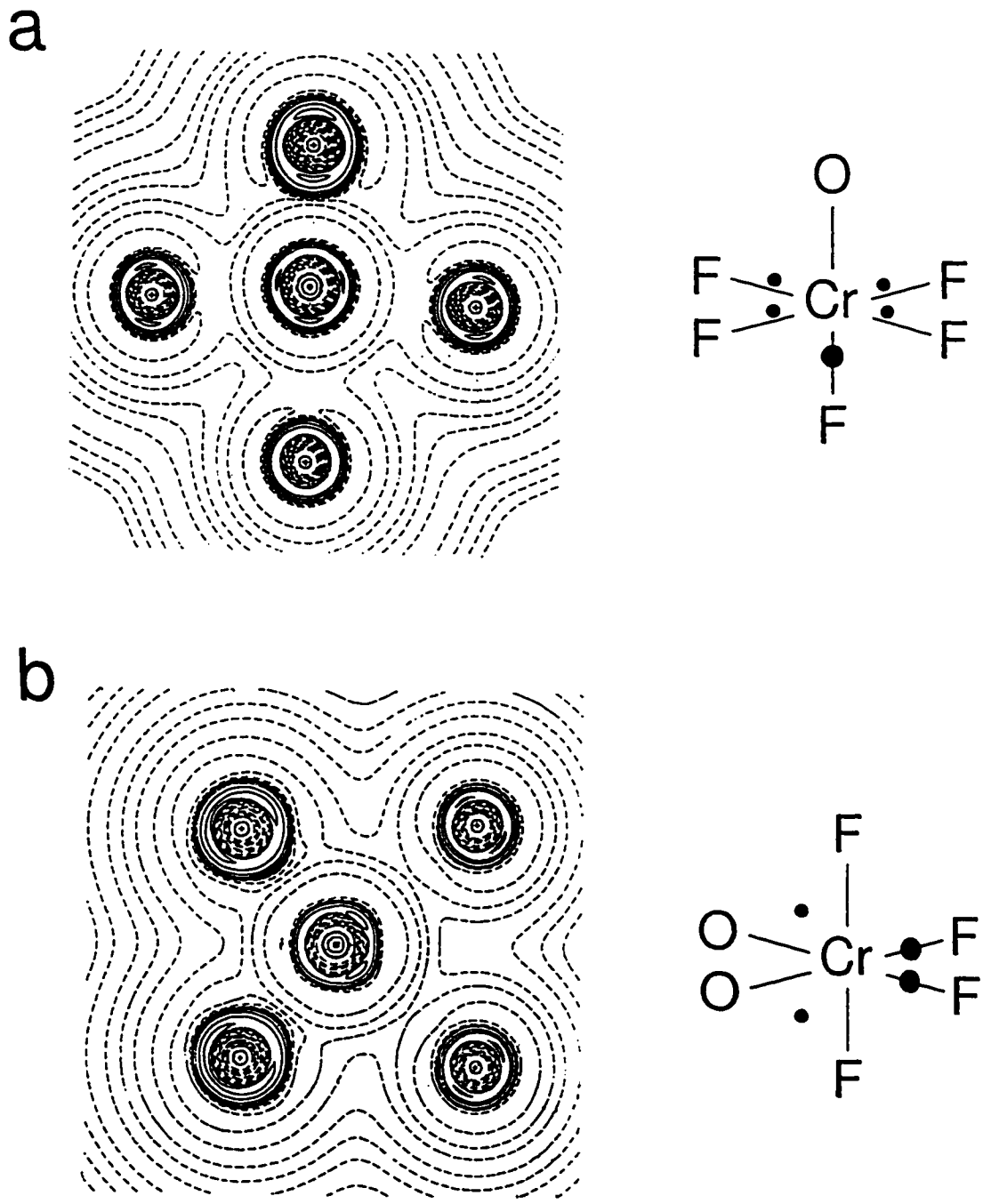

Figure 7.2. Contour maps of $L = -\nabla^2\rho(r)$ for (a) $CrOF_5^-$ through the $[OCrF_3]$-plane and (b) $CrO_2F_4^{2-}$ through the $[O_2CrF_2]$-plane, with the corresponding diagrams showing the positions and relative sizes of the charge concentrations in the outer shell of the core of Cr.

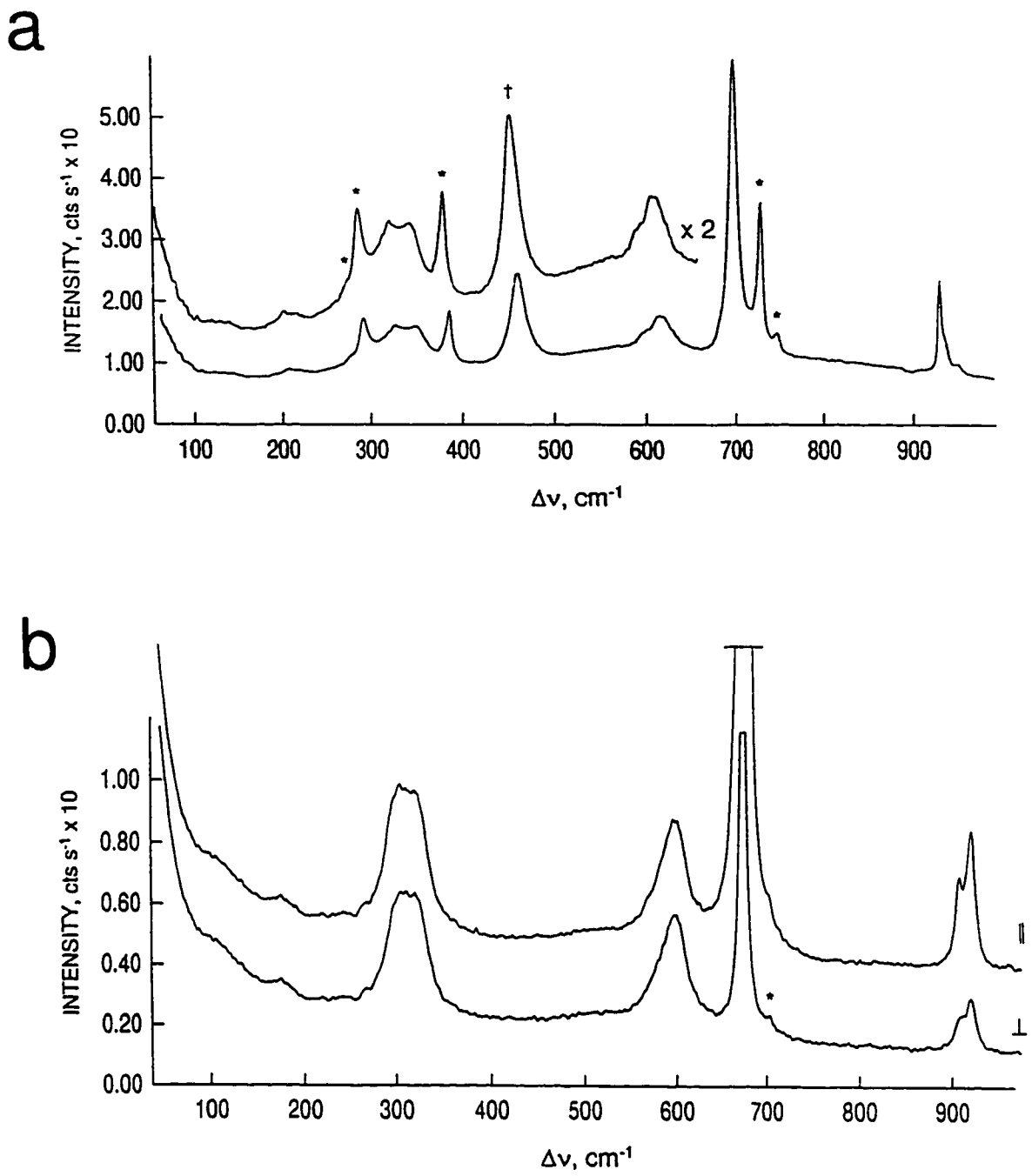

Figure 7.3. Raman spectra of (a) microcrystalline $TcOF_5$ and (b) an HF solution of $TcOF_5$ recorded in FEP at 22 °C using 647.1-nm excitation, with the analyzer oriented parallel (∥) and perpendicular (⊥) to the polarization of the incident beam. Asterisks (*) denote FEP lines and dagger (†) denotes residual KrF_2.

Table 7.1. Experimental and Calculated Raman Frequencies, Assignments and Mode Descriptions for $TcOF_5$ in the Solid State and in HF Solution

Frequencies (cm^{-1})					
exp[a,b]			LDFT[c]		Assignment[d]
solid (22 °C)	solid (-150 °C)	solution	TZ94p	DZVP	C_{4v} point symmetry
952(2) 940(14) 933(28)	939(14),sh 933(45)	937(4),p	988(107)	961(122)	$\nu_1(A_1)$, $\nu(TcO)$
	716(16)		724(388)	721(400)	$\nu_8(E)$, $\nu(TcF_{4e})$
702(100)	703(47) 694(95),sh 690(100)	702(100),p	694(37)	690(38)	$\nu_2(A_1)$, $\nu(TcF_a)$
616(8)	626(29) 620(13),sh 614(57)	624(8),dp	627(0)	627(0)	$\nu_5(B_1)$, $\nu(TcF_{4e})$
601(5)	595(9) 588(11) 581(8) 575(8) 565(6)	598(2),sh,dp	623(40)	620(34)	$\nu_3(A_1)$, $\nu(TcF_{4e})$
351(10)	358(8)	346(10),dp	329(4)	321(4)	$\nu_9(E)$, $\rho_w(TcO)$

Table 7.1. continued

328(10)	337(39) 327(18) 320(8),sh 314(3),sh	329(10),dp	278(0)	277(0)	$\nu_7(B_2)$, $\delta(TcF_{4c})$
278(5)	293(5)	289(2),dp	315(11)	304(11)	$\nu_4(A_1)$, $\pi(TcF_{4c})$
	217(3)		329(4)	321(4)	$\nu_{10}(E)$, $\rho_w(TcF_a)$
207(2)	186(2)	199(2),dp	207(0)	194(0)	$\nu_6(B_1)$, $\pi(TcF_{4c})$
131(1)	154(2) 139(2)	135(1),br,dp	63(1)	66(2)	$\nu_{11}(E)$, $\delta(TcF_{4c})$
	84(4) 66(9)				

[a] Values in parentheses denote relative intensities; sh: shoulder; br: broad; p: polarized; dp: depolarized.

[b] Spectra recorded in FEP using 647.1-nm excitation.

[c] Values in parentheses denote infrared intensities.

[d] ν: stretching; δ: in-plane bending; π: out-of-plane bending; ρ_w: wagging.

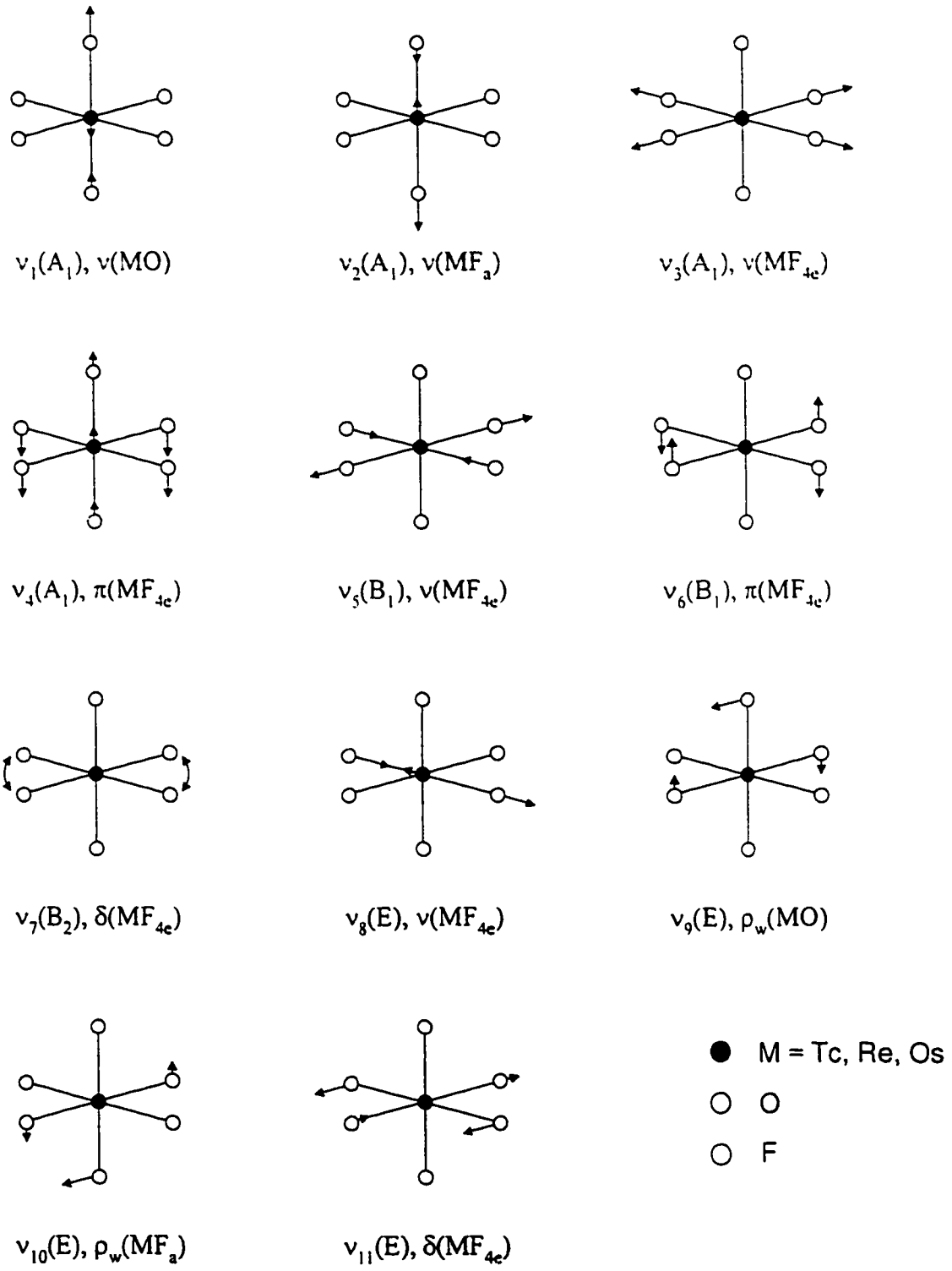

Figure 7.4. Vibrational mode descriptions obtained from the normal coordinate analysis of the vibrational spectra of MOF_5 species (M = Tc, Re, Os).

The Raman spectrum of $TcOF_5$ was assigned by analogy with the spectra of $ReOF_5$ and $OsOF_5$,[16] to which it is remarkably similar. The Tc-O stretching mode was assigned to the polarized band at 933 [937] cm^{-1} (frequency of the solid at 22 °C given with frequency in HF solution in square brackets) and occurs at lower frequency than in TcO_2F_3 (973 cm^{-1}),[41] which is in agreement with the trend observed in going from $ReOF_5$ (990 cm^{-1}) to ReO_2F_3 (1026 cm^{-1}). The intense polarized band at 702 [702] cm^{-1} was assigned to the axial TcF_a stretching mode. Two of the three equatorial Tc-F stretching modes, A_1 and B_1, were assigned to the bands at 601 and 616 [598 and 624] cm^{-1}, respectively, whereas the remaining E mode could not be observed in the Raman spectrum, which is consistent with the Raman spectra of $ReOF_5$ and $OsOF_5$ where this mode is too weak to be observed.[16] The assignment of the deformation modes follows the same ordering as in $ReOF_5$ and $OsOF_5$ and are consistent with the values calculated from the normal coordinate analysis of $TcOF_5$ (*vide infra*). Attempts to confirm the previous assignments by gas phase infrared spectroscopy failed because of the rapid decomposition of $TcOF_5$ in a glass cell equipped with AgCl windows.

The Raman spectrum of $TcOF_5$ at -150 °C is shown in Figure 7.5. The observed frequencies are listed in Table 7.1. The spectrum consists of essentially the same bands as those discussed above, but also shows extensive splitting resulting from coupling of the vibrational modes within the unit cell, i.e., factor-group splitting. Two new bands at 217 and 716 cm^{-1} were tentatively assigned to the E modes that were too weak to be observed at 22 °C (ν_{10} and ν_8) but were calculated from the normal coordinate analysis of $TcOF_5$ and by density functional theory (*vide infra*).

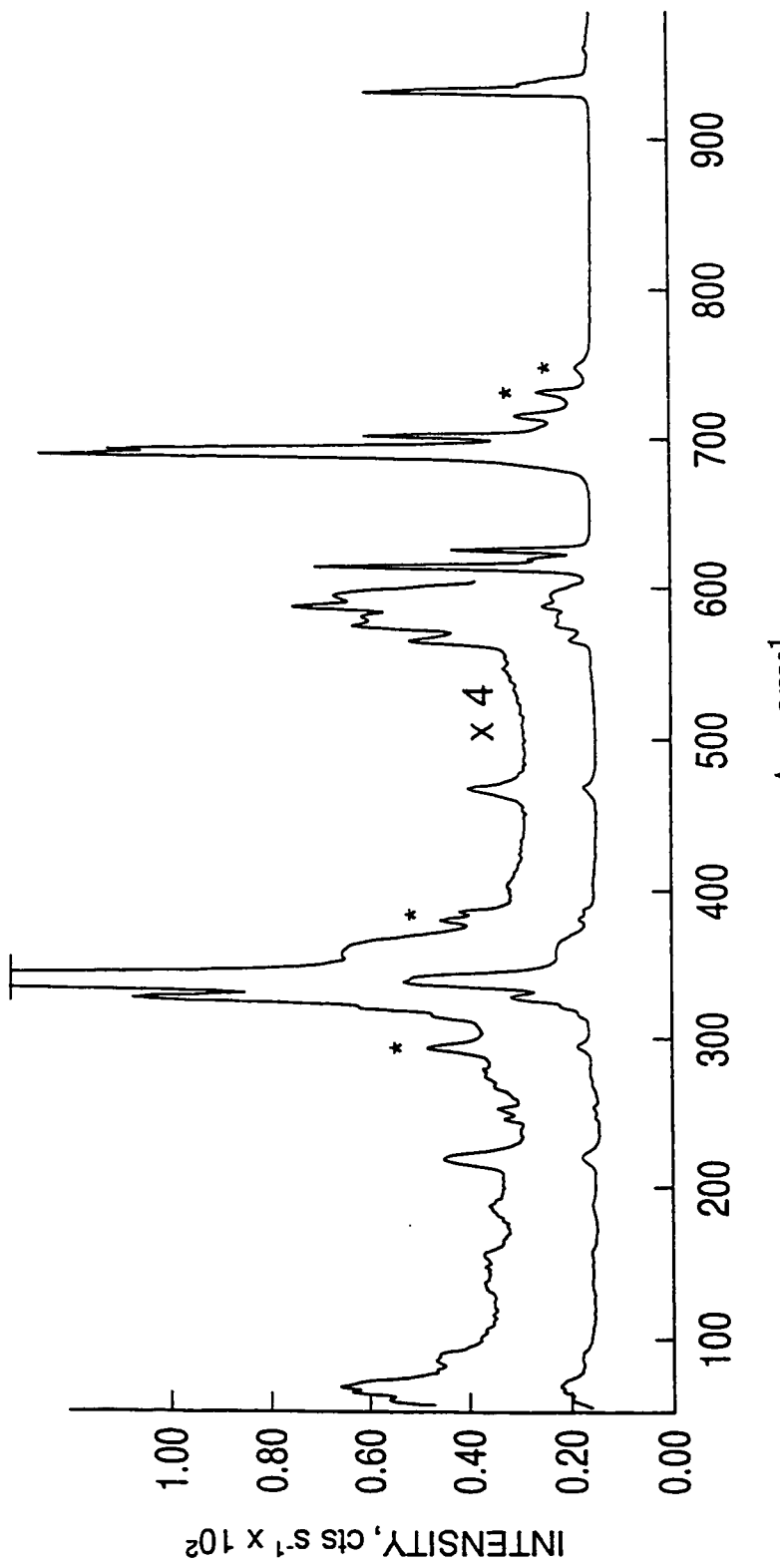

Figure 7.5. Raman spectrum of microcrystalline $TcOF_5$ recorded in FEP at -150 °C using 647.1-nm excitation. Asterisks (*) denote FEP lines.

Computational Results. The molecular geometry of $TcOF_5$ was optimized at the local density theory (LDFT) level with a polarized double-ζ basis set (DZVP) and a polarized triple-ζ basis set (TZ94P). The calculated structure of $TcOF_5$ has C_{4v} point symmetry with a Tc-O bond distance of 1.703 [1.693] Å (DZVP values given, with TZ94P value in square brackets), an equatorial Tc-F bond length of 1.845 [1.858] Å and an axial Tc-F bond length of 1.883 [1.891] Å. Comparable geometric parameters were calculated for $ReOF_5$ and $OsOF_5$ and are listed in Table 7.2.

The calculated vibrational frequencies for $TcOF_5$ are compared with the experimental values in Table 7.1. The frequencies obtained with the TZ94P basis set are somewhat closer to the experimental values than those obtained with the DZVP basis set. No scaling of the stretching frequencies was applied. The calculated vibrational frequencies of $ReOF_5$ and $OsOF_5$ (TZP/pp basis set) are listed in Table 7.3.

Normal Coordinate Analyses. The high-quality vibrational data available for $ReOF_5$ and $OsOF_5$ [16] led to a normal coordinate analysis of these species by Shalabi and Nour[183] who concluded that the axial M-F bonds are significantly stronger than the equatorial bonds, which contrasts with the longer, weaker bonds expected from the *trans* influence of the oxo ligand. However, inconsistencies were found in their data such as the reassignment of frequencies observed in the infrared spectrum to infrared-inactive modes as well as several typographical errors. In order to verify their conclusions, the normal coordinate analyses of $TcOF_5$, $ReOF_5$ and $OsOF_5$ were repeated based on the molecular geometry calculated from local density function theory (LDFT), which predicts an axial M-F bond

Table 7.2. Geometric Parameters Calculated by LDFT for $TcOF_5$, $ReOF_5$ and $OsOF_5$

	$TcOF_5$		$ReOF_5$		$OsOF_5$	
	TZ94P	DZVP	TZP/pp	DZVP	TZP/pp	DZVP
M-O	1.693	1.703	1.718	1.712	1.716	1.708
$M\text{-}F_a$	1.883	1.891	1.920	1.916	1.908	1.900
$M\text{-}F_e$	1.845	1.858	1.871	1.865	1.895	1.886

Table 7.3. Fitted Frequencies (cm^{-1}) from the Normal Coordinate Analysis of the Experimental and Theoretical Vibrational Frequencies of $TcOF_5$, $ReOF_5$ and $OsOF_5$

	$TcOF_5$				$ReOF_5$				$OsOF_5$			
	exp[a]	fit	theor[a]	fit	exp[b]	fit	theor[a]	fit	exp[b]	fit	theor[a]	fit
A_1:	937	937	988	988	990	990	941	941	963	963	965	965
	702	702	694	694	740	740	698	698	717	717	675	675
	598	598	623	615	643	643	619	614	645	641	608	602
	289	289	315	295	309	297	253	253	280	287	216	229
B_1:	624	624	627	619	652	652	637	631	644	640	618	611
	199	199	207	187	234	222	164	164	210	217	133	144
B_2:	329	329	278	277	334	334	333	333	332	332	292	292
E:	c	725	724	730	713	713	681	686	701	704	662	668
	346	346	329	336	367	372	292	292	367	364	309	312
	c	238	233	240	260	264	260	260	263	260	300	289
	135	135	63	63	125	125	164*i*[d]	212	163	163	166	162

[a] This work.

Table 7.3. continued

[b] From ref. 16.

[c] Not observed in the Raman spectrum.

[d] Imaginary frequency; not included in the least-square refinement.

longer than the equatorial bonds for all three molecules (see ***Computational Results***). The calculated force constants are listed in Table 7.4 and the vibrational frequencies fitted to the experimental and theoretical frequencies are listed in Table 7.3. The stretching force constants are significantly larger for the axial M-F bond than for the equatorial bonds and agree well with results obtained by Shalabi and Nour for $OsOF_5$ and $ReOF_5$.[183]

In an attempt to account for the longer axial M-F bond lengths obtained from LDFT calculations, the assignments of the axial and equatorial A_1 M-F stretching modes were reversed. Refinements based on these new assignments were either unstable or diverging, resulting in poor agreement between the observed and calculated frequencies and confirming the correctness of the original assignments. The fact that the normal coordinate analyses based on the theoretical vibrational frequencies still results in stronger axial M-F bonds than equatorial bonds indicates that the calculated force constants for $TcOF_5$, $ReOF_5$ and $OsOF_5$ cannot be used to predict the relative bond lengths in these molecules.

Experimental confirmation of the geometry of the $TcOF_5$ molecule by single-crystal X-ray crystallography is made extremely difficult because of its moisture sensitivity, volatility, radioactivity and instability toward glass. These difficulties may be circumvented in the near future by the use of a low-temperature crystal mounting technique presently under development in Prof. Schrobilgen's laboratory, which consists of coating the crystal with a low-melting, high molecular weight perfluorinated polyether under a cold nitrogen gas stream followed by low-temperature transfer of the sample to

Table 7.4. General Valence Force Constants[a] Calculated from the Normal Coordinate Analysis of the Experimental and Theoretical Vibrational Frequencies of $TcOF_5$, $ReOF_5$ and $OsOF_5$

	$TcOF_5$		$ReOF_5$			$OsOF_5$		
	exp	theor	exp	theor	S&N[b]	exp	theor	S&N[b]
f_D	6.83	7.65	8.40	7.60	8.35	7.97	8.03	7.90
f_R	4.86	4.70	5.63	5.02	5.55	5.30	4.69	5.20
f_r	4.18	4.26	4.69	4.34	4.70	4.60	4.12	4.60
f_α	0.29	0.06	0.26	1.07	0.57	0.47	0.37	0.66
f_β	0.72	0.72	0.98	0.70	0.84	0.97	0.37	0.85
f_γ	1.06	0.99	1.22	0.73	1.27	1.22	1.62	1.17
f_{rr}	-0.09	-0.01	-0.03	-0.06	0.05	0.00	0.84	0.05
$f_{\alpha\alpha}$	-0.37	-0.34	-0.40	0.01	0.12	-0.32	0.19	-0.07
$f_{\beta\beta}$	0.14	0.17	0.15	0.19	0.10	0.15	-0.03	0.11
$f_{\gamma\gamma}$	0.00	0.03	0.01	0.00	0.12	0.00	0.00	0.11

[a] The following internal coordinates were used: M-O = D, $M\text{-}F_{ax}$ = R, $M\text{-}F_{eq}$ = r, $\angle F_{eq}\text{-}M\text{-}F_{eq}$ = α, $\angle F_{eq}\text{-}M\text{-}F_{ax}$ = β, $\angle F_{eq}\text{-}M\text{-}O$ = γ. Stretching force constants in mdyn/Å; deformation constants in (mdyn Å)/rad^2.

[b] From ref. 183.

the diffractometer and acquisition of the data at a temperature below the freezing point of the polyether.

The Fluoride-Ion Donor Properties of $TcOF_5$; the $Tc_2O_2F_9^+$ Cation

When HF solutions of $TcOF_5$ are allowed to react with a five-fold molar excess of the strong Lewis acids AsF_5 or SbF_5, bright yellow precipitates are formed. After removal of the solvent and excess Lewis acid, both solids are stable at room temperature for at least three days under dry nitrogen. The reaction between $TcOF_5$ and SbF_5 was shown by X-ray crystallography to proceed according to equation (7.6) (see ***X-ray Crystal***

$$2\ TcOF_5 + 2\ SbF_5 \xrightarrow{HF} Tc_2O_2F_9^+Sb_2F_{11}^- \qquad (7.6)$$

Structure of $Tc_2O_2F_9^+Sb_2F_{11}^-$), and is analogous to the $ReOF_5/SbF_5$[184] and OsO_2F_4/SbF_5[63] systems which yield the dinuclear $Re_2O_2F_9^+$ and $Os_2O_4F_7^+$ cations, respectively. An accurate combining ratio for the reaction of $TcOF_5$ with AsF_5 could not be obtained because of the small scale at which the reaction was carried out. However, the bands that could be attributed to the cation in the Raman spectrum of $TcOF_5 \cdot AsF_5$ are nearly identical in frequency and relative intensity to those of $Tc_2O_2F_9^+Sb_2F_{11}^-$. In addition, the remaining bands were assigned to AsF_6^- with no bands attributable $As_2F_{11}^-$ anion[189] (see ***Raman Spectroscopy***). Moreover, no room temperature stable salts of the $As_2F_{11}^-$ anion have been isolated and $N(C_2H_5)_4^+As_2F_{11}^-$ and $N(C_3H_7)_4^+As_2F_{11}^-$ have been shown to dissociate to the AsF_6^- salts and AsF_5 at 0 °C.[192] Consequently, the reaction between

$TcOF_5$ and AsF_5 likely proceeds according to equation (7.7), by analogy with the OsO_2F_4/AsF_5 system.[63]

$$2\ TcOF_5 + AsF_5 \xrightarrow{HF} Tc_2O_2F_9^+AsF_6^- \qquad (7.7)$$

X-ray Crystal Structure of $Tc_2O_2F_9^+Sb_2F_{11}^-$. Details of the data collection parameters and other crystallographic information are given in Table 7.5. The final atomic coordinates and the equivalent thermal parameters are summarized in Table 7.6. Important bond lengths, corresponding bond valences and bond angles are listed in Table 7.7.

The structure of $Tc_2O_2F_9^+Sb_2F_{11}^-$ consists of well separated $Tc_2O_2F_9^+$ cations and $Sb_2F_{11}^-$ anions (Figure 7.6). The cations are oriented parallel to the *b*-axis of the unit cell and consist of two fluorine-bridged $TcOF_5$-units in which the oxygens are *trans* to the bridging fluorine (Figure 7.7a). The structure of the cation is very similar to those of the valence-isoelectronic species $W_2O_2F_9^-$ [131] and $Re_2O_2F_9^+$ [184] as well as to $Mo_2O_2F_9^{3-}$ [176] and $V_2O_2F_8(H_2O)^{2-}$.[175] The $Sb_2F_{11}^-$ anions in $Tc_2O_2F_9^+Sb_2F_{11}^-$ are oriented parallel to the *c*-axis of the unit cell (Figure 7.7b).

The Tc-O bond lengths (1.634(6) and 1.629(6) Å) are characteristic of Tc-O double bonds and are slightly shorter than the Tc-O bonds found in $TcO_2F_3{\cdot}SbF_5$ (1.640(6) and 1.643(5) Å) and TcO_2F_3 (1.646(9) Å).[41] The terminal Tc-F_t bond lengths (range: 1.782(4) - 1.799(4) Å) are also slightly shorter than the Tc-F_t bonds in $TcO_2F_3{\cdot}SbF_5$ (1.800(5) and 1.804(5) Å) but significantly shorter than in TcO_2F_3 (1.834(7) Å).[41] The bridging Tc-F_b bond lengths (2.061(3) Å) are significantly shorter than the Tc-F_b bond lengths found in TcO_2F_3 (average, 2.080(5) Å)[41] and in $TcO_2F_3{\cdot}SbF_5$ (1.640(6) and

Table 7.5. Summary of Crystal Data and Refinement Results for $Tc_2O_2F_9^+Sb_2F_{11}^-$

formula	$F_{20}O_2Sb_2Tc_2$
space group	*Pbcm* (57)
a (Å)	6.2925(4)
b (Å)	21.205(2)
c (Å)	11.7040(8)
V (Å^3)	1561.7(2)
molecules/unit cell	4
molecular wt (g mol^{-1})	851.50
calcd density (g cm^{-3})	3.622
T (°C)	-90
colour	yellow
μ (mm^{-1})	5.372
wavelength (Å)	0.71073
final agreement factors	R^a = 0.0368
	wR_2 ^{b} = 0.0896

[a] $R = \Sigma||F_o|-|F_c||/\Sigma|F_o|$

[b] $wR_2 = [\Sigma[w(F_o^2-F_c^2)^2]/\Sigma[w(F_o^2)^2]]^{1/2}$

Table 7.6. Final Atomic Coordinates ($\times 10^4$) and Equivalent Isotropic Displacement Coefficients ($Å^2 \times 10^3$) for $Tc_2O_2F_9^+Sb_2F_{11}^-$

	x	*y*	*z*	U_{eq} [a]
Tc(1)	5403.8(8)	2222.9(3)	2500	22.1(2)
Tc(2)	4847.7(8)	308.8(3)	2500	20.7(2)
Sb(1)	120.5(5)	3787.2(1)	775.5(3)	23.0(2)
O(1)	5558(8)	2978(3)	2500	35(1)
O(2)	5280(7)	-449(3)	2500	31(1)
F(1)	2214(6)	2277(2)	2500	50(1)
F(2)	4982(5)	2107(2)	993(3)	47(1)
F(3)	7722(6)	1941(2)	2500	43(1)
F(4)	4326(7)	1275(2)	2500	33(1)
F(5)	1990(6)	290(2)	2500	36(1)
F(6)	4763(5)	426(2)	987(3)	37.3(8)
F(7)	7563(6)	562(2)	2500	38(1)
F(8)	-1177(6)	3013(2)	943(3)	51.2(9)
F(9)	246(6)	3760(2)	-787(4)	53(1)
F(10)	1407(6)	4568(3)	898(3)	47.0(9)
F(11)	2736(5)	3415(2)	999(3)	51(1)
F(12)	-2504(5)	4170(2)	847(3)	50(1)
F(13)	-27(7)	3828(2)	2500	53(2)

[a] Equivalent isotropic *U* defined as one third of the trace of the orthogonalized U_{ij} tensor.

Table 7.7. Bond Lengths (Å), Bond Valences (v.u.) and Bond Angles (deg) in $Tc_2O_2F_9^+Sb_2F_{11}^-$

Bond Lengths (Å) and Corresponding Bond Valences (v.u.)[a]					
Tc(1)	O(1)	F(1)	F(2,2A)	F(3)	F(4)
Bond valence	1.997	1.132	1.139	1.117	0.536
Bond length	1.634(6)	1.784(4)	1.782(4)	1.789(4)	2.061(3)
Total bond valence: 7.06					
Tc(2)	O(2)	F(5)	F(6,6A)	F(7)	F(4)
Bond valence	2.025	1.087	1.117	1.114	0.516
Bond length	1.629(6)	1.799(4)	1.789(4)	1.790(4)	2.075(3)
Total bond valence: 6.98					

Sb(1)	F(8)	F(9)	F(10)	F(11)	F(12)	F(13)
Bond valence	0.883	0.910	0.869	0.881	0.885	0.544
Bond length	1.843(3)	1.832(5)	1.849(3)	1.844(3)	1.842(3)	2.022(1)
Total bond valence: 4.97						

Bond Angles (deg)			
O(1)-Tc(1)-F(1)	97.7(2)	F(6)-Tc(2)-F(6A)	163.7(2)
O(1)-Tc(1)-F(2)	98.0(1)	F(6)-Tc(2)-F(7)	89.2(1)
O(1)-Tc(1)-F(3)	98.1(2)	F(7)-Tc(2)-F(4)	81.7(2)
O(1)-Tc(1)-F(4)	178.8(2)	Tc(1)-F(4)-Tc(2)	158.2(2)

Table 7.7. continued

F(1)-Tc(1)-F(2)	89.3(1)	F(9)-Sb(1)-F(8)	95.6(1)
F(1)-Tc(1)-F(3)	164.2(2)	F(9)-Sb(1)-F(10)	95.0(2)
F(1)-Tc(1)-F(4)	81.0(2)	F(9)-Sb(1)-F(11)	95.2(2)
F(2)-Tc(1)-F(2A)	164.0(3)	F(9)-Sb(1)-F(12)	95.6(2)
F(2)-Tc(1)-F(3)	88.5(1)	F(9)-Sb(1)-F(13)	179.3(2)
F(2)-Tc(1)-F(4)	82.0(1)	F(8)-Sb(1)-F(10)	169.4(2)
F(3)-Tc(1)-F(4)	83.1(2)	F(8)-Sb(1)-F(11)	89.9(2)
O(2)-Tc(2)-F(4)	179.5(2)	F(8)-Sb(1)-F(12)	89.4(2)
O(2)-Tc(2)-F(5)	98.4(2)	F(8)-Sb(1)-F(13)	84.9(2)
O(2)-Tc(2)-F(6)	98.2(1)	F(10)-Sb(1)-F(11)	89.0(2)
O(2)-Tc(2)-F(7)	97.8(2)	F(10)-Sb(1)-F(12)	89.7(2)
F(5)-Tc(2)-F(4)	82.2(2)	F(10)-Sb(1)-F(13)	84.5(2)
F(5)-Tc(2)-F(6)	88.5(1)	F(11)-Sb(1)-F(12)	169.2(2)
F(5)-Tc(2)-F(7)	163.8(2)	F(11)-Sb(1)-F(13)	85.3(2)
F(6)-Tc(2)-F(4)	81.4(1)	Sb(1)-F(13)-Sb(1A)	172.8(3)

[a]Bond valence units (v.u.) are defined in ref. 110. R_0 = 1.89 (Tc(VII)=O), R_0 = 1.83 (Tc(VII)-F) and R_0 = 1.797 (Sb(V)-F) were used along with B = 0.37; Brown, I.D. Department of Physics, McMaster University, Hamilton, Ontario L8S 4M1, Canada, private communication.

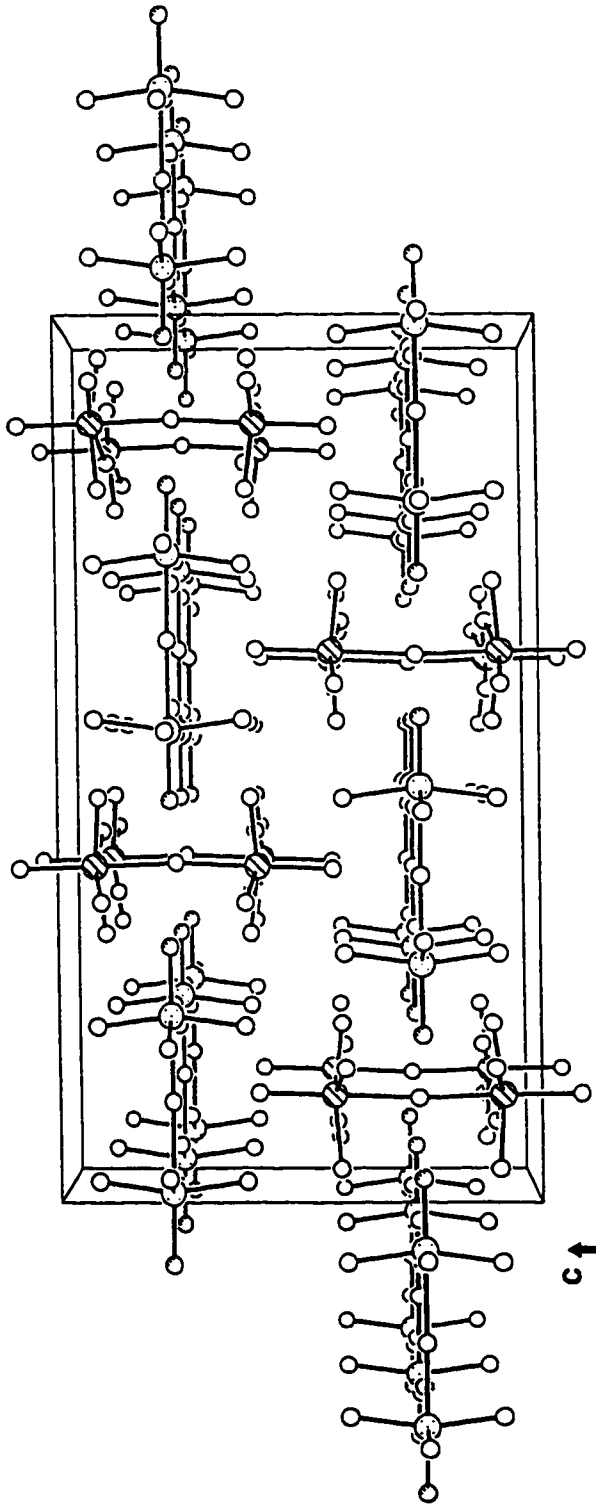

Figure 7.6. View of the unit cell of $Tc_2O_2F_9^+Sb_2F_{11}^-$ showing the packing along the *a*-axis.

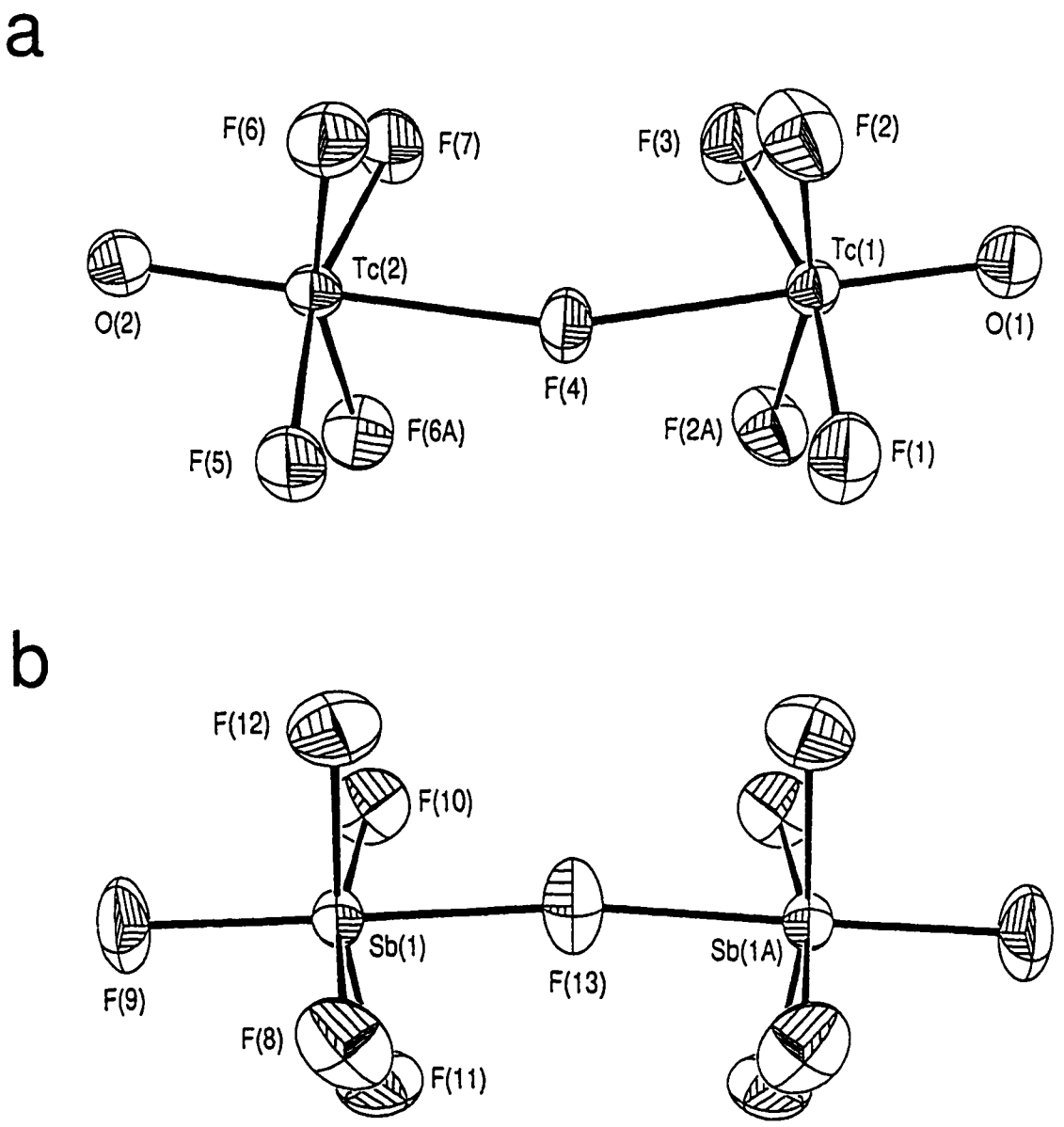

Figure 7.7. Structures of (a) the $Tc_2O_2F_9^+$ cation and (b) the $Sb_2F_{11}^-$ anion in $Tc_2O_2F_9^+Sb_2F_{11}^-$ with thermal ellipsoids at the 50% probability level.

1.643(5) Å). The Sb-F bond lengths in the anion are similar to those reported previously.[190]

The bond valences for individual bonds, as defined by Brown,[110] are given in Table 7.7. The total bond valences for the Tc atoms are 7.06 and 6.98 v.u. (bond valence units), with average contributions of 2.01 v.u./oxygen atom, 1.12 v.u./terminal fluorine atom and 0.53 v.u./bridging fluorine atom. The values for the Tc-O and Tc-F_t indicate that these bonds have the largest covalent character ever observed for a Tc(VII) oxofluoride, which is consistent with the expected increase in electronegativity of the metal resulting from the removal of an oxo ligand. The bond valence value for the bridging Tc-F_b bond approaches 0.50 v.u. and is consistent with the fact that the bridging fluorine is shared equally by the two $TcOF_5$-units of the cation.

The octahedra formed by the light atoms in $Tc_2O_2F_9^+$ are relatively undistorted having averaged O···F_t, F_t···F_t and F_t···F_b distances of 2.584(7), 2.504(5) and 2.538(6) Å, respectively. The bending of the terminal fluorines away from the oxygen is in agreement with the prediction of the VSEPR model[111] and arises from the greater spatial requirement of the oxygen double bond pair domain and its repulsive interaction with the Tc-F single bond pair domains at approximately right angles to it. The average O-Tc-F_t angle is 98.0(2)° and is in excellent agreement with the average of the corresponding angles in $W_2O_2F_9^-$ (99(1)°),[131] $Re_2O_2F_9^+$ (98(1)°)[184] and $V_2O_2F_8(H_2O)^{2-}$ (99.9(1)°).[175] The $Tc_2O_2F_9^+$ cation and the $Sb_2F_{11}^-$ anion adopt eclipsed conformations as observed in the structures of $Re_2O_2F_9^+Sb_2F_{11}^-$ [184] and $Mo_2O_2F_9^{3-}$,[176] and in contrast to the staggered conformation adopted for $W_2O_2F_9^-$ [131] and $V_2O_2F_8(H_2O)_2^-$.[175] The bridging Tc-F-Tc angle (158.2(2)°)

indicates that the packing of the fluorine atoms in $Tc_2O_2F_9^+Sb_2F_{11}^-$ is distorted from hexagonal and cubic closest packing.[130]

The closest cation-anion contact is 2.664(5) Å between an oxygen and a terminal fluorine ligand and is somewhat less than the sum of the van der Waals radii (2.82 Å)[139] whereas the closest interionic fluorine-fluorine contact is 2.894(4) Å which is slightly longer than the sum of the van der Waals radii (2.80 Å).[139]

Raman Spectra of $TcOF_5 \cdot PnF_5$ (Pn = As, Sb). The Raman spectra of $TcOF_5 \cdot PnF_5$ are shown in Figure 7.8. The observed frequencies and their assignments are listed in Table 7.8. The interpretations of the spectra were based on the crystal structure of $Tc_2O_2F_9^+Sb_2F_{11}^-$ using the local symmetry of the $TcOF_5$-unit (C_{4v} point symmetry). Group theory predicts 15 vibrational modes for the $TcOF_5$-unit belonging to the irreducible representations $4A_1 + 2B_1 + B_2 + 4E$ which are all Raman active and the A_1 and E modes which are infrared-active.

A factor-group analysis[115] was carried out in order to evaluate the degree of vibrational coupling within the unit cell of $Tc_2O_2F_9^+Sb_2F_{11}^-$ (Table 7.9). The vibrational modes of the individual $TcOF_5$-units (C_{4v}) were correlated to their site symmetry (C_s) and then to the unit cell symmetry (D_{2h}), space group *Pbcm*, with an adjusted value of 8 for Z. The ν_1-ν_6 and ν_8-ν_{11} modes are each expected to be split into two Raman active A_g, B_{1g}, B_{2g} and B_{3g} components, whereas ν_7-ν_{11} are each split into two inactive A_u components and two infrared-active B_{1u}, B_{2u} and B_{3u} components. However, no factor-group splitting was resolved on the vibrational bands of the cation. The vibrational modes

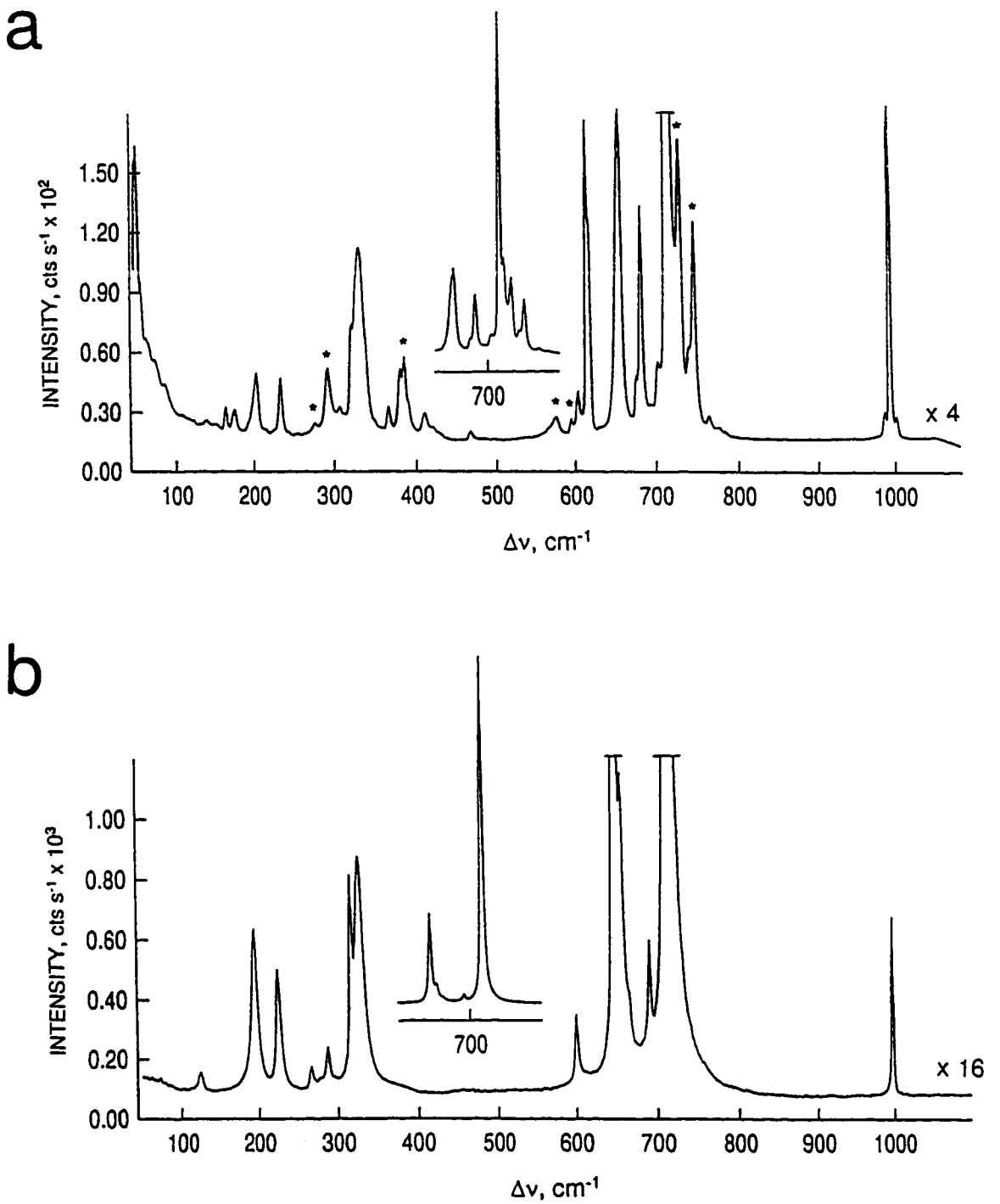

Figure 7.8. Raman spectra of (a) microcrystalline $TcOF_5 \cdot AsF_5$ recorded in FEP at -150 °C and (b) a $TcOF_5 \cdot SbF_5$ single crystal recorded in a Lindemann capillary at 22 °C using 514.5-nm excitation. Asterisks (*) denote FEP lines.

Table 7.8. Raman Frequencies, Assignments and Mode Descriptions for $Tc_2O_2F_9^+Sb_2F_{11}^-$ and $Tc_2O_2F_9^+AsF_6^-$

Frequencies (cm^{-1})[a]		Assignments[b]
$Tc_2O_2F_9^+Sb_2F_{11}^-$ [c]	$Tc_2O_2F_9^+AsF_6^-$ [d]	C_{4v} point symmetry
	1007(1)	
998(4)	998(28)	A_1, ν(TcO)
	992(2)	
		E, $\nu(TcF_{4t})$
	722(28),sh	
717(100)	717(100)	A_1, $\nu(TcF_{4t})$
	706(6)	
692(3)		$Sb_2F_{11}^-$
	685(17)	A_g, $\nu_s(AsF_6)$
666(2), sh		$Sb_2F_{11}^-$
	659(24)	B_1, $\nu(TcF_{4t})$
657(6), sh		$Sb_2F_{11}^-$
650(26)		$Sb_2F_{11}^-$
601(2)		$Sb_2F_{11}^-$
	547(>0),br	E_g, $\nu_{as}(AsF_6)$
458(>0), br	467(>0)	A_1, $\nu(TcF_b)$
	366(2)	T_{2g}, $\delta(AsF_4)$
	339(7),sh	
331(5)	331(14)	E, ρ_w(TcO)
321(4)	321(8),sh	B_2, $\delta(TcF_{4t})$
291(1)		$Sb_2F_{11}^-$
269(1)	253(>0)	A_1, $\pi(TcF_{4t})$
228(3)	233(4)	E, $\delta(TcF_bTc)$
198(3)	202(5)	B_1, $\pi(TcF_{4t})$

Table 7.8. continued

	173(2)	
	162(2)	
128(1)	137(1)	E, $\delta(TcF_4)$
	82(4)	
	59(7)	
	48(21)	

[a] Values in parentheses denote relative intensities; sh: shoulder; br: broad.

[b] ν: stretching; δ: in-plane bending; π: out-of-plane bending; ρ_w: wagging.

[c] Spectrum recorded on single crystal in a Lindemann capillary at 22 °C using 514.5-nm excitation.

[d] Spectrum recorded on microcrystalline solid in FEP at -150 °C using 514.5-nm excitation.

Table 7.9. Correlation Diagrams for the Vibrational Modes of $Tc_2O_2F_9^+Sb_2F_{11}^-$ [a]

$TcOF_5$-unit

		ion local symmetry	site symmetry	crystal symmetry[b]		
		C_{4v}	C_s	D_{2h}		
				A_g (Ra)	$2(\nu_1 - \nu_6),2(\nu_8 - \nu_{11})$	2R,4T
8T	$8(\nu_1 - \nu_4)$	A_1		B_{1g} (Ra)	$2(\nu_1 - \nu_6),2(\nu_8 - \nu_{11})$	2R,4T
8R		A_2	A'	B_{2g} (Ra)	$2(\nu_7 - \nu_{11})$	4R,2T
	$8(\nu_5 - \nu_6)$	B_1		B_{3g} (Ra)	$2(\nu_7 - \nu_{11})$	4R,2T
	$8\nu_7$	B_2	A"	A_u (i.a.)	$2(\nu_7 - \nu_{11})$	4R,2T
8T,8R	$8(\nu_8 - \nu_{11})$	E		B_{1u} (IR)	$2(\nu_7 - \nu_{11})$	4R,T(-T)
				B_{2u} (IR)	$2(\nu_1 - \nu_6),2(\nu_8 - \nu_{11})$	2R,3T(-T)
				B_{3u} (IR)	$2(\nu_1 - \nu_6),2(\nu_8 - \nu_{11})$	2R,3T(-T)

Table 7.9. continued

SbF_6-unit

		ion local symmetry	site symmetry	crystal symmetry[b]		
		C_{4v}	C_1	D_{2h}		
8T	$8(\nu_1 - \nu_4)$	A_1	A	A_g (Ra)	$\nu_1 - \nu_{11}$	3R,3T
8R		A_2		B_{1g} (Ra)	$\nu_1 - \nu_{11}$	3R,3T
	$8(\nu_5 - \nu_6)$	B_1		B_{2g} (Ra)	$\nu_1 - \nu_{11}$	3R,3T
	$8\nu_7$	B_2		B_{3g} (Ra)	$\nu_1 - \nu_{11}$	3R,3T
8T,8R	$8(\nu_8 - \nu_{11})$	E		A_u (i.a.)	$\nu_1 - \nu_{11}$	3R,3T
				B_{1u} (IR)	$\nu_1 - \nu_{11}$	3R,2T(-T)
				B_{2u} (IR)	$\nu_1 - \nu_{11}$	3R,2T(-T)
				B_{3u} (IR)	$\nu_1 - \nu_{11}$	3R,2T(-T)

[a] The symbols T and R denote translatory and rotatory (external) modes, repectively, and R, IR and i.a. in parentheses denote Raman and infrared activity and inactivity, respectively.

[b] Space group *Pbcm*, Z = 4 for $Tc_2O_2F_9^+Sb_2F_{11}^-$, corresponding to 8 $TcOF_5$-units and 8 SbF_6-unit per unit cell.

of the individual SbF_6-units (C_{4v}) were correlated to their site symmetry (C_1) and then to the unit cell symmetry (D_{2h}), with an adjusted value of 8 for Z. Each mode is expected to be split into four Raman active A_g, B_{1g}, B_{2g} and B_{3g} components and three infrared-active B_{1u}, B_{2u} and B_{3u} components.

The Tc-O stretching mode was assigned to the band at 998 [998] cm^{-1} ($Tc_2O_2F_9^+Sb_2F_{11}^-$ frequencies given with $Tc_2O_2F_9^+AsF_6^-$ frequencies in square brackets) and is shifted to high frequency relative to the corresponding mode in $TcOF_5$ (933 cm^{-1}). The symmetric TcF_{4t} stretching mode was assigned to the very intense band at 717 [717] cm^{-1} and is also shifted to high frequency of the corresponding mode in $TcOF_5$ (598 cm^{-1}). This increase in stretching frequencies is consistent with an increase in covalent character of the Tc-O and Tc-F_t bonds resulting from the formal removal of a fluoride ion from $TcOF_5$. The antisymmetric TcF_{4t} stretching B_1 mode is obscured by anion bands in the spectrum of the $Sb_2F_{11}^-$ salt, but occurs at 659 cm^{-1} in the AsF_6^- salt. The remaining antisymmetric TcF_{4t} stretching E mode was not observed, presumably because of its anticipated low intensity in the Raman spectrum. The antisymmetric bridging Tc-F_b stretching mode is expected to be very weak and broad by analogy with the spectra of other fluorine-bridged species, i.e., $MO_2F_3{\cdot}PnF_5$ (M = Tc, Re; Pn = As, Sb), $Os_2O_4F_7^+$ [63] and $Sb_2F_{11}^-$ [152] and were accordingly assigned to the weak band at 458 cm^{-1}. The symmetric stretching and bending modes associated with the Tc-F-Tc bridge are not accounted for in the mode descriptions, but are expected to be very weak and to occur at low frequency. The bending modes were tentatively assigned using the frequency

ordering in $TcOF_5$ and were found to occur at slightly lower frequencies than in $TcOF_5$. The bands at 48, 59 and 82 cm^{-1} are tentatively assigned to lattice modes.

The vibrational modes of the $Sb_2F_{11}^-$ anion[152] were assigned to the bands at 228, 291, 601, 650, 657, 666 and 691 cm^{-1} whereas the modes of the AsF_6^- anion[157] were assigned to the bands at 366, 548 and 685 cm^{-1} and are in agreement with previously reported values.

NMR Spectra of $TcOF_5 \cdot PnF_5$ (Pn = As, Sb). Both $TcOF_5 \cdot AsF_5$ and $Tc_2O_2F_9^+Sb_2F_{11}^-$ are only slightly soluble in anhydrous HF at 25 °C and become completely insoluble at lower temperatures. Attempts to dissolve the solids in SO_2ClF resulted in rapid decomposition at the melting point of the solvent accompanied by the formation of intense blue and red coloured solutions. The ^{19}F NMR spectrum of $TcOF_5 \cdot AsF_5$ in HF at 30 °C consists only of a broad resonance at -191.9 ppm ($\Delta\nu_{1/2}$ = 280 Hz) assigned to HF possibly undergoing fluoride exchange with AsF_6^- and F-on-Tc(VII). The ^{99}Tc NMR spectrum of this solution at 30 °C consists of a broad resonance at 300.8 ppm ($\Delta\nu_{1/2}$ = 300 Hz) and is shielded with respect to $TcOF_5$ (394.5 ppm), which is consistent with the observed shielding of the ^{99}Tc nucleus in going from $TcO_2F_4^-$ (247.4 ppm) to "$TcO_2F_2^+$" (140.3 ppm). No $^1J(^{99}Tc\text{-}^{19}F)$ coupling to the fluorines could be resolved because of the fast quadrupolar relaxation of the ^{99}Tc nucleus. The ^{19}F NMR spectrum of a solution of $Tc_2O_2F_9^+Sb_2F_{11}^-$ in HF at 30 °C consists of broad resonances at 403.4 ppm ($\Delta\nu_{1/2}$ = 1200 Hz) assigned to F-on-Tc(VII), and at -120.3 ppm ($\Delta\nu_{1/2}$ = 8000 Hz) assigned to SbF_6^- or $Sb_2F_{11}^-$ undergoing fluoride exchange, and a singlet at -198.1 ppm ($\Delta\nu_{1/2}$ = 50 Hz) assigned to HF. No signal was

observed that could be assigned to the bridging fluorine of a $Tc_2O_2F_9^+$ cation. The ^{99}Tc NMR spectrum of this solution at 30 °C consists of a broad resonance at 288.0 ppm ($\Delta\nu_{1/2}$ = 960 Hz). These results indicate that HF solutions of both $TcOF_5{\cdot}AsF_5$ and $TcOF_5{\cdot}SbF_5$ produce either the $TcOF_4^+$ cation, the $Tc_2O_2F_9^+$ cation or an equilibrium of the two species. The insolubility of the salts at low temperature prevented the identification of the cationic species present in solution.

The Fluoride-Ion Affinity of $TcOF_5$

Coordination of a fluoride ion to $TcOF_5$ is expected to produce an anion with pseudopentagonal bipyramidal geometry, as was observed for $ReOF_6^-$,[54] WOF_6^{2-},[195] $NbOF_6^{3-}$,[196] $TeOF_6^{2-}$ [197] and IOF_6^-.[198] The affinity of $TcOF_5$ toward the fluoride ion is expected to be lower than that of $ReOF_5$ based on the fluoride-ion affinity trend observed for TcO_2F_3 and ReO_2F_3 (see Chapters 3 and 4). The synthesis of the $TcOF_6^-$ was first attempted by fluorination of $Cs^+TcO_2F_4^-$ with KrF_2 in anhydrous HF according to equation (7.8). However, HF proved to be a stronger fluoro-acid than $TcOF_5$ so that $Cs^+HF_2^-$ was

$$Cs^+TcO_2F_4^- + KrF_2 \xrightarrow{HF} Cs^+TcOF_6^- + {}^1/_2\ O_2 \qquad (7.8)$$

produced instead of $TcOF_6^-$. Another attempt involving the reaction of $TcOF_5$ with CsF in CH_3CN resulted in the reduction of $TcOF_5$ by the solvent. It was also found that $TcOF_5$ does not react when condensed directly over dry CsF at room temperature and that carrying out the reaction at 60 °C over 8 h results in the decomposition of $TcOF_5$ to a dark red solid. Tetramethyl ammonium fluoride, $N(CH_3)_4F$, was not used as a fluoride

source because it would probably be oxidized by $TcOF_5$. Other attempts using NOF and NO_2F as the fluoride-ion sources are presently under way.

Further Fluorination of $TcOF_5$

The synthesis of the TcF_6^+ cation is of particular interest because it is a precursor to TcF_7. Previous attempts to prepare TcF_6^+ salts by direct interaction of TcF_6 with KrF^+ salts were unsuccessful.[193] A better approach would be the fluorination of a Tc(VII) oxofluoride, which was shown to be feasable for $TcOF_5$, OsO_2F_4[63] and $CrOF_4$.[62]

As noted in Chapter 1, the strong oxophilicity of Tc(VII) causes the Tc=O bonds to become increasingly more covalent as the number of oxo ligands decreases. The lone oxygen atom in $TcOF_5$ is therefore very strongly bonded to the Tc, making its replacement by two fluorine ligands rather difficult. The absence of evidence for TcF_7 in the reaction between TcO_2F_3 and KrF_2 indicates that an even stronger fluorinating agent is needed to produce the heptafluoride. Because the KrF^+ cation is the strongest fluorinating agent known,[194] $TcOF_5$ was allowed to react with a five-fold excess of $KrF^+AsF_6^-$ in HF in an attempt to prepare $TcF_6^+AsF_6^-$ [eq. (7.9)]. No evidence for TcF_6^+

$$2\ TcOF_5 + 3\ KrF^+AsF_6^- \xrightarrow[0\ °C]{HF} 2\ TcF_6^+AsF_6^- + 3\ Kr + O_2^+AsF_6^- \qquad (7.9)$$

was found by Raman spectroscopy and no signal corresponding to the formation of $O_2^+AsF_6^-$ could be seen around 1865 cm^{-1}. Instead, a bright yellow solid precipitated from solution and was identified as $Tc_2O_2F_9^+AsF_6^-$ by Raman spectroscopy [eq. (7.10)]. This behaviour is similar to that observed in the reaction of OsO_2F_4 with $KrF^+AsF_6^-$, which did

$$TcOF_5 + KrF^+AsF_6 \xrightarrow{HF} TcOF_5{\cdot}AsF_5 + Kr + {}^1/_2\ F_2 \qquad (7.10)$$

not result in further fluorination, but only in the formation of the dinuclear $Os_2O_4F_7^+$ cation.[63] In both reactions, $KrF^+AsF_6^-$ undergoes autodecomposition to Kr, F_2 and AsF_5 at room temperature. A serious kinetic barrier in these reactions is that they involve the interaction of two cationic species in solution.

Conclusion

The last member of the Tc(VII) oxofluoride series, $TcOF_5$, was synthesized by the reaction of TcO_2F_3 with KrF_2 in anhydrous HF and is the fourth known oxopentafluoride, the others being $ReOF_5$, $OsOF_5$ and IOF_5. The volatile orange solid adopts a C_{4v} geometry as determined by ^{19}F NMR spectroscopy and LDFT calculations. The lengthening of the axial Tc-F bond resulting from the *trans* influence of the oxo ligand was observed in the LDFT-optimized geometry. However, normal coordinate analyses of the vibrational spectra of $TcOF_5$, $ReOF_5$ and $OsOF_5$ indicate that the axial M-F bonds are stronger than the equatorial bonds in each of these molecules.

The fluoride-ion donor behaviour of $TcOF_5$ was investigated and resulted in the synthesis of the AsF_6^- and $Sb_2F_{11}^-$ salts of the dinuclear $Tc_2O_2F_9^+$ cation which consists of two fluorine-bridged $TcOF_5$-units with the bridging fluorine trans to the oxo ligands.

The $TcOF_6^-$ anion could not be prepared from the reaction of $TcOF_5$ with CsF under a number of reaction conditions, which is attributed to the weaker fluoride-ion

affinity of $TcOF_5$ and the possible saturation of the coordination sphere around Tc. The existence of TcF_7^- and TcF_8^{2-} rationalized in terms of thermodynamic stabilization resulting from lattice energy and also the larger size of the valence orbitals of Tc(VI) compared to Tc(VII).

Further fluorination of $TcOF_5$ was attempted using $KrF^+AsF_6^-$ in HF. However, no evidence was obtained to indicate the formation of the TcF_6^+ cation.

CHAPTER 8

SUMMARY AND DIRECTIONS FOR FUTURE RESEARCH

Summary

The fluoride-ion affinities of TcO_2F_3 and ReO_2F_3 were investigated resulting in the full characterization of the $TcO_2F_4^-$ and $ReO_2F_4^-$ anions, which adopt the *cis*-dioxo geometry common to all other d^0 transition metal dioxo-complexes. The stronger Lewis acid character of ReO_2F_3 compared to TcO_2F_3 was demonstrated with the following findings: (a) the increased thermal stability of the solid $ReO_2F_3(CH_3CN)$ adduct at room temperature compared to $TcO_2F_3(CH_3CN)$ which decomposes upon isolation from CH_3CN solvent, (b) the larger CH_3CN complexation shifts in the ^1H and ^{13}C NMR and vibrational spectra of $ReO_2F_3(CH_3CN)$ and (c) the slower exchange rates with the solvent for $ReO_2F_3(CH_3CN)$ than for $TcO_2F_3(CH_3CN)$. The structure of $ReO_3F(CH_3CN)_2 \cdot CH_3CN$, an hydrolysis product of $ReO_2F_3(CH_3CN)$, was determined and the facial arrangement of its oxygens is consistent with the prediction from molecular orbital theory with respect to the optimal overlap between the filled p orbitals of the oxo ligands to the empty $d_{t_{2g}}$ metal orbitals.

The fluorine-bridged dinuclear and trinuclear anions $Re_2O_4F_7^-$ and $Re_3O_6F_{10}^-$ were prepared and structurally characterized. Preliminary evidence for the dinuclear $Tc_2O_4F_7^-$ anion was also found. The structure of polymeric ReO_2F_3 was determined for the first

time in the $K^+Re_2O_4F_7^-\cdot 2ReO_2F_3$ cocrystal and is analogous to that of TcO_2F_3, consisting of infinite chains of fluorine-bridged *cis*-dioxo ReO_2F_4-units with the oxygens *trans* to the fluorine bridges.

Both TcO_2F_3 and ReO_2F_3 act as fluoride-ion donors toward the strong Lewis acids AsF_5 and SbF_5, consistent with the formation of $MO_2F_2^+$ (M = Tc, Re) cations and PnF_6^- (Pn = As, Sb) anions in HF solution. The fluorine-bridged dinuclear cation $Re_2O_4F_5^+$ was identified and structurally characterized by ^{19}F NMR spectroscopy and is the only rhenium species present in a solution of $ReO_2F_3\cdot SbF_5$ in SO_2ClF at room temperature. The proposed fluorine-bridged structure of the cation is a rare example where Re(VII) is five-coordinated instead of its preferred coordination number of six. The structures of $MO_2F_3\cdot AsF_5$ and $MO_2F_3\cdot SbF_5$ (M = Tc, Re) in the solid state consist of alternating fluorine-bridge MO_2F_4- and PnF_6-units as determined by X-ray crystallography and Raman spectroscopy. Dissolution of $ReO_2F_3\cdot SbF_5$ in CH_3CN results in the formation of the thermally unstable $[ReO_2F_2(CH_3CN)_2]^+$ cation and SbF_6^-. The $TcO_2F_3\cdot XeO_2F_2$ was identified as a volatile byproduct of the synthesis of TcO_2F_3 and its structure consists of TcO_2F_3 chains having secondary contacts to XeO_2F_2 chains.

The solution structures of ReO_2F_3 and TcO_2F_3 in SO_2ClF were elucidated by ^{19}F NMR spectroscopy and consist mainly of fluorine-bridged cyclic trimers. Cyclic tetramers and pentamers were also detected for ReO_2F_3, but are present in lower concentrations. Computer simulation was required in order to interpret the spectra of $(ReO_2F_3)_3$, $(ReO_2F_3)_4$ and $(TcO_2F_3)_3$, as they are remarkable examples of magnetic nonequivalence and appear to be unprecedented examples of $(AX_2)_3$ and $(AX_2)_4$ spin systems.

Fluorination of TcO_2F_3 with KrF_2 in anhydrous HF yielded the last member of the technetium(VII) oxofluoride series, $TcOF_5$, and is the fourth oxide pentafluorides known along with $ReOF_5$, $OsOF_5$ and IOF_5. The expected C_{4v} geometry of $TcOF_5$ was confirmed by NMR spectroscopy and by LDFT calculations which also suggest that the axial M-F bonds in MOF_5 (M = Tc, Re, Os) are longer than the equatorial bonds, as expected from the *trans* influence of the oxo ligand. However, normal coordinate analyses on the experimental and theoretical vibrational frequencies of MOF_5 conclude that the stretching force constants are larger for the axial M-F bonds than for the equatorial bonds. These apparently contradictory results suggest that for MOF_5 species, the magnitude of the stretching force constants does not correlated with the bond lengths. The fluoride-ion donor character of $TcOF_5$ was investigated resulting in the synthesis and characterization of the $Tc_2O_2F_9^+$ cation as its $Sb_2F_{11}^-$ and AsF_6^- salts. The structure of the cation consists of two fluorine-bridged $TcOF_5$-units with the oxygens *trans* to bridging fluorine and is similar to its rhenium analogue, $Re_2O_2F_9^+$. The fluoride-ion affinity of $TcOF_5$ was determined to be weaker than that of $ReOF_5$ and attempts to synthesize the $TcOF_6^-$ anion were unsuccessful as well as were attempts to further fluorinate $TcOF_5$ to TcF_6^+.

Conclusions

Our knowledge of the oxofluoride chemistry of Tc(VII) and Re(VII) was significantly expanded though the synthesis and characterization of new compounds ranging from anions to molecular adducts to cations. The noble-gas fluorides XeF_6 and

KrF_2 were instrumental in the synthesis of all of the compounds reported in this Thesis and have proven to be effective, convenient and clean synthetic reagents.

The *cis* arrangement of d^0 transition metal dioxofluorides was observed for all the dioxo-compounds prepared in this Thesis. This "rule", which still has no confirmed exceptions, was interpreted in terms of molecular orbital (MO) theory and atoms in molecules theory,[199] which both provide adequate, although unrelated, explanations for the observed geometries.

The *trans* influence of the oxo ligand was observed for all the six-coordinated Tc and Re dioxo-complexes prepared in this Thesis with the exception of $TcOF_5$, for which this influence still needs to be confirmed. Again, both MO theory and atoms in molecules theory[199] provide adequate interpretations for this phenomenon.

Finally, the Tc(VII) oxofluorides prepared and characterized in this Thesis will help in the identification and better understanding of the behaviour of the technetium species present in the diffusion cascades of UF_6 re-enrichment plants. This will hopefully result in less frequent releases of this radioactive element into the environment.

Directions for Further Research

Further Attempts to Prepare TcO_2^+, TcF_6^+ and TcF_7

It was shown in Chapter 7 that the $TcOF_6^-$ anion cannot be prepared in HF or at elevated temperature because of the weak fluoride-ion affinity of $TcOF_5$ and its relatively low thermal stability. A more promising approach is the reaction of $TcOF_5$ with NO_2F

according to equation (8.1). The use of NOF may also be possible, although it might be oxidized by $TcOF_5$ to NOF_3.

$$TcOF_5 + NO_2F \longrightarrow NO_2^+TcOF_6^- \qquad (8.1)$$

The preparation of $TcF_6^+AsF_6^-$ could be attempted by condensing $TcOF_5$ over solid $KrF^+AsF_6^-$. If this approach is successful, the resulting TcF_6^+ cation could be converted to TcF_7 by fluoride addition using NO_2F. The fluorination of $TcOF_5$ to TcF_7 may also be attempted using O_2F_2 as a fluorinating agent or by low-temperature photolysis with liquid fluorine.

More Complete Characterization of $TcO_3F_2^-$, $TcO_3F_3^{2-}$ and TcO_3^+ and Their Rhenium Analogues

Although TcO_3F has been known for over 35 years,[38] only preliminary work has been published with respect to it fluoride-ion donor-acceptor properties.[40] The rhenium analog, ReO_3F, has been shown to be a moderately strong Lewis acid toward dimethylformamide (DMF) and the fluoride ion,[47] which is rationalized by the tendency of Re(VII) compounds to achieve six-coordination [eq.(8.2) and (8.3)]. Similar reactions

$$ReO_3F + 2\ DMF \longrightarrow ReO_3F(DMF)_2 \qquad (8.2)$$

$$ReO_3F(DMF)_2 + 2\ N(CH_3)_4F \longrightarrow N(CH_3)_4^+ReO_3F_3^{2-} \qquad (8.3)$$

were carried out by mixing the ReO_3F with alkali metal fluorides and heating the mixture to the melting point of ReO_3F.[55] Structural characterization of $ReO_3F_3^{2-}$, $TcO_3F_3^{2-}$ and the

other known valence-isoelectronic anions $OsO_3F_3^-$, $MoO_3F_3^{3-}$ and $WO_3F_3^{3-}$ would be valuable since the arrangement of the ligands in these anions has still not been unequivocally determined. Vibrational spectroscopic studies proposed that $ReO_3F_3^{2-}$ [48] and $WO_3F_3^{3-}$ [200] adopt a C_{2v} meridional arrangement, whereas $OsO_3F_3^-$ [149] and $MoO_3F_3^{3-}$ [148] were assigned a C_{3v} facial geometry. This apparent discrepancy contrasts with the fact that *all* the known d^0 transition metal dioxo species, including those described in this Thesis, adopt *cis* arrangements of oxo ligands around the metal atom. By analogy, the d^0 trioxo transition metal complexes should all adopt facial geometries, which minimize the competition of the oxo ligands for the empty $d_{t_{2g}}$ orbitals of the metal. The synthesis of $TcO_3F_3^{2-}$, $ReO_3F_3^{2-}$ and $OsO_3F_3^-$ could be effectively carried out in CH_3CN using $N(CH_3)_4F$ as the fluoride-ion source according to equations (8.4)-(8.7). It is unlikely that the Tc and

$$MO_3F + 2\ CH_3CN \longrightarrow MO_3F(CH_3CN)_2 \quad (M = Tc, Re) \tag{8.4}$$

$$MO_3F(CH_3CN)_2 + N(CH_3)_4F \xrightarrow{CH_3CN} [N(CH_3)_4^+]_2MO_3F_3^{2-} \tag{8.5}$$

$$OsO_3F_2 + CH_3CN \longrightarrow OsO_3F_2(CH_3CN) \tag{8.6}$$

$$OsO_3F(CH_3CN) + N(CH_3)_4F \xrightarrow{CH_3CN} N(CH_3)_4^+OsO_3F_3^- \tag{8.7}$$

Re anions will be soluble in CH_3CN because of their high charge, however $OsO_3F_3^-$ is expected to be at least slightly soluble so that ^{19}F NMR characterization, solution Raman spectroscopy and crystal growth are possible. If only one equivalent of fluoride is used, it may be possible to prepare $TcO_3F_2^-$ and $ReO_3F_2^-$. The structure of these anions would

be of particular interest since the analogous polymeric $MoO_3F_2^{2-}$ [201] and $WO_3F_2^{2-}$ [202] anions adopt an asymmetric *oxygen-bridged* arrangement, whereas polymeric OsO_3F_2 prefers a symmetric *fluorine-bridged* geometry in the solid state[147] (Figure 8.1). It is worth noting that in both these structures the fluorine ligands are *cis* to each other, which can also be rationalized by invoking the competition of the oxo ligands for the empty $d_{t_{2g}}$ orbitals on the metal (*vide supra*).

The fluoride-ion donor character of TcO_3F and ReO_3F could also be investigated further. So far, only TcO_3^+ was shown to exist by ^{99}Tc and ^{17}O NMR spectroscopy,[40] whereas the ReO_3^+ moiety was characterized by X-ray diffraction in strongly coordinated organometallic complexes such as $(\eta^5\text{-}C_5Me_5)ReO_3$,[203] $[(C_6H_{14}N_3)ReO_3]^+$ [44] and $[(C_6H_{12}S_3)ReO_3]^+$.[45] The reaction of TcO_3F and ReO_3F with AsF_5 or SbF_5 should yield the trigonal planar TcO_3^+ and ReO_3^+ cations according to equation (8.8). Since the MO_3^+

$$MO_3F + PnF_5 \xrightarrow{HF} MO_3^+PnF_6^- \quad (M = Tc, Re;\ Pn = As, Sb) \qquad (8.8)$$

cations are expected to be stronger Lewis acids than their parent MO_3F, dissolution of MO_3^+ salts in a donor solvent such as CH_3CN should yield pseudooctahedral complexes in which the oxo ligands adopt a facial arrangement [eq. (8.9)]. The Tc analog of this

$$MO_3^+PnF_6^- + 3\ CH_3CN \longrightarrow [MO_3(CH_3CN)_3]^+PnF_6^- \qquad (8.9)$$

cation would be of particular interest with respect to its NMR spectra since this facial arrangement of the ligands should yield a near zero electric field gradient at the ^{99}Tc

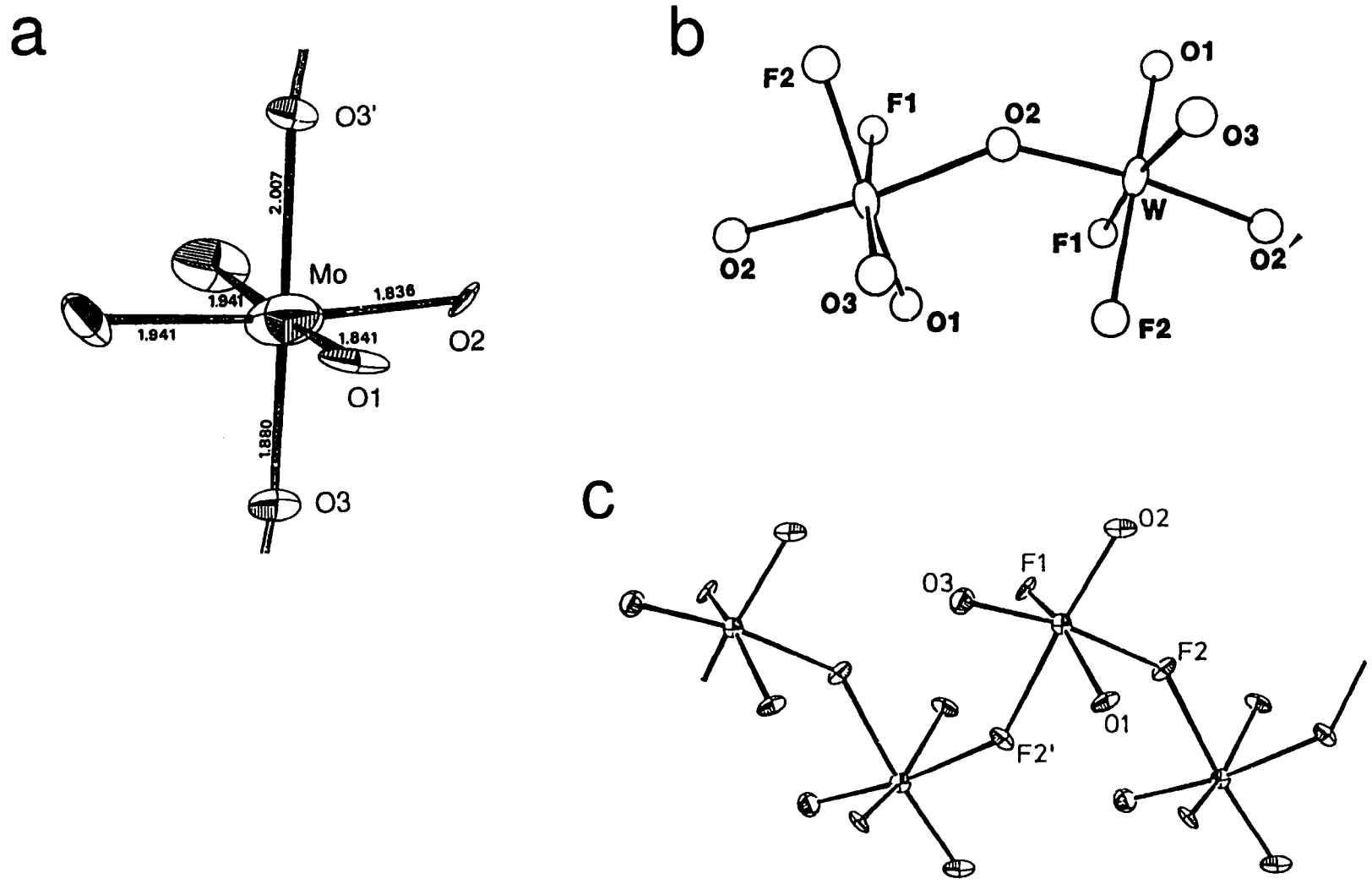

Figure 8.1. Structures of (a) $MoO_3F_2^{2-}$ in $(NH_4)_2MoO_3F_2$,[10] (b) $WO_3F_2^{2-}$ in $Ba_2WO_3F_4$ [11] and (c) OsO_3F_2 [12] (thermal ellipsoids for $MoO_3F_2^{2-}$ and OsO_3F_2 are at the 50% probability level).

nucleus.[59] As a consequence, ^{99}Tc scalar coupling to ^{17}O or even ^{14}N may be observable. Enrichment of the CH_3CN with ^{15}N is also possible.

Now that TcO_2F_3 and ReO_2F_3 can be easily prepared in high purity, their controlled hydrolysis becomes a more convenient route to TcO_3F and ReO_3F than the traditional fluorination in a flow system [eq. (8.10)] .

$$MO_2F_3 + H_2O \xrightarrow{HF} MO_3F + 2\ HF \qquad (8.10)$$

Preparation of Manganese(VII) Oxofluorides

In contrast to Tc(VII) and Re(VII), for which all the oxofluorides are now known, the only fluorine compound of Mn(VII) that has been reported is MnO_3F. This volatile green liquid (m.p. -38 °C) was first synthesized by Wöhler,[204] but is more conveniently prepared according to equation (8.11).[10] A synthetic approach similar to that used to

$$KMnO_4 + IF_5 \longrightarrow MnO_3F + IOF_3 + KF \qquad (8.11)$$

prepare TcO_2F_3, ReO_2F_3 and $TcOF_5$ could be attempted to form the yet unknown MnO_2F_3 and $MnOF_5$. The stronger oxidizing character of the Mn(VII) oxofluoride may require the use of KrF_2 or even KrF^+ in order to fluorinate MnO_3F, according to equations (8.12)-(8.14). By analogy with the observed fluoride-ion donor character of MO_2F_3 and MOF_5 (M = Tc, Re), it can be expected that equations (8.13) and (8.14) would result in the formation of $MnO_2F_3 \cdot AsF_5$ and $MnOF_5 \cdot AsF_5$, respectively. A systematic study of the

fluoride-ion donor and acceptor properties of MnO_3F and the proposed MnO_2F_3 and $MnOF_5$ could also be undertaken.

$$MnO_3F + KrF_2 \xrightarrow{HF} MnO_2F_3 + Kr + {}^1/_2\ O_2 \qquad (8.12)$$

$$MnO_3F + KrF^+AsF_6^- \xrightarrow{HF} 2\ MnO_2F_3 + AsF_5 + 2\ Kr + O_2^+AsF_6^- \qquad (8.13)$$

$$MnO_2F_3 + 2\ KrF^+AsF_6^- \xrightarrow{HF} 2\ MnOF_5 + AsF_5 + 2\ Kr + O_2^+AsF_6^- \qquad (8.14)$$

Preparation of $OTeF_5$ Derivatives of the Tc(VII) Oxofluorides

The $OTeF_5$ group has been described as a pseudohalogen which possesses some characteristics of the fluoride ligand, including a group electronegativity close to that of fluorine and a high resistance to oxidation.[128] Because of the large size and weak basicity of the $OTeF_5$ group, teflated compounds tend not to form bridges in the solid state unlike their fluorinated analogues. The teflated analogues of ReO_2F_3,[128] $ReO_2F_4^-$ [128] and $ReOF_5$,[144] namely $ReO_2(OTeF_5)_3$, $ReO_2(OTeF_5)_4^-$ and $ReO(OTeF_5)_5$, have been previously synthesized and characterized whereas no $OTeF_5$-containing Tc compounds are known. The syntheses of $TcO_3(OTeF_5)$, $TcO_2(OTeF_5)_3$ and $TcO(OTeF_5)_5$ should be relatively straightforward using the ligand exchange method described in equations (8.15)-(8.17).

$$3\ TcO_3F + B(OTeF_5)_3 \xrightarrow{Freon\text{-}114} 3\ TcO_3(OTeF_5) + BF_3 \qquad (8.15)$$

$$TcO_2F_3 + B(OTeF_5)_3 \xrightarrow{Freon\text{-}114} TcO_2(OTeF_5)_3 + BF_3 \qquad (8.16)$$

$$3\ TcOF_5 + 5\ B(OTeF_5) \xrightarrow{\text{Freon-114}} 3\ TcO(OTeF_5)_5 + 5\ BF_3 \qquad (8.17)$$

It should also be possible to form oxoteflate anions of these neutral compounds by reaction with $N(CH_3)_4^+OTeF_5^-$ [eq.(8.18)-(8.19)], and oxoteflate cations by reaction with $As(OTeF_5)_5$, according to equations (8.20)-(8.22).

$$TcO_3(OTeF_5) + N(CH_3)_4^+OTeF_5^- \xrightarrow{SO_2ClF} N(CH_3)_4^+TcO_3(OTeF_5)_2^- \qquad (8.18)$$

$$TcO_2(OTeF_5)_3 + N(CH_3)_4^+OTeF_5^- \xrightarrow{SO_2ClF} N(CH_3)_4^+TcO_2(OTeF_5)_4^- \qquad (8.19)$$

$$TcO_3(OTeF_5) + As(OTeF_5)_5 \xrightarrow{SO_2ClF} TcO_3^+As(OTeF_5)_6^- \qquad (8.20)$$

$$TcO_2(OTeF_5)_3 + As(OTeF_5)_5 \xrightarrow{SO_2ClF} TcO_2(OTeF_5)_2^+As(OTeF_5)_6^- \qquad (8.21)$$

$$TcO(OTeF_5)_5 + As(OTeF_5)_5 \xrightarrow{SO_2ClF} TcO(OTeF_5)_4^+As(OTeF_5)_6^- \qquad (8.22)$$

These compounds are expected to be fairly soluble in SO_2ClF so that characterization by ^{19}F, ^{125}Te and ^{99}Tc NMR as well as solution Raman spectroscopy is possible. In addition, single crystals could be grown by vapour diffusion of Freon-114 into the SO_2ClF solutions, a method that has proven successful for $M(OTeF_5)_6^-$ compounds.

REFERENCES

1. Perrier, C.; Segré, E. *J. Chem. Phys.* **1937**, *5*, 712.
2. Peery, B.F. *Astrophys. J.* **1971**, *163*, L1/L3.
3. (a) Till, J.E.; Shor, R.W.; Hoffman, F.O. *Environmental Effects of the Uranium Fuel Cycle*, ORNL/TM-9150 (NUREG-3738), 1984. (b) Till, J.E. in *Technetium in the Environment*; G. Desmet; C. Myttenaere, Eds.; Elsevier Applied Science: London and New York, 1986; Chapter 1.
4. Möbius, S. in *Gmelin Handbook of Inorganic Chemistry*; 8th ed.; H.K. Kugler; C. Keller, Eds.; Springer-Verlag: Berlin, 1982; Technetium Suppl. Vol. 1, p 195.
5. Giorgi, A.L.; Matthias, B.T. *Phys Rev.* **1978**, *B17*, 2160.
6. Cartledge, G.H. *Corrosion* **1973**, *29*, 361.
7. Schwochau, K. *Angew. Chem. Int. Ed. Engl.* **1994**, *33*, 2258; *Angew. Chem.* **1994**, *106*, 2349.
8. Engelbrecht, A.; Grosse, A.V. *J. Am. Chem. Soc.* **1954**, *76*, 2042.
9. Lotspeich, J.F.; Javan, A.; Engelbrecht, A. *J. Chem. Phys.* **1959**, *31*, 633.
10. (a) Brisdon, A.K.; Holloway, J.H.; Hope, E.G.; Townson, P.J.; Levason, W.; Ogden, J.S. *J. Chem. Soc. Dalton Trans.* **1991**, 3127; (b) Aynsley, E.E. *J. Chem. Soc.* **1958**, 2425.
11. Aynsley, E.E.; Hair, M.L. *J. Chem. Soc.* **1958**, 3747.
12. Beattie, I.R.; Crocombe, R.A.; Ogden, J.S. *J. Chem. Soc. Dalton Trans.* **1977**, 1481.
13. Sunder, W.A.; Stevie, F.A. *J. Fluorine Chem.* **1975**, *6*, 449.
14. Aynsley, E.E.; Peacock, R.D.; Robinson, P.L. *J. Chem. Soc.* **1950**, 1622.
15. Bartlett, N.; Beaton, S.; Reaves, L.W.; Wells, E.J. *Can. J. Chem.* **1964**, *42*, 2531.
16. Holloway, J.H.; Selig, H.; Claassen, H.H. *J. Chem. Phys.* **1971**, *54*, 4305.

17. Alekseichuk, I.S.; Ugarov, V.V.; Sokolov, V.B.; Rambidi, N.G. *J. Struct. Chem. (Engl. Transl.)* **1981**, *22*, 795; *Zh. Strukt. Khim.* **1981**, *22*, 182.
18. Malm, J.G.; Selig, H.; Fried, S. *J. Am. Chem. Soc.* **1960**, *82*, 1510.
19. Malm, J.G.; Selig, H. *J. Inorg. Nucl. Chem.* **1961**, *20*, 189.
20. Claassen, H.H.; Selig, H. *J. Chem. Phys.* **1965**, *43*, 103.
21. Mutterties, E.L.; Packer, K.J. *J. Am. Chem. Soc.* **1964**, *86*, 293.
22. Ruff, O.; Kwasnik, W. *Z. Anorg. Chem.* **1934**, *219*, 65.
23. Hargreaves, G.B.; Peacock, R.D. *J. Chem. Soc.* **1960**, 1099.
24. Peacock, R.D. in *Advances in Fluorine Chemistry*; Peacock, R.D., Ed.; Butterworth: London, 1973; Vol. 7, p 134.
25. Edwards, A.J.; Jones, G.R. *J. Chem. Soc.* **1968**, 2513.
26. Paine, R.T. *Inorg. Chem.* **1973**, *12*, 1457.
27. Claassen, H.H.; Malm, J.G.; Selig, H. *J. Chem. Phys.* **1962**, *36*, 2890.
28. Politov, Yu.A.; Butskii, V.D.; Ellert, O.G.; Pervov, V.S. *Russ. J. Inorg. Chem. (Engl. Transl.)* **1987**, *32*, 290; *Zh. Neorg. Khim.* **1987**, *32*, 520.
29. Lavalle, D.E.; Steele, R.M.; Smith, W.T. *J. Inorg. Nucl. Chem.* **1966**, *28*, 260.
30. Greenwood, N.N.; Earnshaw, A. *Chemistry of the Elements*; Pergamon: Oxford, 1984; Chapter 24.
31. Selig, H.; Chernick, C.C.; Malm, J.G. *J. Inorg. Nucl. Chem.* **1961**, *19*, 377.
32. Hugill, D.; Edwards, A.J.; Peacock, R.D. *Nature* **1963**, *200*, 672.
33. Siegel, S.; Northrop, D.A. *Inorg. Chem.* **1966**, *5*, 2187.
34. Hugill, D.; Peacock, R.D. *J. Chem. Soc. A* **1966**, 1339.
35. Holloway, J.H.; Selig, H. *J. Inorg. Nucl. Chem.* **1968**, *30*, 473.
36. Shamir, J.; Malm, J. *J. Inorg. Nucl. Chem. Suppl.* **1976**, 107.
37. Edwards, A.J.; Jones, G.R.; Sills, R.J. *J. Chem. Soc. A* **1970**, 2521.
38. Selig, H.; Malm, J.G. *J. Inorg. Nucl. Chem.* **1963**, *25*, 349.
39. Binenboym, J.; El-Gad, U.; Selig, H. *Inorg. Chem.* **1974**, *13*, 319.
40. Franklin, K.J.; Lock, C.J.L.; Sayer, B.G.; Schrobilgen, G.J. *J. Am. Chem. Soc.* **1982**, *104*, 5303.

41. Mercier, H.P.A.; Schrobilgen, G.J. *Inorg. Chem.* **1993**, *32*, 145.

42. Schrobilgen, G.J., McMaster University, unpublished results.

43. Herrmann, W.A.; Serrano, R.; Bock, H. *Angew. Chem. Int. Ed. Engl.* **1984**, *23*, 383; *Angew. Chem.* **1984**, *96*, 364.

44. Wieghardt, K.; Pomp, C.; Nuber, B.; Weiss, J. *Inorg. Chem.* **1986**, *25*, 1659.

45. Küppers, H.J.; Nuber, B.; Weiss, J.; Cooper, S.R. *J. Chem. Soc., Chem. Commun.* **1990**, 979.

46. (a) Jacob, E.; Fähnle, M. *Angew. Chem. Int. Ed. Engl.* **1976**, *15*, 159; *Angew. Chem.* **1976**, *88*, 190; (b) Schrobilgen, G.J.; Holloway, J.H.; Russell, D.R. *J. Chem. Soc. Dalton Trans.* **1984**, 1411.

47. Gerlach, U.; Ringel, C. *Z. Chem.* **1977**, *17*, 306.

48. Kuhlmann, W.; Sawodny, W. *J. Fluorine. Chem.* **1977**, *9*, 341.

49. Lis, T. *Acta Crystallogr.* **1983**, *C39*, 961.

50. Kuhlmann, W.; Sawodny, W. *J. Fluorine Chem.* **1977**, *9*, 337.

51. Peacock, R.D. *J. Chem. Soc.* **1955**, 602.

52. Bol'shakov, A.M.; Glushkova, M.A.; Buslaev, Yu. A. *Dokl. Chem. (Engl. Transl.)* **1983**, *273*, 417; *Dokl. Akad. Nauk SSSR*, **1983**, *273*, 1134.

53. Selig, H.; Karpas, Z. *Isr. J. Chem.* **1971**, *9*, 53.

54. Giese, S.; Seppelt, K. *Angew. Chem. Int. Ed. Engl.* **1994**, *33*, 461; *Angew. Chem.* **1994**, *106*, 473.

55. Yagodin, G.A.; Opalovskii, A.A.; Rakov, É.G.; Dudin, A.S. *Dokl. Chem. (Engl. Transl.)* **1980**, *252*, 316; *Dokl. Akad. Nauk. SSSR*, **1980**, *252*, 1400.

56. Harris, R.K. in *NMR and the Periodic Table*; Harris, R.K.; Mann, B.E., Eds.; Academic: London, 1978; Chapter 1.

57. (a) Mason, J. in *Multinuclear NMR*; Mason, J. Ed.; Plenum: New York, 1987; Chapter 2; (b) Sanders, J.C.P.; Schrobilgen, G.J. in *A methodological Approach to Multinuclear NMR in Liquids and Solids - Chemical Applications*; NATO Advanced Study Institute, Magnetic Resonance; Granger, P., Harris, R.K., Eds.; Kluwer Academic: Dordrecht, 1990; Chapter 11.

58 Multinuclear NMR; Mason, J. Ed.; Plenum: New York, 1987; pp 625-629.

59. Akitt, J.W.; McDonald, W.S. *J. Magn. Res.* **1984**, *58*, 401.

60. Rehder, D. in *Multinuclear NMR*; Mason, J., Ed.; Plenum: New York, 1987; Chapter 19.

61. O'Connell, L.A.; Pearlstein, R.M.; Davison, A.; Thornback, J.R.; Kronauge, J.F.; Jones, A.G. *Inorg. Chim. Acta* **1989**, *161*, 39.

62 Christe, K.O.; Wilson, W.W.; Bougon, R.A. *Inorg. Chem.* **1986**, *25*, 2163.

63. Casteel, W.J., Jr.; Dixon, D.A.; Mercier, H.P.A.; Schrobilgen, G.J. *Inorg. Chem.* **1996**, *35*, 4310.

64. AECD Radioisotope Safety Poster INFO-0142-1/Rev. 2, *Rules for Working with Radioisotopes in a Basic Laboratory.*

65. Syvret, T.R.G. Ph.D. Thesis, McMaster University, Hamilton, Ontario, Canada (1987).

66. Schrobilgen, G.J.; Holloway, J.H.; Granger, P.; Brevard, C. *Inorg. Chem.* **1978**, *17*, 980.

67. Christe, K.O.; Wilson, W.W. *J. Fluorine Chem.* **1990**, *47*, 117.

68. Gillespie, R.J.; Netzer, A.; Schrobilgen, G.J. *Inorg. Chem.* **1974**, *13*, 1445.

69. (a) Mercier, H.P.A.; Sanders, J.C.P.; Schrobilgen, G.J.; Tsai, S.S. *Inorg. Chem.* **1993**, *32*, 386; (b) C.J. Haffman, *Inorg. Synth.*, **1953**, *4*, 150.

70. Chernick, C.L.; Malm, J.G. *Inorg. Synth.* **1966**, *8*, 258.

71. Bezmel'nitsyn, V.N.; Legasov, V.A.; Chainvanov, B.B. *Proc. Acad. Sci. USSR (Engl. Transl.)* **1997**, *235*, 365; *Dokl. Akad. Nauk. SSSR* **1977**, *235*, 96.

72. Kinkead, S.A.; Fitzpatrick, J.R.; Foropoulos, J., Jr.; Kissane, R.J.; Purson, J.D. In *Inorganic Fluorine Chemistry, Towards the 21st Century*, ACS Symposium Series 555; Thrasher, J.S.; Strauss, S.H., Eds., ACS, Washington, DC: 1994; p 40.

73. Christe, K.O.; Wilson, W.W.; Wilson, R.D.; Bau, R.; Feng, J.-A. *J. Am. Chem. Soc.* **1990**, *112*, 7619.

74. Selig, H.; Fried, S. *Inorg. Nucl. Chem. Lett.* **1971**, *7*, 315.

75. SMART and SAINT, Release 4.05; Siemens Energy and Automation Inc.: Madison, WI, 1996.

76. Sheldrick, G.M. SADABS (Siemens Area Detector Absorption Corroections), personnal communication, 1996.

77. Walker, N.; Stuart, D. *Acta Crystallogr.* **1983**, *A39*, 158.

78. Sheldrick, G.M. SHELXTL PLUS. Release 4.21/V: Siemens Analytical X-Ray Instruments Inc.: Madison, WI, 1993.

79. Sheldrick, G.M. SHELXL, Release 5.03; Siemens Analytical X-Ray Instruments Inc.: Madison, WI, 1994.

80. Martin, J.S.; Quirt, A.R. *J. Magn. Reson.* 1971, 5, 318.

81. Xsim package, copyright 1998, University of Manitoba.

82. Laatikainen, R.; Niemitz, M.; Sundelin, J.; Hassinen, T. Perch Package, University of Kuopio, Finland, 1995.

83. Claassen, H.H.; Selig, H.; Shamir, J. *Appl. Spectrosc.* **1969**, *23*, 8.

84. Mukherjee, A.; Spiro, T.G. SVIB program 656, Bulletin 15(1), Quantum Chemistry Program Exchange, Indiana University, 1995.

85. Andzelm, J.; Wimmer, E.; Salahub, D. R. In *The Challenge of d and f Electrons: Theory and Computation*; Salahub, D. R.; Zerner, M. C., Eds.; ACS Symposium Series, No. 394, American Chemical Society: Washington D.C., 1989; p.228; Andzelm, J. In *Density Functional Theory in Chemistry*; Labanowski, J.; Andzelm, J., Eds.; Springer-Verlag: New York, 1991, p.155; Andzelm, J.; Wimmer, E. *J. Chem. Phys.* **1992**, *96*, 1280. DGausss, is a density functional program which is part of Unichem and is available from Oxford Molecular.

86. Godbout, N.; Salahub, D. R.; Andzelm, J.; Wimmer, E. *Can. J. Chem.* **1992**, *70*, 560.

87. Lee, C. Unpublished results. See the Unichem manual, Version 3.0.

88. Vosko, S. J.; Wilk, L.; Nusair, W. *Can. J. Phys.* **1980**, *58*, 1200.

89. Becke, A. D. *Phys. Rev. A* **1988**, *38*, 3098; Becke, A. D. In *The Challenge of d and f Electrons: Theory and Computation*; Salahub, D. R.; Zerner, M. C., Eds.;

ACS Symposium Series, No. 394, American Chemical Society: Washington D.C., 1989; p. 166; Becke, A. D. *Int. J. Quantum. Chem. Symp.* **1989**, *23*, 599.

90. Perdew, J. P. *Phys. Rev. B* **1986**, *33*, 8822.
91. Komornicki, A.; Fitzgerald, G. *J. Chem. Phys.* **1993**, *98*, 1398 and references therein.
92. Christe, K.O.; Bougon, R.J. *J. Chem. Soc., Chem. Commun.* **1992**, 1056.
93. Christe, K.O.; Dixon, D.A.; Mack, H.G.; Oberhammer, H.; Pagelot, A.; Sanders, J.C.P.; Schrobilgen, G.J. *J. Am. Chem. Soc.* **1993**, *115*, 11279.
94. Mattes, R.; Müller, G.; Becher, H.J. *Z. Anorg. Allg. Chem.* **1972**, *389*, 177.
95. (a) Vlasse, M.; Moutou, J. M.; Cervera-Marzal, M.; Chaminade, J. P.; Hagenmuller, P. *Rev. Chim. Minér.* **1982**, *19*, 58. (b) Chaminade, J. P.; Moutou, J. M.; Villeneuve, G.; Couzi, M.; Pouchard, M.; Hagenmuller, P. *J. Solid State Chem.* **1986**, *65*, 27.
96. Buslaev, Y.A.; Petrosyants, S.P. *J. Struct. Chem. (Engl. Transl.)* **1969**, *10*, 983; *Zh. Strukt. Khim.* **1969**, *10*, 1105.
97. (a) Buslaev, Y.A.; Shcherbakov, V.A. *J. Struct. Chem. (Engl. Transl.)* **1966**, *7*, 332; *Zh. Strukt. Khim.* **1966**, *7*, 345. (b) Buslaev, Y.A.; Petrosyants, S.P.; Tarasov, V.P. *J. Struct. Chem. (Engl. Transl.)* **1970**, *11*, 574; *Zh. Strukt. Khim.* **1970**, *11*, 616. (c) Buslaev, Y.A.; Petrosyants, S.P.; Tarasov, V.P. *Dokl. Phys. Chem. (Engl. Transl.)* **1970**, *193*, 548; *Dokl. Akad. Nauk SSSR*, **1970**, *193*, 611.
98. Sergienko, V.S.; Porai-Koshits, M.A.; Khodashova, T.S. *J. Struct. Chem. (Engl. Transl.)* **1972**, *13*, 431; *Zh. Strukt. Khim.* **1972**, *13*, 461.
99. Grandjean, D.; Weiss, R. *Bull. Soc. Chim. France* **1967**, *36*, 3049.
100. Ryan, R.R.; Martin, S.H.; Reisfeld, M.J. *Acta Crystallogr.* **1971**, *B27*, 1270.
101. Leimkühler, M.; Mattes, R. *J. Solid State Chem.* **1986**, *65*, 260.
102. Raghavan, P. *At. Data Nuc. Data Tables* **1989**, *42*, 189.
103. A weak resonance at 304.0 ppm was also observed and is tentatively assigned to the dinuclear anion $Tc_2O_4F_7^-$.

104. A weak resonance at 1235 ppm was also observed and is tentatively assigned to the dinuclear anion $Tc_2O_4F_7^-$.

105. Buslaev, Y.A.; Kokunov, Y.V.; Bochkareva, V.A. *J. Struct. Chem. (Engl. Transl.)* **1972**, *13*, 570; *Zh. Strukt. Khim.* **1972**, *13*, 611.

106. Buslaev, Y.A.; Kokunov, Y.V.; Bochkaryova, V.A.; Shustorovich, E.M. *J. Inorg. Nucl. Chem.* **1972**, *34*, 2861.

107. Hibbert, R.C. *J. Chem. Soc., Chem. Commun.* **1985**, 317.

108. Krebs, B. *Z. Anorg. Allg. Chem.* **1971**, *380*, 146.

109. German, K.E.; Grigor'ev, M.S.; Kuzina, A.F.; Gulev, B.F.; Spitsyn, V.I. *Dokl. Chem. (Engl. Transl.)* **1986**, *287*, 60; *Dokl. Akad. Nauk SSSR* **1986**, *287*, 650.

110. (a) Brown, I.D. *J. Solid State Chem.* **1974**, *11*, 214; (b) Brown, I.D. In *Structure and Bonding in Crystals*; O'Keefe, M., Navrotsky, A., Eds.; Academic Press: London, 1981; Vol. 2, p 1; (c) Brown, I.D.; Altermatt, D. *Acta Crystallogr.* **1985**, *B41*, 244.

111. Gillespie, R.J.; Hargittai, I. *The VSEPR Model of Molecular Geometry*; Allyn and Bacon, Boston, MA, 1991.

112. Rhiel, M.; Wocadlo, S.; Massa, W.; Dehnicke, K. *Z. Anorg. Allg. Chem.* **1996**, *622*, 1195.

113. Christe, K.O.; Wilson, R.D.; Schack, C.J. *Inorg. Chem.* **1981**, *20*, 2104.

114. Gillespie, R.J.; Bytheway, I.; Tang, T.H.; Bader, R.F. *Inorg. Chem.* **1996**, *35*, 3954.

115. Carter, R.J. *J. Chem. Educ.* **1971**, *48*, 297 and references therein.

116. Mercier, H.P.A.; Sanders, J.C.P.; Schrobilgen, G.J. *J. Am. Chem. Soc.* **1994**, *116*, 2921.

117. Berg, R.W. *Spectrochim. Acta* **1978**, *34A*, 655.

118. Bottger, G.L.; Geddes, A.L. *Spectrochim. Acta* **1978**, *21*, 1701.

119. Kabisch, G.; Klose, M. *J. Raman Spectrosc.* **1978**, *7*, 311.

120. Kabisch, G. *J. Raman Spectrosc.* **1980**, *9*, 279.

121. Wilson, W.W.; Christe, K.O.; Feng, J.; Bau, R. *Can. J. Chem.* **1989**, *67*, 1898.

122. (a) Günthard, H.H.; Kováts, E. *Helv. Chim. Acta* **1952**, *35*, 1190. (b) Yamadera, R.; Kremm, S. *Spectrochim. Acta* **1968**, *24A*, 1677.

123. Reedijk, J.; Zuur, A.P.; Groeneveld, W.L. *Rec. Trav. Chim.* **1967**, *86*, 1127.

124. Sosa, C.; Andzelm, J.; Elkin, B.C.; Wimmer, E.; Dobbs, K.D.; Dixon, D.A. *J. Phys. Chem.* **1992**, *96*, 6630.

125. Karakida, K.; Fukuyama, T.; Kuchitsu, K. *Bull. Chem. Soc. Jpn.* **1974**, *47*, 299.

126. Selig, H.; El-Gad, U. *J. Inorg. Nucl. Chem.* **1973**, *35*, 3517.

127. Peacock, R.D. *J. Chem. Soc.* **1955**, 603.

128. Casteel, W.J., Jr.; MacLeod, D.M.; Mercier, H.P.A.; Schrobilgen, G.J. *Inorg. Chem.* **1996**, *35*, 7279.

129. Edwards, A.J.; Steventon, B.R. *J. Chem. Soc. A* **1968**, 2507.

130. Edwards, A.J.; Jones, J.R. *J. Chem. Soc A* **1968**, 2074. Although bridging oxygens were originally reported for the tetrameric WOF_4 structure, it is now clear that the anomalously short terminal W-F bonds observed in the structure must be attributed to terminal W-O double bonds and that the structure is actually fluorine-bridged.

131. Hoskins, B.F.; Linden, A.; O'Donnell, T.A. *Inorg. Chem.* **1987**, *26*, 2223.

132. Cady, G.H.; Hargreaves, G.B. *J. Chem. Soc.* **1961**, 1568.

133. Elemental fluorine showed no signs of reaction with ReO_3F in HF at room temperature, over a 24 h period.

134. Smith, D.F. *J. Am. Chem. Soc.* **1963**, *85*, 816.

135. Buslaev, Yu.A.; Kokunov, Yu.V.; Bochkareva, V.A.; Shostorovich, E.M. *J. Struct. Chem. (Engl. Transl.)* **1972**, *13*, 491; *Zh. Strukt. Khim.* **1972**, *13*, 526.

136. Holloway, J.H.; Schrobilgen, G.J. *Inorg. Chem.* **1980**, *19*, 2632.

137. Holloway, J.H.; Schrobilgen, G.J. *Inorg. Chem.* **1981**, *20*, 3363.

138. Bacon, J.; Dean, P.A.W.; Gillespie, R.J. *Can. J. Chem.* **1970**, *48*, 3413.

139. Bondi, A. *J. Phys. Chem.* **1964**, *68*, 441.

140. The anion···cation contacts are defined as a distance being smaller or equal than the sum of the ionic radii of the cation (Li^+ = 1.38 Å, K^+ = 1.51 Å and Cs^+ =

1.67 Å for a coordination number of 6, 8 and 6, respectively) and the van der Waals radii of the F (1.40 Å) or O (1.42 Å) they make contact with.

141. Chaminade, J.P.; Moutou, J.M.; Villeneuve, G.; Couzi, M.; Pouchard, M.; Hagenmuller, P. *J. Solid State Chem.* **1986**, 65, 27.

142. Sens, I.; Stenger, H.; Müller, J.; Dehnicke, K. *Z. Anorg. Allg. Chem.* **1992**, *610*, 117.

143. Arnaudet, L.; Bougon, R.; Bau, R.; Charpin, P.; Isabey, J.; Lance, M.; Nierlich, M.; Vigner, J. *Can. J. Chem.* **1990**, *68*, 507.

144. Turowsky, L.; Seppelt, K. *Z. Anorg. Allg. Chem.* **1990**, *590*, 37.

145. (a) Krebs, B.; Müller, A.; Beyer, H. *J. Chem. Soc., Chem. Commun.* **1968**, 263; (b) Krebs, B.; Muller, A.; Beyer, H.H. *Inorg. Chem.* **1969**, *8*, 436.

146. Fawcett, J.; Holloway, J.H.; Russell, D.R. *J. Chem. Soc. Dalton Trans.* **1981**, 1212.

147. Bougon, R.; Buu, B.; Seppelt, K. *Chem. Ber.* **1993**, *126*, 1331.

148. Griffith, W.P. *J. Chem. Soc. A* **1969**, 211.

149. Jones, P.J.; Levason, W.; Tajik, M. *J. Fluorine Chem.* **1984**, *25*, 195.

150. ReO3(CH3CN)2+

151. Yagodin, G.A.; Dudin, A.S.; Rakov, É.G.; Opalovskii, A.A. *Rus. J. Inorg. Chem. (Engl. Transl.)* **1980**, *25*, 91; *Zh. Neorg. Khim.* **1980**, *25*, 170.

152. Gillespie, R.J.; Landa, B. *Inorg. Chem.* **1973**, *12*, 1383.

153. Gillespie, R.J.; Moss, K.C. *J. Chem. Soc. A* **1966**, 1170.

154. (a) Dean, P.A.W.; Gillespie, R.J.; Hulme, R.; Humphreys, D.A. *J. Chem. Soc. A* **1971**, 341; (b) Moore, J.W.; Baird, H.W.; Miller, H.B. *J. Am. Chem. Soc.* **1968**, *90*, 1358.

155. Buchholz, N.; Leimkühler, M.; Kiriazis, L.; Mattes, R. *Inorg. Chem.* **1988**, *27*, 2035.

156. Davidovich, R.L.; Zemskova, L.A. *Russ. Chem. Bull. (Engl. Transl.)* **1978**, 1492; *Izv. Akad. Nauk SSSR (Ser. Khim.)* **1978**, 1708.

157. Christe, K.O.; Charpin, P.; Soulie, E.; Bougon, R.; Fawcett, J.; Russell, D.R. *Inorg. Chem.* **1984**, *23*, 3756.

158. (a) Brown, S.D.; Gard, G.L. *J. Chem. Phys.* **1976**, *64*, 1219; (b) Kochikov, I.V.; Yagola, A.G.; Kuramshina, G.M.; Kovba, V.M.; Pentin, Yu.A. *Spectrochim. Acta* **1985**, *41A*, 185.

159. Kidd, R.G.; Matthews, R.W. *Inorg. Chem.* **1972**, *11*, 1156.

160. Buslaev, Yu.A.; Kokunov, Yu.V.; Bochkareva, V.A.; Shustorovich, E.M. *Russ. J. Inorg. Chem. (Engl. Transl.)* **1972**, *17*, 1675; *Zh. Neorg. Khim.* **1972**, *17*, 3184.

161. Reedijk, J.; Groeneveld, W.L. *Rec. Trav. Chim.* **1968**, *87*, 1079.

162. Peterson, S.W.; Willett, R.D.; Huston, J.L. *J. Chem. Phys.* **1973**, *59*, 453.

163. Martins, J.F.; Bright Wilson, Jr., E. *J. Mol. Spectrosc.* **1968**, *26*, 410.

164. Templeton, D.H.; Zalkin, A.; Forester, J.D.; Williamson, S.M. in *Noble Gas Compounds*; Hyman, H.H., Ed.; University of Chicago: Chicago, 1963, p 221.

165. Turowsky, L.; Seppelt, K. *Z. Anorg. Allg. Chem.* **1992**, *609*, 153.

166. Gillespie, R.J.; Robinson, E.A. *Angew. Chem. Int. Ed. Engl.* **1996**, *35*, 495; *Angew. Chem.* **1996**, *108*, 539.

167. Christe, K.O.; Wilson, W.W. *Inorg. Chem.* **1988**, *27*, 3763.

168. (a) Boldrini, P; Gillespie, R.J.; Ireland, P.R.; Schrobilgen, G.J. *Inorg. Chem.* **1974**, *13*, 1690; (b) McKee, D.E.; Zalkin, A.; Bartlett, N. *Inorg. Chem.* **1973**, *12*, 1713; (c) Gillespie, R.J.; Martin, D.; Schrobilgen, G.J. *J. Chem. Soc. Dalton Trans.* **1977**, 2234.

169. (a) Adams, C.J.; Bartlett, N. *Isr. J. Chem.* **1978**, *17*, 114; (b) Bartlett, N.; Gennis, M.; Gibler, D.D.; Morrell, B.K.; Zalkin, A. *Inorg. Chem.* **1973**, *12*, 1717; (c) Bartlett, N.; Einstein, F.; Stewart, D.F.; Trotter, J. *J. Chem. Soc., Chem. Commun.* **1966**, 550; (d) Bartlett, N.; Einstein, F.; Stewart, D.F.; Trotter, J. *J. Chem. Soc. A* **1967**, 1190; (e) Frlec, B.; Bohinc, M.; Charpin, P.; Drifford, M. *J. Inorg. Nucl. Chem.* **1972**, *34*, 2938.

170. Peacock, R.D. in *Advances in Fluorine Chemistry*; Peacock, R.D Ed.; Butterworth: London, 1973; Vol. 7, p 113.

171. Edwards, A.J.; Steventon, B.R. *J. Chem. Soc. A* **1968**, 2503.

172. Il'in, E.G.; Ignatov, M.E.; Golovanov, B.V.; Butskii, V.D.; Buslaev, Yu. A. *Dokl. Chem. (Engl. Transl.)* **1984**, 92; *Dokl. Akad. Nauk SSSR* **1984**, *275*, 379.

173. Edwards, A.J.; Taylor, P. *J. Chem. Soc., Chem. Commun.* **1971**, 1376.174. Haase, W. *Acta Crystallogr.* **1974**, *B30*, 2465.

175. Hilbers, M.; Leimkühler, M.; Mattes, R. *Z. Naturforsch.* **1989**, *44b*, 383.

176. Leimkühler, M.; Buchholz, N.; Mattes, R. *Z. Naturforsch.* **1989**, *44b*, 389.

177. Bovey, F.A.; Jelinski, L.; Miran, P.A. *Nuclear Magnetic Resonance Spectroscopy*; 2nd ed.; Academic: San Diego, 1988; pp 157-158.

178. Jones, R.G.; Hirst, R.C.; Bernstein, H.J *Can. J. Chem.* **1965**, *43*, 683.

179. Jameson, C.J. in *Multinuclear NMR*; Mason, J., Ed.; Plenum: New York, 1987; p 108.

180. Meublat, L.; Lance, M.; Bougon, R. *Can. J. Chem.* **1989**, *67*, 1729.

181. Bougon, R.; Cicha, W.V.; Lance, M.; Meublat, Nierlich, M.; Vigner. J. *Inorg. Chem.* **1991**, *30*, 102.

182. Bartlett, N.; Trotter, J. *J. Chem. Soc. A* **1968**, 543.

183. Shalabi, A.S.; Nour, E.M.E.; *Gazz. Chim. Ital.* **1991**, *121*, 555.

184. Schrobilgen, G.J.; Holloway, J.H.; Russell, D.R. *J. Chem. Soc. Dalton Trans.* **1984**, 1441.

185. Grinberg, A.A. *Acta Physicochim. URSS*, **1935**, *3*, 573.

186. Syrkin, Y.K. *Izv. Akad. Nauk SSSR, Otd. Khim. Nauk* **1948**, 69.

187. Chatt, J.; Duncanson, L.A.; Venanzi, L.M. *J. Chem. Soc.* **1955**, 4456.

188. Orgel, L.F. *J. Inorg. Nucl. Chem.* **1956**, *2*, 137.

189. Barraclough, C.G.; Besida, J.; Davies, P.G.; O'Donnell, T.A. *J. Fluorine Chem.* **1988**, *38*, 405.

190. Davies, C.G.; Gillespie, R.J.; Ireland, P.R.; Sowa, J.M. *Can. J. Chem.* **1974**, *52*, 2048.

191. The *trans* influence is the tendency of a ligand to weaken the bond *trans* to itself and is an equilibrium phenomenon, whereas the *trans* effect is a kinetic

phenomenon and describes the tendency of a ligand to influence the rate of substitution of the ligand *trans* to itself.

192. Dean, P.A.W.; Gillespie, R.J.; Hulme, R. *J. Chem. Soc. D* **1969**, 990.

193. Schrobilgen, G.J. private communication.

194. Christe, K.O.; Dixon, D.A. *J. Am. Chem. Soc.* **1992**, *114*, 2978.

195. Sakharov, S.G.; Kokunov, Yu.V.; Gustyakova, M.P.; Buslaev, Yu.A. *Dokl. Chem. (Engl. Transl.)* **1984**, *276*, 385; *Dokl. Akad. Nauk. SSSR*, **1984**, *276*, 148.

196. Stomberg, R. *Acta Chem. Scand.* **1983**, *A37*, 453.

197. Christe, K.O.; Dixon, D.A.; Sanders, J.C.P.; Schrobilgen, G.J.; Wilson, W.W. *Inorg. Chem.* **1993**, *32*, 4089.

198. Christe, K.O.; Dixon, D.A.; Mahjoub, A.R.; Mercier, H.P.A.; Sanders, J.C.P.; Seppelt, K.; Schrobilgen, G.J.; Wilson, W.W. *J. Am. Chem. Soc.* **1993**, *115*, 2696.

199. Bader, R.F.W. *Atoms in Molecules: A Quantum Theory*; Oxford University: Oxford, England, 1990.

200. (a) Dehnicke, K.; Pausewang, G.; Rüdorff, W. *Z. Anorg. Allg. Chem.* **1969**, *366*, 64; (b) Couzi, M.; Rodriguez, V.; Chaminade, J.P.; Fouad, M.; Ravez, J. *Ferroelectrics* **1988**, *80*, 109.

201. Mattes, R.; Müller, G.; Becher, H.J. *Z. Anorg. Allg. Chem.* **1975**, *416*, 256.

202. Torardi, C.C.; Brixner, L.H. *Mat. Res. Bull.* **1985**, *20*, 137.

203. Herrmann, W.A.; Serrano, R.; Schäfer, A.; Küsthardt, U. *J. Organomet. Chem.* **1984**, *272*, 55.

204. (a) Wöhler, F. *Ann. Chim. Phys.* **1828**, *37*, 101; (b) Wöhler, F. *Ann. Miner.* **1828**, *3*, 163. (From reference 17b).